



# **Designed Monomeric and Dimeric Molecular Tweezers for Functional Protein Targeting**

**Dissertation**

**Inesa Hadrović, M. Sc.**

**Essen, 2020**

# **Designed Monomeric and Dimeric Molecular Tweezers for Functional Protein Targeting**

**Dissertation**

submitted to attain the academic degree of

Doctor of natural sciences

**Dr. rer. nat.**

presented by

**Inesa Hadrović**

born Semić

Faculty of Chemistry

University Duisburg-Essen

Essen, 2020

# DuEPublico

Duisburg-Essen Publications online

UNIVERSITÄT  
DUISBURG  
ESSEN

*Offen im Denken*

ub | universitäts  
bibliothek

Diese Dissertation wird via DuEPublico, dem Dokumenten- und Publikationsserver der Universität Duisburg-Essen, zur Verfügung gestellt und liegt auch als Print-Version vor.

**DOI:** 10.17185/duepublico/74090

**URN:** urn:nbn:de:hbz:465-20230328-080048-4

Alle Rechte vorbehalten.

# **Maßgeschneiderte monomere und dimere molekulare Pinzetten für funktionales Proteintargeting**

**Dissertation**

zur Erlangung des akademischen Grades eines  
Doktors der Naturwissenschaften

**Dr. rer. nat.**

vorgelegt von

**Inesa Hadrović**

geb. Semić

Fakultät für Chemie  
Universität Duisburg-Essen

Essen, 2020

*This page intentionally left blank.*

The presented work was realized in the period from January 2017 to September 2020 at the Department of Organic Chemistry, University of Duisburg-Essen, under the supervision of Prof. Dr. Thomas Schrader within Collaborative Research Center (CRC) 1093, funded by Deutsche Forschungsgemeinschaft (DFG).

The first examiner: **Prof. Dr. Thomas Schrader**

The co-examiner: **Prof. Dr. Shirley Knauer**

The external examiner: **Prof. Dr. Luc Brunsveld**

Chair of the examination board: **Prof. Dr. Bettina Siebers**

Date of doctoral exam: **21.01.2021**

*This page intentionally left blank.*

Die vorliegende Arbeit wurde im Zeitraum von Januar 2017 bis September 2020 im Arbeitskreis von Prof. Dr. Thomas Schrader am Institut für Organische Chemie der Universität Duisburg-Essen im Rahmen des Sonderforschungsbereichs (SFB) 1093 durchgeführt und durch die Deutsche Forschungsgemeinschaft (DFG) gefördert.

Referent: **Prof. Dr. Thomas Schrader**

Korreferent: **Prof. Dr. Shirley Knauer**

Drittgutachter: **Prof. Dr. Luc Brunsveld**

Vorsitzende des Prüfungsausschusses: **Prof. Dr. Bettina Siebers**

Der Tag der mündlichen Prüfung: **21.01.2021**



*This page intentionally left blank.*



## DECLARATION

Herewith, I declare that acc. § 7 para. (2) c) + e) of the doctoral degree regulations of the Faculty of Chemistry at University Duisburg-Essen, the presented dissertation entitled:

**„Designed Monomeric and Dimeric Molecular Tweezers for Functional Protein Targeting”**

was written by myself and that I did not use any other than given sources. The dissertation has not been submitted to any other university in this or a similar form.

Essen, 13. October 2020

---

Inesa Hadrović

*This page intentionally left blank.*

## DIE EIDESSTATTLICHE ERKLÄRUNG

Hiermit erkläre ich gem. § 7 Abs. (2) c) + e) der Promotionsordnung der Fakultät für Chemie zur Erlangung des Dr. rer. nat., dass ich die vorliegende Dissertation mit dem Titel:

**„Maßgeschneiderte monomere und dimere molekulare Pinzetten für funktionales Proteintargeting“**

selbstständig verfasst habe und bei der Abfassung der Dissertation nur die angegeben Hilfsmittel benutzt und alle wörtlich oder inhaltlich übernommenen Stellen als solche gekennzeichnet habe. Die vorliegende Dissertation wurde in dieser oder ähnlicher Form noch bei keiner anderen Universität eingereicht.

Essen, 13. Oktober 2020

---

Inesa Hadrović

*This page intentionally left blank.*

## PUBLICATIONS AND CONFERENCES

Some parts of this cumulative dissertation have been published, submitted to scientific journals, or presented at conferences and symposia.

### Publications based on this dissertation

- I **Hadrović, I.**, Rebmann, P., Klärner, F.-G., Bitan, G., Schrader, T. *Molecular Lysine Tweezers Counteract Aberrant Protein Aggregation*. *Frontiers in Chemistry* 7, 657, **2019**. DOI: 10.3389/fchem.2019.00657
- II Guillory, X., **Hadrović, I.**, de Vink, P., Brunsveld, L., Schrader, T., Ottmann, C. *Supramolecular Enhancement of Natural 14-3-3 Protein Ligands*. *J. Am. Chem. Soc.*, 143, 13495–13500, **2021**. DOI: org/10.1021/jacs.1c07095
- III Meiners, A., Bäcker, S., **Hadrović, I.**, Heid, C., Beuck, C., Ruiz-Blanco, Y., Mieres-Perez, J., Pörschke, M., Grad, J.-N., Vallet, C., Hoffmann, D., Bayer, P., Sanchez-Garcia, E., Schrader, T., Knauer, S. *Targeting a protein epitope: Specific inhibition of the Survivin-CRM1-interaction by peptide-modified Molecular Tweezers*. *Nature Commun.* 12, 1505, **2021**. DOI: org/10.1038/s41467-021-21753-9
- IV van der Meer, S.-B., **Hadrović, I.**, Meiners, A., Loza, K., Heggen, M., Knauer, S., Bayer, P., Schrader, T., Beuck, C., Epple, M. *New tools to probe the protein surface: Ultrasmall gold nanoparticles carry amino acid binders*. *J. Phys. Chem. B*, 125, 115-127, **2021**. DOI: doi.org/10.1021/acs.jpccb.0c09846

### Other Publications

- V Li, Z., Siddique, I., **Hadrović, I.**, Kirupakaran, A., Zhang, Y., Klärner, F.-G., Schrader, T., Bitan, G., *Lysine-selective molecular tweezers are cell-penetrant and concentrate in lysosomes*, *Commun. Biol.*, 1076, **2021**. DOI:10.1038/s42003-021-02603-2
- VI Vaquero, M.H., Bouquiobc, D., Kallaba, M. Biggs, K., Nairb, G., Ochoabd, J., Garvina, A.H., Heid, C., **Hadrović, I.**, Poewe, W., Wenning, G.K., Klärner, F.G., Schrader, T., Bitan, G., Stefanova, N. *The molecular tweezer CLR01 reduces aggregated, pathologic, and seeding-competent  $\alpha$ -synuclein in experimental multiple system*

*atrophy*. Molecular Basis of Diseases, Biochimica et Biophysica Acta, Vol. 1865; Issue 11, 165513, **2019**. DOI: 10.1016/j.bbadis.2019.07.007

- VII Semić, I., Čavar-Zeljковиć S.** *The Influence of Some 4-Methylcoumarins on the Electrodeposition and Characteristics of Zinc Coating*, Protection of Metals and Physical Chemistry of Surfaces, Vol. 51, 131–137, **2015**. DOI: 10.1134/S2070205115010141

## Conferences

- I Smolin, D., Kujawski, K., Heid, C., Sowislok, A., Hadrović, I., Gsell, C.** *Designed Copolymers and Molecular Tweezers for Protein Surface Recognition*. 2<sup>nd</sup> International CRC1903 Symposium "Supramolecular Chemistry on Protein" in Essen, 20. – 21.09.2017.
- II Hadrović, I., Heid, C., Bitan, G., Schrader, T.** *Development of new molecular tweezers against neurodegenerative diseases*. WORKSHOP - Strategies & tools for modulating pathologic protein self-assembly, i3S Porto, 21. – 22.03.2019.
- III Hadrović, I., Meiners, A., van der Meer, S.B., Seiler, S., Guillory, X., de Vink, P., Heid, C., Beuck, C., Niemeyer, F., Vallet, C., Epple, M., Bayer, P., Hartmann, L., Ottmann, C., Knauer, S. K., Schrader T.** *Molecular Hybrid Tweezers – New Concepts for Protein Specificity*. 3<sup>rd</sup> International CRC1903 "Symposium Supramolecular Principles in Biological System" in Essen, 10. – 12.09.2019.
- IV Hadrović, I., Heid, C., Epple, M., Bayer, P., Hartmann, L., Ottmann, C., Knauer, S. K., Schrader T.** *Molecular Tweezers as modulators of protein – protein interactions*. 10<sup>th</sup> Young Chemists' Ruhr Symposium in Essen, 19.09.2019.
- V Hadrović, I., Heid, C., Epple, M., Bayer, P., Hartmann, L., Ottmann, C., Knauer, S. K., Schrader T.** *Molecular Tweezers as modulators of protein – protein interactions*. Indo-German Workshop 2019 Multivalent and Adaptive Bioinspired Material" in Essen, 25 – 27.09.2019. Best Poster Award.



## SUMMARY

One motivation behind supramolecular chemistry is the design of artificial receptors that can mimic or even overrule certain natural processes for therapeutic and diagnostic purposes. The specific recognition of a hot region on a protein surface is critical for the functioning of many biological systems. With this in mind, the presented cumulative dissertation brings up the rational design and synthesis of the new generation of water-soluble macrocyclic receptors – molecular tweezers as well as probing their abilities to influence target functions of different proteins of interest, such as amyloid, Survivin, and 14-3-3 proteins. Each of those proteins has a relevant role in widely spread diseases of the modern age, such as Alzheimer’s and Parkinson’s disease, different types of cancer, diabetes, obesity, and cardiovascular diseases, respectively.

Firstly, the detailed introduction (Chapter 1) provides the state of the knowledge before the beginning of this dissertation, at the same time pointing on scientific gaps, which need to be fulfilled by this work. The introduction starts with a concise overview of the context and development of supramolecular chemistry, followed by a description of the most prominent host scaffolds. Here, the accent was put on diverse molecular tweezers as synthetic receptors. Afterwards, the concept and application of Klärner’s and Schrader’s water-soluble molecular tweezers have been introduced together with the first experimental pieces of evidence on their selectivity towards specific natural amino acids in aqueous media, describing the first major scientific breakthrough in the field. The second discussed breakthrough was discovery that molecular tweezers beside recognition of isolated single molecules, can exhibit affinities towards peptides and proteins featured with well-exposed basic amino acids. This served as a good starting point for the elucidation of supramolecular chemistry on proteins. Subsequently, the first examples of protein recognition by molecular tweezer and other supramolecular host scaffolds are shown. Furthermore, the possible pathways in which various synthetic molecules can influence protein-protein interactions are explained. The structural as well as functional characteristics of the three proteins of interest are summarized in a separate chapter, followed with an overview of known modulators molecules, respectively.

After outlining the dissertation’s aim coherently (Chapter 2), its detailed implementation has been shown separately in the four most prominent publications from

this work– related to the three above mentioned proteins (Chapter 3). Besides the published part, the further realization of the dissertation’s aim can be found in the next chapter, represented by the work that has not been published yet (Chapter 4). The first section in the unpublished part reveals the work dedicated to an important implementation of molecular tweezers, namely as aggregation inhibitors of amyloid proteins. This section describes the synthesis of the novel fluorinated molecular tweezer, made to enhance tweezer’s ability to penetrate the blood-brain barrier. The second section in the unpublished part presents the synthesis of divalent molecular tweezers and the first experimental insights gained in their application for biological purposes.

Achieved results are summarized in the conclusion section (Chapter 5), reflecting on the existing literature sources presented at the beginning of the work. However, the remaining challenges and further possibilities for improving molecular tweezers’ features are given in outlook (Chapter 5.2). At the end of the dissertation, there is an explanation of the author’s contributions to the presented publications (Chapter 6)., unpublished experimental part relevant for unpublished part (Chapter 7), and *appendix* containing the list of abbreviations used, the author’s acknowledgement and *curriculum vitae*.

## ZUSAMMENFASSUNG

Eine Motivation der supramolekularen Chemie ist das Design künstlicher Rezeptoren, welche in der Natur vorkommenden Prozesse imitieren oder außer Kraft setzen können; diese Tatsache lässt sich für die Diagnose und Therapie von Krankheiten nutzen. Die spezifische Erkennung aktiver Zentren auf Proteinoberflächen ist essenziell für viele biologische Systeme. Vor diesem Hintergrund vereint die vorliegende kumulative Dissertation sowohl rationales Design, als auch die Synthese einer neuen Generation wasserlöslicher, makrozyklischer Rezeptoren - hier molekulare Pinzetten, und legt deren Leistung dar, gezielte Funktionen verschiedener Proteine, wie beispielsweise Amyloid, Survivin und 14-3-3 Proteine, zu beeinflussen. Jedes dieser Proteine spielt eine relevante Rolle in heutzutage weitverbreiteten Krankheiten wie Morbus Alzheimer, Morbus Parkinson, verschiedensten Arten von Krebs, Diabetes, Übergewicht und kardiovaskulären Erkrankungen.

In der ausführlichen Einleitung (Kapitel 1) wurde der Wissensstand zu Beginn der Dissertation aufgezeigt, sowie die offenen wissenschaftlichen Lücken in diesem Themenbereich, welche durch diese Dissertation geschlossen werden sollten. Zudem bietet die Einleitung dieser Arbeit eine gezielte Übersicht über Zusammenhang und Entwicklung der supramolekularen Chemie, gefolgt von der Beschreibung der prominentesten Wirtsgerüste. Der Fokus wurde hierbei auf verschiedenste molekulare Pinzetten in der Funktion als synthetische Rezeptoren gelegt. Im nächsten Schritt wurden Konzeptionierung und Anwendung von Klärner's und Schrader's wasserlöslichen molekularen Pinzetten erläutert, sowie die ersten experimentellen Hinweise auf ihre Selektivität gegenüber natürlich vorkommender Aminosäuren in wässriger Umgebung, welches den ersten großen wissenschaftlichen Durchbruch beschreibt. Es konnte gezeigt werden, dass nicht nur zwischen einzelnen, isolierten Molekülen ein Einschlusskomplex gebildet wird, sondern dieser auch zwischen Peptiden und Proteinen entstehen kann, deren Aminosäuren ungehindert erreicht werden können. Diese Tatsache diente als Anhaltspunkt zur Aufklärung der supramolekularen Chemie an Proteinen, hier explizit die Proteinerkennung vom molekularen Pinzette und anderen supermolekularen Wirtsgerüsten. Weiterhin wird erläutert, welche unterschiedlichen Arten der Beeinflussung synthetischer Moleküle auf Protein-Protein-Wechselwirkungen möglich sind. Die strukturellen und

funktionellen Charakteristika, der drei näher betrachteten Proteine werden, separat zusammengefasst, gefolgt von einer Übersicht bekannter regulierender Moleküle.

Nach Darstellung der Zielsetzung dieser Dissertation (Kapitel 2) wird anhand der vier hervorstechender Publikationen, welche sich mit den drei am Anfang genannten Proteinen (Kapitel 3) befassen, die detaillierte Anwendung der vorliegenden Arbeit gezeigt. Neben dem bereits publizierten Teil wird das Ziel der Dissertation im darauffolgenden Kapitel behandelt und mit Ergebnissen gestützt, die bisher nicht veröffentlicht wurden (Kapitel 4). Das erste Kapitel des unveröffentlichten Teiles behandelt eine weitere, wichtige Weise der Implementierung molekularer Pinzetten, hier als Aggregationsinhibitoren von Amyloidproteinen. Dieses Kapitel beschreibt detailliert die Synthese neuartiger, fluorierter molekularer Pinzetten vor dem Hintergrund der Fähigkeit dieser Moleküle, die Blut-Hirn-Schranke zu passieren. Das zweite Kapitel dieses Teiles des unveröffentlichten Teiles präsentiert die Synthese bivalenter molekularer Pinzetten und erste, experimentell gestützte Einsicht in die Anwendung für biologische Zwecke.

Die erzielten Ergebnisse dieser Dissertation werden in der Zusammenfassung (Kapitel 5) dargestellt, unter Berücksichtigung der am Anfang der Arbeit vorgestellten Literatur. Weitere Herausforderungen und Möglichkeiten für die Verbesserung der Eigenschaften von molekularen Pinzetten werden im Ausblick zusammengefasst (Kapitel 5.2). Am Ende der Dissertation wird schließlich der Beitrag des Autors bei den vorgestellten Publikationen diskutiert (Kapitel 6). Zusätzlich ist am Ende noch der unveröffentlichte experimentelle Teil (Kapitel 7), der relevant ist für den unveröffentlichten Ergebnisabschnitts, sowie Abkürzungsverzeichnis, Danksagung und der Lebenslauf angehängt.

---

## CONTENTS

<b>Declaration</b> .....	<b>i</b>
<b>Die Eidesstattliche Erklärung</b> .....	<b>iii</b>
<b>Publications And Conferences</b> .....	<b>I</b>
<b>Summary</b> .....	<b>III</b>
<b>Zusammenfassung</b> .....	<b>V</b>
<b>Contents</b> .....	<b>VII</b>
<b>1 Introduction</b> .....	<b>1</b>
1.1 Supramolecular Chemistry – Context and Development .....	1
1.1.1 From Molecular to Supramolecular Chemistry .....	2
1.2 Molecular Recognition .....	4
1.2.1 Host-Guest Chemistry, Self-Assembly, and Lattice Inclusion .....	4
1.2.2 The most Prominent Host Scaffolds .....	6
1.3 Diverse Molecular Tweezers as Synthetic Receptors .....	10
1.4 Water-soluble Molecular Tweezers – Concept and Applications .....	14
1.4.1 Klärner’s Molecular Clips and Tweezers.....	14
1.4.2 Development of Water-soluble Molecular Tweezers.....	19
1.5 Utilization of Molecular Tweezer Features in Enzyme Inhibition .....	27
1.6 Supramolecular Chemistry on Proteins.....	29
1.6.1 Protein Recognition .....	29
1.6.2 Protein – Protein Interactions PPI.....	30
1.6.3 Amyloid Proteins.....	33
1.6.4 14-3-3 Proteins .....	41
1.6.5 Survivin.....	51
<b>2 Aim Of The Dissertation</b> .....	<b>64</b>
2.1 Design of Peptide-modified Molecular Tweezers .....	64
2.2 Design of Di- and Multivalent Tweezer Skeletons.....	67
2.3 The Covalent Fusion of Recognition Units to Molecular Tweezers .....	69
<b>3 Publications Based on This Dissertation</b> .....	<b>71</b>

3.1	Publication I .....	72
3.2	Publication II .....	82
3.3	Publication III .....	89
3.4	Publication IV .....	102
<b>4</b>	<b>Unpublished Work From This Dissertation.....</b>	<b>116</b>
4.1	Trifluoromethoxy Molecular Tweezer as a Drug Candidate .....	116
4.1.1	Background Information.....	116
4.1.2	Silver-mediated Oxidative Trifluoromethylation.....	117
4.1.3	Synthesis of Novel Fluorinated Molecular Tweezer .....	118
4.1.4	Conclusion and Outlook.....	119
4.2	Design of Divalent Molecular Tweezer Constructs of Defined Geometries ...	121
4.2.1	Background Information.....	121
4.2.2	Tailormade Divalent Tweezer Constructs for Targeting Survivin .....	122
4.2.3	Synthesis of Double Tweezer-precision Oligomer Conjugates .....	125
4.2.4	Results and Discussion.....	128
<b>5</b>	<b>Conclusion And Outlook .....</b>	<b>134</b>
5.1	Conclusion .....	134
5.2	Outlook .....	136
<b>6</b>	<b>Author's Contributions to Presented Publications .....</b>	<b>143</b>
<b>7</b>	<b>The Experimental Part Relevant for Unpublished Work .....</b>	<b>145</b>
7.1	Materials and methods.....	145
7.1.1	Reagents .....	145
7.1.2	Solvents .....	145
7.1.3	Freeze-drying.....	145
7.1.4	Chromatography .....	146
7.1.5	Oxygen-free Techniques.....	146
7.1.6	NMR Spectrometry .....	146
7.1.7	Mass Spectrometry .....	147
7.1.8	Molecular Modeling.....	147
7.1.9	Isothermal Titration Calorimetry.....	148
7.1.10	Pull-down assays and Western Blotting Analysis .....	148

---

7.2	Synthesis .....	149
7.2.1	Synthesis of 57 .....	149
7.2.2	Synthesis of 58 .....	151
7.2.3	Synthesis of 59 .....	157
7.2.4	Synthesis of 60 .....	158
7.2.5	Synthesis of 64 .....	162
7.2.6	Synthesis of 65 .....	165
7.2.7	Synthesis of 66 .....	168
<b>8</b>	<b>References.....</b>	<b>171</b>
<b>9</b>	<b>Appendix.....</b>	<b>180</b>
9.1	List of Abbreviations.....	180
9.2	ACKNOWLEDGMENTS – DANKSAGUNG – ZAHVALNICA.....	184
9.3	<i>CURRICULUM VITAE</i> .....	189

*Mojim Rediteljima*



## 1 INTRODUCTION

### 1.1 Supramolecular Chemistry – Context and Development

The word *Supramolecule* was known in the literature as early as 1937 when German scientist Wolf introduced the term *Übermolekül* to describe the intermolecular interaction of coordinatively saturated species.<sup>[1]</sup> However, supramolecular chemistry as an individual multidisciplinary research area was first recognized in 1987 when the Nobel Prize in Chemistry was awarded to Lehn, Pedersen, and Cram. The trio was acknowledged for the development and use of molecules with structure-specific interactions of high selectivity.<sup>[2]</sup> Thereupon, the Nobel laureate Lehn defined supramolecular chemistry as the study of assemblies of molecules that bind and organize into entities of greater complexity than individual units.<sup>[3]</sup>

Indeed, the brief throwback about the beginnings of supramolecular chemistry brings up the question: Why did it take more than 40 years from the introduction of the term *Übermolekül* to Lehn's definition of supramolecular chemistry? To answer it, one must consider the paradigm in thinking of the relevant scientific community at that time. The persuasion that properties of molecules are properties of the molecules themselves, while the interactions with the environment are considered small and negligible, significantly hindered the development of supramolecular chemistry as an independent field of research. Besides, one must consider the lack of specialized experimental methods and equipment to investigate the binding kinetics of complex supramolecular assemblies as the second, although somewhat technical, but still no less critical answer. Nevertheless, due to building evidence of the importance of the environmental influence on molecule properties, e.g., solvent effects, it became clear that the surroundings almost always have a non-negligible effect. Consequently, the intermolecular interactions were gradually placed in the focus of research, and a new research area was born.<sup>[4]</sup> Supramolecular chemistry opens opportunities to chemists, biologists, physicists, computational and material scientists, and others to work synergistically towards novel discoveries.

As a relatively young research area, supramolecular chemistry has considerably matured over the last few decades. Several significant steps forward have been made

toward the construction of larger and more complex architectures such as macromolecules, multimetallic helicates, rotaxanes, photo switchable catalysts, metal-organic frameworks, coordination polymers, *etc.*<sup>[5,6]</sup> Further research achievements along the same lines, led to the 2016 Nobel Prize in Chemistry, being awarded to Sauvage, Stoddart, and Feringa for the design and construction of complex synthetic molecular machines.<sup>[7]</sup> Their studies are applied as guidance for the advanced application of supramolecular chemistry in the field of nano architectonics in drug-delivery systems and functional polymeric supramolecular materials.<sup>[5,8]</sup>

### 1.1.1 From Molecular to Supramolecular Chemistry

While traditional chemistry generally focuses on the covalent binding between molecular precursors, according to Lehn, supramolecular chemistry emphasizes going “beyond molecular chemistry” (Figure 1).<sup>[9]</sup> It monitors reversible and directional non-covalent intermolecular interactions that exist extensively in numerous vital biological processes.<sup>[10]</sup>

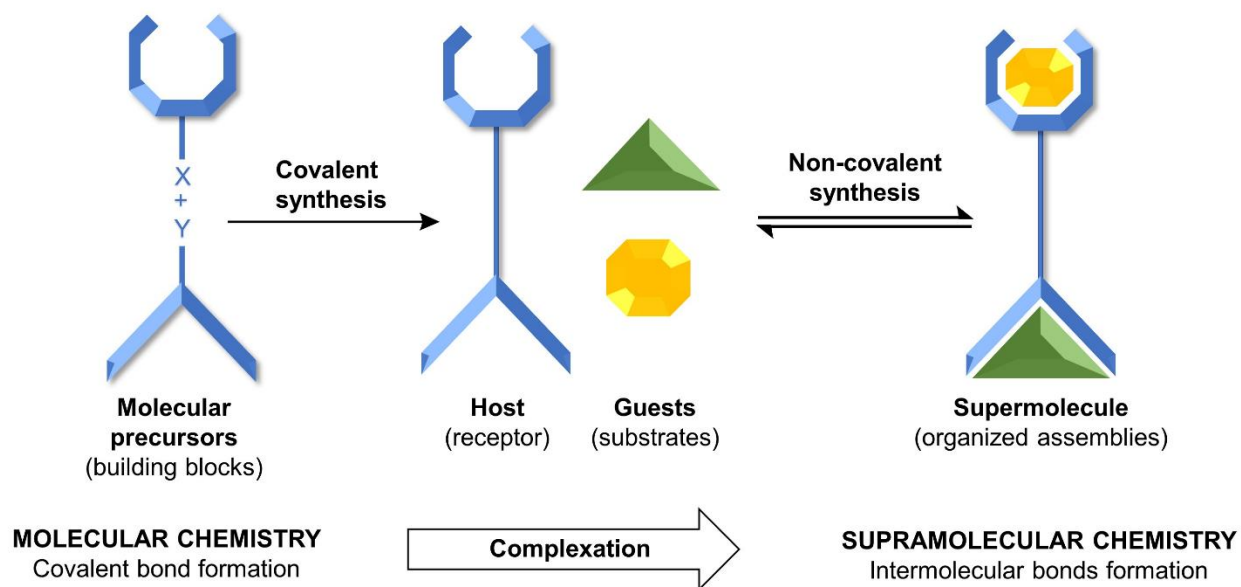


**Figure 1.** Comparison between the scope of molecular and supramolecular chemistry.

The design of supramolecular systems invokes engagement of interactions that are weaker than single covalent bonds (35 – 110 kcal/mol). Non-covalent interactions include hydrophobic forces, dispersive forces,  $\pi$ - $\pi$  stacking, ion- $\pi$  interactions, hydrogen bonding, dipole-dipole forces, electrostatic forces, and metal coordination.<sup>[11,12]</sup>

They range from  $< 1$  kcal/mol (2 kJ/mol) for dispersion interactions to 70 kcal/mol (300 kJ/mol) for ion-ion interactions (Table 1). The intramolecular cooperativity of these highly dynamic and rather weak interactions dictates the assembly of discrete building blocks. Interestingly, the properties of the resulting supramolecular complexes are far beyond the summation of the individual components.<sup>[8]</sup>

**Table 1.** Summary of the non-covalent supramolecular interactions and their strengths.<sup>[12]</sup>

<b>Non-covalent Interactions</b>	<b>Strength (kcal/mol)</b>
Ion-ion	50-70
Ion-dipole	10-50
Dipole-dipole	1-10
Hydrogen bonding	1-30
Cation- $\pi$	1-20
$\pi$ - $\pi$	0-12
Van der Waals	$< 1$ , dependant on the surface area
Hydrophobic	Related to the solvent-solvent interaction energy

Understanding the intermolecular interactions engaged in building supramolecular structures is vital to explore the endless potential of supramolecular chemistry. With this in mind, chemists were suddenly able to give rise to concepts of molecular recognition, transportation, catalysis, self-assembly, and many other aspects into which supramolecular chemistry meanwhile diversified.<sup>[5,9]</sup>

## 1.2 Molecular Recognition

The process of molecular recognition of guest molecules by a synthetic host is of great interest in supramolecular chemistry.<sup>[13]</sup> Molecular recognition has been defined as the selective binding of a substrate by a molecular receptor to form a supermolecule.<sup>[3]</sup> A process of recognition involves both binding and the selection of substrates by a given receptor molecule, based on the molecular information stored in the interacting partners. The receptor molecule must fulfil certain steric and electronic requirements that are complementary to those of the substrate to be bound. Molecular recognition, thus, is a question of *information storage* and *read out* at the supramolecular level.<sup>[14]</sup> Based on how molecules recognize and organize among themselves, supramolecular chemistry can be split into two broad categories: host-guest chemistry and self-assembly.<sup>[12]</sup> The main difference between the two fields is the question of size and shape.

### 1.2.1 Host-Guest Chemistry, Self-Assembly, and Lattice Inclusion

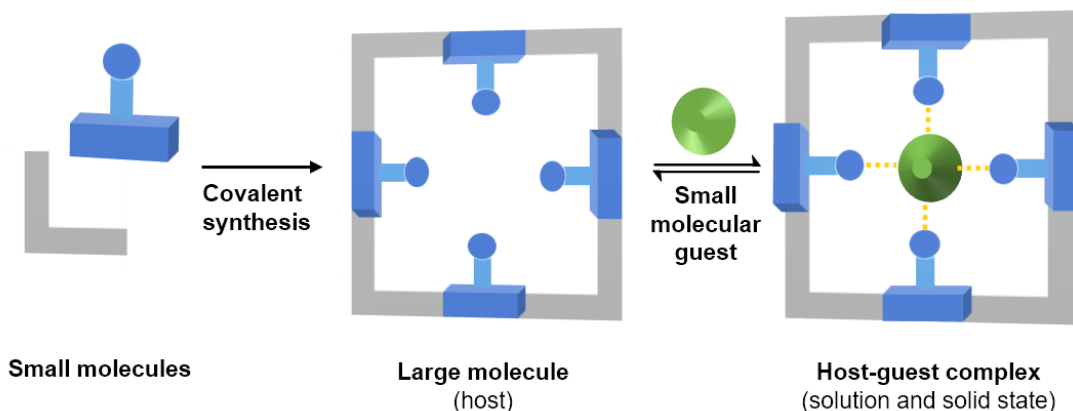


**Figure 2.** Illustration of host-guest chemistry process.<sup>[12]</sup>

A significantly bigger molecule in size, capable of wrapping and accommodating the smaller molecule inside of its cavity is termed as the “host,” and the smaller – enveloped molecule becomes its “guest” (Figure 2). The host, as well as the guest molecule, needs to fulfill requirements of the correct size, geometry, and chemical nature to interact with each other. A region on the host or the guest molecule that is directly involved in complexation is called the binding site.<sup>[15]</sup> Therefore, the covalently synthesized host

illustrated in Figure 2 has four binding sites that converge on a central guest binding pocket.<sup>[12]</sup>

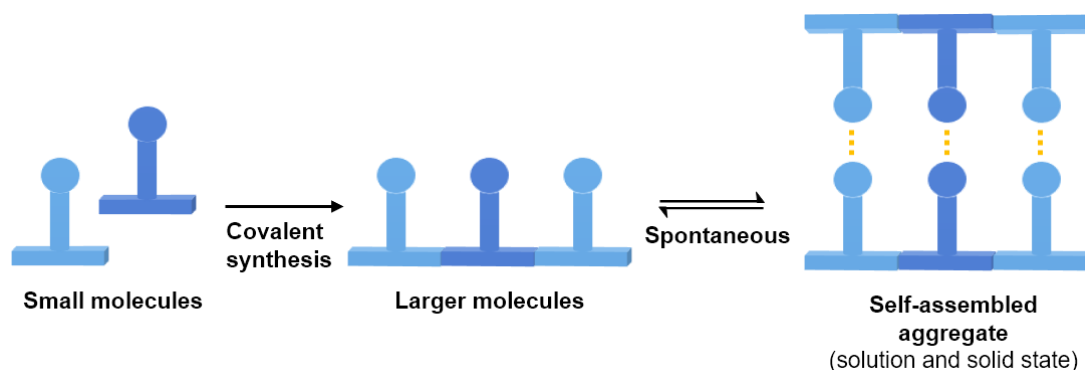


**Figure 3.** Self-assembly between complementary molecules.<sup>[12]</sup>

The non-covalent joining of two or more species that are similar in size and none of them is acting as a host for another is termed as self-assembly. Strictly, self-assembly is an equilibrium between two or more molecular components resulting in aggregate with a structure that is dependent only on the information contained within the chemical building blocks (Figure 3).<sup>[12]</sup> It is the process in which individual species spontaneously build organized structures, as a result of specific, non-covalent interactions among themselves.<sup>[16]</sup> Even if defined as a spontaneous process, self-assembly may be influenced by solvation effects or by the nucleation and crystallization processes (in the case of solids).<sup>[17]</sup>

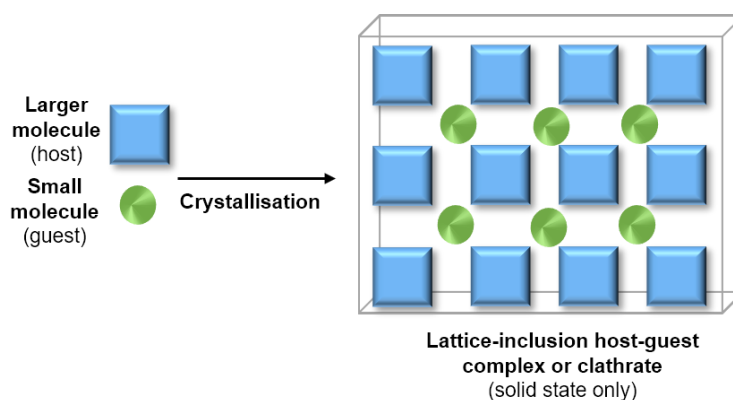


**Figure 4.** Lattice inclusion.<sup>[12]</sup>

On the other hand, the class of solid-state inclusion compounds exhibits host-guest behavior only in the form of crystalline solids. Here, the guest ends up trapped within a

cavity (hole) formed as a result of the irregular crystallization of the host lattice (Figure 4).<sup>[12]</sup> Such compounds are generally termed clathrates, derived from the Greek *klethra*, meaning “with bars, latticed.” According to IUPAC, clathrates are defined as inclusion compounds, “in which the guest molecule is in a cage formed by the host molecule or by a lattice of host molecules.”<sup>[18]</sup>

### 1.2.2 The most Prominent Host Scaffolds

A definite milestone for the origin of molecular recognition is considered to be the proposal of the steric fit *lock and key* concept enunciated by Emil Fischer in 1894.<sup>[8]</sup> He investigated the binding of substrates by enzymes, describing the enzyme as the lock and the substrate as the key; thus, the substrate-guest has a complementary size and shape to the enzyme-host binding site. However, the lock and key analogy is an overly simplistic representation of a biological system because enzymes are highly flexible and conformationally dynamic in solution, unlike the concept of a rigid lock.<sup>[12]</sup>

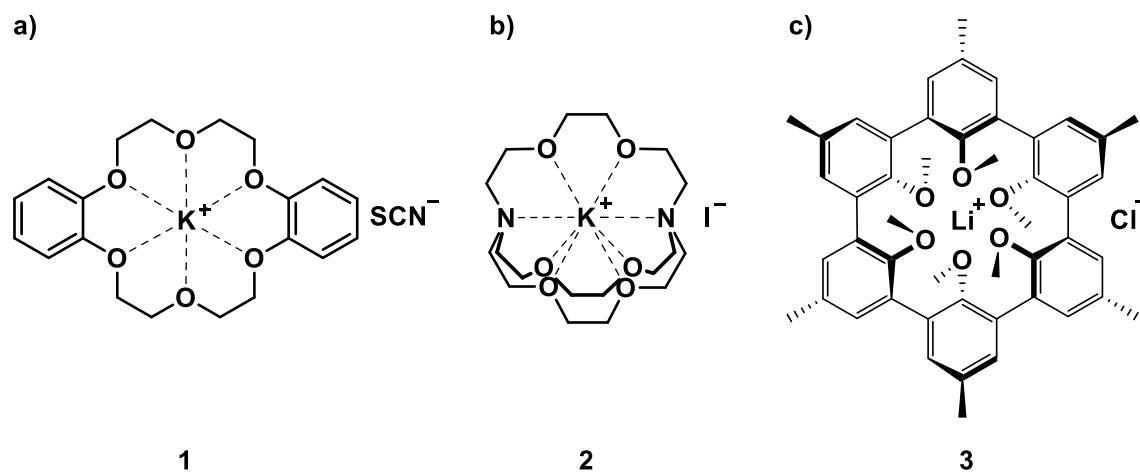


**Figure 5.** Preorganization does matter. **a)** Crown ether complex **1** according to Pedersen; **b)** Cryptand complex **2** according to Lehn; **c)** Host-guest spherand complex **3** according to Cram.<sup>[2]</sup>

The first described examples of artificial host molecules capable of molecular recognition and corresponding host-guest complexes were those awarded with the 1987 Nobel Prize (Chapter 1.1). After Pedersen discovered crown ethers by chance, the molecules that can capture individual metallic atoms, Jean-Marie Lehn found related molecules in 1969 that he called cryptands (Figure 5).<sup>[19]</sup> Cram, in particular, has designed

completely immobile host molecules that form particularly stable complexes of extremely high selectivity towards alkali metal ions based on their size by using advanced organic-synthetic engineering and molecular mechanics calculations.<sup>[2]</sup>

One common motivation behind their work is the design of chemical systems that mimic biological processes. Supramolecular host molecules containing intramolecular cavities can serve as receptors that can capture certain types of molecules, thereby forming an inclusion complex reminiscent of protein-ligand complexes. The most prominent examples of such host molecules are cyclodextrins, calixarenes, resorcinarenes, pillararenes, and cucurbituriles. Besides well-preorganized macrocycles, there are noncyclic compounds proved to be effective as synthetic receptors, known as molecular tweezers and clips (Figure 6).<sup>[20,21]</sup> They provide an impressive example of a large non-classical hydrophobic contribution to binding affinities in the absence of a closed cavity.

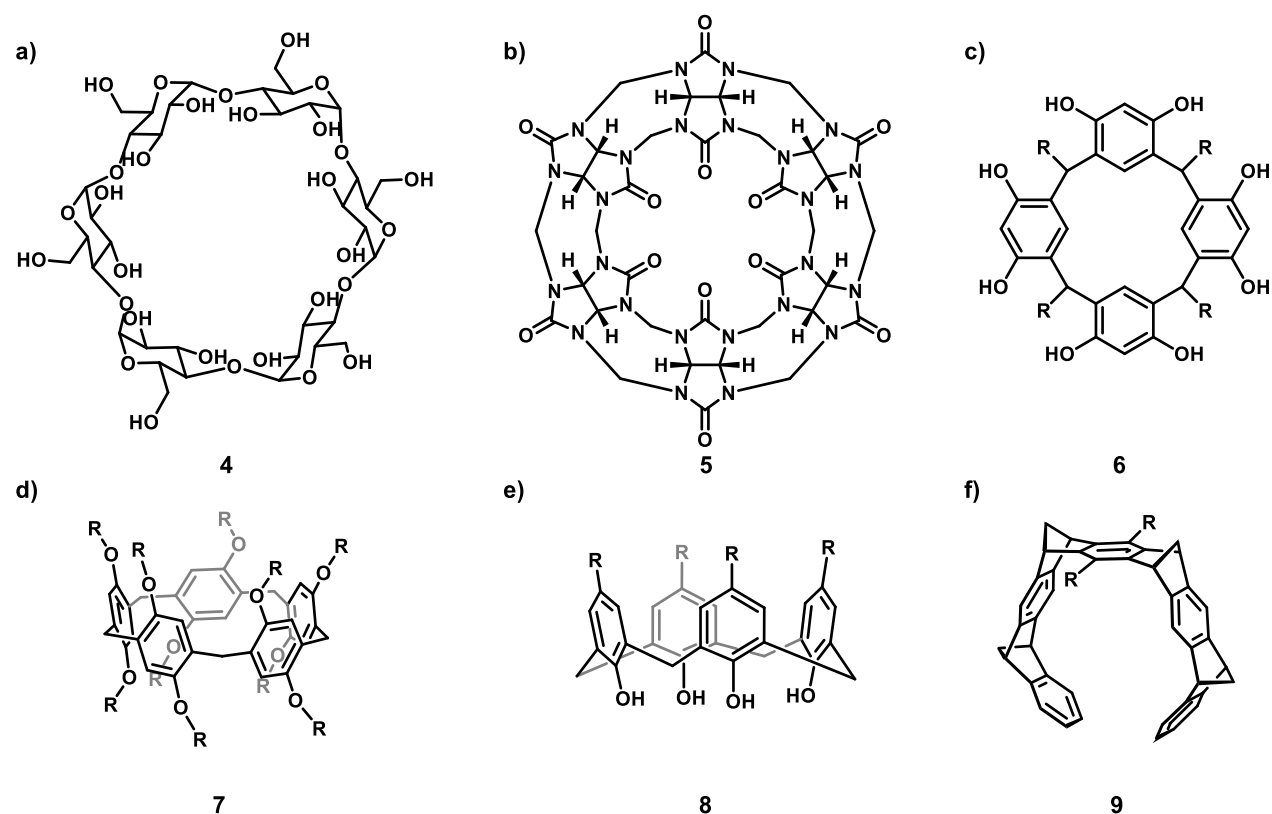


**Figure 6.** Structures of the most prominent host scaffolds; **a)**  $\beta$ -cyclodextrin **4**, **b)** cucurbituril **5**, **c)** resorcin[4]arene **6**, **d)** pillar[5]arene **7**, **e)** calix[4]arene **8**, and **f)** molecular tweezer **9**.

Over the last few decades, tremendous progress has been made employing the non-covalent bond and generating the topologically new molecules, leading to the development of precursors for molecular machines such as rotaxanes **10@11**, knotanes **12**, catenanes **13**, and Borromean rings **14** (Figure 7).<sup>[22–26]</sup>

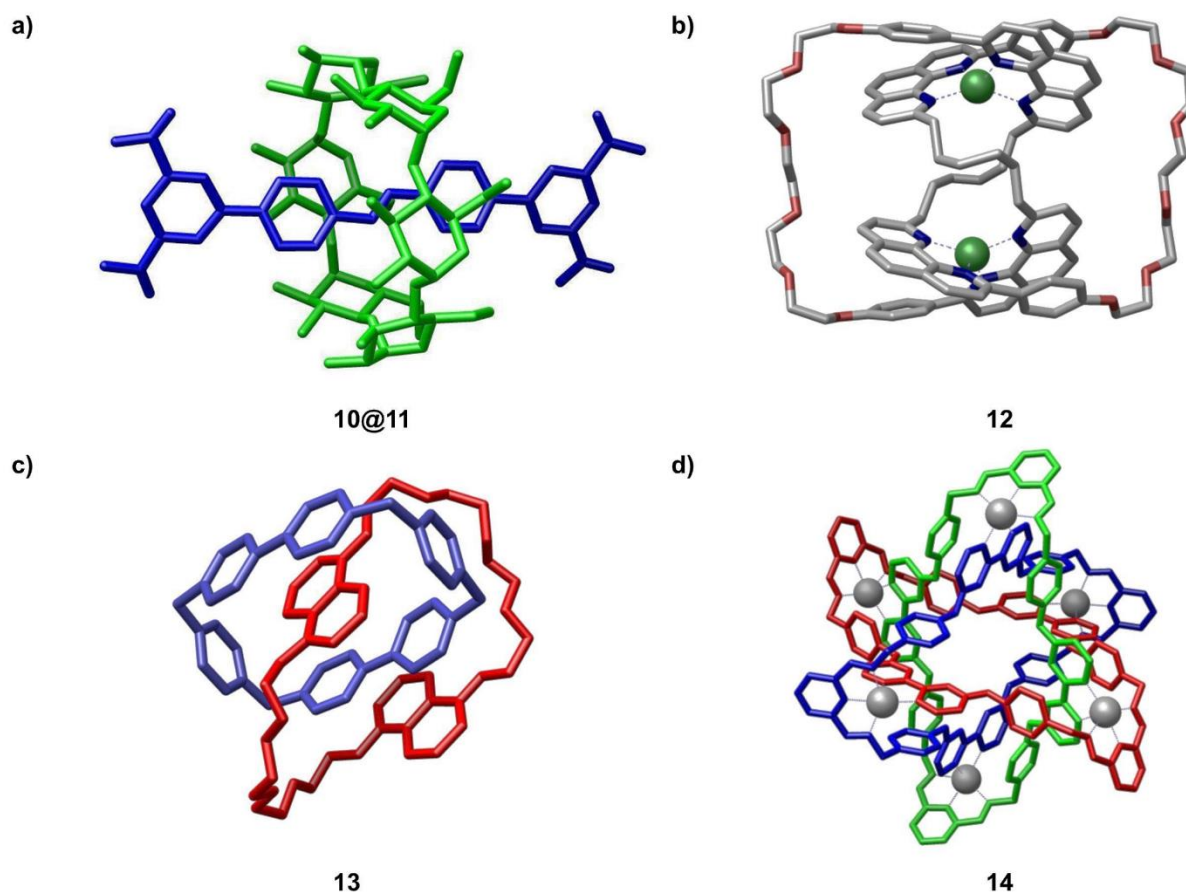


**Figure 7.** Molecular machines; **a)** rotaxane **10** with an  $\alpha$ -cyclodextrin macrocycle **11**<sup>[23]</sup>, **b)** molecular knot **12** with two copper(I) templating ions<sup>[24]</sup>, **c)** catenane **13**<sup>[25]</sup>, and **d)** molecular Borromean rings employing transition metal ions **14**.<sup>[26]</sup>

Molecular machines exhibit controlled repetitive motion and function at the nanoscale. Thus, such materials have great potential in the field of nanotechnology. The key focus in this field is to control directional motion, and thus a variety of rotaxane/catenane based systems have been employed. Rotaxane based machines and catenane based rotors are known as molecular walkers.<sup>[27]</sup> To accomplish directional transport at the molecular level, the molecular walker should fulfill essential requirements



such as processivity (there should be a minimum one contact point of a molecule with the track during the whole operation) and directionality (molecule walker should move towards one end).<sup>[28]</sup> Interlocking compounds such as rotaxanes, pseudorotaxanes, and catenanes play central roles in designing synthetic molecular machines.<sup>[29]</sup> For example, Sauvage *et al.* demonstrated the degree of control over the rotary motion of different components of catenanes (Figure 7. c).<sup>[25]</sup> Similarly, the Stoddart group developed a complex rotaxane device called a “molecular elevator” where high control of the motion of a moving plane between two “floors” separated by a distance of 0.7 nm could be achieved (Figure 8).<sup>[30,31]</sup> The two different states of the molecule can be switched by an external stimulus, such as a change in pH value.

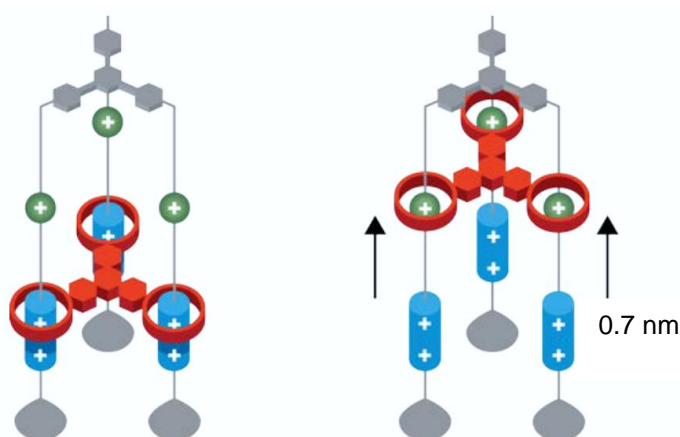


**Figure 8.** Rotaxane-based molecular elevator developed by a research group of Nobel Laureate Stoddart.<sup>[30,31]</sup>

The aim of supramolecular chemistry to develop organized functional units in the molecular dimensions, to interpret, store, process, and transmit information is likely to be achieved through tremendous effort that has been made in the field of molecular machines in the last few decades. Artificial machines can be utilized for the preparation of new materials and energy storage systems. Nobel Laureate Stoddart predicted that “the artificial motors prepared in the lab will compete with natural machines in a few decades.”<sup>[31]</sup>

### 1.3 Diverse Molecular Tweezers as Synthetic Receptors

As previously explained (Chapter 1.2.2), molecular tweezers are noncyclic host molecules, characterized by open cavities capable of binding guest molecules using various supramolecular interactions.<sup>[32]</sup> Since neutral  $\pi$ - $\pi$  interactions, even in the most favorable cases, are too weak for practical purposes, the supremacy of effective tweezer systems employs enhanced donor-acceptor  $\pi$ - $\pi$  interactions, most of the time supplemented by hydrogen bonding and hydrophobic attraction.<sup>[33,34]</sup> More than 40 years ago, Chen and Whitlock introduced the term molecular tweezers to describe a specific supramolecular host system equipped with two aromatic “pincers” linked together by a “spacer” (Figure 9).<sup>[35]</sup>

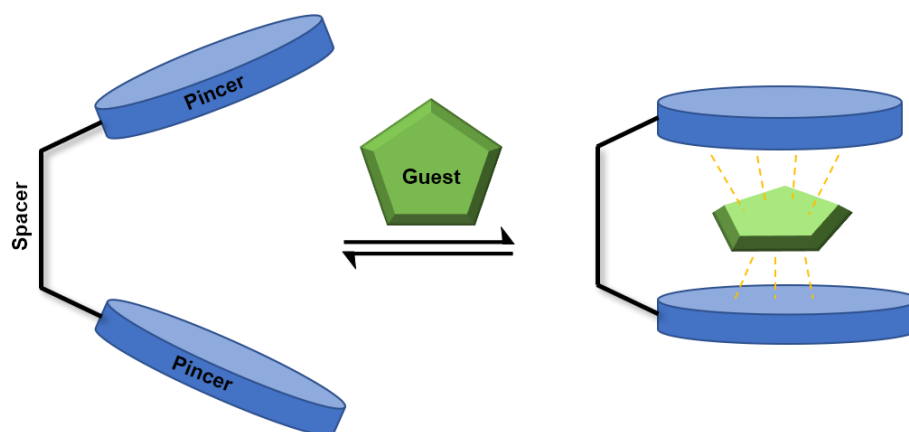


**Figure 9.** A typical “hold-and-release” mode of action of molecular tweezers. Dot-dashed yellow lines indicate non-covalent forces keeping the host-guest complex assembled.

The two caffeine chromophores that served as pincers were interconnected by a diacetylene spacer (Figure 10). This design of the first known molecular tweezers led to selectivity in binding of planar small,  $\pi$ -conjugated molecules as 2,6-dihydroxybenzoate (DHBA) or 1,3-dihydroxy-2-naphthoate (DHNA). Noteworthy, association constants ( $K_a \approx 10^4$  M) were determined in aqueous potassium phosphate buffer at neutral pH value.<sup>[35]</sup>

Subsequently, three criteria were established to define a molecular tweezer.<sup>[36,37]</sup> These are: (i) the presence of a spacer that prevents self-association, (ii) a spacer that establishes a distance of ca. 7 Å between the pincers suitable for the inclusion of a single

aromatic guest molecule, and (iii) a spacer that holds the pincers rigidly in a *syn*-conformation.<sup>[32]</sup> However, the third structural feature, i.e., rigid *syn*-conformation, was not met by Whitlock's molecular tweezer since the diyne spacer allows the free rotation of the two caffeine pincers out of the preferred *syn*-conformation.

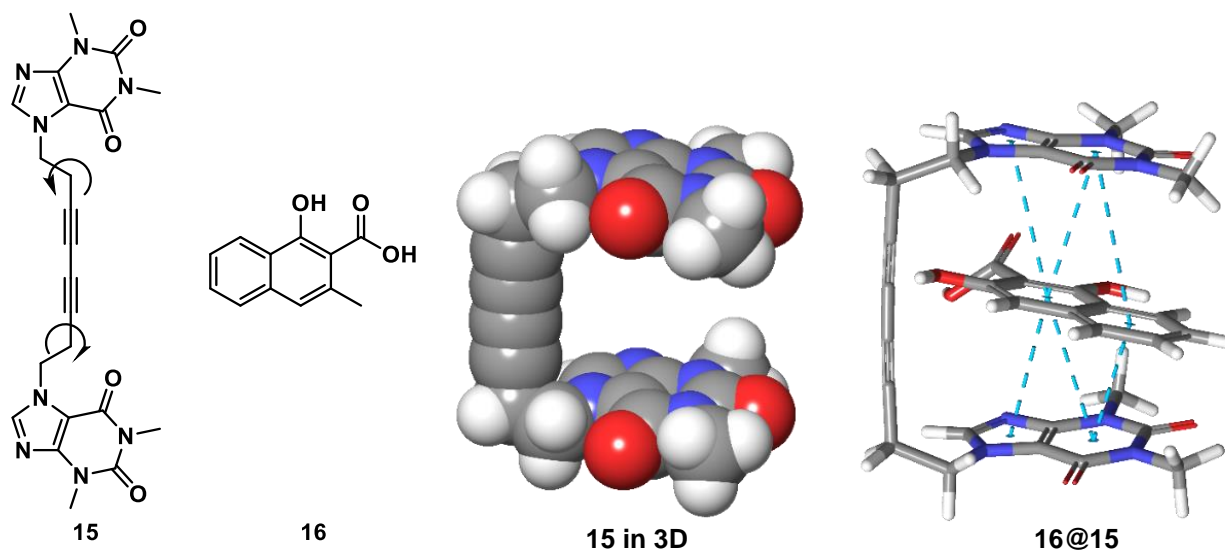


**Figure 10.** Chen and Whitlock's molecular tweezer **15**, as the first reported molecular tweezers and its host **16**. The energy-minimized 3D structure of **15** is shown with gray spheres. The resulting complex **16@15** is presented with sticks. Dashed blue lines indicate non-covalent forces ( $\pi$ - $\pi$  stacking), keeping the host-guest complex assembled.

Nevertheless, the definition and criteria established by Whitlock *et al.* set the stage for further developments. Since then, a large number of synthetic host systems based on this principle have been designed. There are two structural differences one can perceive in the term of development and design of molecular tweezers. The first one appears to be the variations in the chemical nature of the pincer, which carries combinations of specific electronic information and represents the active unit in terms of molecular recognition. The second differing parameter is the nature of the connecting platform between both pincers, whose attribute is the control of spatial separation and keeping pincers in *syn*-conformation.<sup>[32]</sup> The spacer can be rigid, flexible, or stimuli-responsive.<sup>[38]</sup> The combination of both provides the source of selective recognition of molecular tweezers.

Zimmerman *et al.* exploited these principles in the mid-1980s to the early 1990s to design new molecular tweezers that made use of a rigid spacer that enforced a *syn*-conformation of the complexing pincers of the tweezer (Figure 11.).<sup>[36,39]</sup> The exciting feature of this type of tweezers is the functional group embedded deep within the cavity of the molecule, which has been used to bind adenine with very high affinity. The association constant,  $K_a \approx 10^5$  M, was determined by NMR titration of the tweezer **17** with propyladenine **18** in deuterated chloroform and represented the most significant reported constant to date for a complex between a synthetic receptor and a nucleic acid-base.

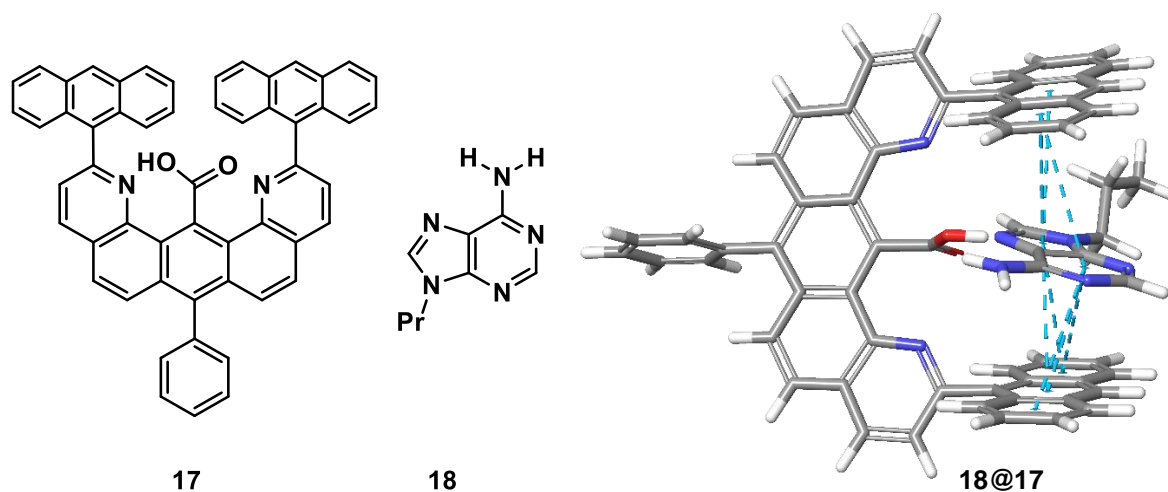


**Figure 11.** Example of rigid molecular tweezer **17** prepared by the Zimmerman group. The resulting host-guest complex **18@17** is presented with sticks. Dashed blue lines indicate non-covalent forces ( $\pi$ - $\pi$  stacking), keeping the host-guest complex assembled.

Fukazawa and co-workers introduced a different class of molecular tweezers in the term of spacer nature.<sup>[40]</sup> Rather than possessing a rigid spacer between the pincers, these systems are sufficiently flexible to adapt conformation necessary for guest binding. Indeed, Fukazawa's tweezer **19** can form 1:1 complexes with electron-deficient planar guests in the solid-state and solution in which the pincers do clamp down on the guest **20** (Figure 12).<sup>[37]</sup> Kurebayashi *et al.* reported that the crystalline complex has a triple-decker type donor-acceptor-donor sandwich arrangement in which is the guest located between the two terminal aromatic chromophores of the host.<sup>[40]</sup>

Beside above-elucidated examples of remarkable tweezers like rigid molecular tweezers described by Zimmerman *et al.* in 1991<sup>[33]</sup> and 1993<sup>[36]</sup> and flexible molecular tweezers revealed by Fukazawa *et al.* in 2001<sup>[40]</sup>, there are many other types of known

molecular tweezers and have been disclosed in several publications in the past on this topic.

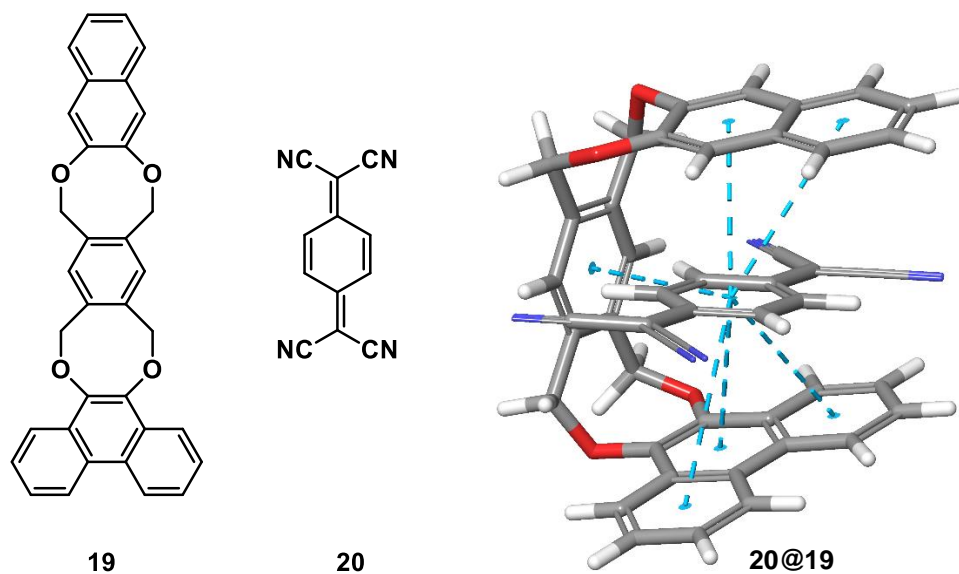


**Figure 12.** Fukazawa's tweezer **19** capable of adapting to electron-deficient planar guest **20**. Dashed blue lines indicate non-covalent forces ( $\pi$ - $\pi$  stacking), keeping the host-guest complex assembled.

For example, Nolte *et al.* presented various further elegant solutions to this challenge in work based on glycoluril-based molecular clips published in 1995<sup>[41]</sup> and 1999<sup>[42]</sup>; Harmata published in 2004 with a focus on chiral molecular tweezers<sup>[37]</sup>; Martín *et al.* described molecular tweezers designed explicitly for fullerene binding in 2010.<sup>[43]</sup> Details on the chemistry of distinct molecular tweezers are clearly beyond the scope of this work, which is based on host-guest chemistry of noncyclic molecular tweezers with flexible cavities, that were established by Klärner in 1996<sup>[44]</sup>, and are being further developed by Schrader.<sup>[45-49]</sup>

## 1.4 Water-soluble Molecular Tweezers – Concept and Applications

Supramolecular chemistry in water is a continually growing research field because non-covalent interactions in aqueous media are playing a pivotal role in the attainment of better understanding and control of the major processes in nature.<sup>[50]</sup> So far, given examples of molecular tweezers operated mostly in organic solvents and their application in biology remained mainly rare. The successful supramolecular recognition in aqueous solutions is still limited. The most common issues are solubility limitations in aqueous media, as well as the weakness of assemblies that rely on only low-strength hydrogen bonding and weak ion-pair interactions. To overcome these limitations and to reinforce the non-covalent interactions, additional binding motifs must be introduced into the receptors. Such modifications can be realized by combining the cooperative binding modes such as hydrophobic, ion-pair, cation– $\pi$  interactions, multiple complementary H-bonds, or metal coordination.<sup>[51]</sup>

However, the development of molecular tweezers went into the direction of making biologically applicable molecules owing to Dr. Frank-Gerrit Klärner, Professor Emeritus of Organic Chemistry at the University of Duisburg-Essen in Germany, who laid the groundwork for polyarene molecular tweezers and clips.<sup>[21]</sup> In collaboration with Prof. Dr. Thomas Schrader, they introduced anionic groups to the tweezers' skeletons generating the new hosts water-soluble.<sup>[49]</sup> With this significant change, molecular recognition became possible in a buffered aqueous media, opening the door for applications of a new tweezer generation under physiological conditions.<sup>[47]</sup>

### 1.4.1 Klärner's Molecular Clips and Tweezers

The class of molecular tweezers and clips, respectively, pioneered by Klärner and co-workers are represented by hydrocarbon-based di-, tri- and tetramethylene-bridged compounds (Figure 13).<sup>[21]</sup> These molecules represent precursors for later developed water-soluble molecular clips and tweezers (Chapter 1.4.2) Dimethylen-bridged molecules **21** and **23** have been referred to as molecular clips because they form complexes by “clipping” an aromatic substrate inside the receptor cavity.<sup>[32]</sup> Even the concepts of molecular tweezers and molecular clips are nowadays considered

separately – still, some authors state that there seems to be relatively little to distinguish between the two groups.<sup>[32,37]</sup>

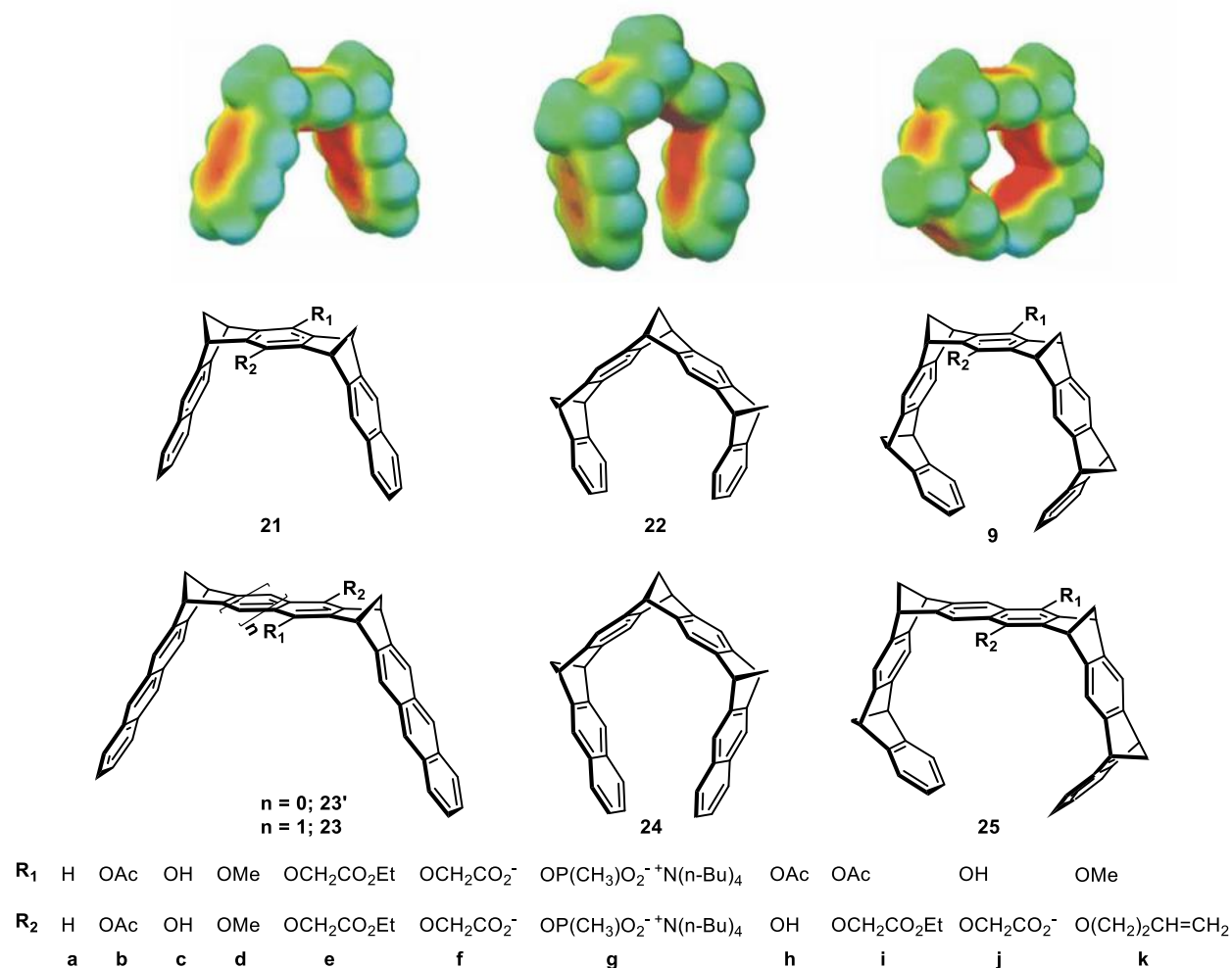


**Figure 13.** Electrostatic surface potential (ESP) and chemical structures of the tetra-, tri-, and dimethylene-bridged polyaromatic clips and tweezers. The color code spans from -25 (red) to +25 kcal/mol (blue).<sup>[21]</sup>

Until relatively recently, all the molecular tweezers and clips designed to complex  $\pi$ -conjugated systems have incorporated planar pincers.<sup>[52]</sup> Remarkably, the concept of molecular tweezer, as defined by Whitlock *et al.*, is slightly modified by Klärner's examples in **9**, **22**, **24**, and **25**. Thus, the tweezers' pincers are not parallel, although being held apart by the rigid spacer. Despite the rigid spacer, it has been shown that these two-armed acyclic receptors possess flexible cavities that can wrap around guests or clip them between two rigid molecular planes, respectively. A certain degree of cavity's flexibility is induced thanks to the fact that bond angle distortions require little energy and, therefore,

can allow the receptor “arms” to be expanded and compressed during the substrate complexation, ensuring the regular fit to the structure of potential host molecule.<sup>[44]</sup> This unique architecture was achieved utilizing repetitive Diels-Alder reactions, through a convergent synthesis based on a molecular “Lego” set, consisting of (bis-)dienophiles and (bis)dienes.<sup>[32]</sup> Diels-Alder reactions proceeded without exception stereospecifically on the *exo*-face of the (bis-)dienophiles and the *endo*-face of (bis-)dienes, resulting in a belt-like concave-convex topography.<sup>[44]</sup> This architecture allows an aromatic guest to be sandwiched *via* multiple  $\pi$ - $\pi$  and CH- $\pi$  interactions inside of the receptor’s cavity. Its size and shape can be tuned by varying the number and size of the spacer units to fit with the substrate topography.

X-ray measurements showed that the distance between the clip’s pincers is around 14 Å before guest complexation, as measured between the endmost, equivalent carbon atoms at each end of the structure.<sup>[37]</sup> This distance has been reduced to 6.5 Å after reaction with 1,2,4,5-tetracyanobenzene **26** (TCNB) in the resulting host-guest complex (Figure 14).<sup>[53]</sup>

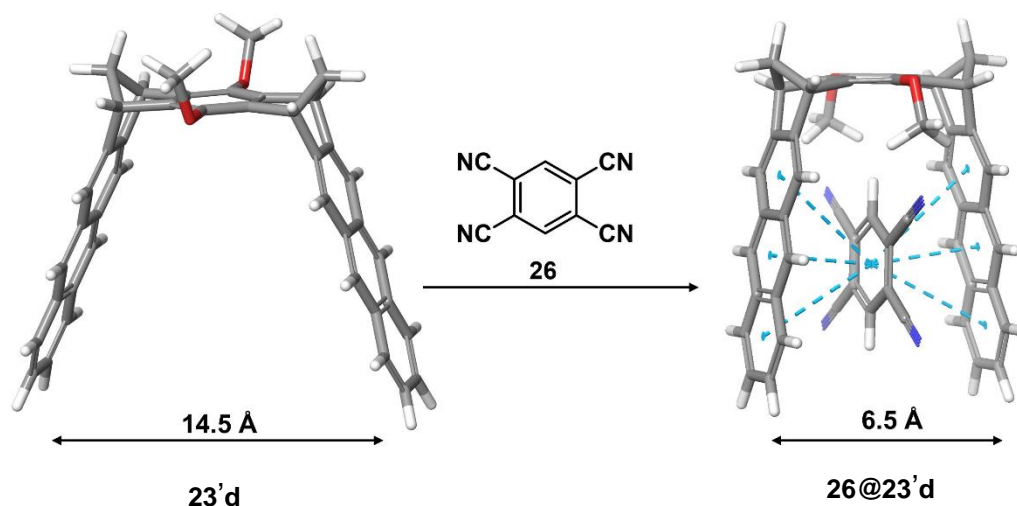


**Figure 14.** Single-crystal structure analyses of the clip **23'd**, and the complex TCNB **26@23'd** <sup>[21,54]</sup> The resulting complex **26@23'd** is presented with sticks. Dashed blue lines indicate  $\pi$ - $\pi$  stacking, while dashed green lines represent cation- $\pi$  interactions.<sup>[53]</sup>

Further, the binding affinities of the molecular tweezers with longer naphthalene pincers **24** toward the electron-deficient aromatic guests were explored in detail. The best 1:1 association constant ( $K_a = 1.43 \times 10^7 \text{ M}^{-1}$  in  $\text{CHCl}_3$  at 25 °C) is observed for the TCNB



complex. Besides the important information on the complex structures provided by single crystal-structures, additional insight into the binding event is given by complexation-induced  $^1\text{H}$  NMR shifts,  $\Delta\delta_{\text{max}}$ , of the substrate protons. Klärner *et al.* found out that TCNB forms a very stable complex with the naphthalene tweezer **23'd** showing  $^1\text{H}$  NMR shift of the TCNB protons by  $\Delta\delta_{\text{max}} = 5.9$  ppm in solution. The complex formation is shown to be largely the result of an enthalpic receptor-substrate interaction ( $\Delta H < 0$ ).<sup>[21]</sup> Moreover, the complex TCNB@**23'd** was described as the first example of charge-transfer luminescence from host-guest complexes. These act as potential chemical sensors with characteristic color changes observed upon complex formation, from colorless to red or purple.<sup>[32]</sup> The association/dissociation dynamics between the receptors **25** and **24**, and electron-deficient aromatic guest TCNB was further examined and discussed concerning the receptor topology.<sup>[55]</sup> Association/dissociation barriers formation ( $\Delta G = -7.9$  kcal/mol for TCNB@**25** and  $-9.0$  kcal/mol for TCNB@**24**) were determined as well as dissociation values of host-guest complexes ( $\Delta G^\ddagger = 15.7$  kcal/mol for TCNB@**25** and  $12.4$  kcal/mol for TCNB@**24**). These observations are shown to be consistent with the close topology of tweezers **25**, which makes the inclusion of a guest molecule kinetically a rather difficult process. Contrariwise, clip **24**, presenting a more opened shape, allows an easier inclusion of the guest molecules, thereupon accompanied by a lower activation barrier.<sup>[32,55]</sup>

Subsequently, molecular tweezers turned out to be effective and selective receptors for both neutral electron-deficient aromatic, aliphatic, as well as organic cationic substrates.<sup>[44,56]</sup> The results of  $^1\text{H}$  NMR binding studies of molecular tweezers **9a** with various aliphatic and aromatic cations in organic solvents were described by Klärner *et al.* in 1999.<sup>[56]</sup> Due to the solubility issues of substrates, the studies were performed only with better soluble secondary ammonium salts like dibutylammonium tetrafluoroborate **27** ( $n\text{-Bu}_2\text{NH}_2\text{BF}_4$ ) in  $\text{CDCl}_3$  (Figure 15). The  $^1\text{H}$  NMR signal assigned to the  $\alpha$ -protons in **27** shows a dramatic upfield shift after the addition of **9a**. The association constant  $K_a = 30 \text{ M}^{-1}$  and the maximum chemically induced shift  $\Delta\delta_{\text{max}} = 3.2$  ppm were determined, as well as the  $\Delta G$  value of  $-2$  kcal/mol. Klärner *et al.* showed that the alkyl chains were pulled through the **9a** tweezer's cavity like a thread, keeping the nitrogen atom of ammonium ion **27** in the central position, fixed by multiple cation- $\pi$  interactions. The

collected experimental data doubtlessly prove that the hydrocarbon tweezer **9a**, due to its electronic and topological properties, can selectively bind cationic substrates in organic media via moderate non-covalent interactions.

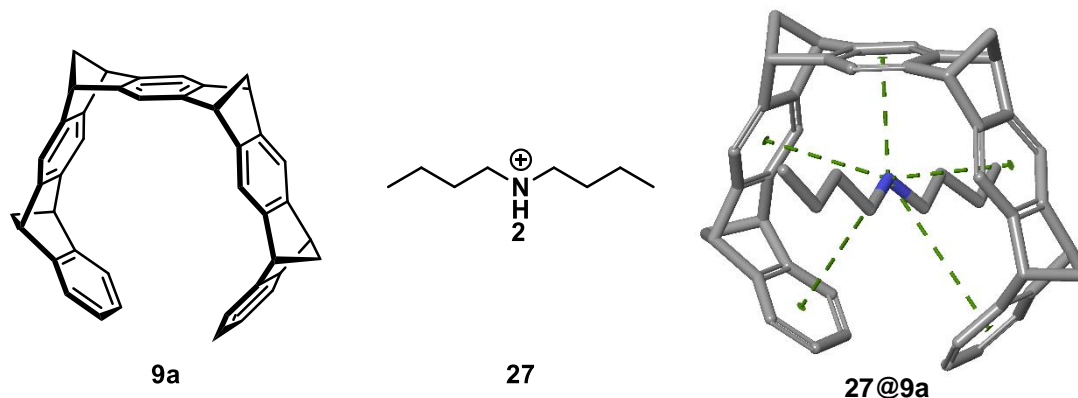


**Figure 15.** Binding studies of molecular tweezers **9a** with aliphatic cations guest **27**, and the resulting complex **27@9a**. Alkyl chains are pulled through the **9a** tweezer's cavity like a thread, keeping the nitrogen atom of ammonium ion **27** in the central position, fixed by multiple cation- $\pi$  interactions indicated with dashed green lines.<sup>[56]</sup>

As shown, Klärner modified the already existing concept of molecular tweezers in several aspects. He introduced architectures that are not necessarily offering parallel interaction sites. Besides, he described the new molecular tweezers that can provide a well fit to straight hydrocarbon chains inside their cavities – contrarily as defined by Chen and Whitlock, who described molecular tweezers designed to bind planar  $\pi$ -conjugated molecules exclusively.<sup>[21,35,44,53,56,57]</sup> Binding of alkyl cationic guests inside modernized tweezer skeletons represented a significant discovery regarding the later development of functionalized tweezer capable of targeting guests of the same chemical nature but with importance for biomedical applications.

### 1.4.2 Development of Water-soluble Molecular Tweezers

In collaboration with his successor Schrader, Klärner and co-workers achieved substantial enhancement in water solubility, as well as in binding selectivity, by the introduction of polar and ionic functional groups into the spacer units of the rigid molecular tweezers. Depending on the substituents in the central arene ring, sulfate **28**, OCH<sub>2</sub>-carboxylate **9f**, methane phosphonate **29**, and phosphate **30** tweezers were generated (Figure 16).<sup>[45]</sup> Various derivatives of **9**, including polyglycerol-tagged molecular tweezers, were also evaluated.<sup>[34]</sup>

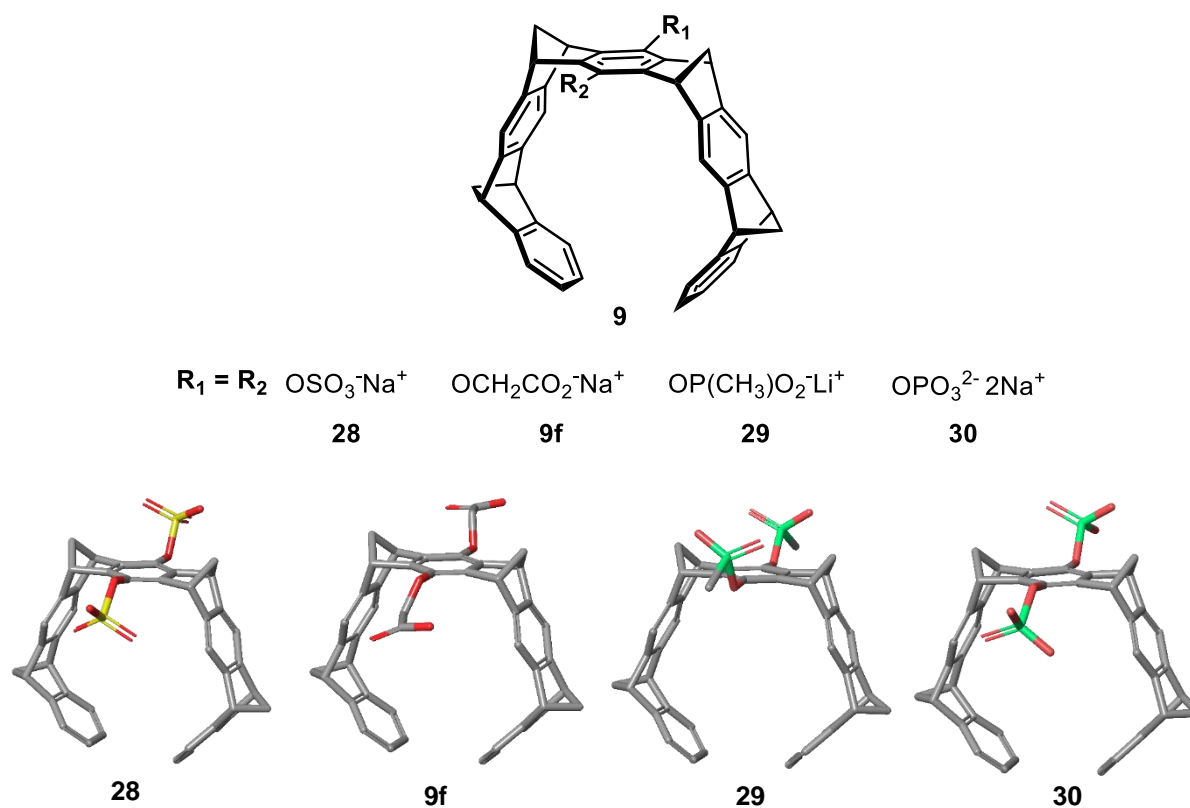


**Figure 16.** Water-soluble molecular tweezers with varying anions and their 3D structures of optimized by Schrodinger Maestro Software.

Unlike previous limitations to examine the simple hydrocarbon chains soluble in organic solvents only, this chemical change in the structure allowed molecular recognition in buffered aqueous solution, opening the door for biological applications and a possibility to screen the new host compounds against a large number of small biomolecules.<sup>[47]</sup> Derivatives that contained an ammonium group, which is an essential component of amino acids and other biological molecules, were shown to be preferred guests of the

water-soluble tweezers.<sup>[58]</sup> Due to their unique binding mode, these functionalized tweezer molecules demonstrate good affinity toward certain heterocyclic compounds of biomedical importance, such as enzyme cofactor model *N*-methyl nicotinamide iodidenicotinamide, as well as enzyme cofactor adenine dinucleotide (NAD<sup>+</sup>)<sup>[59,60]</sup>, thiamine diphosphate (TPP)<sup>[61]</sup> and nucleoside antibiotic 3'-azido-2',3'-dideoxythymidine (AZT) **33** shown in Figure 17.<sup>[62]</sup> The authors reported strong binding of NAD<sup>+</sup>, TPP, and AZT to the clip **21** (R = OP(CH<sub>3</sub>)O<sub>2</sub><sup>-</sup>) in D<sub>2</sub>O with  $K_a = 8.3 \times 10^4 \text{ M}^{-1}$ ,  $9.1 \times 10^3 \text{ M}^{-1}$ ,  $1.4 \times 10^4 \text{ M}^{-1}$ , and  $7 \times 10^3 \text{ M}^{-1}$ , respectively. Non-covalent forces such as hydrophobic, cation- $\pi$ , CH- $\pi$ , and  $\pi$ - $\pi$  interactions between guests and the naphthalene sidewalls are the driving force for complex formations. Nevertheless, the contributing effect has ion-pair interactions between the phosphonate (or phosphate) moiety of the host **21** and the part of the guest containing a hydrogen-bonding site and positively charged quaternary ammonium or sulfonium groups. This type of interaction is usually fragile in water but plays an essential role in the case of multivalent host-guest interactions in aqueous media.<sup>[50]</sup>

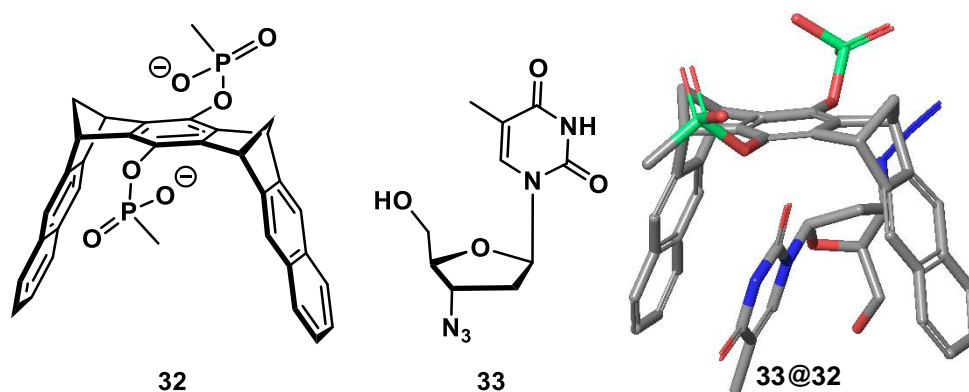


**Figure 17.** Calculated complex for clip **32** and nucleoside antibiotics AZT **33**: MacroModel 7.1, OPLS-AA, H<sub>2</sub>O; Monte Carlo simulation 1000 steps.<sup>[62]</sup>

Further computational and <sup>1</sup>H NMR studies published in 2006 revealed a significant role of nonclassical hydrophobic effect affecting the host-guest tweezer binding and dimerization in water.<sup>[46]</sup> The quantum chemical <sup>1</sup>H NMR shift calculations have shown that anthracene clip **23'** and naphthalene tweezer **25** hosts (both substituted with lithium methane phosphonate groups in the central spacer unit; R = OP(CH<sub>3</sub>)O<sub>2</sub><sup>-</sup>Li<sup>+</sup>) form highly stable dimers in aqueous solution **34** and **35**, respectively (Figure 18).

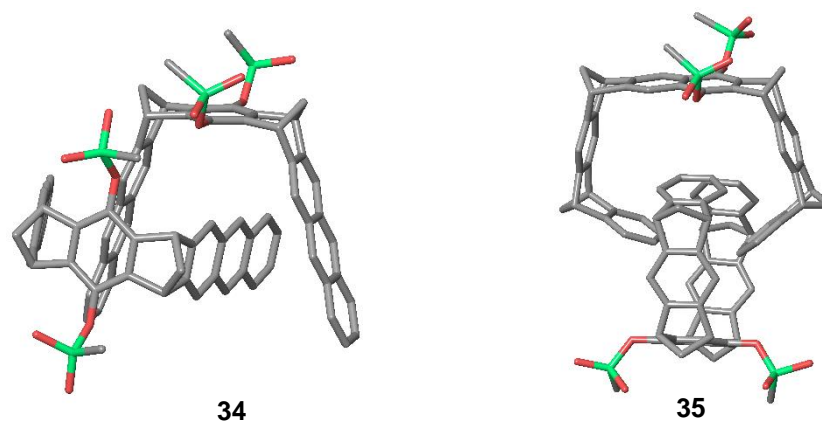


**Figure 18.** Dimerization in water; dimer structures of phosphonate substituted anthracene clip **34** and naphthalene tweezer **35**.<sup>[46]</sup>

Binding affinities for the methyl-phosphonate substituted hosts with cationic – enzyme cofactor model *N*-methyl nicotinamide iodide (NMNA) **38** were examined in D<sub>2</sub>O and MeOD by <sup>1</sup>H NMR dilution titration experiments at various temperatures (Figure 19).

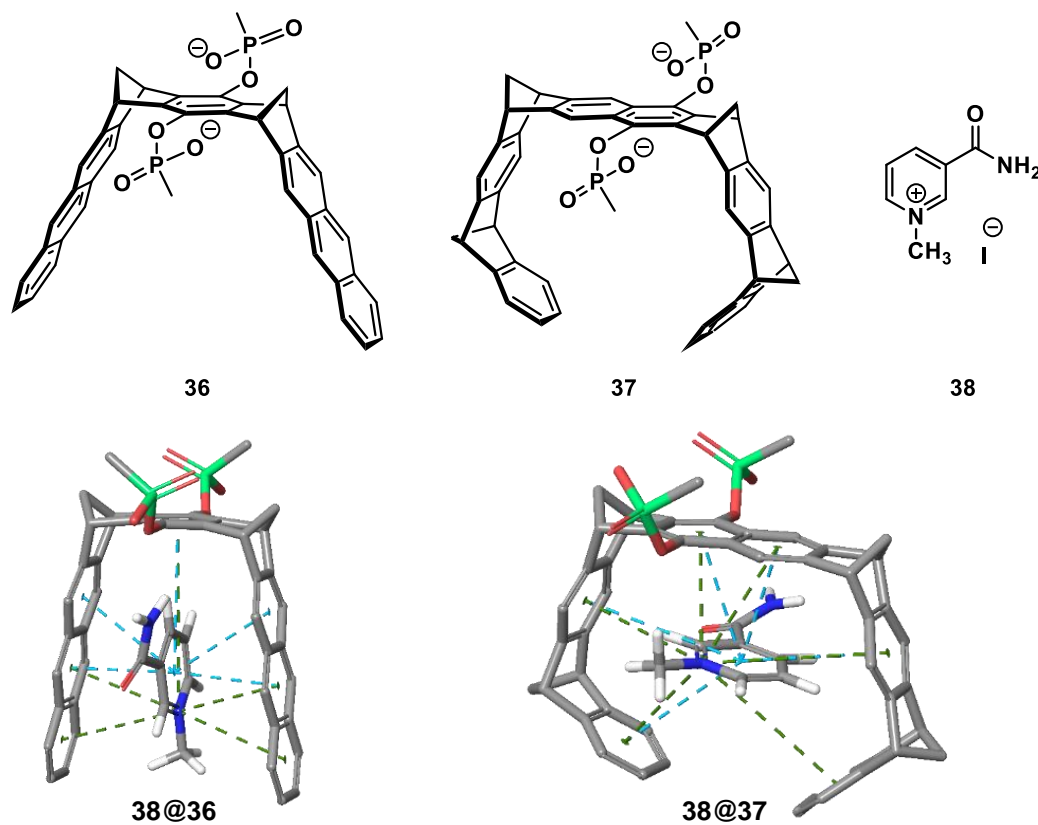


**Figure 19.** Structure of the complexes **38@36** and **38@37**. Dashed blue lines indicate π-π stacking, while dashed green lines represent cation-π interactions.

Reported associations constants were strong in both solvents reaching, for example,  $11.9 \times 10^4 \text{ M}^{-1}$  for **37** and  $1.04 \times 10^4 \text{ M}^{-1}$  for the clip **36** in methanol;  $28.8 \times 10^5 \text{ M}^{-1}$  for **37** and  $1.6 \times 10^5 \text{ M}^{-1}$  for **36** in  $\text{D}_2\text{O}$  (Table 2). Interestingly, the tweezer **37** showed a high tendency to dimerize in water, but not in methanol. Attractive aromatic  $\pi$ - $\pi$  and CH- $\pi$  interactions are presumably responsible for the formation of the self-assembled dimers in water.<sup>[63]</sup>

**Table 2.** Determined for the self-assembling of tweezer 37 and clip 36 in aqueous solution, by  $^1\text{H}$  NMR dilution titration experiments<sup>[46]</sup>

Complex	$\Delta\delta_{\text{max}}$ ( <b>38</b> )		$K_{\text{a}}$		$\Delta G$	$\Delta H$	$T\Delta S$
	[ppm]		[ $10^5 \text{ M}^{-1}$ ]		[kcal/mol]	[kcal/mol]	[kcal/mol]
	N-CH <sub>3</sub>	MeOD	MeOD	D <sub>2</sub> O			
<b>38@37</b>	2.75	1.19	22.80		-8.70	-20.90	-12.20
<b>38@36</b>	1.61	0.10	1.60		-7.10	-13.80	-6.70

According to the obtained thermodynamic parameters, the strong binding of **36** and **37** to NMNA, as well as their self-assembly, is strongly enthalpy-driven ( $\Delta H \ll 0$ ) and accompanied by an unfavorable entropy loss ( $T\Delta S < 0$ ). This is in agreement with the so-called nonclassical hydrophobic effect.<sup>[46,64]</sup> This finding may be explained by the release of the water molecules solvating the free onium ion.<sup>[46]</sup> Computational methods have underlined the importance of enthalpy gain due to the liberation of water from tweezers' and clips' cavity. The liberation of solvating water molecules enables more cohesive water – water interactions in the bulk solvent, which leads to an enthalpy gain and brings an entropic advantage.<sup>[65]</sup> Water-box simulations were used to characterize the different contributions from high-energy water, suggesting that the release of high-energy water is more important for the parent clip **21** than for the benzene-spaced tweezer **9**, showing only a little tendency to form dimers in aqueous solution ( $K_{\text{dim}} < 100 \text{ M}^{-1}$ ,  $\Delta\delta < 0.1 \text{ ppm}$ ).<sup>[46,49]</sup>

Heid *et al.* reported in 2018 the new strategical approach in the synthesis of new generation molecular tweezers, equipped with additional recognition units (Figure 20).<sup>[66]</sup> The trichloroacetonitrile route was followed in the functionalization of the molecular

tweezer with the clickable ester alcohol moiety (shown in purple in Figure 20) as a principal endowment allowing further variations in both structure and the function.

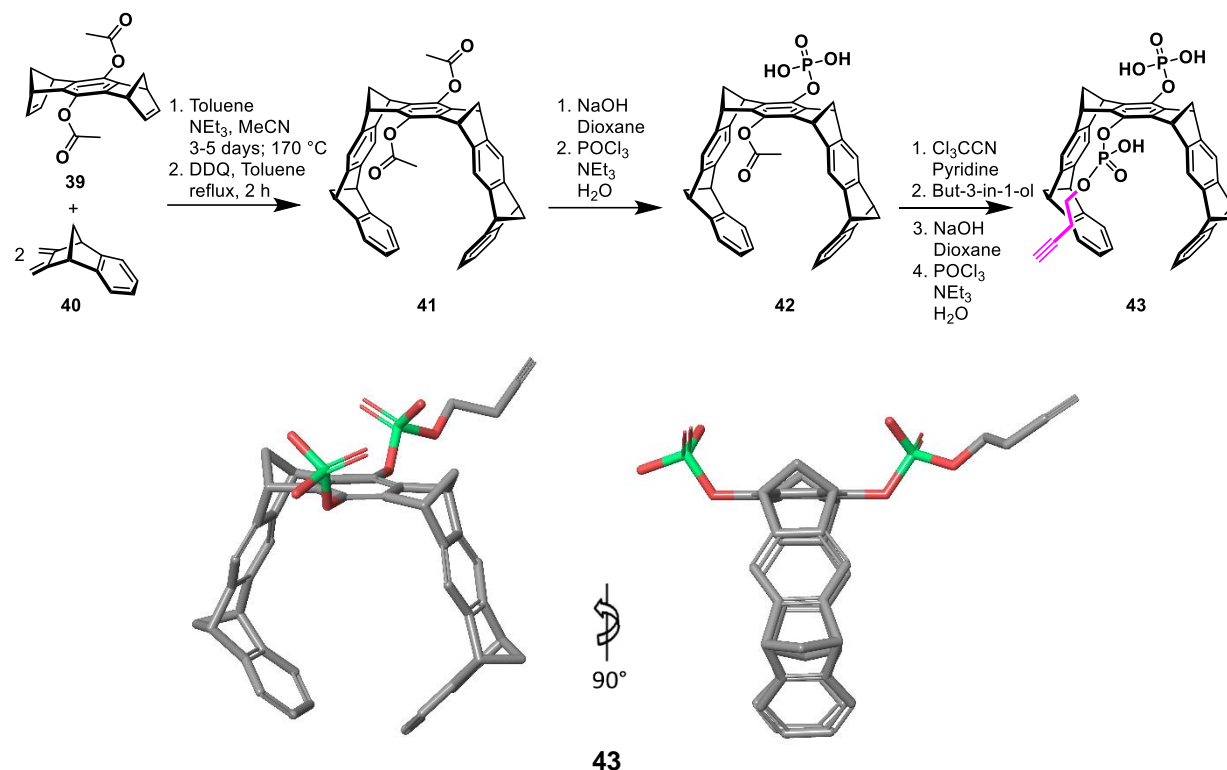


**Figure 20.** Synthesis of “clickable” monobutynyl phosphate tweezer **43** and its 3D sticks representation (color code: carbon-gray, oxygen-red, phosphorus-green).

Equipping the tweezer with an entity that can be further utilized applying the click chemistry approach allows expanding the repertoire of specific artificial recognition units for the predictable manipulation of biochemical functions, as well as enhancement of the tweezers ‘specificity, which is the main aim of the presented work (Chapter 2).

#### 1.4.2.1 Molecular Tweezers Selective for Lysine and Arginine

Being inspired by previously discussed findings, Schrader came up with the ingenious idea to broaden the scope of examined cationic guests toward natural amino acids, which furnished only two hits and proclaimed the molecular tweezer as the selective binder for side chains of lysine (Lys) and arginine (Arg).<sup>[47]</sup> Besides, the binding strength of the tweezers as potential hosts increased substantially and yielded with affinities in the low micromolar range in phosphate buffer ( $K_a = 5 \times 10^3 \text{ M}^{-1}$  for Lys and  $2 \times 10^3 \text{ M}^{-1}$  for Arg).<sup>[49]</sup> Exquisite selectivity for the two cationic amino acids is achieved

by threading the whole amino acid side chain through the tweezer's cavity (Figure 21. a), and subsequent locking by the formation of a salt bridge between the anionic substituent located on the central benzene ring of the tweezer and the included ammonium (Lys) or guanidinium cation (Arg).<sup>[67]</sup>

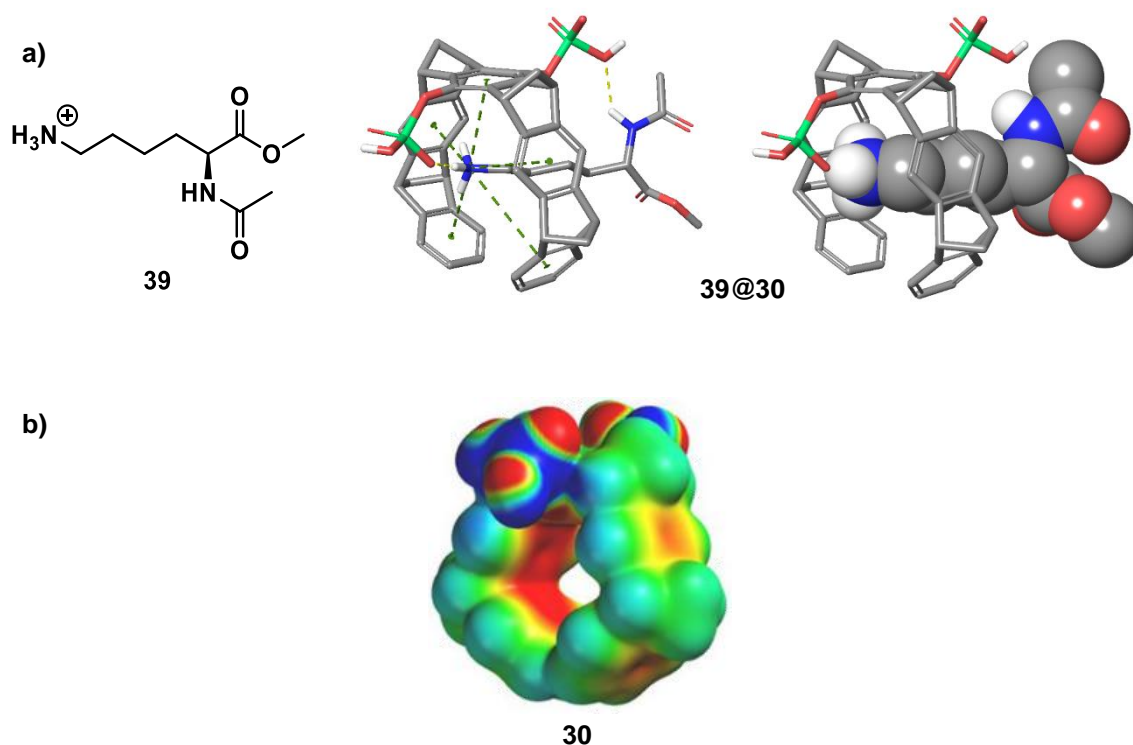


**Figure 21. a)** The binding mode between diphosphate molecular tweezer **30** and lysine residue **39**. Dashed green lines represent cation- $\pi$  interactions, while yellow lines represent salt bridges. **b)** EPS of diphosphate molecular tweezer. The color code spans from -25 (red) to +25 kcal/mol (blue).<sup>[68]</sup>

Electrostatic potential surface calculations show that tweezer's cavity construction is electron-rich, perfectly symmetric, and open to host aliphatic side chains of cationic amino acids (Figure 21. b).<sup>[49,67]</sup> The unique recognition mode is enabled thanks to the host's unique topology, which allows engagement of dispersive van der Waals interactions, substantial electrostatic contributions, and the non-classical hydrophobic effect in a synergistic, cooperative manner. Described binding mode results in a kinetically fast and reversible recognition process, which is of the utmost importance for application in biological processes.<sup>[67]</sup> In 2005, Fokkens *et al.* have shown that phosphonate molecular tweezer **29** (R=OPMeO<sub>2</sub>Li) is not only the excellent receptor for lysine and arginine, but it is also able to recognize simply protected peptides in water ( $K_a$  values for



AcLysOMe and TsArgOEt in D<sub>2</sub>O are  $2.3 \times 10^4 \text{ M}^{-1}$  and  $7.8 \times 10^3 \text{ M}^{-1}$ , respectively).<sup>[49]</sup> The presented findings were encouraging and led to an assumption that molecular tweezers can bind lysine or arginine incorporated into the peptidic framework, serving as a convenient supramolecular tool for addressing biological constructs of interest (Figure 22).

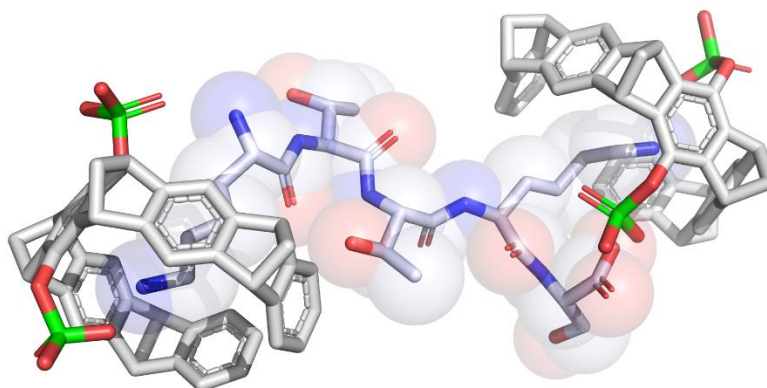


**Figure 22.** N-terminal lysine residues in KTTKS peptide (spheres) threaded through separate tweezer cavities (sticks). The color code: carbon-gray, oxygen-red, phosphorus-green, nitrogen-blue.

For this purpose, short peptides containing basic amino acids in their sequences found in the hot-spot region of proteins were tested. For example, the KKL VFF peptide contains two terminal Lys in its sequence. Moreover, it represents the self-complementary, central hydrophobic part of A $\beta$  peptide, which has been identified as the nucleation site that initiates pathological protein aggregation, fibril formation, and subsequent plaque occurrence in Alzheimer's disease.<sup>[69]</sup> Therefore this important signal peptide was chosen as an attractive start point for complex investigations of tweezer's binding mode.<sup>[49]</sup> The high selectivity for lysine has been proven in NOESY measurements through the chemical shift analysis, variable temperature experiments, isothermal titration calorimetry (ITC) as well as through <sup>1</sup>H NMR titrations, elucidating enthalpy-driven process where KKL VFF peptide displays an enhanced affinity towards host in aqueous solution ( $K_a = 3.8 \times 10^4 \text{ M}^{-1}$  determined in 25 mM NaH<sub>2</sub>PO<sub>4</sub> buffer in D<sub>2</sub>O/CD<sub>3</sub>OD 1:1). Substantial upfield shifts in NMR are observed exclusively at the methylene protons of the Lys side chains, confirming the host's high selectivity for this basic amino acid again. Thermodynamic data refer to a strongly exothermic process. Here, the binding affinity of molecular tweezer to KLVFF peptide with a 1:1 stoichiometry

was found to be  $15.2 \mu\text{M}$ , and the enthalpic contribution  $\Delta H$  of  $-6.4 \text{ kcal/mol}$ , which is dominating over the small entropy term  $-T\Delta S$  of  $-0.2 \text{ kcal/mol}$ .<sup>[45]</sup> The emission maximum of molecular tweezers in fluorescence spectra is at  $330 \text{ nm}$ , and the excitation maximum is located at  $285 \text{ nm}$ . Trapping of guest molecules in the tweezer's cavity results in a partial quenching of their emission bands (Figure 23). The quenching is generally accompanied by a slight blue shift of the emission maximum. Thus, the complex formation can be monitored by fluorescence spectroscopy and the respective binding constants  $K_a$  and, hence, the dissociation constants  $K_D$  can be determined by fluorometric titration experiments. Dissociation constants for a single lysine inclusion determined by fluorometric titrations were reported in the range of  $5 - 20 \mu\text{M}$ .<sup>[45,67]</sup>

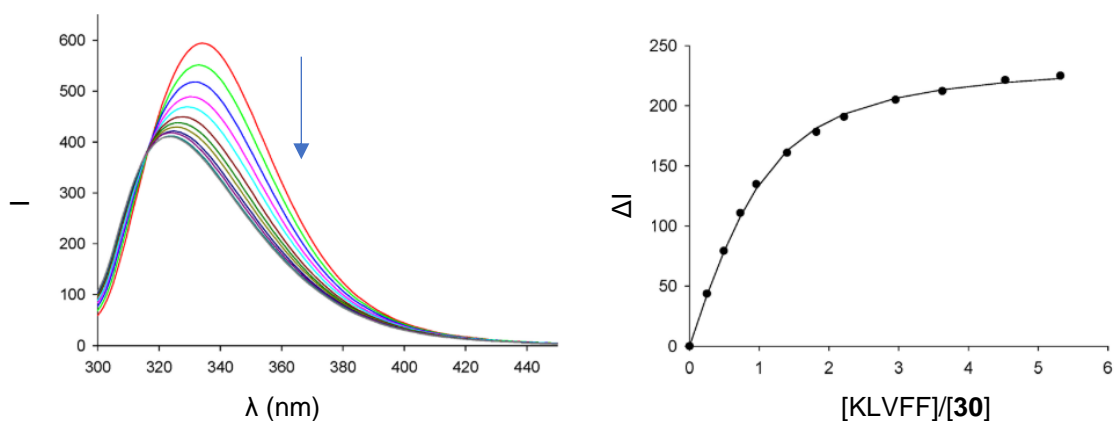


**Figure 23.** The emission bands at  $\lambda_{em} = 336 \text{ nm}$  of the tweezer **30** ( $\lambda_{exc} = 285 \text{ nm}$ ) in fluorescent titration measurements with the guest KLVFF done in aqueous phosphate buffer.<sup>[45]</sup>

Accumulated experimental evidence revealed that molecular diphosphate tweezers are biocompatible water-soluble molecules capable to selectively bind the side chains of lysine and arginine inside their cavity.<sup>[67]</sup> This interaction, characterized by moderate affinity, occurs in a kinetically fast and reversible manner. The importance of such a binding mode reflects that interactions of the same kind play a crucial role in numerous protein-protein interactions. Therefore, molecular tweezers show high potential to disrupt or enhance such events.

## 1.5 Utilization of Molecular Tweezer Features in Enzyme Inhibition

Due to tweezers' (and clips) proven ability to selectively bind natural enzyme cofactors and amino acid side chains (Chapters 1.4.2 and 1.4.2.1), these systems have found applications and opened new enzyme perspectives inhibition.<sup>[46,59–61]</sup> The strong binding of **36** and **37** to NMNA was an encouraging and promising result for the subsequent study conducted in 2008 to answer whether the new host molecules selectively bind enzyme cofactors such as nicotinamide adenine dinucleotide (NAD<sup>+</sup>) at their active sites. The effect of phosphate-substituted clip **21** and the tweezer **30** on the enzymatic oxidation of ethanol catalyzed by alcohol dehydrogenase (ADH), using NAD<sup>+</sup> as a cofactor, was examined in buffered aqueous solution at neutral pH. It has been found that the two artificial host molecules were able to block the enzymatic oxidation of ethanol by ADH *in vitro* via two different mechanisms.<sup>[70]</sup> The clip **21** pulls out NAD<sup>+</sup> from the Rossman fold and thereby decreases the cofactor level below the critical threshold, whereas the Lys-selective tweezer **30** decorates the whole enzyme surface, especially the cofactor entrance site (Figure 24).<sup>[70]</sup>

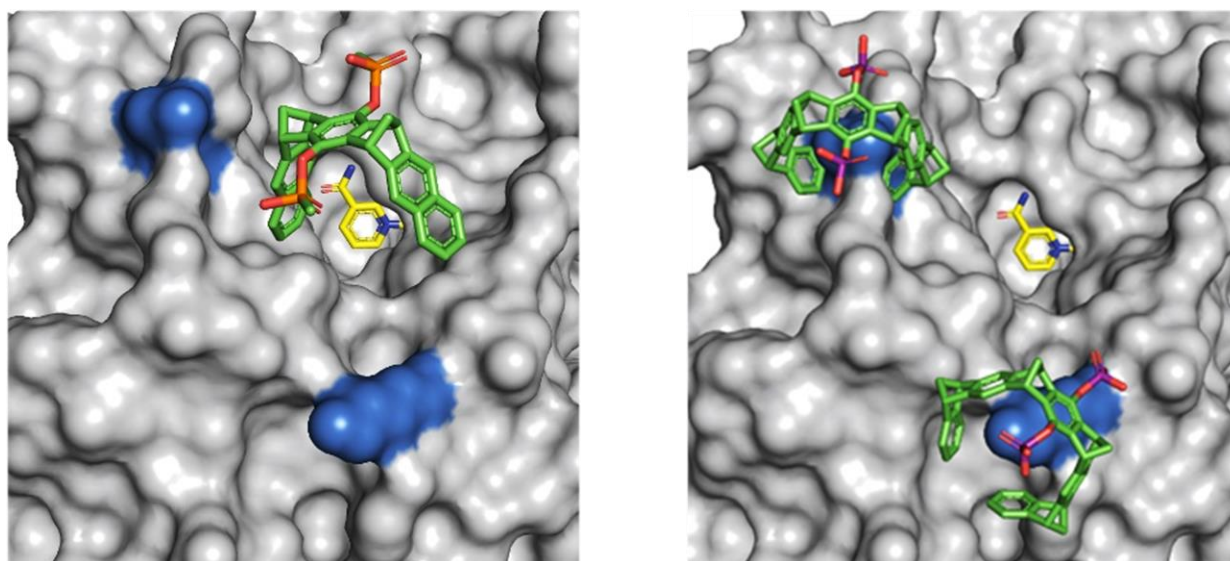


**Figure 24.** Crystal structure of ADH (PDB ID: 1PS0) illustrating the two different inhibition mechanisms of clip **21** (left) and tweezer **30** (right) at the entry to the Rossman fold. Color code: protein-gray surface, cofactor-yellow sticks, Lys-blue spheres, clip **21**, and tweezer **30**-green.

Through further investigations, the molecule **30** made a big breakthrough in terms of its application. As the molecule with the most promising features from the tweezers' family, it was proclaimed for the lead drug candidate compound. Nowadays, the **30** is widely known as CLR01 (CLR stands for clearance and refers to breaking plaque deposits of misfolded  $\beta$ -amyloid in the brain as well as the prevention of forming the new  $\beta$ -amyloid assemblies).<sup>[47]</sup> The selective affinity toward the natural amino acid lysine and arginine residues in proteins of this relatively simple molecular tweezer enabled its massive application for biological purposes. The CLR01 interferes with abnormal protein folding and aggregation implicated in neurodegenerative diseases such as Alzheimer's and Parkinson's disease.<sup>[71]</sup> In subsequent studies, this new amyloid assembly inhibitor demonstrates superior binding properties compared to other known inhibitors, such as sugar scylloinositol and polyphenol epigallocatechin gallate.<sup>[72]</sup> Similar to amyloid assembly inhibition, the CLR01 also acts as an inhibitor of  $\alpha$ -synuclein neurotoxicity in vitro and in vivo, whose deposition causes multiple system atrophy (MSA).<sup>[73,74]</sup> Moreover, the CLR01 was shown to be an effective drug against more than 30 human diseases, including diabetes type-2<sup>[75]</sup>, lysosomal storage disease<sup>[76]</sup>, herpes simplex, and hepatitis C virus, HIV<sup>[77]</sup>, Ebola, and ZIKV virus.<sup>[78]</sup> It is currently progressing toward clinical trials. Interestingly, still unpublished results of the studies done in collaboration with virologists suggest the positive effect of the CLR01 derivatives against SARS-CoV-2. Beside its combined anti-amyloid and antiviral activities, the CLR01 is capable of modulating 14-3-3 PPI via binding to a single surface-exposed lysine in proximity to the central channel, which will be discussed in details in following chapters .<sup>[34,48]</sup>

## 1.6 Supramolecular Chemistry on Proteins

### 1.6.1 Protein Recognition

Nature exhibits rich and versatile examples of supramolecular chemistry. At the basis of many biological processes lies the ability of molecules to recognize each other and assemble into well-defined, functional complexes.<sup>[79]</sup> There are many examples where nature creates functionalized assemblies relying only on the non-covalent interactions (Figure 25).

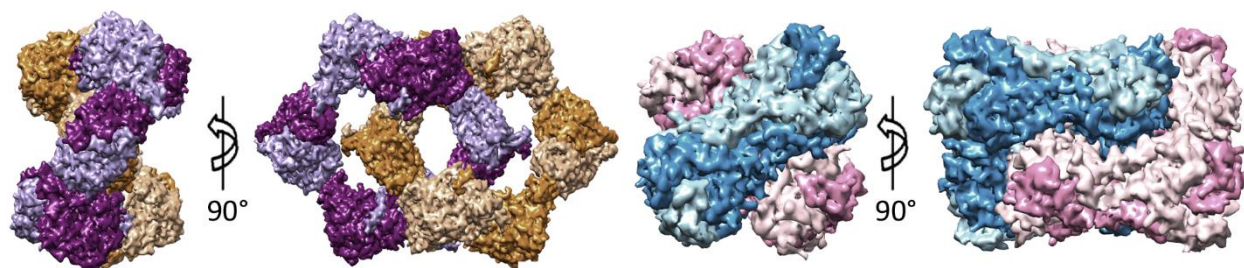


**Figure 25.** Examples of supramolecular catenane-like protein assemblies stabilized solely by non-covalent interactions (PDB ID: 4ERP and 3TEO).<sup>[80]</sup>

The concept of recognition resulting in the formation of a supramolecule is crucial in biological systems. Well-known examples are substrates bound to enzymes allowing the enzyme action, signal substances bound to receptors allowing molecular transport, antibodies bound to antigens, processing of genetic information, and protein assemblies.<sup>[81]</sup> In most cases, one or more compounds of low molecular weight bind to specific regions – called hot spots in a high-molecular-weight compound, most often a nucleic acid or a protein.

Proteins are biologically functional, complex molecules essential for all living systems. They represent important biomaterials responsible for the cell structural integrity, regulation of the signalling process, transport, catalysis, and communication.<sup>[82,83]</sup> Nature builds proteins by a bottom-up approach, in which the primary sequence of amino acids largely determines the proteins' tertiary three-dimensional structure.<sup>[80]</sup> Most of the characterized proteins, however, are organized in higher hierarchical quaternary structures, either by forming homo-oligomeric assemblies

(i.e., proteins made by identical polypeptide chains) or hetero-oligomeric assemblies (i.e., proteins made by different polypeptide chains).<sup>[80,84]</sup>

### 1.6.2 Protein – Protein Interactions PPI

The vast majority of proteins are organized in complexes. Therefore, nature controls protein functions *via* modulation of PPI. Numerous examples of natural products that serve as PPI modulators have already found applications as essential drugs.<sup>[85]</sup> PPI are involved in almost all physiological processes and diseases.<sup>[86]</sup> There are 130,000 to 650,000 PPI estimated in humans. A newer approach in rational modulation of PPI comes with the fact that small, synthetic molecules can bind at the protein-protein complex interface. This represents tremendous potential for chemical biology and drug development. The target proteins are usually modulated in their enzymatic activity, subcellular localization, and ability to interact with further protein partners. Not all residues on protein-protein interfaces contribute equally to the binding events. Usually, the significant contribution to the binding free energy comes from a small set of residues directly involved in interactions. Clackson *et al.* defined the term hot spot as a residue in which substitution by an alanine leads to a significant decrease in the free energy of binding ( $\Delta\Delta G_{\text{binding}} > 1.5 \text{ kcal/mol}$ ).<sup>[87,88]</sup> The high-level application of supramolecular host-guest chemistry in water represents the biomolecular recognition of hot-spots on protein surfaces. The contact surfaces involved in protein – small-molecule interactions are much smaller ( $\sim 300 - 1,000 \text{ \AA}^2$ ) in comparison to those involved in PPI ( $\sim 1,500 - 3,000 \text{ \AA}^2$ ).<sup>[89]</sup>

Hot regions are defined as tightly packed clusters of hot spots, resulting in networks of conserved interactions.<sup>[87]</sup> The networked interactions of this kind are cooperative in stabilizing PPI. One example of hot regions on a protein-protein interface is shown in Figure 26 on example of  $\beta$ -catenin.

According to Hamachi and co-workers, there are three possible ways in which protein surfaces can be selectively recognized: (i) recognition of a substructure is defined by the peptide sequence on the protein surface; (ii) recognition of the exposed functional groups that represent a fingerprint of each protein; and (iii) protein recognition by using protein-ligand interactions.<sup>[51,90]</sup>

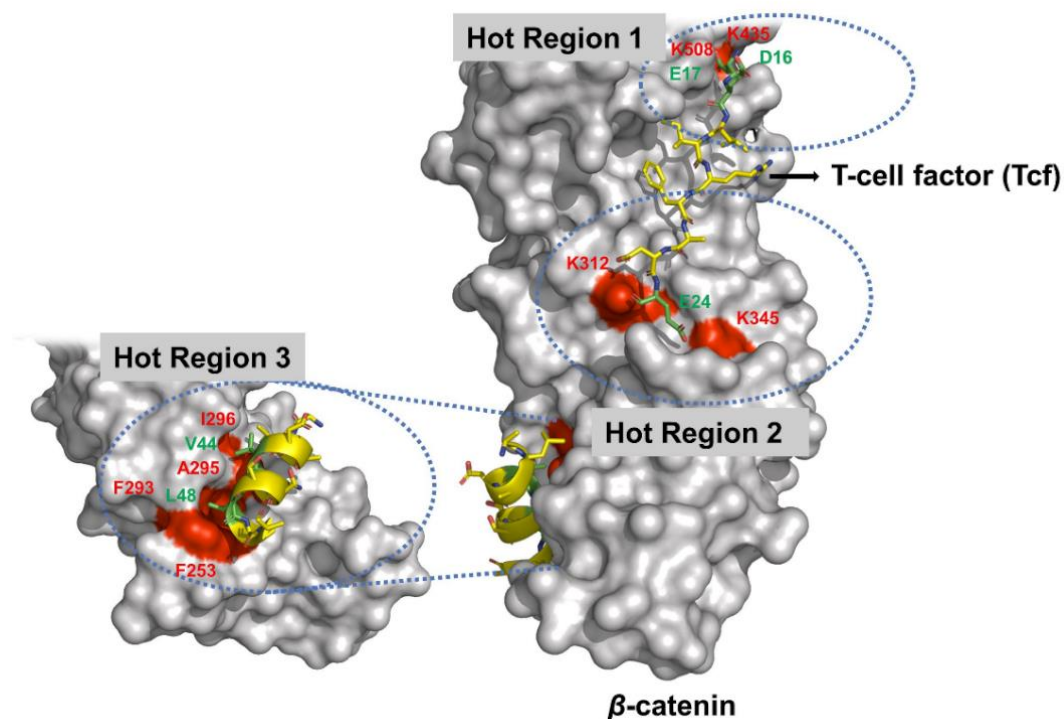


**Figure 26.** The crystal structure of  $\beta$ -catenin in complex with T-cell factor shows three hot regions (PDB ID: 1G3J).<sup>[87]</sup>

Protein recognition by synthetic molecules is moreover often divided into two categories based on the available binding sites: interactions that take place within the interior of the protein and interactions that take place on the surface.<sup>[51]</sup> Several synthetic host molecules have been reported in the literature that recognize protein interfaces through supramolecular host-guest interactions: crown ethers<sup>[91]</sup>, pillararenes<sup>[92]</sup>, porphyrins<sup>[93]</sup>, cucurbiturils<sup>[94]</sup>, cyclodextrins<sup>[95]</sup>, calixarenes<sup>[96]</sup>, and molecular tweezers (Figure 27).<sup>[83]</sup>

The main driving force for the formation of these supramolecular host-guest systems is due to the hydrophobic effects, which occur between the nonpolar regions of protein residues and the artificial guests, which is similar to PPIs. Whereas, hydrogen bonding and the electrostatic complementarity of the interacting protein surface and the synthetic guest only promotes the formation and lifetime of the complex and does not play a pivotal role in contrast to PPI.<sup>[87]</sup>

The unique molecular features of synthetic guest molecules enable the recognition of amino acids, peptides, and even whole protein surfaces, which can be applied as an

approach to the modulation and assembly of proteins.<sup>[83]</sup> Further examples of artificial PPI modulators and their mechanism of action will be discussed in Chapter 1.6.4.1 in the case of 14-3-3 PPI and Chapter 1.6.5.1 in the case of Survivin.

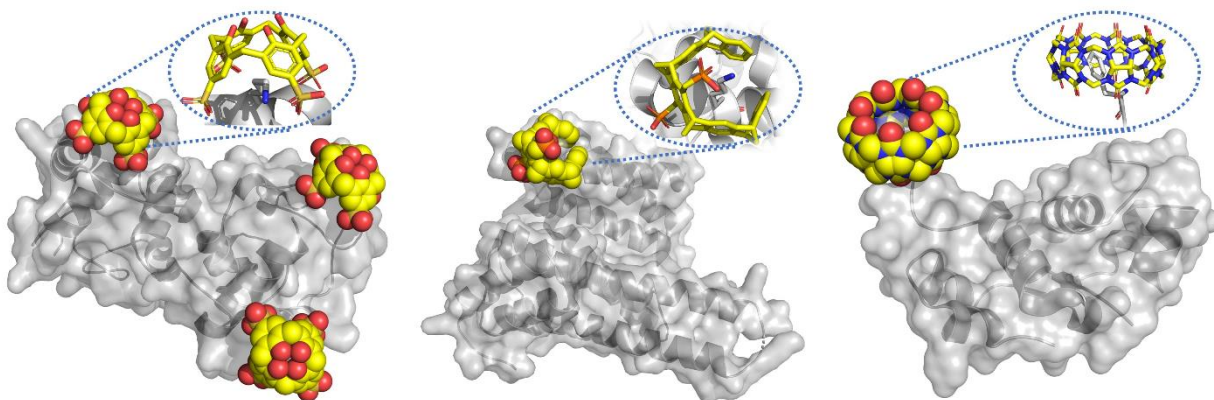


**Figure 27.** **a)** Crystal structure of sulfonatocalix[4]arene bound at three positions to an asymmetric cytochrome *c* dimer with a zoom-in on the calixarene binding site with Lys89 (PDB ID: 3TYI). **b)** Crystal structure of molecular tweezer binding protein 14-3-3 $\sigma$  with a zoom-in on the tweezer binding site with Lys214 (PDB ID: 4HQW). **c)** Crystal structure of cucubituril complexed with the N-terminal Phe of insulin (PDB ID: 3Q6E).<sup>[83]</sup>



### 1.6.3 Amyloid Proteins

Alois Alzheimer, a famous German psychiatrist and neuroanatomist, was the first scientist who precisely described the long-term study of the female patient Auguste D. in 1906. Auguste D. was suffering from a lethal disorder that has later become known as Alzheimer's disease (AD). Alois Alzheimer had followed her for five years through conditions manifested as paranoia, memory disturbance, aggression, and confusion.<sup>[97]</sup> Since then, many diseases have been associated with amyloids.

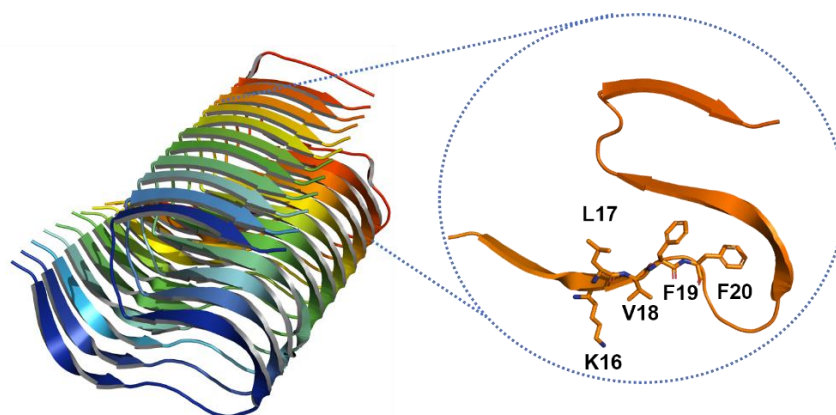


**Figure 28.** Crystal structure of S-shaped (PDB ID: 2MXU) and its monomer (11-42) shown in the orange cartoon and the critical peptide KLVFF (the central hydrophobic part of A $\beta$ 42) in orange sticks.

The first amyloid was observed and described in 1854 by Rudolph Virchow.<sup>[98]</sup> Amyloids are insoluble protein-carbohydrate complexes that form when normally soluble proteins become misfolded and adopt a fibril structure (Figure 28). Sunde *et al.* characterized amyloids in 1997 as the protein aggregates with elongated fibrillar morphology of 7-13 nm in diameter and a  $\beta$ -sheet secondary structure, able to bind the dye Congo red.<sup>[99]</sup> The amyloid structures' stability is maintained through non-covalent bonds between side and main chains, along with mostly hydrogen bonds, hydrophobic interactions, and  $\pi$ - $\pi$  stacking interactions.<sup>[100]</sup> Amyloid fibrils are abundant, thermodynamically stable, self-associated supramolecular assemblies, representing a promising source of ordered nanomaterials.<sup>[100]</sup> Physical studies reveal that amyloid fibers are comparable to steel in their strength and silk in their mechanical stiffness.<sup>[101]</sup> Apart from serving as a biomaterial of fascinating features, amyloids are being proclaimed as pathological agents, whose presence/formation leads to many severe disorders in the

human body.<sup>[102]</sup> A pathological phenomenon of abnormal self-assembly of peptides and proteins into toxic oligomers and aggregates causes proteinopathies or amyloidoses.<sup>[103]</sup> Today, more than 30 amyloid-forming proteins have been identified and associated with severe diseases. Those include amyloid- $\beta$  peptide 1-42 ( $A\beta_{42}$ ) associated with AD;  $\alpha$ -synuclein with Parkinson's disease (PD) and other synucleinopathies like multiple system atrophy (MSA); huntingtin protein (HTT) with Huntington disease (HD); islet amyloid polypeptide (IAPP) with diabetes type 2; and transthyretin (TTR) with familial amyloid polyneuropathy, familial amyloidotic cardiomyopathy, and senile systemic amyloidosis.<sup>[104,105]</sup>

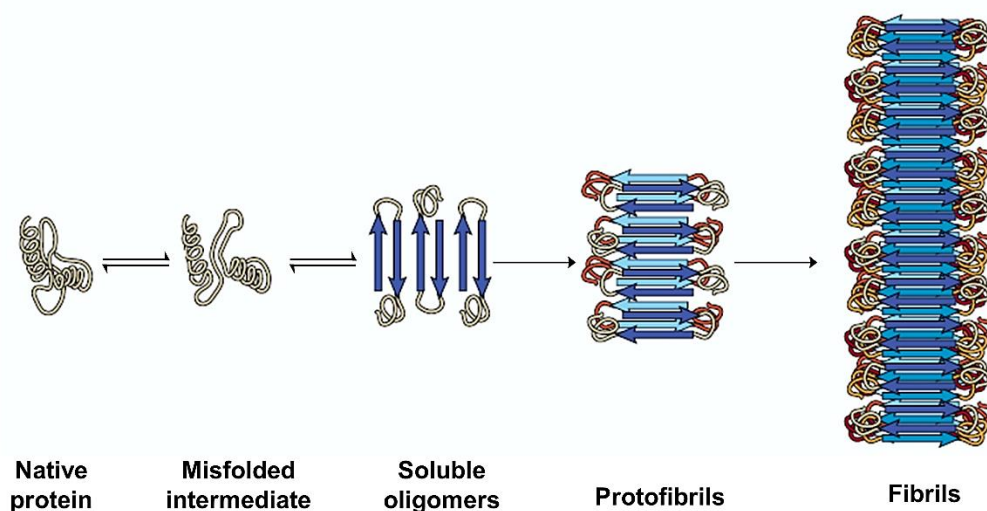


**Figure 29.** The proposed mechanism of irreversible fibril formation pathway leading to protein misfolding and aggregation according to Sottero *et al.*<sup>[106]</sup>

The proteins associated with the proteinopathies mentioned above have no obvious similarity in sequences, native structures, or function. However, they do share characteristics in their amyloid state as they can undergo structural rearrangements leading to the formation of amyloid fibrils and therefore undergoing so-called “process-specific mechanism”.<sup>[105,107]</sup> Pathogenic amyloids form when previously healthy proteins misfold – lose their normal structure and physiological functions and assemble into fibrous deposits in the form of insoluble plaques (Figure 29), whose presence can disrupt the healthy function of cell clusters. The fundamental “amyloid cascade hypothesis” suggested that the deposition of amyloid- $\beta$  protein ( $A\beta$ ) into  $\beta$ -sheets is the causative

agent of neurodegenerative pathologies such as Alzheimer's disease with consequences as tau hyperphosphorylation and aggregation (neurofibrillary tangles), cell loss, vascular damage, and dementia.<sup>[108]</sup> Nevertheless, the scientific community claims that the elusive and toxic  $A\beta$  oligomers are to be blamed as the cause for the resulting inflammations and pathologies rather than the deposited amyloid fibrils.<sup>[109]</sup> Aside from the debate on the causative role of  $A\beta$  aggregation in the pathogenesis of AD, a significant obstacle in the drug discovery comes with the fact that  $A\beta$  oligomers are existing in continually changing dynamic mixtures since the forces holding them together are much weaker than the intramolecular forces which assure the very stable amyloid structure. Therefore, the oligomers lack a stable and well-defined structure, which represents a prerequisite for successful drug discovery.

### 1.6.3.1 The effect of Molecular Tweezers on Protein Aggregation

The diphosphate-substituted molecular tweezer, patented as CLR01, is well-known for its broad-spectrum inhibitory potential in the self-assembly of toxic and amyloidogenic proteins.<sup>[110]</sup> Various instrumental methods elucidated binding positions of CLR01 ligand on the  $A\beta$  peptide, suggesting binding at all possible locations, Lys 16, Lys 28, and Arg 5 (Figure 30).

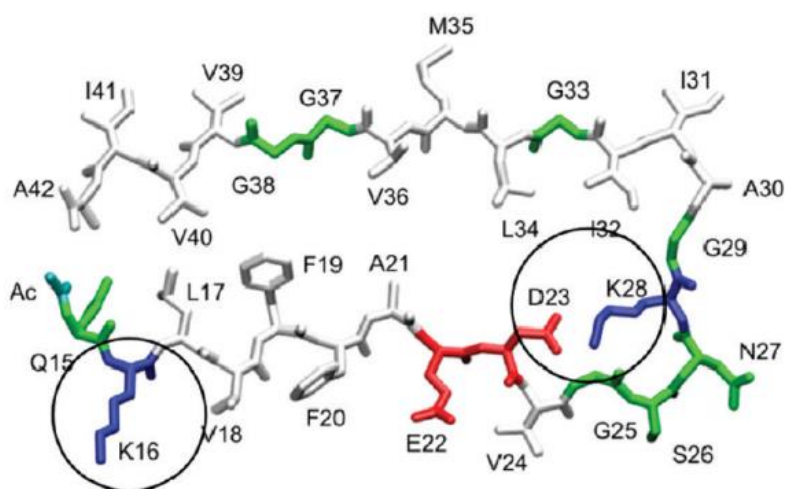


**Figure 30.** Misfolded part of  $A\beta_{42}$  in fibrils with critical lysine residues K16 and K28, which are selectively complexed by CLR01. Presumably, CLR01 interferes with the formation of the salt bridge between Lys 28 and Asp 23.<sup>[107]</sup>

Encouraging results were obtained using the CLR01 molecular tweezer in A $\beta$  fibrillation and  $\alpha$ -synuclein studies, respectively, while investigating the effect of CLR01 in the case of several proteinopathies, including prominent examples such as AD and PD.<sup>[47,58,72–78,110]</sup>

The two reviews presented by Schrader *et al.* in 2016 and later in 2019 by Hadrovic *et al.* provide an *in-depth* overview of using molecular tweezers as promising candidates for disease-modifying therapy. This opens entry to the evolution of supramolecular concepts towards biological application.<sup>[47,67]</sup> The detailed discussion on the binding mode of molecular tweezers and results from biophysical experiments clearly demonstrates how these non-toxic supramolecular tools work well to disrupt toxic aggregates oligomeric and fibrillar protein species and turn them to benign assemblies. Given the significance and great potential of molecular tweezers in practical applications and their correlation to protein recognition in host-guest chemistry, such an overview may arouse interests from experts in supramolecular chemistry. It should also inspire the further design of prodrugs with increased bioactivity.

#### 1.6.3.1.1 Blood-Brain Barrier Targeting Strategies

Aiming to improve the pharmacokinetics of CLR01, two different approaches have been developed: (i) the approach of lowering the molecular weight of the parent molecular tweezers CLR01, and (ii) the so-called “prodrug strategic approach”. Prodrugs are pharmacologically inactive chemical derivatives of a parent drug molecule that require a transformation within the body to release the active drug.<sup>[111]</sup> To promote the prodrug project in a targeted manner, it is necessary further to improve the blood-brain barrier (BBB) penetration. This could be achieved by increasing the hydrophobicity of CLR01 derivatives. Qualitatively, drugs that passively diffuse through the BBB are generally lipophilic and have a molecular weight of less than 500 Da.<sup>[112]</sup> Therefore, new molecular tweezer derivatives have been designed, in which phosphate groups were replaced by biologically stable groups (Figure 31).<sup>[68]</sup> Furthermore, the fluorinated derivative CLRF was introduced, and thanks to its lipophilic features, it represents a promising step in enhancing BBB penetration (for synthesis, please see Chapter 4.1).

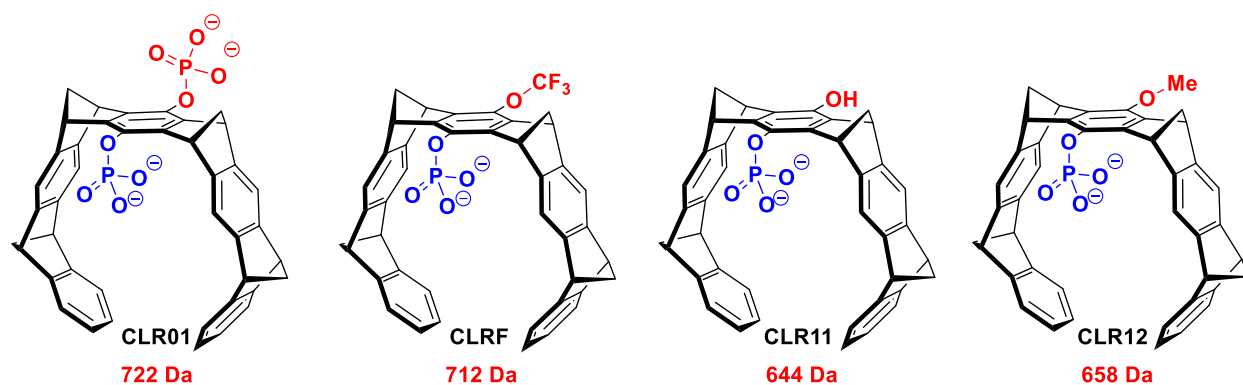


**Figure 31.** The approach of lowering the molecular weight. Various tweezer derivatives lower in the molecular weight than CLR01.

Moreover, the chemical method of modifying molecular tweezers by attaching fluorophores and signal peptides has been successfully established and might be beneficial also in the prodrug project.

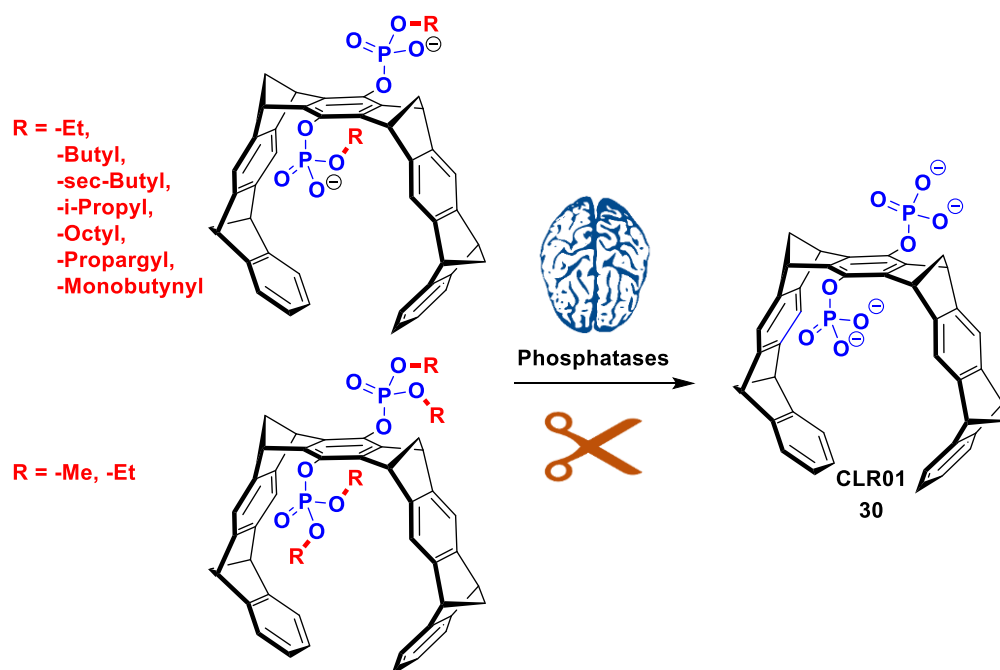


**Figure 32.** The prodrug approaches.

The modifying approach of lowering the charge (from -4 to -2) has been realized by esterification of the phosphate group with alcohol on both sides of the spacer. Besides diesters, Figure 32 illustrates two tetraesters, which are both neutrally charged, where phosphates are completely esterified with alcohol (discharge from -4 to 0).<sup>[68]</sup> Prodrug

strategic approach is realized by attaching labile (not biologically stable) ester groups to the CLR01 core, which are being cleaved *in vivo* by phosphatases in the brain (Figure 32).

Heid reported the synthesis of versatile symmetrical diesters and tetraesters relevant for the prodrug approach in 2019.<sup>[68]</sup> Two different synthetic strategies were successfully applied to the starting hydroquinone molecular tweezer (Figure 33). The synthesis of symmetrical tetraesters proceeded straightforward using phosphor oxychloride at -78 °C to obtain phosphorylated molecular tweezer, which was further esterified using the excess of the desired alcohol. The same synthetic approach was not working out in the case of symmetrical diesters since the synthesis does not proceed selectively, and the resulting mixture of the product is not easily separable. To overcome this problem, Heid applied the synthetic strategy developed by Cramer and Weimann, which lead from phenyl phosphates in the presence of trichloroacetonitrile and alcohol to the desired ester, leaving one unreacted -OH group at the phosphate.<sup>[113]</sup>

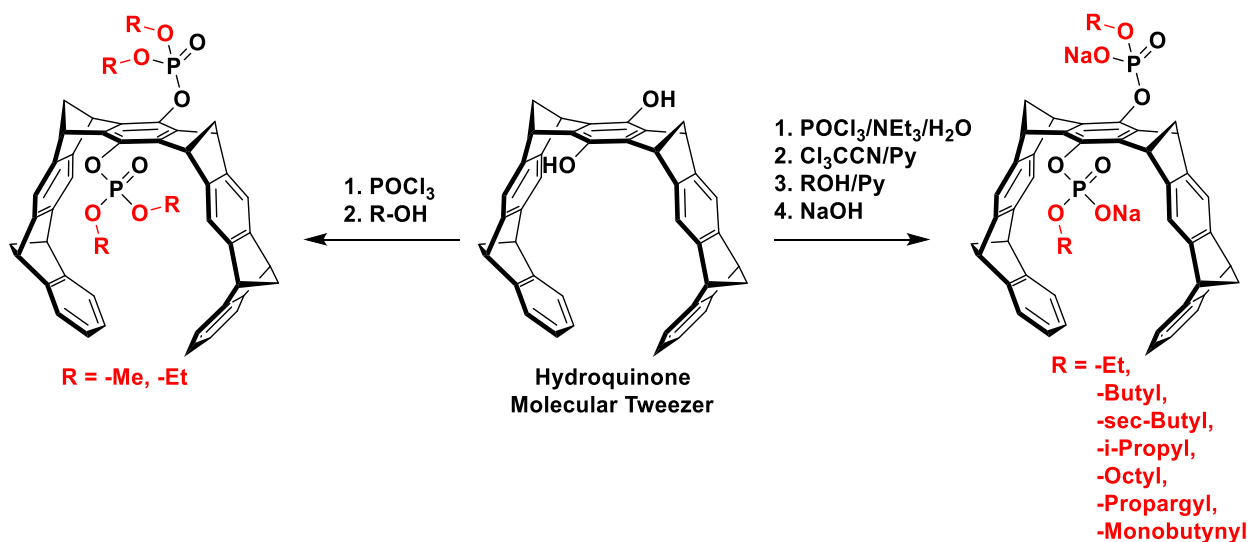


**Figure 33.** Synthesis of symmetrical diesters and tetraesters.

The group of Gal Bitan at UCLA did pharmacokinetics of versatile, newly designed prodrug candidates. Firstly, the cell toxicity of CLR01 derivatives has been tested applying colorimetric MTT assays on the PC12 cell line (derived from a pheochromocytoma of the rat adrenal medulla).

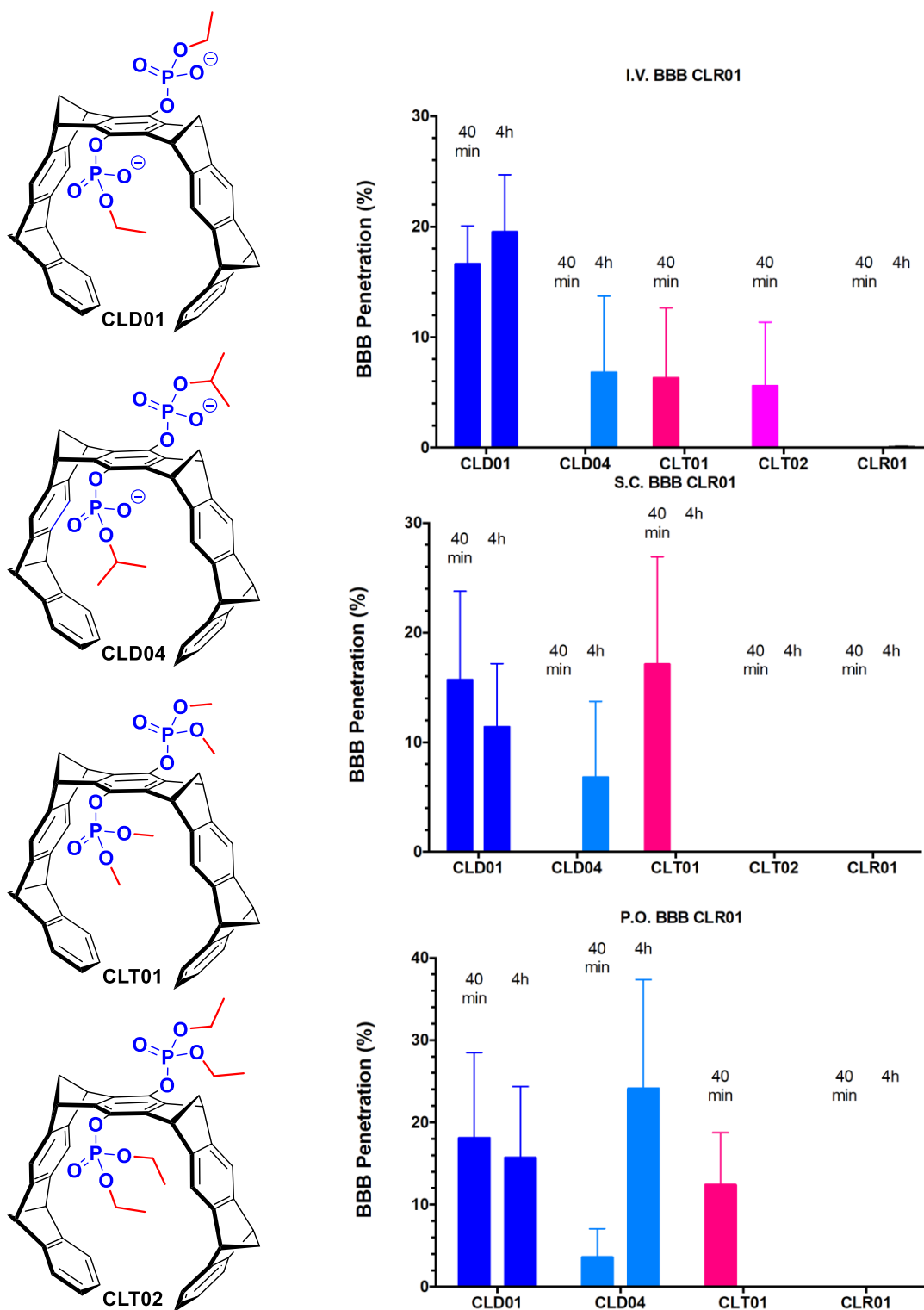


**Figure 34.** Leading prodrug candidates and their BBB penetration followed in time intervals depending on three different ways of administration; intravenously (I.V.), subcutaneously (S.C.), and perorally (P.O.)

The derivatives whose presence at the maximal concentration of 100  $\mu\text{M}$  did not result in cell death were further examined using the same assay to determine if they were active toxicity inhibitors of  $\text{A}\beta$  in the presence of 10  $\mu\text{M}$ . Interestingly, the prodrugs CLD01 and CLD04 exhibit high activity in protection from  $\text{A}\beta$ -induced toxicity than the parent molecular tweezer CLR01, whereas the ester derivative, which contained four or more C atoms in the alkyl side-chains, were toxic. Based on the results collected from the cell toxicity assays, the lead prodrug candidates were chosen for further pharmacokinetic (Figure 34). The Bitan lab at UCLA used 8-10-week-old wild-type mice for pharmacokinetic investigations. Mice were given the tweezers via three different administration forms. The intravenous (I.V.) and subcutaneous (S.C.) administration was carried out with 2 mg/kg body weight and the oral (P.O.) administration with 10 mg/kg body weight. Mice were sacrificed after 40 minutes and 4 hours of each administration, respectively. The blood and brain were collected and homogenized, and the concentration of CLR01 was examined utilizing HPLC-MS. It has been shown that the prodrugs are substantially more brain penetrant than CLR01, leading to similar brain concentrations following intravenous and subcutaneous administration, and much higher brain concentrations following preoral administration (Figure 34).



### 1.6.4 14-3-3 Proteins

One of the proteins of interest in the Collaborative Research Center (CRC) 1093 "Supramolecular Chemistry on Proteins" is the family of 14-3-3 proteins. The 14-3-3 proteins are a group of a small (~30 kD), acidic polypeptides that mainly exist assembled as dimers, forming both homo- and heterodimers.<sup>[114]</sup> The protein's peculiar name originates from the late 1960s when it was first identified, showing the characteristic migration pattern while using the starch gel electrophoresis to analyze the brain tissue.<sup>[115]</sup> The 14-3-3 proteins are expressed in all eukaryotic cell types and are highly abundant in the human nervous system. The number of isoforms found in various organisms ranges from 2 in yeast to 7 isoforms found in humans ( $\alpha/\beta$ ,  $\epsilon$ ,  $\eta$ ,  $\gamma$ ,  $\theta/\tau$ ,  $\delta/\xi$ ,  $\sigma$ ).<sup>[114]</sup> Each monomer consists of nine  $\alpha$ -helices forming an amphipathic groove, composed of many basic residues that can recognize protein partners through their antiparallel bivalent binding sites (Figure 35).<sup>[116]</sup>

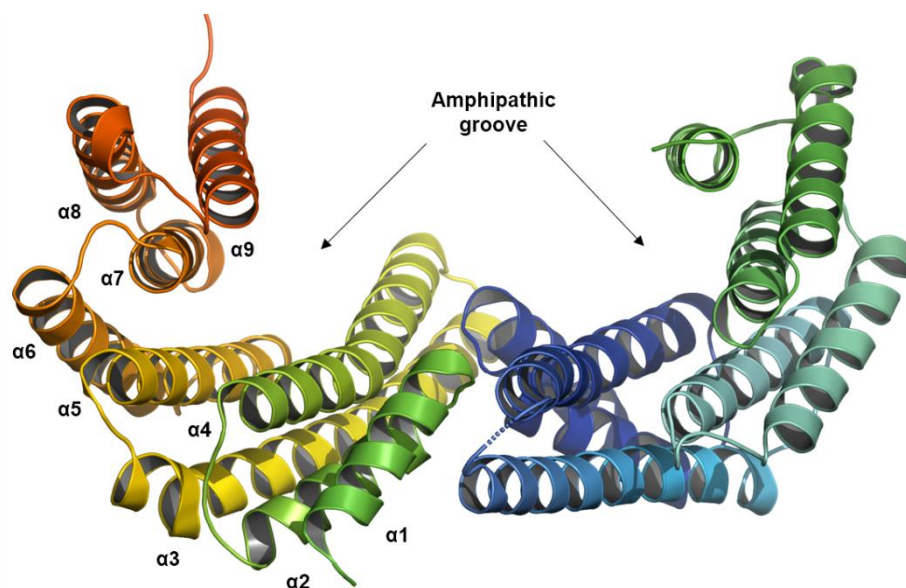


**Figure 35.** The overall architecture of 14-3-3 dimer (PDB ID:1QJB). Ribbon representation nine  $\alpha$ -helices.

14-3-3 proteins were the first protein modules to be discovered to bind specifically to phosphorylated substrates. This finding provided the foundation for their prominent role in cell signaling.<sup>[117]</sup> The binding protein partners mostly contain phosphorylated peptidic units (phosphoserine/phosphothreonine) in their sequences. Therefore, 14-3-3 proteins can function as adaptors, bringing two proteins that would not otherwise associate in such

proximity. Nevertheless, there are examples of 14-3-3 proteins binding their targets via unphosphorylated motifs, e.g., cytotoxin exoenzyme S (ExoS).<sup>[118]</sup>

The diversity in biological functions of this protein family is illustrated by proteomic studies in affinity purification of cellular 14-3-3 binding proteins that provide evidence for several hundred different binding partners (possibly > 700).<sup>[119]</sup> 14-3-3 proteins are proteins associated with most cellular processes such as cell-cycle control, signal transduction, protein trafficking, apoptosis, and survival.<sup>[85,120]</sup> Potential 14-3-3 targets and hence its importance in metabolic pathway control of diseases like cancer, diabetes, obesity, and cardiovascular disease are widely distributed.<sup>[119]</sup> A striking feature of the 14-3-3 proteins is their ability to interact with diverse disease-relevant signaling proteins, including kinases (regulate the activity of the kinase C-Raf), phosphatases (cell-division cycle phosphatase Cdc), and transmembrane receptors (transcriptional modulator YAP).<sup>[85,121]</sup> The isoform 14-3-3 $\sigma$  has been most directly linked to cancer. It is stabilizing the tumor suppressor p53 by inhibiting cell-cycle progression. Inactivation of 14-3-3 $\sigma$  indicates that it has a crucial role in tumor formation.<sup>[122]</sup> Loss of 14-3-3 $\sigma$  expression facilitates the treatment of tumor cells with conventional cytostatic drugs.<sup>[122]</sup> Therefore, the modulation of 14-3-3 $\sigma$  activity may represent an attractive therapeutic approach.

#### 1.6.4.1 14-3-3 PPI Stabilizers and Inhibitors

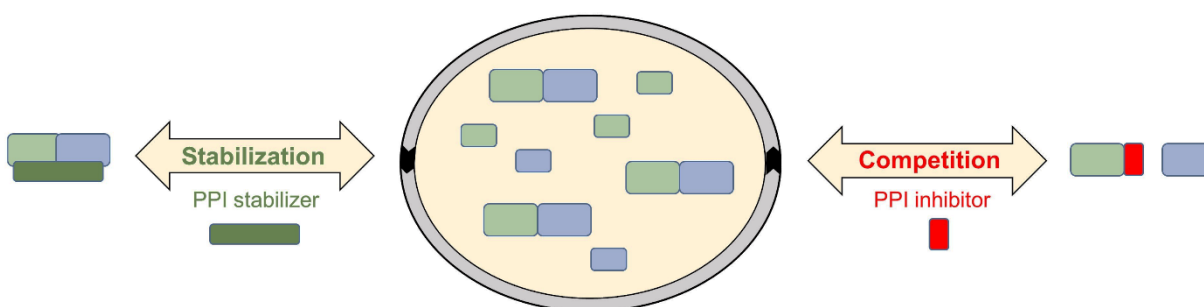


**Figure 36.** Modulation of PPI.<sup>[123,124]</sup>

Many direct PPI mediate the physiological activity of 14-3-3 proteins. The building evidence shows that either peptidic units or small-molecules can address PPI. These findings based on possible modulation approaches and a better understanding of PPI

represent tremendous potential for drug discovery, especially for diseases that cannot be targeted via conventional approach using enzymes, receptors, or ion-channels.<sup>[83]</sup> Modulation of PPI by small-molecules is the most attractive approach so far – achieved in two complementary ways: (i) by stabilization or (ii) inhibition (Figure 35).<sup>[123,124]</sup> The equilibrium between monomeric and multimeric proteins can be controlled either by altering the local concentration of protein components or influencing the binding affinity, determined by geometrical and physicochemical properties of the interface.<sup>[124]</sup>

The 14-3-3/PMA2/FC complex is known as nature's example of stabilizing 14-3-3 interactions by fungal phytotoxin fusicoccin (FC), a diterpene glycoside which acts like a "molecular glue".<sup>[125]</sup> The dissociation constant determined by isothermal titration calorimetry experiments reveals enhanced binding affinity for two orders of magnitude for PMA2 in the presence of fusicoccin ( $K_D = 27$  nM) *versus* binding to PMA2 to 14-3-3 alone ( $K_D = 2500$  nM).<sup>[126]</sup> The toxin's action mechanism can be understood from the crystal structure of 14-3-3 complex with phosphorylated pentapeptide of PMA2 (QSYpTV-COOH), an H<sup>+</sup>-ATPase isoform – a regulatory domain of the plasma membrane. FC closes the hydrophobic gap that remains in the 14-3-3 groove after binding phosphopeptide, leading to mutual stabilization of both ligands (Figure 37).<sup>[126]</sup>

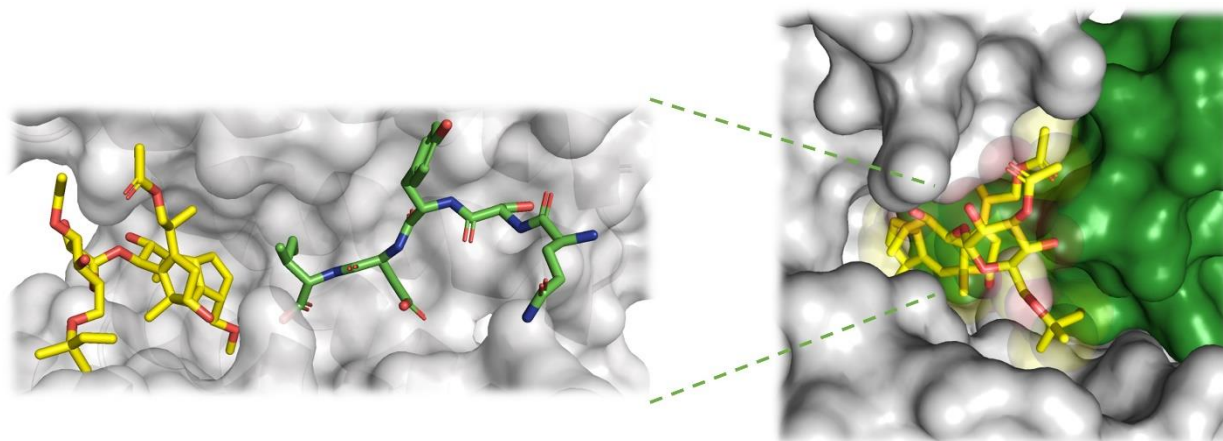


**Figure 37.** Binding of PMA2 (green) to 14-3-3 (gray) stabilized by fusicoccin (yellow) (PDB ID: 2O98).

FC's sugar moiety stays exposed to the solvent while burying its terpene ring deep in a funnel-like pocket formed by 14-3-3 and the C terminus of PMA2.<sup>[123]</sup> Besides FC, another representative small-molecule example from literature among 14-3-3 PPI stabilizers is a plant growth regulator Cotylenin A (CN-A), which binds to the contact

surface of 14-3-3 and C-Raf and stabilizes 14-3-3/C-Raf complex, which is expected to inhibit tumorigenic Raf activities. The fluorescence polarization assays (FP) showed significant improvement of the apparent  $K_D$  from 346 nM in the absence of CN-A to 20 nM in the CN-A presence.<sup>[127]</sup> It has been proven that both FC and CN-A successfully promote the interaction of 14-3-3 proteins with the human potassium channel Task3.<sup>[128]</sup>

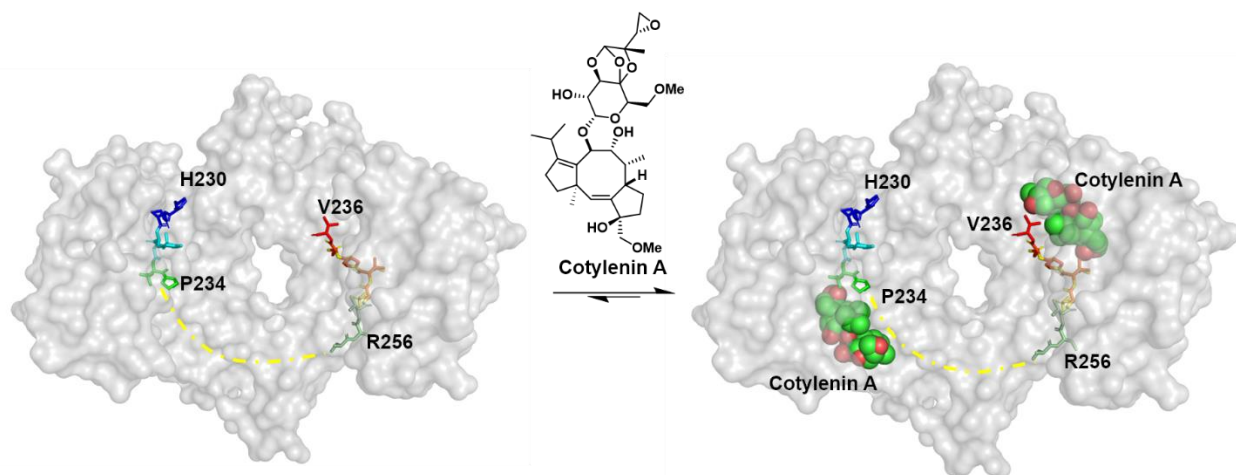


**Figure 38.** Complex 14-3-3/C-RafpS233pS259 (left). On the right is shown how CN-A (green spheres) binds to the contact surface of 14-3-3 (gray surface) and C-Raf (rainbow sticks) and stabilizes the 14-3-3/C-Raf complex (PDB ID: 4IHL)

Beside mentioned natural products that act as stabilizers of 14-3-3 PPI, there are several known examples of artificial supramolecular ligands that stabilize PPI. Rigid supramolecular host molecules such as cucurbiturils (CB) show high PPI stabilizing potential. The double-sided carbonyl rims, together with the hydrophobic interior, dictate the preference of CB to recognize cationic and hydrophobic protein residues (Figure 6 and 25).<sup>[83]</sup>

De Vink *et al.* explored CB-mediated stabilization of 14-3-3 PPI with the breast-cancer target, estrogen receptor ( $ER\alpha$ ).<sup>[129]</sup> The phenylalanine–glycine–glycine FGG tripeptide motif was fused to the N-terminus of the 14-3-3-binding epitope of  $ER\alpha$  for selective binding CB, resulting in the formation of a binary and bivalent protein assembly platform. The fluorimetric titration assays based on the displacement of acridine orange (AO) from the cavity of CB are showing that the formation of the bivalent platform is directed by two FGG-functionalized 14-3-3 binding epitopes, which was synergistically

controlled by the CB host and 14-3-3 protein dimer (Figure 39).<sup>[129]</sup> Multiple supramolecular interactions between the protein, peptide, and the supramolecular host are present in the crystal structure of the CB-induced ternary complex 14-3-3/FGG-ER $\alpha$ /CB (PDB ID: 5N10). A water network established by amino acid residues from the 14-3-3 is showed to lock CB into place in the crystal. In addition to that, the polar and hydrophobic contacts between CB and FGG-ER $\alpha$  were evident.

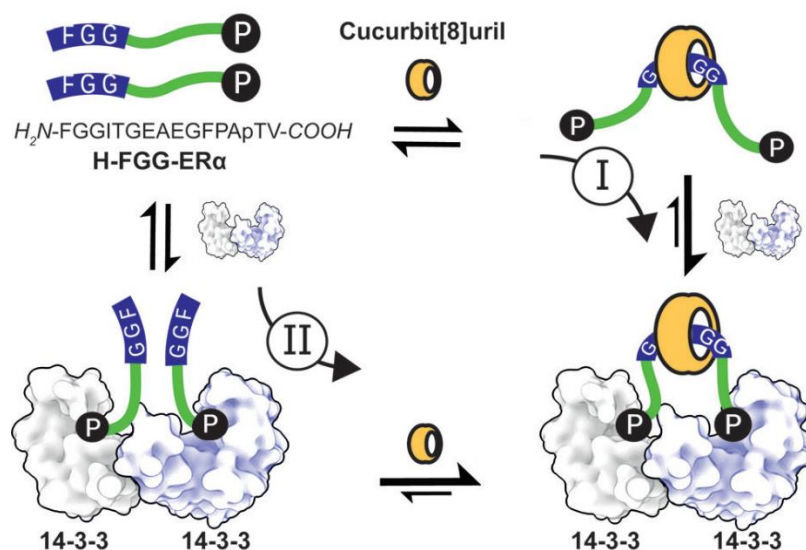


**Figure 39.** Binary bivalent protein assembly is directed synergistically by the CB and 14-3-3 protein dimers. Independent of the supramolecular assembly pathway (I or II), the two distinct binding epitopes of the two FGG-ER $\alpha$  phosphopeptides steer the formation of the multicomponent supramolecular platform. The figure is taken from de Vink *et al.* <sup>[129]</sup>

Gigante *et al.* recently published a new and potent class of supramolecular stabilizers of the interaction between 14-3-3 $\xi$  and C-Raf, Tau, and Task3.<sup>[130]</sup> The cationic ligands library containing the guanidiniocarbonyl pyrrole (GCP) moiety and a peptidic unit was screened to identify the potential PPI modulators. Therefore, GCP moiety is weakly basic and only partially protonated under physiological conditions ( $pK_a$  6–7).<sup>[51]</sup> It mimics arginine and forms very stable ion pairs with oxyanions such as carboxylates or phosphates (Figure 40). According to the collected ITC and FP data, ligands with a higher level of multivalency enhance the protein interaction with the effector peptides (C-Raf, Tau, Task3) by nearly two orders of magnitude. The GCP derivatives are the first known synthetic stabilizers for Tau peptide to 14-3-3 $\xi$ . Moreover, they were shown to be more

potent in comparison with the described CN-A for 14-3-3 $\xi$ /C-Raf interaction with EC<sub>50</sub> values in the low micromolar range (8.4  $\mu$ M in the best case).<sup>[130]</sup>

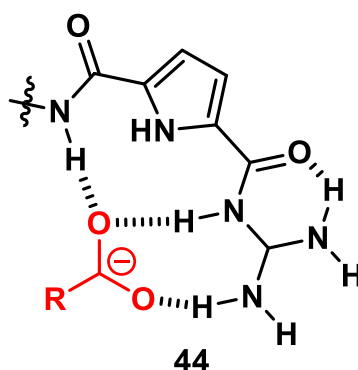


**Figure 40.** The illustration of the GCP unit (black) binding mode to oxoanions (red).

There are several prominent examples of small-molecules capable of interacting with the 14-3-3 binding interface and inhibit contact between protein binding partners such as hyperphosphorylated Tau epitopes<sup>[131]</sup>, phosphoserine mimetic prodrugs<sup>[132]</sup>, and non-peptidic inhibitors derived from BV02 (4-amino antipyrine scaffold).<sup>[85]</sup> It has already been mentioned that there are examples where 14-3-3 proteins bind their targets via unphosphorylated motifs (Chapter 1.6.2).

Fu *et al.* were the first to report a 14-3-3 PPI inhibitor, namely the peptide termed R18 (20 amino acid residues), identified by screening phage display libraries<sup>[133]</sup>. R18 exhibited a high affinity for different isoforms of 14-3-3 with estimated  $K_D$  values of 7 - 10  $\times 10^{-8}$  M, thus blocking the binding of kinase Raf-1 to 14-3-3 efficiently. The inhibitory effect of R18 on 14-3-3-ligand interactions is well explained by the cocrystal structure of R18 in complex with 14-3-3 $\xi$  (PDB ID: 1A38). The structure reveals the 14-3-3 amphipathic binding groove occupancy by the central sequence of R18 peptide (WLDLE). In addition to salt-bridge interactions between the carboxyl group of the glutamic acid side chain and three arginines of 14-3-3, there is a sizeable hydrophobic contact surface between the two leucine residues of R18 and several 14-3-3 residues (Figure 41).<sup>[134]</sup> By blocking the binding groove, R18 efficiently competes for both phosphorylation-dependent and -independent 14-3-3 PPI. Beside R18, the most prominent phosphorylation-independent interaction described so far occurs between 14-3-3 and virulence factor exoenzyme S (ExoS), an ADP-ribosyltransferase toxin of the pathogenic

bacterium *Pseudomonas aeruginosa*.<sup>[118]</sup> *Pseudomonas* are a common cause of hospital-acquired airway and wound infections that may lead to death.<sup>[136]</sup>

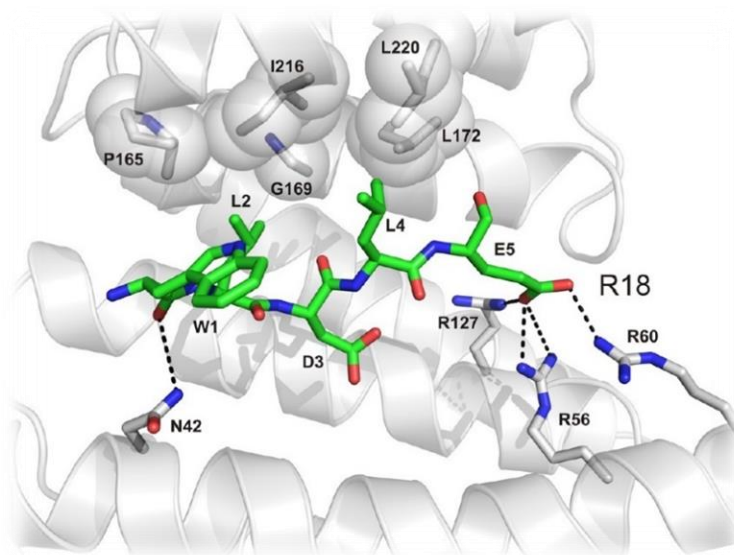


**Figure 41.** Binding of peptide R18 (green sticks) to 14-3-3 $\zeta$  (white cartoon). Residues from 14-3-3 important for interaction with R18 are shown as sticks. Polar interactions are depicted as black dotted lines, and hydrophobic contact surfaces from 14-3-3 are displayed as semitransparent spheres (PDB ID:1A38).<sup>[134,135]</sup>

14-3-3 proteins are essential cellular binding partners ExoS, and therefore the interaction between virulence factor ExoS and human 14-3-3 is considered to be a potential antibiotic target.<sup>[137]</sup> The structural analysis shows that the binding of ExoS motif to 14-3-3 amphipathic groove is mostly based on hydrophobic contacts (Figure 42). Besides the crystal structure, the cytotoxicity analysis supports the described binding mode, revealing that the corresponding hydrophobic residues' mutation significantly weakens the ability of ExoS to induce cell death.<sup>[136]</sup>

The research groups of Ottmann and Grossmann investigated macrocyclic peptides derived from ExoS that were proved to be useful modulators of biological functions, particularly as PPI inhibitors. These inhibitors were prepared from the ExoS peptide stretch that binds to 14-3-3 in an irregular and mostly extended conformation (sequence Q<sup>420</sup>GLLDALDLAS<sup>430</sup>) by replacing two hydrophobic residues crucially involved in 14-3-3 binding with non-natural amino acid residues cross-linked by a (CH<sub>2</sub>)<sub>n</sub> chain. Furthermore, a strategy for the macrocyclization of bioactive peptides was

introduced to stabilize an irregular peptidic structure and enhance target binding. Here, the ring-closing alkyne metathesis was used to stabilize an irregular peptide secondary structure for the first time. The cross-links were rationally designed to be involved in target binding, showing that macrocyclic molecules derived from peptides containing 14-3-3 binding motifs can efficiently inhibit the interaction between these adaptor proteins and their binding partners. In the most efficient macrocyclic inhibitor, residues L422 and A425 were replaced with a cross-linked chain containing 12 methylene groups. The lead inhibitor binds to 14-3-3 $\zeta$  with a 30-fold higher affinity than the unmodified ExoS peptide. This is due to the interactions between the hydrophobic chain and the non-polar residues within the binding groove of 14-3-3.<sup>[134]</sup>

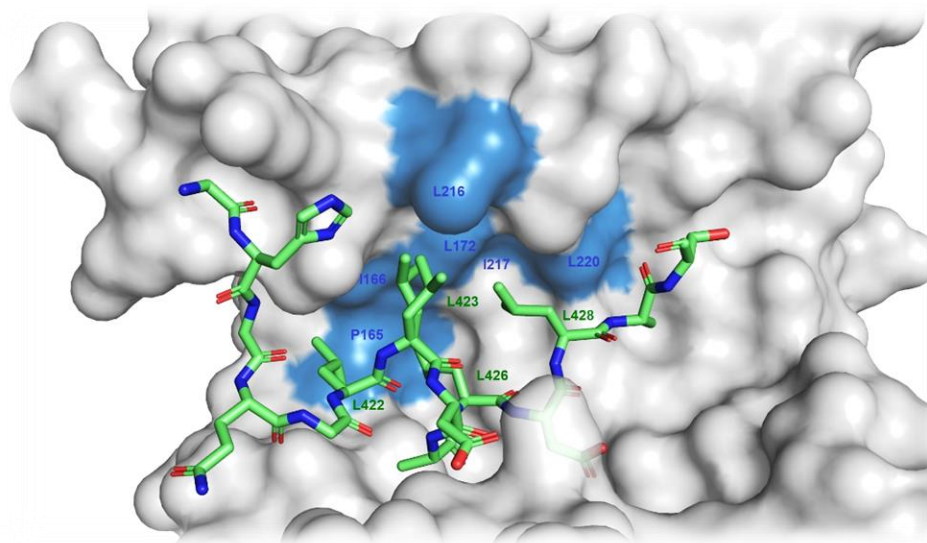


**Figure 42.** Binding of ExoS peptide segment (residues 417-430) shown in green sticks to 14-3-3 $\zeta$  (gray surface). An extensive hydrophobic contact interface is established binding to the hydrophobic part (sky-blue surface) in the 14-3-3 groove consisted of four leucine residues (L422, L423, L426, L428) (PDB ID: 2O02).<sup>[118,134]</sup>

#### 1.6.4.2 Modulation of 14-3-3 PPI using Molecular Tweezers

The binding mode of molecular tweezers was discussed in Chapter 1.4.2.1. Thanks to their “process-specific” capability to selectively recognize lysines and exhibit moderate binding affinities in a kinetically fast and reversible manner, molecular tweezers can be employed as modulators of various PPI. In 2013, Bier *et al.* reported the cocrystal structure of CLR01 with a 14-3-3 protein dimer.<sup>[48]</sup> Utilizing the combination of functional



binding assays, X-ray crystallography, and molecular simulations, a new class of phosphate-containing inhibitors of 14-3-3 PPI was proclaimed.<sup>[48]</sup> Although there are seventeen well-accessible Lys residues on the 14-3-3 surface in total, the structural analysis manifests only a single host-guest complex formation between CLR01 and K214 (Figure 27. b). The K214 is located at the edge of the amphipathic binding groove of 14-3-3 $\sigma$  and appears to be the only residue with favorable environmental surroundings. The three neighboring apolar residues Y213, T217, and L218 form predominantly hydrophobic interaction surface and shield CLR01 from the bulk water, which implies to be beneficial for a stable accommodation of the tweezer molecule (Figure 43).

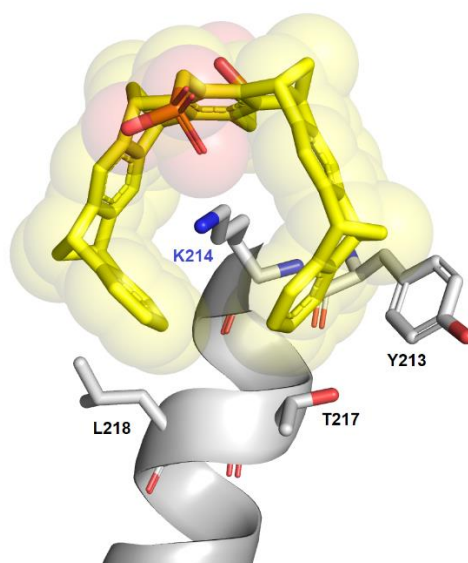


**Figure 43.** CLR01 (yellow sticks and surface) binding to K214 of 14-3-3 $\sigma$  (gray cartoon and sticks).

The influence of CLR01 presence on the binding of phosphorylated C-Raf and unphosphorylated ExoS to 14-3-3 $\sigma$  was monitored *via* fluorescence anisotropy. Estimated  $K_D$  values from FP assays between 14-3-3 protein and fluorescein (FAM)-labeled synthetic peptides C-RafpS259 (FAM-<sup>255</sup>QRSTpSTPNVH<sup>264</sup>-COOH) and ExoS (FAM-<sup>416</sup>SGHGQGLLDALDLAS<sup>430</sup>) in the absence of the tweezer were 12  $\mu$ M and 17  $\mu$ M, respectively. However, in the tweezer's presence, specific binding of the FAM-labelled peptides to the 14-3-3 protein was inhibited. The resulting half-maximum inhibitory concentration ( $IC_{50}$ ) values were in 480 and 520 mM range for C-RafpS259 and ExoS, respectively. Being bound in the vicinity to the protein binding region of many

binding partners (Figure 44), CLR01 can interfere with the function of 14-3-3 as an adapter protein and act as an efficient supramolecular inhibitor.<sup>[134]</sup>

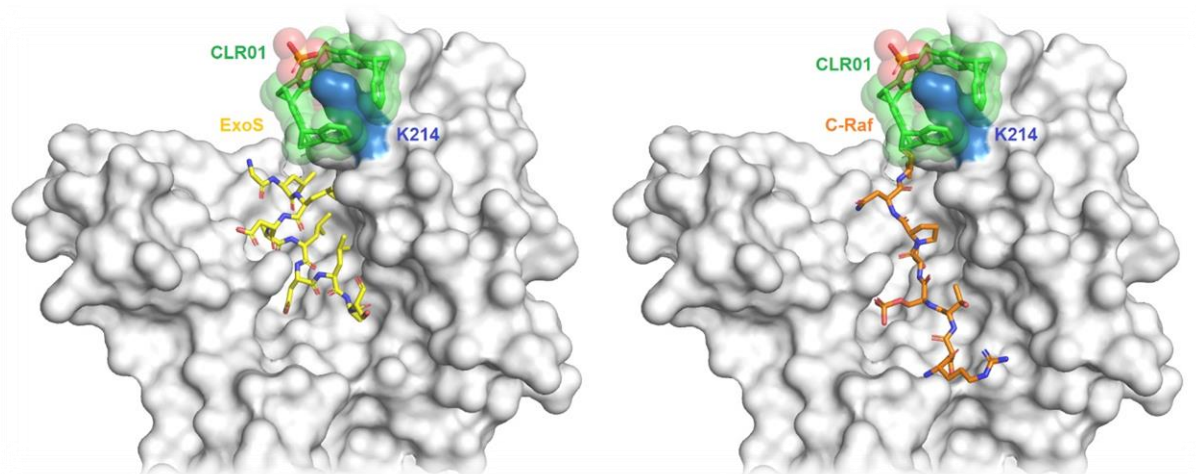


**Figure 44.** The relative position of the CLR01 (green spheres) binding site K214 (sky-blue surface) compared to ExoS – right (yellow sticks) and C-RafS253 – left (brown sticks).

### 1.6.5 Survivin

Besides the above discussed 14-3-3 proteins, another prominent example of proteins of interest in the CRC 1093 is the cancer-relevant protein Survivin, in literature also known as BIRC5. This name stands for the baculoviral inhibitor of apoptosis repeat (BIR)-containing 5.

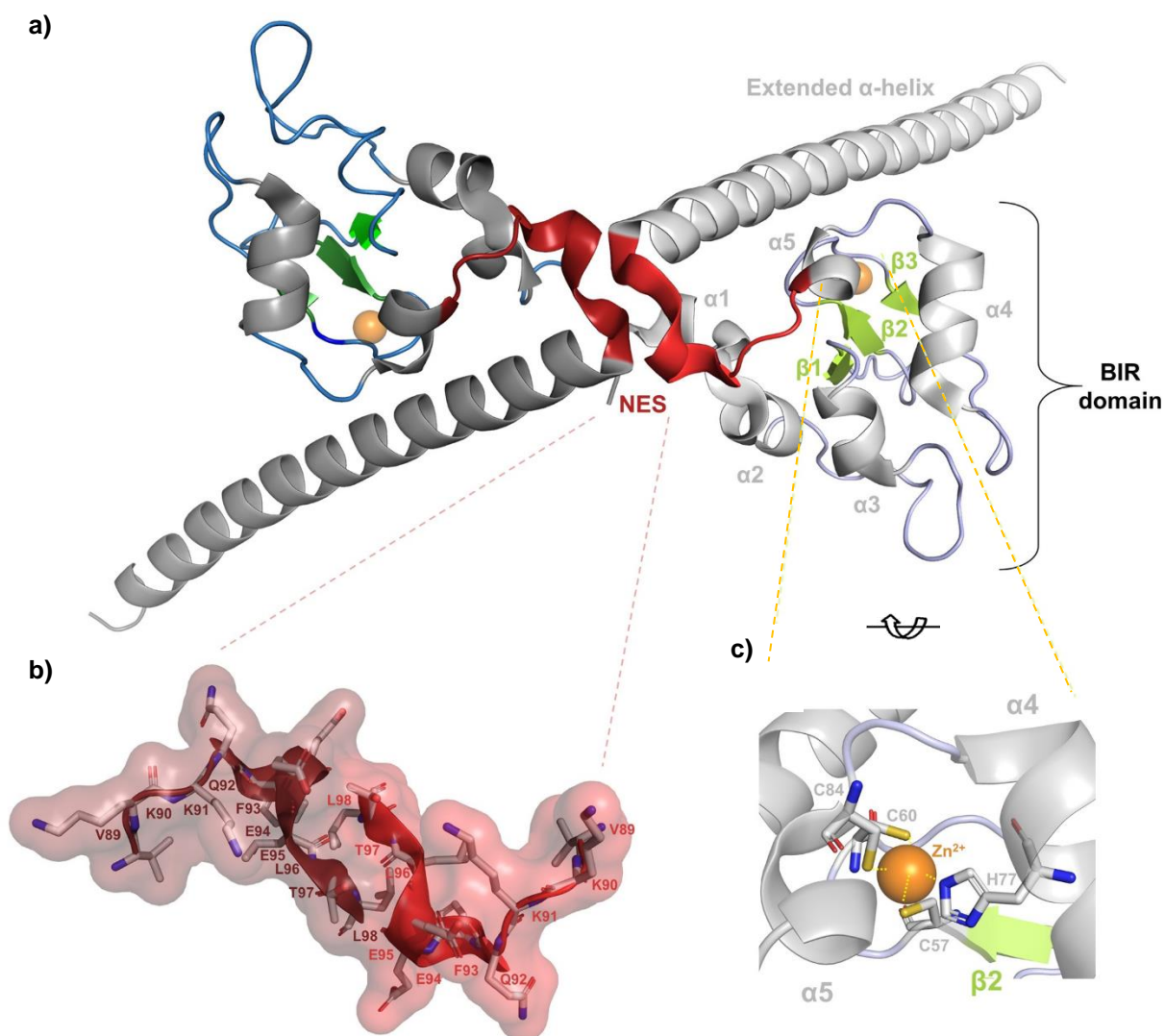


**Figure 45.** **a)** Crystal structure of Survivin dimer (PDB ID: 1F3H). One monomer is colored in darker nuances than the other one (color code:  $\alpha$ -helices – gray cartoons;  $\beta$ -strands – green sheets, loops – blue; NES – red; zinc cation – orange spheres). **b)** Zoom-in to the Survivin's dimer interface which partially overlaps with NES, addressed as one of Survivin's hot regions. **c)** Close view of the coordinative  $Zn^{2+}$  binding site. The depicted orientation corresponds to the monomer colored in lighter nuances, including vertical rotation of  $\sim 90$  degrees.

The BIR domain is a structural motif characteristic exclusively for proteins that interfere with programmed cell death (i.e., apoptosis), being first detected in insect viruses.<sup>[138]</sup> Survivin's crystal structure reveals that the protein crystallizes as a bow tie-shaped homodimer.<sup>[139]</sup> Two defined domains characterize Survivin, an N-terminal BIR domain (~ 70 amino acids zinc-finger fold), and an extended C-terminal helix. The N-terminal BIR globular domain (residues 15-89) represents two-thirds of the protein and is linked to an amphipathic C-terminal  $\alpha$ -helix spanning 11 helical turns (residues 98-142).<sup>[140]</sup> The BIR domain consists of a three-stranded antiparallel  $\beta$ -sheet surrounded by four small  $\alpha$ -helices (Figure 45. a).<sup>[139]</sup> The conserved residues, namely three cysteines (C57, C60, C84) and one histidine (H77), coordinate the zinc cation, which contributes to the stability of the BIR domain (Figure 45. c).<sup>[140]</sup> Survivin possesses a leucine-rich nuclear export signal (NES), centrally placed between the BIR domain and the  $\alpha$ -helix, partially overlapping with the dimerization interface (Figure 45. b). NES (residues 89-98) is recognized by the export receptor CRM1 and represents the important protein region. The extended C-terminal helices are stabilized by non-covalent interactions between the BIR domain and the first few turns of the  $\alpha$ -helix. Furthermore, there are hydrophobic clusters along the helix with the potential for PPI.<sup>[140]</sup> The specific interactions and the biological relevance of all three Survivin's structural elements, the BIR domain, NES, and  $\alpha$ -helix, will be discussed individually in the following chapters (1.6.5.1 and 1.6.5.2). Survivin is almost twice as small in size as compared to the previously described 14-3-3 protein (142 amino acids; 16.5 kDa) – representing the smallest member in the family of eight known inhibitors of apoptosis proteins (IAP) in humans.<sup>[141]</sup> The inhibition of apoptosis and, thus, promoting cell survival (hence the name Survivin) is only one of the two Survivin's major functional features. Further, Survivin is essential in regulating the cell cycle through cell division, playing an essential role in the mitotic process. Survivin's expression occurs in various cell organelles, including the cytoplasm, nucleus, mitochondria, and cytoskeleton.<sup>[138]</sup> In addition to the wild type (WT), there are six known Survivin isoforms (2B,  $\Delta$ Ex3, 3B, 2 $\alpha$ , 3 $\alpha$ , and SI) that structurally differ in carboxyl end but share the entire N-terminal region, including partially or entirely BIR domain.<sup>[142]</sup> Apart from structural varieties, the isoforms show differences in localization as well. For example, Survivin- $\Delta$ Ex3 isoform is predominantly located in the nucleus, while

Survivin-2B is detected in the cytoplasm.<sup>[142]</sup> The isoforms are mainly expressed only in low concentrations, and therefore presumably do not interfere in function with the primary transcript.<sup>[143]</sup>

Interestingly, Survivin has a very distinctive expression pattern. It is upregulated only during the early stages of embryonal development as well as in actively proliferating cells, unlike being absent in healthy resting mature tissues.<sup>[144]</sup> Still, Survivin can be found overexpressed in most types of cancer cells, including lung, breast, brain, gastric, pancreatic, liver, uterine, and ovarian cancer tissues.<sup>[142,145–147]</sup> The overexpression of Survivin in cancer versus healthy adult cells makes it a useful cancer diagnosis tool. It occurs in occurs in various cell organelles, including the cytoplasm, nucleus and mitochondria.<sup>[138]</sup> In cancer cells, mitochondrial and cytoplasmic Survivin enhance cell resistance enhancing cell resistance to apoptosis, consequently increasing resistance against chemo- and radiotherapy.<sup>[146]</sup> Survivin's capability to inhibit the programmed death of malign cells and facilitate their proliferation is an undesirable event that leads to tumor expansion and poor clinical outcome.

### 1.6.5.1 Survivin PPI

Survivin is assigned to the adaptor protein family since it has no enzymatic activity of its own. Instead, Survivin fulfills its dual function, i.e., regulating the cell division and inhibiting apoptosis, through the PPIs in association with its binding partners.

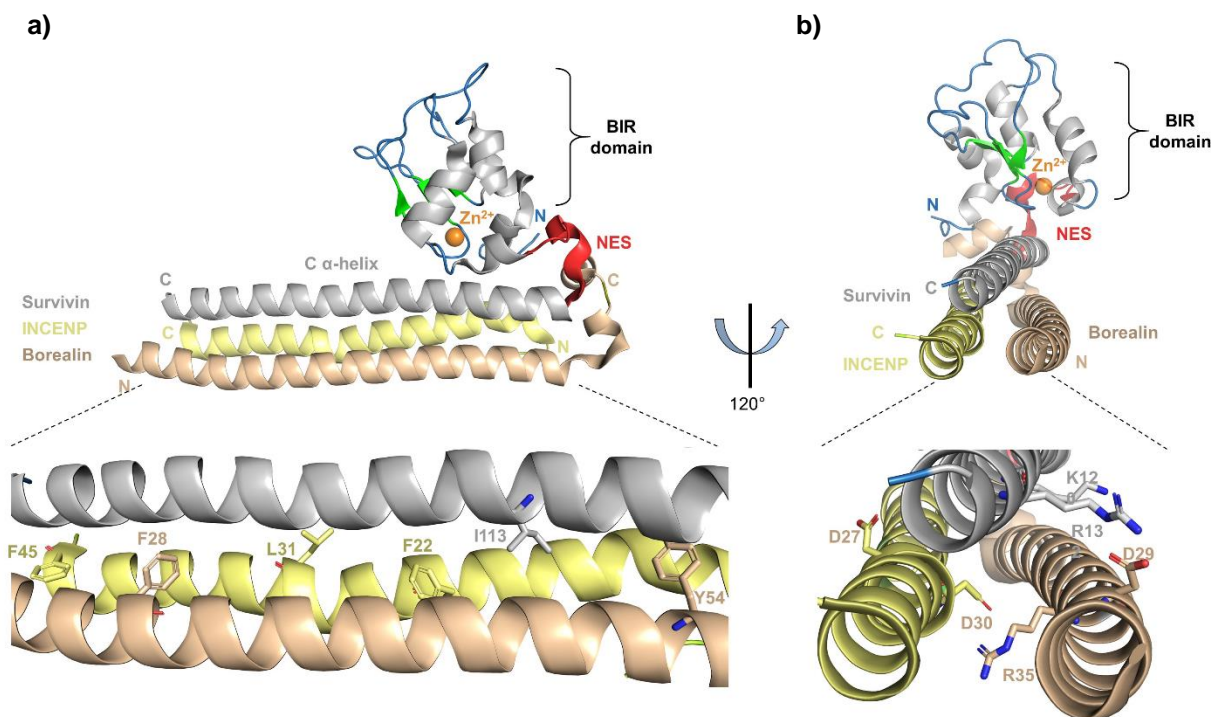


**Figure 46.** Crystal structure of a Survivin-Borealin-INCENP core complex (color code: Survivin – please see Figure 45; INCENP – pale-yellow; Borealin – sand color). **a)** The close-up view shows the core interactions in the three-helical bundle that include hydrophobic contacts. **b)** The close-up view in the right panel shows the core interactions on the surface of the helical bundle that include intermolecular salt bridges, resulted in rotation of  $120^\circ$  about the vertical axis (PDB ID: 2QFA).<sup>[148]</sup>

Nuclear Survivin plays a vital role in the regulation of cell division. It acts as an integral mediator for the correct localization of chromosome passenger complex (CPC).<sup>[142]</sup> Aside from Survivin, the CPC consists of two more regulatory subunits – Borealin and the inner centromere protein (INCENP) that synergistically stabilize the complex and one enzymatic subunit – Aurora B kinase. Survivin employs its central linker region (residues 90-102) to interact with N-terminal domains of both mitotic partners Borealin (residues 17-56) and INCENP (residues 1-46), forming a three-helical bundle (Figure 46).<sup>[149]</sup> Even if three different proteins influence the function of Aurora B, they operate as a single unit, equally contributing to the stabilization of the CPC. They

are connected through a dense network of hydrophobic intermolecular interactions and stabilized through the ability to form intramolecular salt bridges (please see Figure 46 for details). Specific disruption in any of the four CPC subunits can lead to a defect in chromosomal segregation and affect cellular homeostasis.<sup>[142]</sup>

In contrast to nuclear Survivin, which regulates cell division, the cytoplasmic Survivin controls cell viability as it inhibits activation of death proteases (caspase-cysteinyI-aspartate specific protease) and thus prevents apoptosis. However, the mechanisms by which Survivin counteracts apoptosis are still controversial. While there is plenty of evidence that caspase activity (a key biomarker of apoptosis) is reduced by Survivin expression, Survivin does not bind to caspases at physiological concentrations.<sup>[150]</sup> The reason could be the fact that Survivin does not possess the N-terminal extension responsible for docking of caspase-3 to the BIR domain.<sup>[139]</sup> In addition to this, there are three distinct mechanisms on Survivin's IAP function described in the literature. All three mechanisms are based on PPI between Survivin and caspase-9, hepatitis B X-interacting protein (HBXIP), and pro-apoptotic proteins called secondary mitochondria-derived activator of caspase (SMAC), respectively, in order to disrupt specific cascades and prevent programmed cell death.<sup>[142,151]</sup>

Also, there is evidence that survivin may inhibit apoptosis by inhibiting tumor protein p53.<sup>[152]</sup> Besides its role as a CPC and IAP member, Survivin protein is associated with polymerized tubulin and regulates microtubule dynamics and nucleation during cell division.<sup>[153]</sup> A cancer-relevant PPI between Survivin and export receptor CRM1 (chromosome region maintenance 1) will be disclosed separately in the following chapter due to its relevance for the presented work.

### **1.6.5.2 Targeting the Survivin-CRM1 Interaction**

#### **1.6.5.2.1 Nucleocytoplasmic Transport**

Nucleocytoplasmic transport is an essential process that dictates the nuclear-cytoplasmic localization of many proteins and RNAs.<sup>[154]</sup> There are seven known exportins in eucaryotic cells. CRM1 (also known as Exportin-1 and XPO1), one of the major export receptors which exports hundreds of diverse-functioning proteins through recognizing their leucine-rich NES.<sup>[155,156]</sup> CRM1 has a molecular weight of 123.4 kDa

(1071 amino acids), including 21 HEAT repeats (protein tandem build of two  $\alpha$ -helices linked *via* a short loop).<sup>[145]</sup> This kind of architecture assures structural flexibility during the transport cycle. The outer, convex surface of CRM1 is built of  $\alpha$ -helices, and the inner, concave surface consists of the  $\beta$ -helices.<sup>[156]</sup> Crystallographic investigations of CRM1 have shown that it undergoes conformational changes at equilibrium from extended to compact conformation (Figure 47).<sup>[157]</sup> Five hydrophobic binding pockets characterize the NES binding cleft. It is closed in free – unbound form and open in loaded – compact conformation. This structural feature facilitates the NES region's recognition sterically, making it more accessible, which consequently results in an increased binding affinity towards CRM1 binding partners.

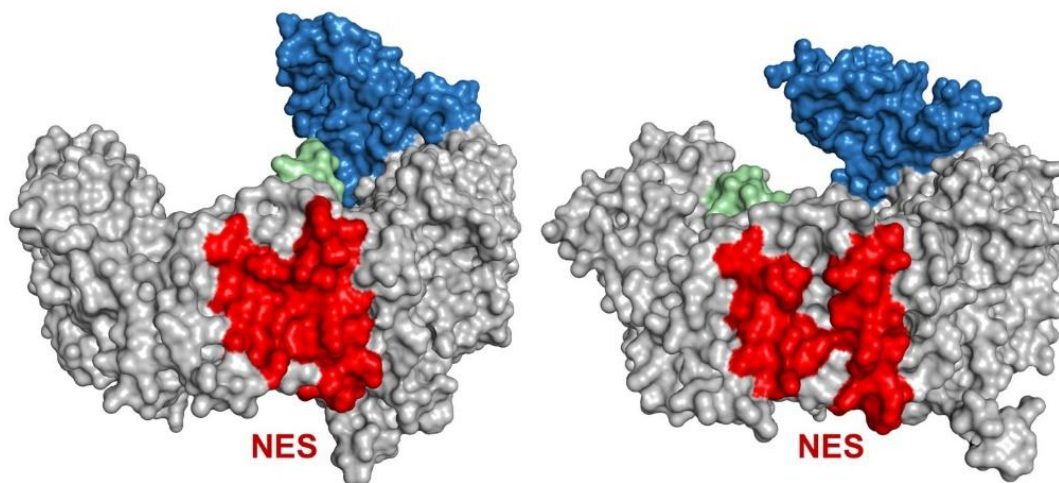


**Figure 47.** Structural variations of CRM1 during an export cycle. The conformational changes from extended (free-unbound) to compact (loaded-bound) CRM1 has been shown with an accent on the “breathing movements” in the NES binding cleft (color code: CRM1 – gray surface; CRIME domain – sky-blue; the acidic loop – pale green, and the NES – red), PDB IDs: 4FGV and 3GJX.

The nuclear export begins with CRM1 binding to GTP-ase binding protein Ran (RanGTP, where Ran stands for RAs-related Nuclear antigen and GTP for guanosine triphosphate) as illustrated by Figure 48 a). This causes a conformational change in CRM1, increasing its affinity for the NES-bearing export cargo. Hence, both RanGTP and the cargo protein bind in a cooperative fashion to CRM1.<sup>[154]</sup> Monecke *et al.* suggested that binary interactions with either RanGTP or cargo stabilize the compact and active state of CRM1, making it energetically favorable for binding the second ligand to form the



ternary CRM1-RanGTP-cargo complex.<sup>[154,158]</sup> Once the cargo is bound, the RanGTP-CRM1-cargo complex leaves the nucleus passing the nuclear pore complex (NPC) on its way to the cytoplasm (Figure 48. b). The hydrolysis of RanGTP to RanGDP (guanosine diphosphate – GDP) releases CRM1 and results in exportin conformational change as well as in decreasing affinity towards cargo protein (Figure 48. c). Hence, once no longer bound to Ran, the complex CRM1-cargo protein falls apart. Thereupon, both CRM1 and RanGDP are recycled for the next export cycle, and CRM1 returns to the nucleus ready to repeat the nuclear export (Figure 48. d).<sup>[145,159]</sup>

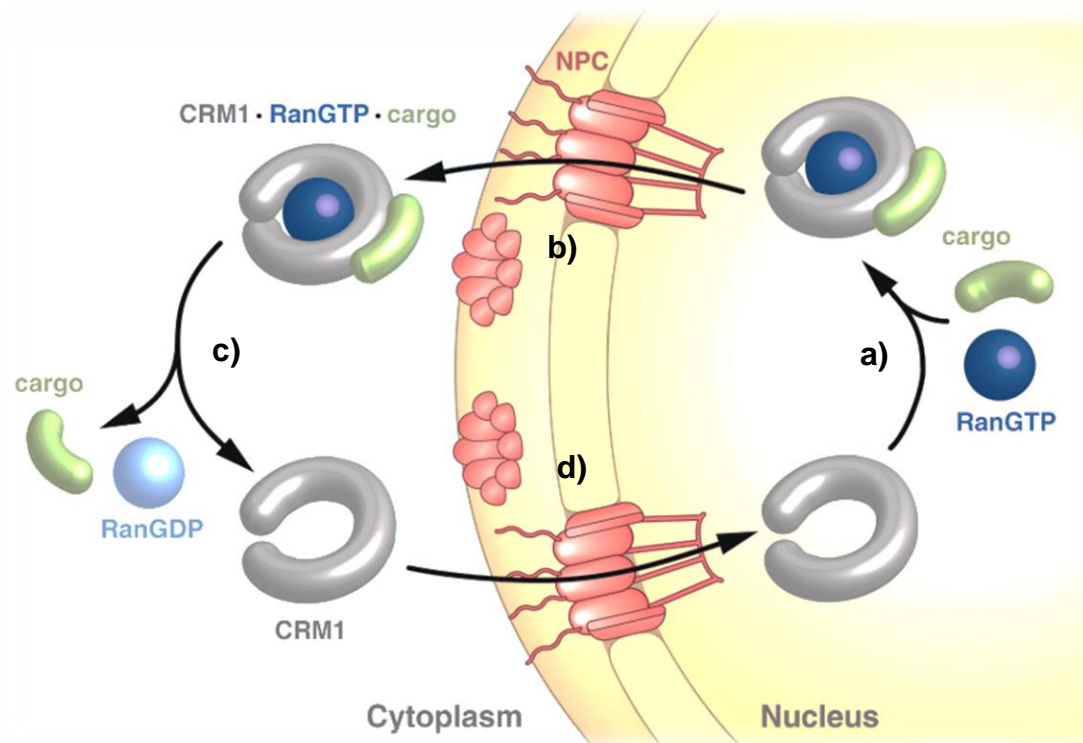


**Figure 48.** CRM1 mediated transport cycle. Conformational changes of bound *versus* unbound form are illustrated with open and closed circular discs.<sup>[145]</sup>

### 1.6.5.2.2 The Most Prominent Inhibitors of CRM1 Mediated Export

Targeting nuclear CRM1 mediated export represents a promising strategy to fight cancer by preventing the cytoplasmic accumulation of cancer-relevant protein such as Survivin.<sup>[160]</sup> The previously described mechanism of CRM1 action indicates that targeting of nucleocytoplasmic transport could be realized at various levels, including the interaction between Ran regulators and the export receptor CRM1, the interaction between CRM1 and cargo proteins, and the NPC.<sup>[159]</sup> The natural product Leptomycin B (LMB), an anti-fungal antibiotic, is the first drug identified as CRM1 inhibitor, capable of blocking the NES-binding cleft and thus interfering with its PPIs. However, a phase I clinical trial showed substantial dose-dependent toxicity proclaiming LMB unsuitable for further clinical use.<sup>[161]</sup> LMB is a 540 Da polyketide chain with a simple  $\alpha,\beta$ -unsaturated  $\delta$ -lactone ring (Figure 49).

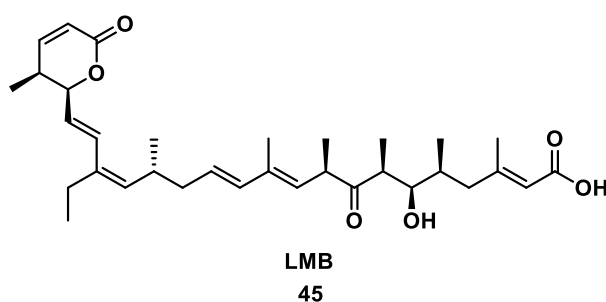


**Figure 49.** The structure of LMB.

It retains most of the biological activity by forming the reversible covalent bond with a reactive cysteine residue (Cys 528) in the NES-groove of human CRM1 *via* thia-Michael addition, as reported by Sun *et al.*<sup>[162]</sup> First, the alkene in the LMB lactone ring **45** forms a covalent bond with the thiol of the Cys residue (Figure 50 a). Subsequent lactone hydrolysis is driven by the nucleophilic attack of **48** with a water molecule. Presumably, the oxyanion hole assembled from the basic residues (Lys and Arg) in the vicinity of the reactive cysteine stabilizes the transition state of the reaction. The resulting hydroxyl and carboxylate groups (shown as red spheres in the final structure in Figure 50) of the hydrolyzed lactone **50** make extensive polar – electrostatic interactions with residues located at the top and bottom of the NES groove. In addition, the polyketide of LMB makes hydrophobic interactions with the same CRM1 groove residues that interact with the NES of cargo proteins. In summary, these interactions are probably crucial for LMB's extensive

and stable coverage of the NES groove and, therefore, the efficient interference with PPI.<sup>[163]</sup>

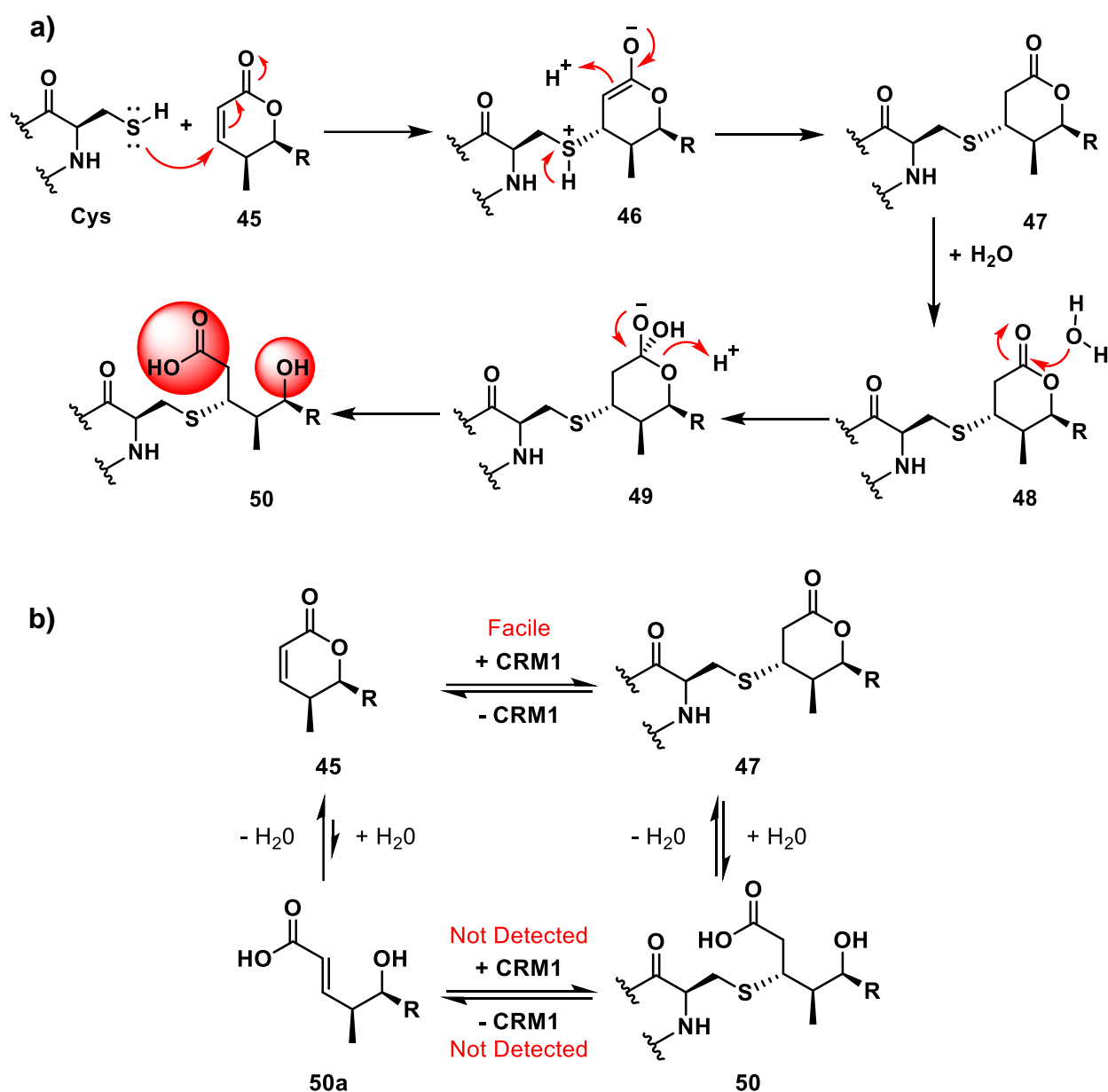


**Figure 50.** **a)** The mechanism of reversible covalent conjugation of Cysteine residue and  $\alpha,\beta$ -unsaturated  $\delta$ -lactone ring 45, representing LMB. **b)** The equilibria showing how lactone hydrolysis decreases the reversibility of covalent conjugation.<sup>[162]</sup>

Subsequent lactone hydrolysis by CRM1 optimizes LMB-CRM1 interactions and the irreversibility of conjugation and, thus, inhibitor potency.<sup>[162]</sup> After showing how ring-opening should enable lactone-based inhibitors to attach more persistently to CRM1 in

Figure 50, the equilibria of conjugation and hydrolysis for CRM1 inhibition by LMB is shown in Figure 50 b. The reversibility of the conjugate addition of cysteine should be kinetically controlled, with deprotonation of the inhibitor  $\alpha$ -proton as the rate-determining step (Figure 50 b). The  $\alpha$ -proton of the hydrolyzed (carboxylate) inhibitor is less acidic than the  $\alpha$ -proton of the lactone. Thus, ring-opening should enable lactone-based inhibitors to attach more persistently to CRM1 than analogous inhibitors without this capability.<sup>[162]</sup>

Sun *et al.* also reported that CRM1-mediated lactone hydrolysis seems to be significant for long-lived inhibition by LMB and other  $\alpha,\beta$ -unsaturated lactone polyketide inhibitors, but it is not crucial to inhibit NES recognition by CRM1.<sup>[162]</sup> This example comes with the new second-generation class of CRM1 inhibitors, called selective inhibitors of nuclear export (SINE). The most promising SINE candidate is Selinexor, a small, fully synthetic molecule. It is recently optimized to selectively inhibit the nuclear export called Selinexor (Xpovio or KPT-330) (Figure 51).<sup>[164]</sup>

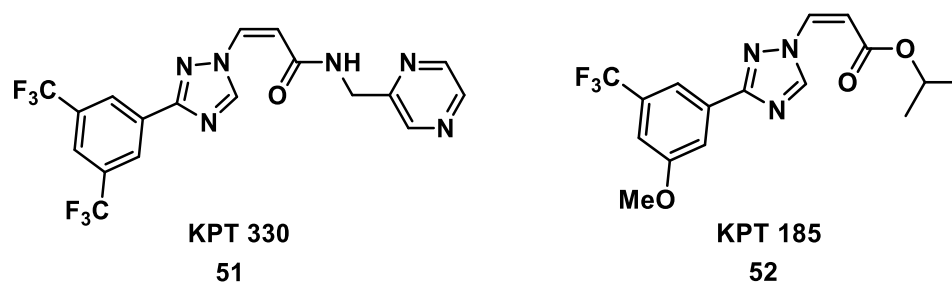


**Figure 51.** The structure of KPT 330 **51** and KPT 185 **52**.

Selinexor was developed utilizing low-cost computational methods in a structure-based design process known as induced-fit docking. As of 2019, this N-azolyacrylate drug is undergoing Phase III clinical studies being already approved by the Food and Drug Administration (FDA).<sup>[165]</sup> Selinexor form a slowly reversible, covalent bond with the cysteine residue (Cys 528/539) of the cargo-binding pocket of CRM1.<sup>[166]</sup> causing accumulation of tumor-suppressive proteins in the nucleus, which is directly correlated with the induction of cell cycle arrest and subsequent apoptosis. However, the specificity of this drug-target interaction in cancer cells is still not validated.<sup>[167]</sup>

The small-molecules from the KPT family conjugate to the same reactive cysteine in the CRM1 groove as LMB, but are less toxic than LMB. The reason for better pharmacological performance can be likely explained with a slightly different mechanism of action. In contrast to LMB, the smaller KPT inhibitors occupy the NES groove only partially, leaving more than half of the hydrophobic groove unoccupied (Figure 52).<sup>[154]</sup> Thus, the moderate binding affinity can increase the rate of synthetic inhibitor release, while enabling cargo binding sufficient for average cell survival and preventing aberrant events.<sup>[145]</sup>

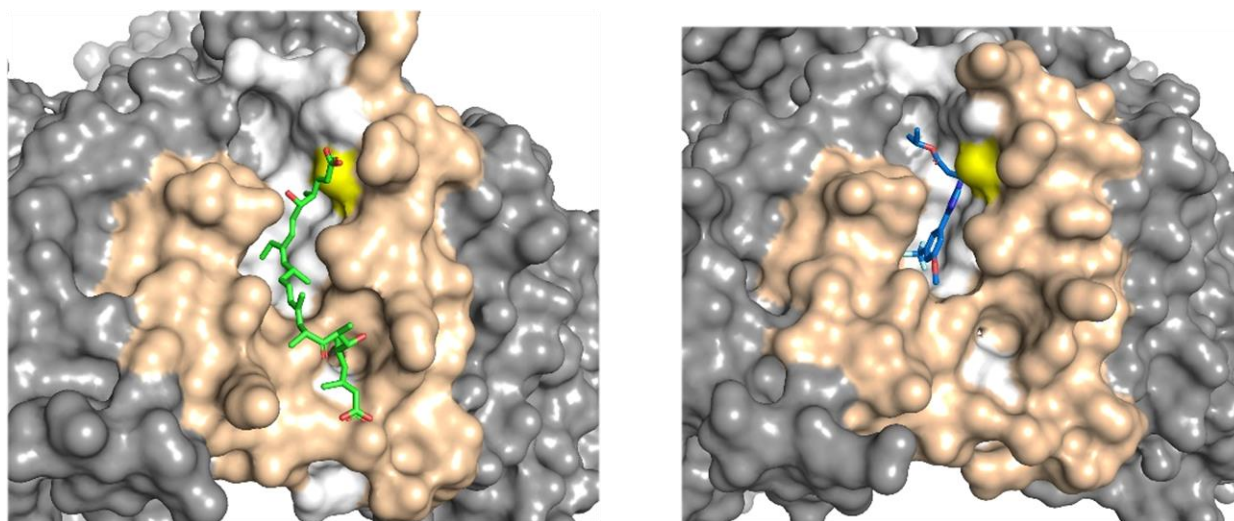


**Figure 52.** The crystal structures of LMB (green sticks) and KPT 185 (blue sticks) bound to the CRM1 binding groove. Cys 539 (equivalent to Cys528 of human XPO1) in both structures is shown in the yellow surface. The NES region is shown as a sand-colored surface. (PDB IDs: 4HAT and 4GMX)

Furthermore, the electrostatic contacts are excluded, since the non-polar trifluoromethyl groups of the inhibitors are buried deep in the NES binding groove, resulting in hydrophobic interactions exclusively. The reduced side effects observed in *in vivo* studies can further be explained by the fact that synthetic compounds bind to CRM1 irreversibly in contrast to the natural products. The evidence points out that the subsequent hydrolysis is not taking place after conjugation of synthetic molecules to wild-type CRM1, although the reactive enone (Michael acceptor moiety) of KPT molecules is chemically similar to LMB.<sup>[145]</sup> The enones and their side chains are buried deep into the binding cleft of CRM1, being protected both sterically and electronically from the potential nucleophilic attacks and the oxyanion hole that has been proven to facilitate hydrolysis in

the case of LMB. The lack of the hydrolysis step further allows only slow and reversible binding into the NES-groove.<sup>[162]</sup>

### 1.6.5.2.3 The Survivin-CRM1 Interaction

Lately, the Survivin-CRM1 interaction as a breakthrough target for cancer therapy attracted growing attention from oncologists, cell biologists, and supramolecular chemists.<sup>[146,168,169,170]</sup> Knauer *at al.* reported that Survivin's contains an evolutionary conserved leucine-rich NES (<sup>89</sup>VKKQFEELTL<sup>98</sup>), which is the classical prerequisite for interactions with CRM1, but from the other side, it lacks a classical import signal (NLS), resulting in its localization in the cytoplasm.<sup>[169]</sup> Still, the low molecular weight of Survivin allows slow entering the nucleus by passive diffusion in both monomeric and dimeric form. The importance of Survivin's NES region in binding to CRM1 was proved experimentally by employing the Survivin NESmut variant, in which two critical hydrophobic residues (L96 and L98) are mutated to alanine. Indeed, it shows decreased binding to the export receptor CRM1, disabled inhibition of nuclear export, therefore losses its anti-apoptotic function.<sup>[170]</sup>

Various therapeutic approaches have been envisaged to disrupt either Survivin's expression or function in cancer cells. In comparison to obtaining an the immune response to Survivin, the approach of designing small-molecules is way more attractive for the sake of easier manipulation, lower costs, and shorter development time.<sup>[142]</sup> By joined efforts, the scientific community is striving to come up with a suitable small-molecule inhibitor, able to interrupt the export of Survivin into the cytoplasm, i.e., disable the progression of different aberrant cells through mitosis.<sup>[141,142]</sup> Several novel small-molecule inhibitors designed to target protein-PPI between Survivin and other partner proteins have been evaluated in various *in vitro* and *in vivo* studies (i.e., YM-155,<sup>[171]</sup> EM-1421,<sup>[172]</sup> FL118<sup>[173]</sup> and GDP366<sup>[174]</sup> – chemical structures can be found in Figure 53). YM-155, as the most successful among the so far known inhibitors, passed phase I clinical trials, while failing in further clinical development on different cancer types, also causing a cascade of side effects.<sup>[138]</sup> Despite different mechanisms of action and exhibited efficiencies, none of the known small-molecule is proclaimed for an efficient Survivin-agent yet. Usually, the main encountered obstacle is that Survivin operates

through multiple mechanisms, and therefore, inhibiting a single pathway does not necessarily lead to a complete shut-down of Survivin's functions. Nevertheless, drugs that specifically address the Survivin-CRM1 interaction might provide a new strategy to interfere with multiple functions of Survivin as this PPI is essential for Survivin's mitotic as well as anti-apoptotic functions.<sup>[170]</sup>

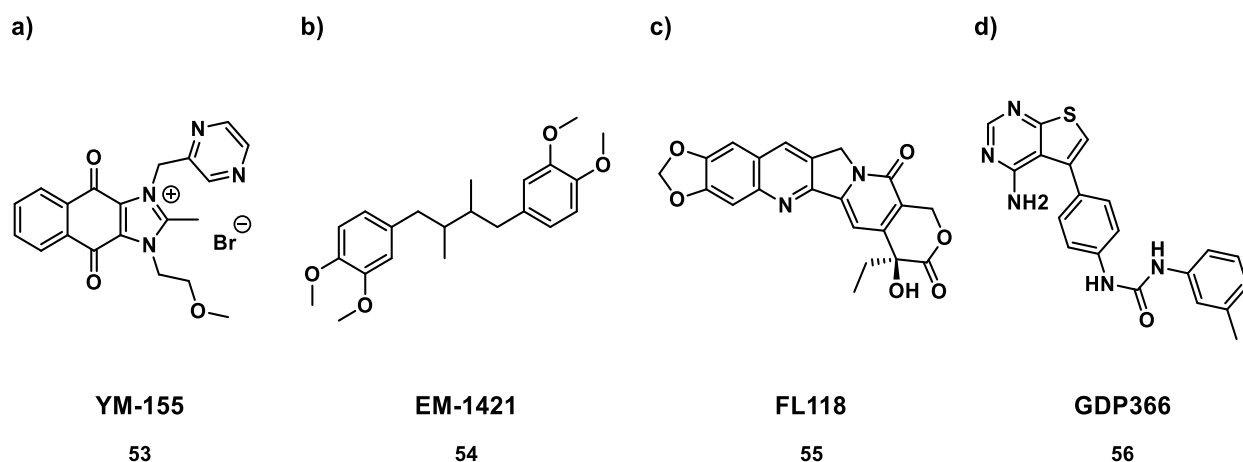


**Figure 53.** Small-molecules applied in targeting Survivin PPI.

This might be due to the preinstalled compensatory proliferative cell apparatuses.<sup>[142]</sup> Providing the strong resistance against chemotherapeutic drug-induced apoptosis, up to date, Survivin remained “undruggable”.<sup>[142]</sup> A new generation of molecular tweezers, equipped with an additional peptidic recognition unit, exhibit promising characteristics as targeting agents of Survivin's NES region, as disclosed in Chapter 3.3.

## **2 AIM OF THE DISSERTATION**

The aim of this work is to construct a new generation of molecular tweezers able to target hot regions of selected proteins and therewith influence their PPIs (the importance of controlled modulation of PPIs has been evaluated in the previous chapters). To realize the given aim, one must first inspect the proteins' crystal structures and define well accessible Lys and Arg, located either directly in the protein-protein interfaces or their close vicinities. The exposed basic amino acids are meant to serve as anchors for the tweezer molecule itself. The collected information about topologies in the vicinity of the targeted amino acids can be further utilized for the rational design of novel molecular tweezers. To achieve the specificity in binding, the advanced molecular tweezers must distinguish between accessible Lys and Arg on the protein's surface. The directed binding can be eventually achieved by introducing an additional binding motif capable of recognizing the epitopes around Lys/Arg. Therefore, the two individual strategic concepts were followed in designing the novel molecular tweezers: (i) design of molecular tweezer equipped with a peptide as an additional recognition unit and (ii) design of di- and multivalent tweezer skeletons of defined geometries. A well designed, covalently attached, additional binding motif(s) should lead the tweezer to the desired region on the proteins' surface and enhance the binding affinity. Each strategic approach will be explained separately in the following chapters.

### **2.1 Design of Peptide-modified Molecular Tweezers**

By equipping molecular tweezer with additional peptidic recognition units, we aim to design a new generation of specific protein binders with exquisite selectivity for well-defined protein flanks. For example, Survivin's NES (<sup>89</sup>VKKQFEELTL<sup>99</sup>) is partially overlapping with its natural dimer interface. We aim to take advantage of this unique physiological phenomenon for our peptide design, in targeting Survivin-CRM1 interaction. The rational design, as well as the optimization of the novel ligands, as the first significant strategic step, is feasible with means of computational chemistry. We aim to obtain information on steric fit and dynamic events on the molecular level employing software for visualization, 3D docking, and molecular dynamic (MD) simulations. The collected



data could facilitate the preliminary prediction of whether the designed system is reasonable to proceed within experimental work or not.

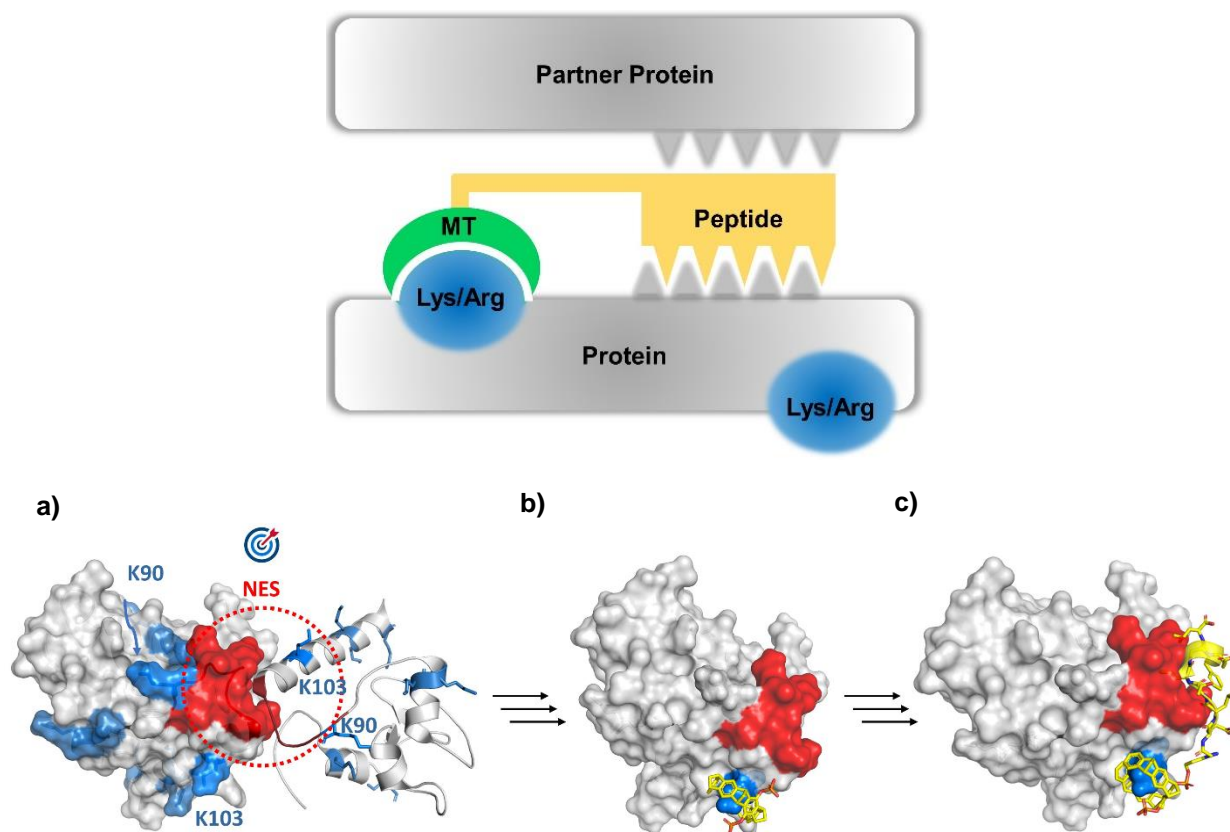


**Figure 55.** Design of peptide-modified molecular tweezers (top). The rational design of peptide-modified molecular tweezer for targeting NES in Survivin. **a)** Identifying Lys residues (marine blue) within/near the targeted area (NES) on Survivin. **b)** 3D docking of the molecular tweezer (yellow sticks) to the best accessible Lys 103 (blue spheres) located in the vicinity of NES, using Schrödinger software. **c)** Connecting molecular tweezer to corresponding peptidic sequence as an additional recognition unit, and subsequent MD simulation (100 ns). (PDB ID: 1XOX)

A similar concept is applied in the case of 14-3-3 proteins as well. The rational design of peptide-modified molecular tweezer for targeting 14-3-3 hydrophobic binding groove is shown in Figure 56. The well accessible Lys 214 found in the vicinity of the protein's binding groove is meant to serve as the anchor for the molecular tweezer carrying an additional recognition unit. The additional binding unit should recognize the hydrophobic protein hot region and hinder further PPIs. The already known crystal structure of molecular tweezer binding to Lys 214 (Figure 56. a) and ExoS peptidic unit as natural

14-3-3 binder (Figure 56. b) can serve as the starting point in the rational design of the new supramolecular receptor (Figure 56. c).

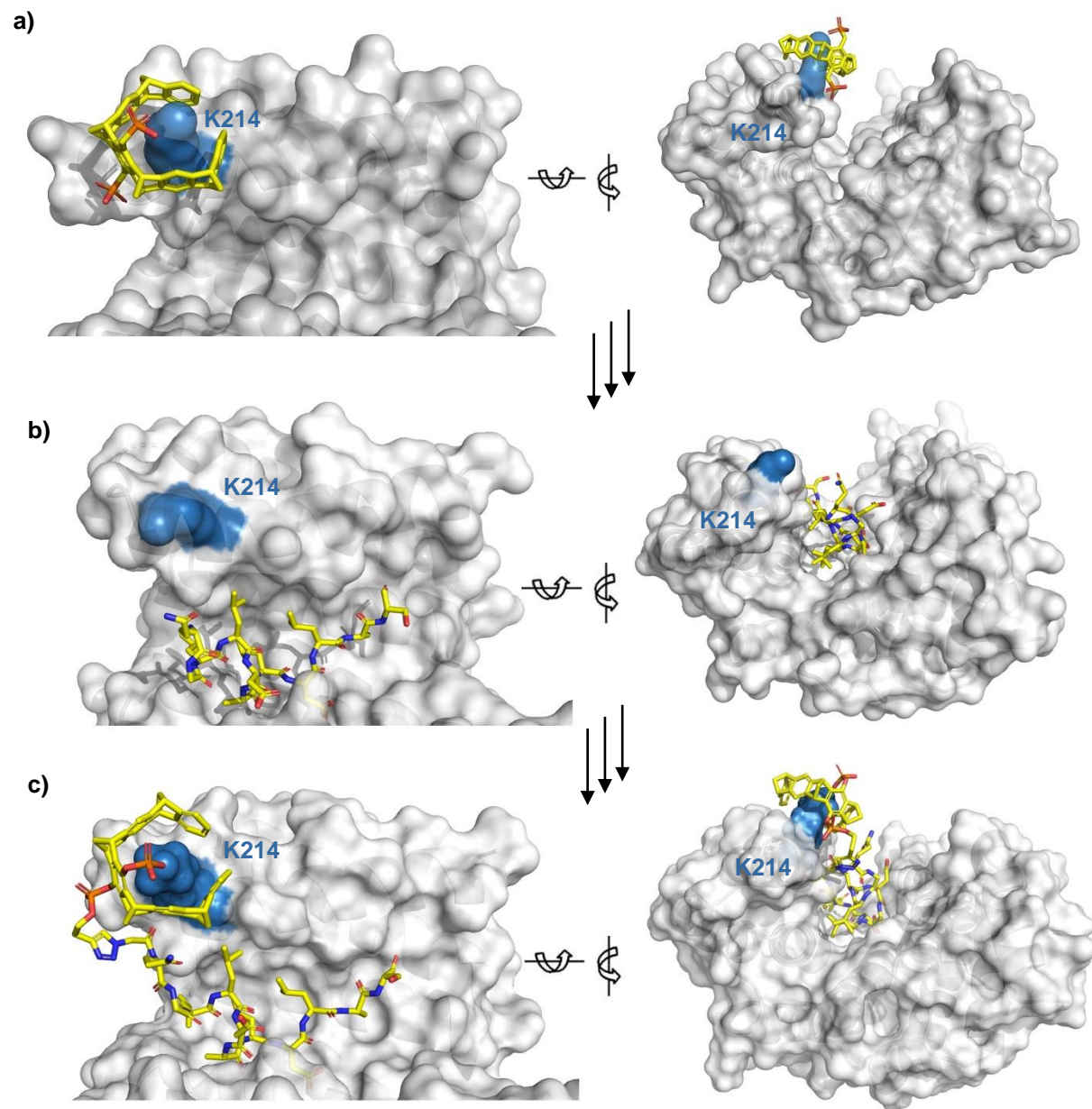


**Figure 56.** The rational design of peptide-modified molecular tweezer for targeting 14-3-3 hydrophobic binding groove. **a)** Crystal structure of molecular tweezer (yellow sticks) binding Lys 214 (marine blue spheres) of protein 14-3-3 $\sigma$  (gray surface). (PDB ID: 4HQW) **b)** X-ray crystal structure of 14-3-3 $\zeta$  (gray surface) in complex with ExoS (yellow sticks) considered as a good start point in a rational design approach towards (PDB ID: 4N7G). **c)** Potent inhibitor of PPI representing the covalent fusion of molecular tweezer and non-phosphorylated ExoS motif (yellow sticks) that is occupying the binding groove of the protein (MD simulation 200 ns).

## **2.2 Design of Di- and Multivalent Tweezer Skeletons**

Our second strategic approach to improve molecular tweezers' specificity in addressing protein surfaces and targeting basic amino-acid residues in critical hot-regions can be achieved through simultaneous multivalent binding. Nevertheless, to yield a successful recognition, the distance between molecular tweezers and the geometry of the resulting construct must fulfill steric and electronic requirements predetermined by proteins as the interaction partners (Figure 57). In the rational design of di- and multivalent tweezer skeletons, it is crucial to inspect the corresponding crystal structures of given proteins, determine the topologies, well-accessible Lys/Arg, and corresponding distances. In the first step, we aim to design a skeleton which would carry two molecular tweezers as two recognition units within one single molecule.

For example, the detailed analysis of the protein interface revealed two well-exposed Lys shielding the NES region (K90/K103 or K91/R106) responsible for Survivin-CRM1 PPI (Chapter 1.6.5.2.3). Therefore, we aim to design divalent tweezer skeletons specific for the Survivin's NES region. This macromolecular ligand should include two tweezer motifs that can address two critical Lys at the same time. The length of the required inter-ligand spacing can be determined from the crystal structure by measuring the distance between the amino acids of interest (Figure 57. a). In this case, the linker length of 20-30 Å between tweezer molecules should allow the conjugate to reach the well-exposed Lys in the NES vicinity simultaneously. This directed binding might be a solid promise for further interference with the Survivin-CRM1 PPI.

Beside Survivin, the described approach can be implemented to modulate PPIs of several proteins of interest within CRC 1093, such as 14-3-3 proteins, Ndc80-microtubule, and N-D1 interface of p-97 protein. All mentioned proteins exhibit the network of well-exposed Lys and Arg, whose distance can be easily determined by inspection of known crystal structures (Figure 57). Spacing between the basic amino acids of interest dictates the design and geometry of the artificial supramolecular ligands. Based on the information collected from crystal structures, we aim to design divalent, trivalent, and multivalent tweezer constructs of defined geometries that could be beneficial tools for addressing epitopes of the proteins shown below.

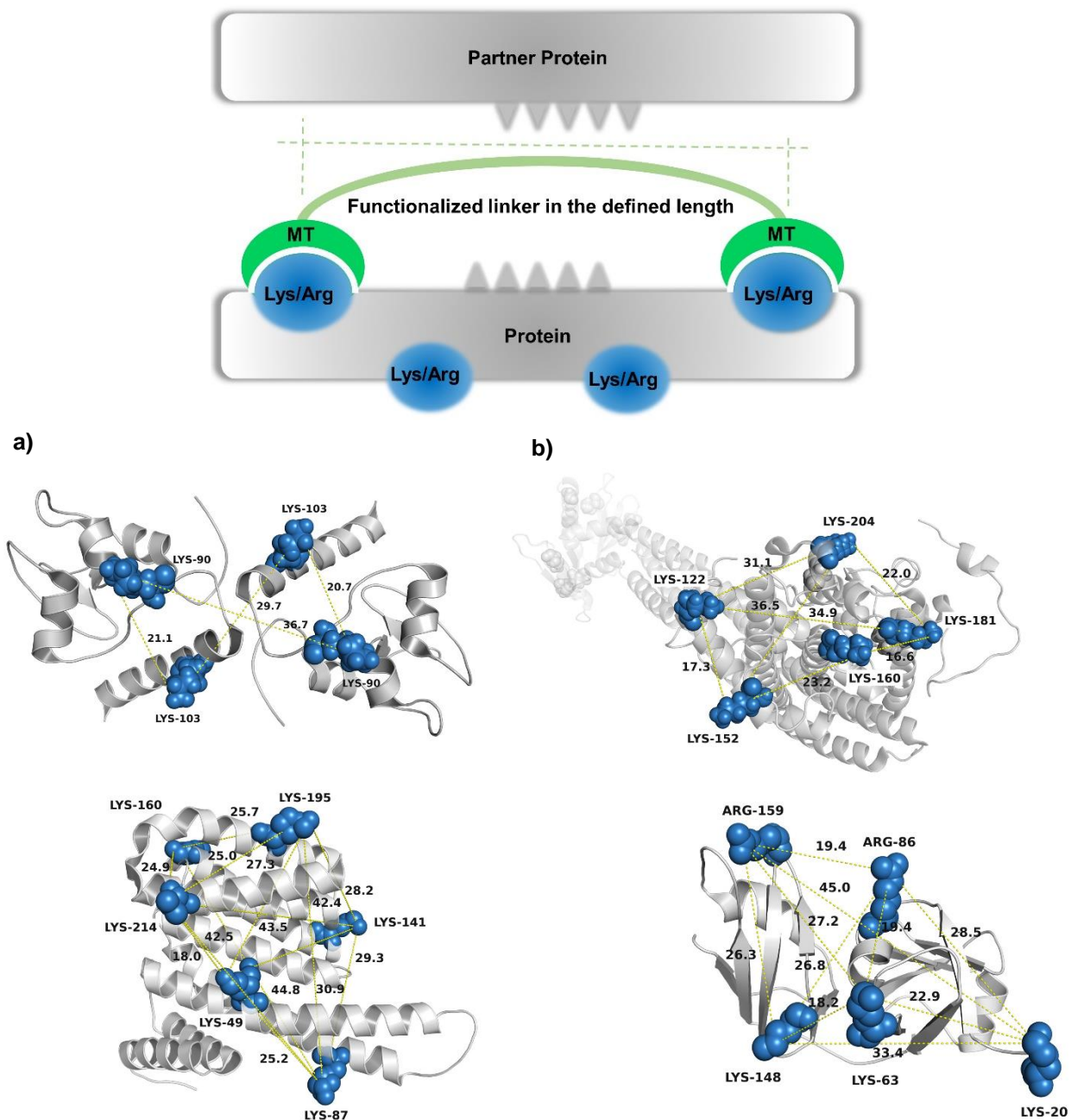


**Figure 57.** Design of di- and multivalent tweezer skeletons of defined geometries. Inspected crystal structures of **a)** Survivin (PDB ID: 1XOX), **b)** Ndc-80 (PDB ID: 5TCS), **c)** 14-3-3 (PDB ID: 3P1N), and **d)** p-97 (PDB ID: 3QQ7) represented as gray cartoons. Well-accessible lysines are shown as marine blue spheres and distances between them (given in Å) as dashed yellow lines.

## 2.3 The Covalent Fusion of Recognition Units to Molecular Tweezers

After the promising design, the next practical challenge is the covalent fusion of molecular tweezer with either additional recognition units or corresponding linkers into a multivalent conjugate for targeted protein interfaces. The latest novelty in the tweezer skeleton, i.e., clickable ester alcohol moiety (shown in red in Figure 58), is introduced by Heid *et al.*<sup>[68]</sup> This important modification allows utilization of the click chemistry and, thus, covalent attachment of either additional recognition units or functionalized linker to yield multivalent skeletons.

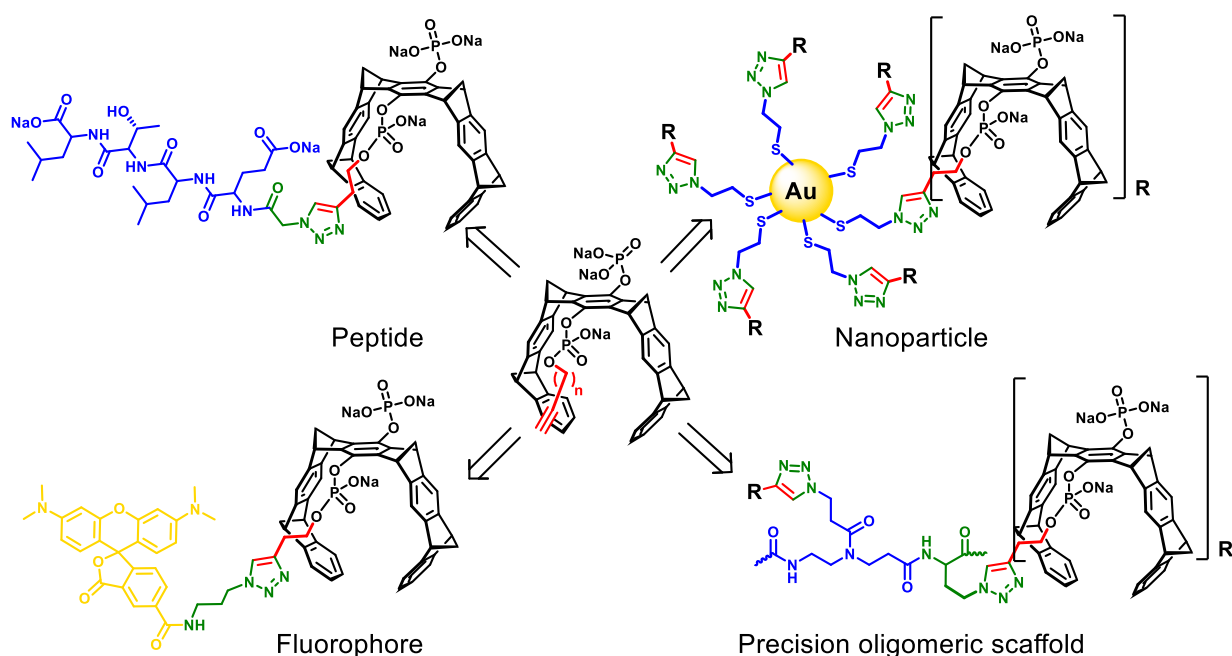


**Figure 58.** Tweezer conjugates accessible by click chemistry for various biological purposes.

Aiming to advance known both structural and functional tweezers' properties, molecular tweezers can be equipped, among others, with elements such as:

- fluorophores (allow direct cell read-out as well as fluorescence polarization assays),
- peptides (serve as an additional binding unit that can recognize specific patterns on the proteins' surface and therefore enhance tweezers' specificity),
- precision oligomeric scaffolds (provide possibilities to connect and distribute molecular tweezers into flexible multivalent networks of defined length and size), and

- nanoparticles (besides providing possibilities to obtain multivalent tweezer constructs, the gold nanoparticles can facilitate penetration of the cell membrane and serve as good carriers).

Once the desired molecules are obtained, different biophysical instrumental methods will be used to determine binding affinities, stoichiometry, and thermodynamic parameters between the advanced ligands and our partner's proteins. Beside the design, synthesis, and characterization of a novel generation of molecular tweezer, we aim to select the best candidates for supramolecular recognition based on their performance in protein binding assays. We will also try to understand the underlying mechanisms and way of tweezers' actions to implement tweezers as compatible PPI partners into a range of novel applications, such as drug design.

### 3 PUBLICATIONS BASED ON THIS DISSERTATION

#### *Per Visum*

In this chapter, the four publications based on this cumulative dissertation will be presented. **Publication I** represents a review that provides a detailed account of the interaction between peptides/aggregating proteins and molecular tweezers as promising candidates for disease-modifying therapy. The binding mode of molecular tweezers and recognition of lysine and arginine for controlling the aberrant protein aggregation are discussed in detail. The collected results from various biophysical experiments served to show how molecular tweezers, as non-toxic supramolecular tools, work well to disrupt toxic aggregates of oligomeric and fibrillar protein species.

**Publication II** and **Publication III** arose from fruitful collaborations within CRC 1093 during the last three years. They demonstrate the utilization of concepts discussed in Chapter 2, especially the first explained strategic approach based on the design of peptide-modified molecular tweezers. The peptidic units were rationally designed to recognize the epitopes around well-exposed Lys in the 14-3-3 binding groove and Survivin's binding interface. Such a unit attached to the tweezer's skeleton significantly contributed to enhancing the binding affinity, as confirmed by various experimental methods. Furthermore, the specificity in targeting predefined amino acids and thus directed binding is introduced for the first time.

**Publication IV** is also realized within CRC 1093, with Project A5 in collaboration with Department for Inorganic Chemistry. Its approach regarding protein recognition tools differs compared to the previous two publications. In particular, it reveals how covalent attachment of multiple molecular tweezers to the surface of ultrasmall nanoparticle can generate a comprehensive tool for probing versatile protein surfaces. The concept of multivalent skeletons for protein recognition corresponds to the second strategic approach of this dissertation explained in Chapter 2.2.

### 3.1 Publication I

#### **Molecular Lysine Tweezers Counteract Aberrant Protein Aggregation**

The unique recognition mode of molecular tweezers selective for lysine and arginine is enabled by a torus-shaped macrocyclic framework equipped with two hydrophilic phosphate groups. Cationic amino acid residues are bound by the synergistic effect of dispersing, hydrophobic and electrostatic interactions in a kinetically fast reversible process. Interactions of the same kind play a key role in numerous protein-protein interactions, as well as in pathologic protein aggregation. Therefore, molecular tweezers show a high potential to disrupt such events and indeed inhibit misfolding and self-assembly of amyloidogenic polypeptides without toxic side effects.

The review describes the synthesis of advanced molecular tweezers with optimized properties, biophysical experiments that elucidate their mechanism of action, and application in cell culture and animal models of many neurodegenerative diseases. The instrumental methods for detecting amyloid proteins, including Thioflavin T fluorescence and Electron Microscopy, and the new techniques, such as ECD-MS and NMR for probing the complexation sites, are reviewed. Specifically, we show how toxic aggregates of oligomeric and fibrillar protein species are dissolved and redirected to form amorphous, benign assemblies. Importantly, these new chemical tools are not protein- but process-specific. Low nanomolar tweezer concentrations in animal brains suffice for complete control over pathologic aggregates. *In vivo* studies demonstrated how transgenic mice recovered their normal behavior, memory, and mobility in Alzheimer's and Parkinson's disease models. Thus, MTs are highly promising candidates for disease-modifying therapy in the early stages of neurodegenerative diseases. This is an outstanding example in the evolution of supramolecular concepts towards biological application.

Publication as originally published in: *Hadrovic I, Rebmann P, Kläner F-G, Bitan G and Schrader T (2019) Molecular Lysine Tweezers Counteract Aberrant Protein Aggregation. Front. Chem. 7:657. DOI: 10.3389/fchem.2019.00657. Available at: <https://www.frontiersin.org/articles/10.3389/fchem.2019.00657/full>*





# Molecular Lysine Tweezers Counteract Aberrant Protein Aggregation

Inesa Hadrovic<sup>1</sup>, Philipp Rebmann<sup>1</sup>, Frank-Gerrit Klärner<sup>1</sup>, Gal Bitan<sup>2</sup> and Thomas Schrader<sup>1\*</sup>

<sup>1</sup> Faculty of Chemistry, University of Duisburg-Essen, Essen, Germany, <sup>2</sup> Department of Neurology, University of California, Los Angeles, Los Angeles, CA, United States

## OPEN ACCESS

### Edited by:

De-Xian Wang,  
Institute of Chemistry (Chinese  
Academy of Sciences), China

### Reviewed by:

Lihua Yuan,  
Sichuan University, China  
Guoqiang Feng,  
Central China Normal University, China

### \*Correspondence:

Thomas Schrader  
thomas.schrader@  
uni-duisburg-essen.de

### Specialty section:

This article was submitted to  
Supramolecular Chemistry,  
a section of the journal  
Frontiers in Chemistry

Received: 15 July 2019

Accepted: 13 September 2019

Published: 01 October 2019

### Citation:

Hadrovic I, Rebmann P, Klärner F-G,  
Bitan G and Schrader T (2019)  
Molecular Lysine Tweezers Counteract  
Aberrant Protein Aggregation.  
Front. Chem. 7:657.  
doi: 10.3389/fchem.2019.00657

Molecular tweezers (MTs) are supramolecular host molecules equipped with two aromatic pincers linked together by a spacer (Gakh, 2018). They are endowed with fascinating properties originating from their ability to hold guests between their aromatic pincers (Chen and Whitlock, 1978; Zimmerman, 1991; Harmata, 2004). MTs are finding an increasing number of medicinal applications, e.g., as bis-intercalators for DNA such as the anticancer drug Ditercalinium (Gao et al., 1991), drug activity reverters such as the bisglycoluril tweezers Calabadion 1 (Ma et al., 2012) as well as radioimmuno detectors such as Venus flytrap clusters (Paxton et al., 1991). We recently embarked on a program to create water-soluble tweezers which selectively bind the side chains of lysine and arginine inside their cavity. This unique recognition mode is enabled by a torus-shaped, polycyclic framework, which is equipped with two hydrophilic phosphate groups. Cationic amino acid residues are bound by the synergistic effect of disperse, hydrophobic, and electrostatic interactions in a kinetically fast reversible process. Interactions of the same kind play a key role in numerous protein-protein interactions, as well as in pathologic protein aggregation. Therefore, these particular MTs show a high potential to disrupt such events, and indeed inhibit misfolding and self-assembly of amyloidogenic polypeptides without toxic side effects. The mini-review provides insight into the unique binding mode of MTs both toward peptides and aggregating proteins. It presents the synthesis of the lead compound CLR01 and its control, CLR03. Different biophysical experiments are explained which elucidate and help to better understand their mechanism of action. Specifically, we show how toxic aggregates of oligomeric and fibrillar protein species are dissolved and redirected to form amorphous, benign assemblies. Importantly, these new chemical tools are shown to be essentially non-toxic *in vivo*. Due to their reversible moderately tight binding, these agents are not protein-, but rather process-specific, which suggests a broad range of applications in protein misfolding events. Thus, MTs are highly promising candidates for disease-modifying therapy in early stages of neurodegenerative diseases. This is an outstanding example in the evolution of supramolecular concepts toward biological application.

**Keywords:** molecular tweezers, amino acids, neurodegeneration, amyloids, protein aggregation

## INTRODUCTION

A major challenge in modern medicine is the field of neurodegenerative diseases. Their pathology is dominated by misfolding and subsequent aggregation of characteristic peptides or proteins in the brain, which is correlated with severe impairment of cognitive functions. As the most prominent example, the amyloid  $\beta$ -peptide ( $A\beta$ ) plays a key role in the development and progression of Alzheimer's disease (AD) (Hardy and Higgins, 1992; Hardy and Selkoe, 2002). Senile plaques composed of aggregated  $A\beta$ , forming extracellular  $\beta$ -sheet fibril morphologies, are histopathological hallmarks found in the brains of AD patients. In recent years however, small soluble  $A\beta$  oligomers were identified as the most neurotoxic species (Shankar et al., 2008; Zhao et al., 2012; Sengupta et al., 2016). Despite intense research, the underlying mechanisms of spontaneous misfolding, aggregation, and lesion of nerve cells are still poorly understood. To date only symptom-relieving drugs are clinically approved for AD treatment. Strategically, it seems desirable to develop drug candidates which are able to interfere with the early stages of the disease mechanism. Classical approaches include the reduction of  $A\beta$  production by inhibitors of  $\beta$ - and  $\gamma$ -secretase, the increase of  $A\beta$  removal via anti- $A\beta$  immunotherapy, and direct interference with  $A\beta$  aggregation (Hardy and Selkoe, 2002; Roland and Jacobsen, 2009). The latter can be achieved with a diverse set of peptides and small molecules. Well-known milestones in this field are Congo red (Podlisny et al., 1998), scyllo-Inositol (McLaurin et al., 2000), amino-propane sulfonic acid (Gervais et al., 2007), Clioquinol (Cherny et al., 2001), methylene blue (Necula et al., 2007), and polyphenol (-)-epigallocatechin (EGCG) (Ehrnhoefer et al., 2008).

However, some of these compounds are toxic, others are only active in cell culture or animal experiments, and until today no drug candidate made it through clinical trial. In addition, little structural information is available about the direct interaction between  $A\beta$  and most aggregation inhibitors. Thus, there is clearly a need for new rational approaches. Supramolecular Chemistry has gained a much-improved understanding and quantitative description of those non-covalent interactions which are involved in protein aggregation. In addition, molecular modeling now allows extended MD simulations of complex ensembles with large sampling times and discrete solvent treatment—resulting in predictive power for new supramolecular binders. In our group we developed a highly selective host molecule for lysine and arginine, which is able to draw their side chains into its cavity and shield them from the environment. These molecular tweezers turned out to completely disrupt existing  $\beta$ -sheets formed by amyloidogenic proteins. Our discovery started an intense and very fruitful collaboration between supramolecular chemists and neurologists, which has reached the state of animal experiments and behavioral testing with transgenic mice and holds promise for the development of disease-modifying therapy. This mini-review summarizes the chemical aspects of the endeavor—from deciphering the

binding mode of the tweezers over structural elucidation of their complexes with aggregating proteins to the characterization of their anti-aggregatory effect on various proteins. Finally, toxicity, metabolism, and bioavailability issues will also be briefly discussed.

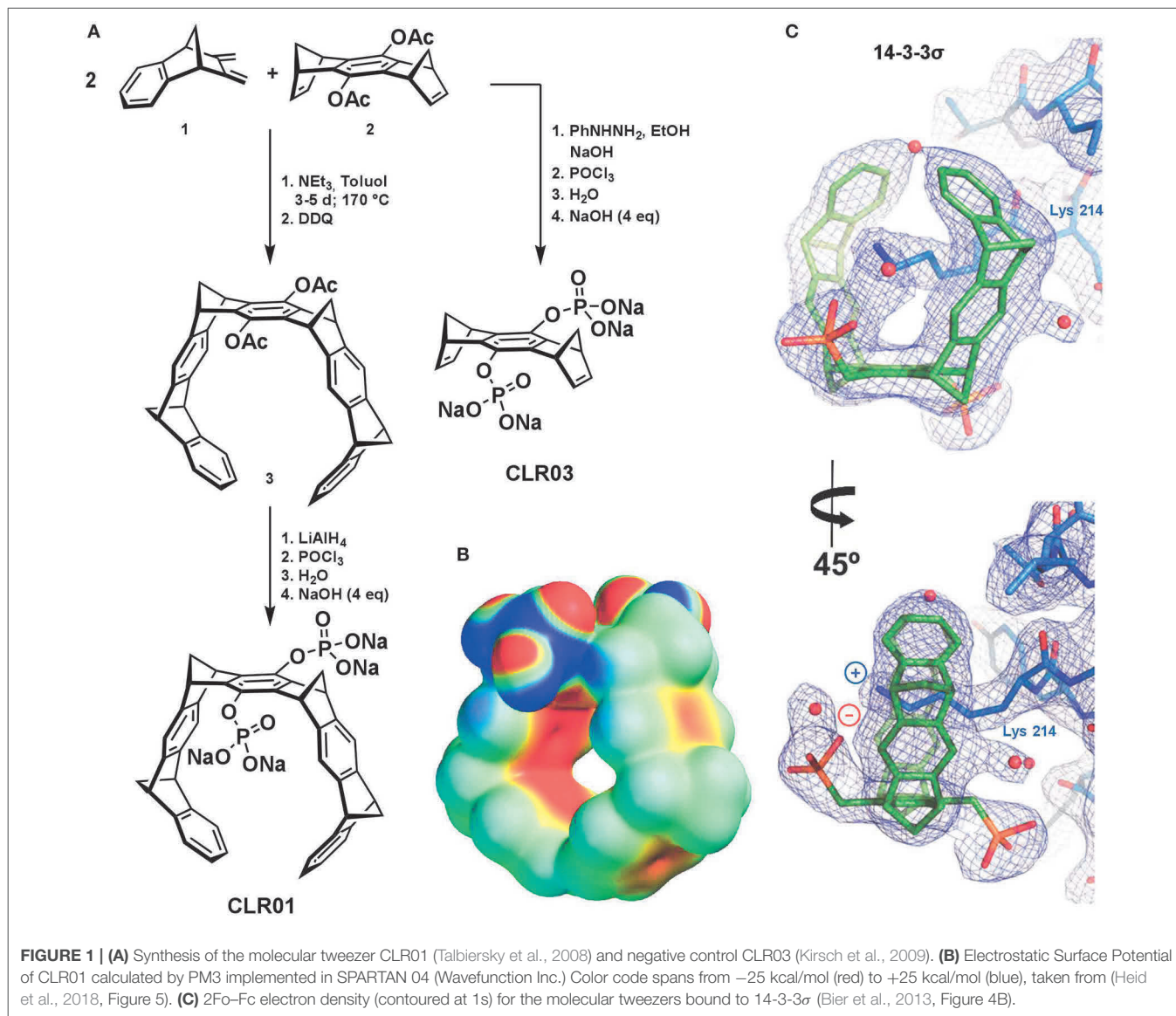
## THE DEVELOPMENT OF MOLECULAR TWEEZERS AS LYSINE AND ARGININE BINDERS

### Structure and Binding Mode of Molecular Tweezers

There are numerous artificial binding motifs for naturally occurring amino acids, but only a few of them are selective and mild enough to find biological application (Crini, 2014; Barrow et al., 2015; Neri et al., 2016). Molecular tweezers were designed rationally, combining supramolecular knowledge, and total synthesis to obtain water-soluble horseshoe-shaped molecules. They are characterized by their well-preorganized torus-shaped, polycyclic non-polar framework, equipped with two hydrophilic phosphate groups. The uniqueness of MTs is reflected in their capability to selectively accommodate exclusively the side chains of basic amino acids, namely lysine and arginine, inside their cavity under physiological conditions. Electrostatic potential surface (EPS) calculations demonstrate that their cavity construction is electron-rich, perfectly symmetric, and open to receive cationic appropriately shaped guests (Figure 1B). It appears that even in PBS buffer tweezer dimerization is negligible (Dutt et al., 2013; Heid et al., 2018).

MTs bind cationic amino acid residues via threading their side chains through the cavity in a non-covalent fashion followed by formation of a salt bridge between the tweezer phosphate and the included ammonium or guanidinium cation. This is facilitated by exploiting in a synergistic way van der Waals interactions, substantial electrostatic contributions, and the non-classical hydrophobic effect; this binding mode results in a kinetically fast and reversible recognition process. Quantum chemical and molecular mechanics (QM/MM) calculations and various analytical experiments strongly support this postulated binding mode between MTs and their amino acid guests. Monte Carlo (MC) and molecular dynamics (MD) simulations, isothermal titration calorimetry (ITC) measurements, NMR, and fluorescence titrations, as well as NOESY and variable temperature (VT) experiments clearly point to inclusion of the lysine and arginine side chain inside the tweezer cavity in an enthalpy-driven process. QM/MM calculations confirm the existence of these favorable host-guest complexes in buffered aqueous solution formed via the threading mode (Fokkens et al., 2005; Dutt et al., 2013).

Recently, a crystal structure of the complex between MT and a 14-3-3 protein beautifully demonstrated the threading of the well accessible Lys-214 side chain through the tweezers' cavity accompanied in solution with a substantial inhibition of the complex formation between the 14-3-3 and its natural cargo proteins (Bier et al., 2013).



## Tweezer Synthesis

The characteristic MT framework consists of nine annulated 6-membered rings, which are alternating phenyl and norbornadiene ring systems. The construction of this hydrocarbon torus is achieved in the key step via double Diels-Alder (DA) cycloaddition using two equivalents of diene **1** which forms the walls and one equivalent of dienophile **2** which is the center-piece (**Figure 1A**). The exocyclic diene is obtained in six steps from indene and maleic acid anhydride while the dienophile is made from 1,4-benzophenone in a four-step sequence. The neutral DA reaction requires elevated temperatures; it proceeds stereoselectively *endo* in **1** and *exo* in **2** and thus leads after DDQ (2,3-dichloro-5,6-dicyano-1,4-benzoquinone) oxidation to the desired tweezer (**3**) having the four methylene bridges in all-*syn* configuration (Klärner et al., 1996, 1999; Talbiersky et al., 2008; Schrader et al., 2016).

The two acetoxy-groups can be cleaved in a symmetric or asymmetric fashion, releasing hydroquinone OH groups which can be further functionalized with negatively charged groups for enhanced water-solubility (e.g., phosphates, carboxylates, and sulfates) (Dutt et al., 2013). In the course of several years of intense biophysical and biological testing, the tweezers CLR01 with its two phosphate esters evolved as a lead compound, while its truncated derivative without the side walls, CLR03, served as a negative control. CLR03 represents the central part of the MT molecule; due to the lack of the torus-shaped cavity, it is not able to bind Lys and Arg by inclusion (Schrader et al., 2016).

## INTERACTION WITH BIOACTIVE PEPTIDES

CLR01 was initially tested with small, biologically relevant small peptides (Fokkens et al., 2005). The KLVFF peptide

is located inside the central hydrophobic part of the amyloid- $\beta$  protein, and it was identified as a nucleation site for pathologic protein aggregation, fibril formation, and subsequent plaque occurrence in Alzheimer's disease. NMR and fluorescence titrations with this small peptide revealed inclusion of the *N*-terminal lysine inside CLR01 and a moderate affinity of 10  $\mu$ M ( $K_d$ ) in buffered aqueous solution (PBS) (Dutt et al., 2013).

ITC measurements provide further insight into the postulated binding mode. The binding event between host CLR01 and its KLVFF guest was shown to be a favorable, strongly exothermic process. Here the MT peptide affinity was found to be 15  $\mu$ M, with a 1:1 stoichiometry, and an enthalpic contribution  $\Delta H$  of  $-6.6$  kcal/mol, which is prevailing over the small entropy term  $-T\Delta S$  of  $-0.2$  kcal/mol. Arginine complexation in other peptides was found to be slightly weaker, in the range of 30  $\mu$ M, most likely due to its delocalized guanidinium ion and shorter side chain. The remarkably exothermic character of the binding event correlates well with the assumed threading procedure and the resulting van der Waals interactions between the host cavity and the respective amino acid side chain. The above-reported  $K_d$  values, although moderate in biological terms, place these MT among the most efficient receptor molecules for basic amino acids known today (Fokkens et al., 2005; Dutt et al., 2013).

In general, dissociation constants obtained from ITC measurements agree well with the data determined independently by fluorescence or  $^1\text{H}$  NMR titrations, in spite of the different concentration regimes (NMR  $10^{-3}$  M, ITC  $10^{-4}$  M, Fluoresc.  $10^{-5}$  M). The emission intensity maximum of MTs in fluorescence spectra is found around 330 nm, while the excitation maximum is located at 285 nm ( $\pi, \pi^*$ ). Trapping of guest molecules inside the tweezers cavity results in significant quenching of the fluorescence emission. This proves guest inclusion and allows quantification of the binding event at low concentrations. In most cases affinities for a single lysine inclusion determined by fluorometric titrations are in the range of 5–20  $\mu$ M  $K_d$ . Structurally, the MT's preference for lysine inclusion has been proven in numerous  $^1\text{H}$  NMR titrations in buffer, which reveal drastic upfield shifts of up to 4 ppm ( $\delta\Delta_{\text{max}}$ ) at the  $\delta$ - and  $\epsilon$ -methylene protons of the basic amino acid side chains. NOESY measurements as well as variable temperature experiments strongly support the guest inclusion (Fokkens et al., 2005).

Molecular tweezers with their unique binding mode for lysine and arginine and their unexpected powerful effect as aggregation inhibitors have attracted the attention of many research groups worldwide in the last decade. Numerous fruitful collaborations demonstrated that these lysine binders represent a widely applicable useful tool against pathologic protein misfolding. In addition, sophisticated analytical methods opened our understanding of the underlying supramolecular mechanism of action. Today we know that advanced MTs are able to specifically disrupt undesired protein-protein interactions; however perhaps even more important is the fact that MTs indeed inhibit misfolding and self-assembly of amyloidogenic polypeptides without toxic side effects (Sinha et al., 2011).

## INTERACTION BETWEEN MOLECULAR TWEEZERS AND AGGREGATING PROTEINS

The pathogenesis of every amyloidosis is caused by aberrant protein aggregation and most likely begins with protein misfolding. AD, Parkinson's disease and type-2 diabetes are the best examined examples of this pathologic process. In the course of AD, the largely unstructured naturally occurring monomeric state of the amyloid- $\beta$  peptides was shown to adopt a conformation rich in  $\beta$ -sheets and which aberrantly forms toxic oligomers and aggregates (Billings et al., 2005).  $A\beta_{40}$ ,  $A\beta_{42}$  and the group of tau proteins mainly participate in this neurologically highly relevant aggregation process which ultimately disposes extracellular plaque formed from  $\beta$ -sheet-rich fibrils. Lysine residues are reported to play an important role in this particular assembly (Usui et al., 2009; Sinha et al., 2012).

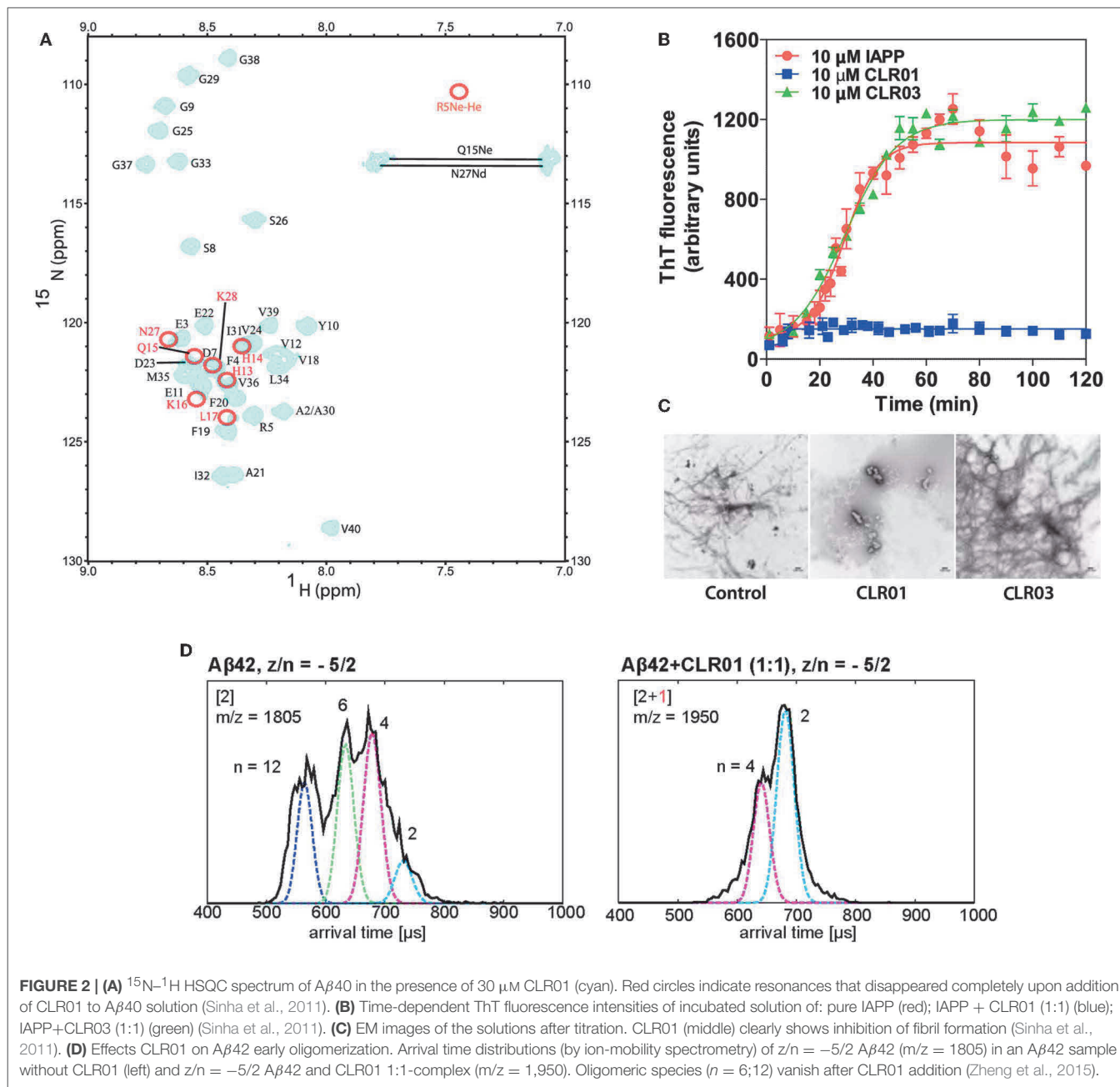
Gratifyingly, MT were found to interfere with the aggregation process of most amyloidogenic proteins. In recent years, many different experiments have been designed and conducted which confirmed CLR01 to be capable of dissolving fibrils, preventing their formation as well as eliminating their toxic precursor oligomers. Structurally, it was important to identify the tweezer binding sites on these proteins. For the most prominent representative, the Alzheimer's peptide, the preferred complexation sites of the tweezers were validated by electron capture dissociation (ECD) mass experiments (EDC-MS/MS) as well as by NMR spectroscopy (Sinha et al., 2011).

### ECD-MS/MS

In the monomeric form of  $A\beta_{40}$  and  $A\beta_{42}$  there are three basic residues, Arg-5, Lys-16, and Lys-28. All of these are simultaneously complexed as confirmed by mass spectrometry. In EDC-MS/MS experiments complexes of MT and a  $A\beta$  protein were collected in a linear ion trap and smoothly fragmented inside. The recorded MS spectra found MT bound to many overlapping protein fragments. The mass spectra show peaks for  $A\beta_{40}$  bound by one, two and three MTs, respectively. In the fragmentation pattern CLR01- $A\beta$ -fragment peaks were only found for fragments bearing a Lys or Arg residue, indicating a retained amino acid selectivity in  $A\beta$  complexation. Most importantly, peptide cleavage did not occur around the two lysine binding sites, because these were protected by the tweezers. The exact binding mode of this complexation event was subsequently investigated by NMR experiments (Sinha et al., 2011).

### NMR Experiments

$^1\text{H}$ - $^{15}\text{N}$  and  $^1\text{H}$ - $^{13}\text{C}$  heteronuclear single quantum coherence (HSQC) NMR experiments confirmed these results. An HSQC spectrum of  $A\beta_{40}$  alone and together with 0.5 equivalents of MT were compared. Upon tweezer binding, the cross peaks of the complexed residue as well as its neighboring amino acids show a significant chemical shift perturbation (CSP) due to the altered magnetic environment. Some signals vanished completely, indicated by red circles in **Figure 2A**. In two-dimensional H(N)CO experiments MT were titrated to a protein solution; already at a 1:10 ratio of CLR01 relative to  $A\beta_{40}$  the CSP



became significant. Amino acid residues surrounding Lys-16 and Lys-28 showed a higher degree of perturbation compared to those in proximity to Arg-5. This implies a stronger affinity of MT for the  $\text{A}\beta$  Lys residues, consistent with the general Lysine preference of CLR01. At elevated CLR01 concentration all three positions were occupied. The negative control CLR03 showed no effects in the whole NMR-setup (Sinha et al., 2011). Similarly, a three-dimensional HN(CO)CACB NMR experiment was recently used to detect binding sites of MT in the phosphorylated and unphosphorylated tau protein (Despres et al., 2019).

The combination of EDC-MS/MS and NMR spectroscopy underlines the importance of the tweezer cavity for complex

formation with  $\text{A}\beta_{40}$  and  $\text{A}\beta_{42}$ , and strongly supports the binding mode elucidated with small peptides (Figure 1C).

If CLR01 binds to every sterically accessible basic residue on a peptide or protein, why is it not toxic then? It was indeed shown that the MT are non-toxic in biological applications at concentrations necessary to inhibit protein aggregation. We believe, that the key lies in kinetically fast reversible binding and moderate affinity. Biophysical experiments indicate fast on and off rates and labile complexation as well as moderate dissociation constants in the low  $\mu\text{M}$  range (Talbiersky et al., 2008; Bier et al., 2013). These key features of our MT safeguard healthy proteins from damage induced by conformational changes, so that they

retain their natural biological function. Indeed, enzymes could be inhibited by MT, albeit only at millimolar concentrations, 100 times higher than those required for the anti-aggregatory effect. The specificity of CLR01 toward the process of aberrant protein aggregation is outstanding because it is a new principle which may be transferred to other drugs as well. It appears that MTs bind their protein guests with the same combination of non-covalent interactions which is also active in the unwanted aggregation process. This unique way of action toward protein aggregation, represents the first example of a “process-specific” aggregation inhibitor; it was examined with various biophysical methods (Schrader et al., 2016).

## PREVENTION OF PATHOLOGIC PROTEIN AGGREGATION

Until 2011 experimental evidence was accumulated for the fact that lysine-specific MT are active against a wide range of aggregating proteins, with detailed experiments performed on the assembly and toxicity of nine prominent amyloid proteins (Sinha et al., 2011).

In this comprehensive investigation a synopsis of various state-of-the-art biophysical experiments gave the full picture: Thioflavin T (ThT) fluorescence, Electron Microscopy (EM), Circular Dichroism spectroscopy (CD), Dynamic Light Scattering (DLS), Mass Spectrometry (MS), and NMR Spectroscopy.

### Thioflavin T (ThT) Fluorescence

ThT is an amyloid dye indicator which turns highly fluorescent upon binding to existing  $\beta$ -sheets (LeVine, 1999). ThT fluorescence was used to monitor the kinetics of  $\beta$ -sheet formation for various amyloid proteins in the presence or absence of CLR01. The tweezers represented the active drug, whereas their truncated derivative, CLR03, was used as negative control. Measurements were performed regularly during a time span of up to 120 h at pH 7.4 in 10 mM phosphate buffer. CLR01 was added in up to 10-fold excess relative to the protein and was able to completely suppress the typical drastic fluorescence enhancement caused by aggregation and protein misfolding. Equimolar concentration of CLR01 was likewise shown to totally disrupt  $\beta$ -sheets of the tau protein. CLR03 displayed no effect in any of the investigated proteins because it lacks the hydrophobic side walls and consequently, the ability to complex Lys residues. Importantly, CLR01 not only inhibited the *de novo* aggregation of amyloidogenic proteins such as A $\beta$ 40/A $\beta$ 42,  $\alpha$ -synuclein and IAPP (Figure 2B) (Prabhudesai et al., 2012), but also disaggregated pre-formed fibrils over several weeks when added at a 10-fold excess, as being confirmed by EM.

### Electron Microscopy (EM)

EM measurements were carried out in parallel to ThT assays, by spotting 10  $\mu$ L aliquots taken from each aggregation reaction, on glow discharged, carbon-coated Formvar grids, using a CX 100 transmission electron microscope. Visualization of the

protein morphology showed that IAPP and other examined amyloidogenic protein samples incubated in the presence of MTs did not form fibrils anymore, strongly supporting conclusions drawn from the ThT measurements (Figure 2C) (Sinha et al., 2011).

### CD Spectroscopy

All  $\beta$ -sheets and therefore also all pathologic protein aggregates produce a dominant characteristic  $\beta$ -sheet band at 215 nm in the CD spectrum. In the presence of a 3-fold excess of CLR01, this band was rapidly reduced and completely disappeared after 1 h, indicating efficient inhibition of  $\beta$ -sheet formation in case of A $\beta$ 40 and A $\beta$ 42. Equimolar CLR01 lead to partial inhibition. Interestingly, CLR01 completely inhibited tau aggregation already at the equimolar level, which correlates with the higher number of exposed Lys residues in the tau sequence in comparison to A $\beta$  (Sinha et al., 2011).

### Dynamic Light Scattering (DLS)

Dynamic light scattering provides a direct and non-invasive way to monitor the formation of larger aggregates. It was employed to monitor the influence of CLR01 on oligomer size and distribution of A $\beta$ . Experiments were performed with CLR01 in 10-fold excess or equimolar relative to A $\beta$ , controls were run with A $\beta$  alone. Intriguingly, the DLS results indicate that CLR01 does not prevent oligomer formation but rather modulates A $\beta$  self-assembly into formation of structures that are neither amyloidogenic nor toxic (Sinha et al., 2011).

### Mass Spectrometry (MS)

In recent years, advanced methods in mass spectrometry have been exploited for the mechanistic elucidation of protein aggregating events. Thus, Bowers et al. used mild ionization conditions and high resolution to monitor the impact of small molecule modulators on A $\beta$  oligomerization (Zheng et al., 2015). The effect of different concentrations of CLR01 and its related derivative, CLR03 on the A $\beta$  assembly was investigated with a custom-built ion mobility spectrometry-mass spectrometer (IMS-MS) which consisted of a nano electrospray ionization (nano-ESI) source, an ion funnel, a temperature-controlled drift cell, and a quadrupole mass filter followed by an electron multiplier for ion detection (Wytenbach et al., 2001). Consistent with earlier studies (Sinha et al., 2011), these experiments confirmed Arg-5, Lys-16, and Lys-28 as preferred binding sites for MT on A $\beta$ . The authors associated four distinct peaks with A $\beta$ 42 alone, while in the presence of a 10-fold CLR01-excess three sets of peaks occurred corresponding to different charge states of the complexes of A $\beta$ 42 with up to four bound tweezers (Bernstein et al., 2009). No dimers or higher oligomers were observed (Figure 2D). This is a good indication that CLR01 not only prevents formation of A $\beta$ 42 dimers, but also of higher order oligomers. Importantly, no free, unbound A $\beta$ 42 was found in the mass spectrum, supporting the assumption that MT bind directly to A $\beta$ 42 with rather high affinity ( $\sim$  1  $\mu$ M). The authors concluded that CLR01 can remodel the early oligomerization of A $\beta$ 42 not only immediately upon dissolution

but also after the oligomers have already been formed (Zheng et al., 2015).

Native Top-Down Mass Spectrometry and IMS were likewise used to characterize the interaction between MT and the Tau Protein (Nshanian et al., 2018).

Very recently, Loo also reported that no toxic oligomers are left as the result of the efficient interaction between MT and SOD1 (Superoxide Dismutase 1). With ECD, the covalent peptide bonds of the polypeptide could be cleaved, whereas non-covalent forces sufficed to hold the ligand bound to the macromolecule. Tandem MS (MS/MS) or “top-down” MS of the protein–ligand complex allowed to explore the main binding site(s) of MT on the SOD1 surface. Surprisingly, MT preferred to bind to Lys-70 and/or Lys-75 although none of these residues is directly involved in the aggregation process of SOD1. This may explain why at least a 5-fold MT excess is required to affect the aggregation (Malik et al., 2019).

In this investigation, CLR01 inhibited abnormal SOD1 self-assembly *in vitro*, as well as *in vivo*, as being shown on the G93A-SOD1 mouse model of amyotrophic lateral sclerosis (ALS). By applying therapeutic amounts of CLR01 to recombinant wild type and mutant SOD1, their *in vitro* aggregation speed was significantly lowered for all SOD1 forms. *In vivo*, misfolded SOD1 in the spinal cord was significantly reduced, yet not enough to overcome motor deficits, most likely due to the fast disease progression. Further insight came from experiments on SOD1 with ThT and EM at the end of each aggregation. For a potential SOD1 treatment, advanced tweezer derivatives with improved performance must be designed in the future (Malik et al., 2019).

## CONCLUSION AND OUTLOOK

The above-discussed synopsis of structural and biophysical experiments strongly suggests that molecular tweezers dock onto sterically accessible lysine and arginine on aggregating proteins. The resulting Lys/Arg shielding prevents misfolding and/or subsequent protein aggregation into toxic oligomers. It also dissolves existing  $\beta$ -sheets and redirects their path of aggregation to benign amorphous structures.

The same effects are observed with a large number of aggregating proteins, so that these lysine binders seem to act in a process-specific manner and are clearly not protein-specific. In all cases where lysine or arginine residues are involved in the aggregation process, molecular tweezers seem to prevent their ordered aggregation into fibrillar toxic structures. It may be argued that unselective multiple lysine binding should greatly disturb protein function; however, their moderate affinity (10–30  $\mu\text{M}$   $K_d$ ) and fast on- and off-rates apparently preserve natural protein folding and function. Indeed, for enzyme inhibition 100-fold higher concentrations are needed (1 mM), providing a large potential therapeutic window.

After the initial aggregation assays with isolated proteins, cell culture experiments demonstrated powerful protection against

oligomer or fibril lesion from exactly those proteins whose aggregation could also be rescued *in vitro* (Xu et al., 2017; Malik et al., 2018). Finally, triply transgenic mice were treated with low daily doses of CLR01 (40  $\mu\text{g}/\text{kg}$ ) and showed dramatic reduction of plaque load in their cortices (stained histological brain slices). Subsequent behavioral tests (Y-Maze, Pole climbing) revealed significant memory and mobility improvement after treatment with CLR01 (Richter et al., 2017).

Although no systematic metabolism studies have been carried out yet, no degradation product could be found so far, e.g., after treatment with strong acid (pH 0) and base (pH 12) and common phosphatases. We assume that the steric demand of the tweezer skeleton prevents most chemical transformations at the two phosphate groups, and that the doubly phosphorylated stage is recognized as a water-soluble metabolite ready for urinary excretion.

CLR01 was tritium-labeled and could be detected in mouse brains. In addition, HPLC-MS assays of brain extracts revealed 2–3 nM concentrations of CLR01. We are currently optimizing the tweezer structure to generate aggregation inhibitors of lower polarity which will cross the blood-brain barrier (BBB) much more efficiently, hopefully even after oral administration. In some of these projects the results are so promising that we hope to enter clinical trial within the next few years.

Thus, a supramolecular host molecule for basic amino acids was turned into a powerful tool against pathologic protein aggregation and showed highly promising effects in various cell types and animal models. This is an outstanding example in the evolution of supramolecular concepts toward biological application.

## AUTHOR CONTRIBUTIONS

PR wrote the chapters about structure, synthesis, and binding of MTs. IH wrote the chapters about prevention of pathologic protein aggregation by MTs. TS wrote the introduction and conclusions section. F-GK invented the molecular tweezers, GB carried out biological experiments, and both supervised the revision of the mini-review.

## FUNDING

The work summarized in this Mini-Review was performed within the Collaborative Research Centre 1093: Supramolecular Chemistry on Proteins, Subproject A3, which is now in the second grant period and has been funded by the Deutsche Forschungsgemeinschaft DFG. The authors also acknowledge the NIH/NIA R01 AG050721 for the funding and AG050721-02S1 and AG050721-05S1 for administrative supplements.

## ACKNOWLEDGMENTS

Funding by the Deutsche Forschungsgemeinschaft (CRC 1093, Project A3) is gratefully acknowledged.

## REFERENCES

- Barrow, S. J., Kasera, S., Rowland, M. J., del Barrio, J., and Scherman, O. A. (2015). Cucurbituril-based molecular recognition. *Chem. Rev.* 115, 12320–12406. doi: 10.1021/acs.chemrev.5b00341
- Bernstein, S. L., Dupuis, N. F., Lazo, N. D., Wyttenbach, T., Condron, M. M., Bitan, G., et al. (2009). Amyloid- $\beta$  protein oligomerization and the importance of tetramers and dodecamers in the aetiology of Alzheimer's disease. *Nat. Chem.* 1, 326–331. doi: 10.1038/nchem.247
- Bier, D., Rose, R., Bravo-Rodriguez, K., Bartel, M., Ramirez-Anguita, J. M., Dutt, S., et al. (2013). Molecular tweezers modulate 14-3-3 protein-protein interactions. *Nat. Chem.* 5, 234–239. doi: 10.1038/nchem.1570
- Billings, L. M., Oddo, S., Green, K. N., McGaugh, J. L., and LaFerla, F. M. (2005). Intraneuronal A $\beta$  causes the onset of early Alzheimer's disease-related cognitive deficits in transgenic mice. *Neuron* 45, 675–688. doi: 10.1016/j.neuron.2005.01.040
- Chen, C. W., and Whitlock, H. W. (1978). Molecular tweezers: a simple model of bifunctional intercalation. *J. Am. Chem. Soc.* 100, 4921–4922. doi: 10.1021/ja00483a063
- Cherny, R. A., Atwood, C. S., Xilinas, M. E., Gray, D. N., Jones, W. D., Mclean, C. A., et al. (2001). Treatment with a copper-zinc chelator markedly and rapidly inhibits  $\beta$ -amyloid accumulation in alzheimer's disease transgenic mice. *Neuron* 30:665–676. doi: 10.1016/S0896-6273(01)00317-8
- Crini, G. (2014). Review: a history of cyclodextrins. *Chem. Rev.* 114, 10940–10975. doi: 10.1021/cr500081p
- Despres, C., Di, J., Cantrelle, F. X., Li, Z., Huvent, I., Chambraud, B., et al. (2019). Major differences between the self-assembly and seeding behavior of heparin-induced and in vitro phosphorylated tau and their modulation by potential inhibitors. *ACS Chem. Biol.* 14, 1363–1379. doi: 10.1021/acschembio.9b00325
- Dutt, S., Wilch, C., Gersthagen, T., Talbiersky, P., Bravo-Rodriguez, K., Hanni, M., et al. (2013). Molecular tweezers with varying anions: a comparative study. *J. Org. Chem.* 78, 6721–6734. doi: 10.1021/jo4009673
- Ehrhoffer, D. E., Bieschke, J., Boeddrich, A., Herbst, M., Masino, L., Lurz, R., et al. (2008). EGCG redirects amyloidogenic polypeptides into unstructured, off-pathway oligomers. *Nat. Struct. Mol. Biol.* 15, 558–566. doi: 10.1038/nsmb.1437
- Fokkens, M., Schrader, T., and Klärner, F. G. (2005). A molecular tweezer for lysine and arginine. *J. Am. Chem. Soc.* 127, 14415–14421. doi: 10.1021/ja052806a
- Gakh, A. A. (2018). "Molecular tweezers," in *Mol Devices - An Intro to Technomimetics Its Biol Appl*. 1st Edn. (Hoboken, NJ: John Wiley & Sons, Inc), 213–310.
- Gao, Q., Williams, L. D., Egli, M., Rabinovich, D., Chen, S. L., Quigley, G. J., et al. (1991). Drug-induced DNA repair: X-ray structure of a DNA-ditercalinium complex. *Proc. Natl. Acad. Sci. U.S.A.* 88, 2422–2426. doi: 10.1073/pnas.88.6.2422
- Gervais, F., Paquette, J., Morissette, C., Krzywkowski, P., Yu, M., Azzi, M., et al. (2007). Targeting soluble A $\beta$  peptide with Tramiprosate for the treatment of brain amyloidosis. *Neurobiol. Aging* 28, 537–547. doi: 10.1016/j.neurobiolaging.2006.02.015
- Hardy, J., and Higgins, G. A. (1992). Alzheimer's disease: the amyloid cascade hypothesis. *Science* 256, 184–185. doi: 10.1126/science.1566067
- Hardy, J., and Selkoe, D. J. (2002). The amyloid hypothesis of alzheimer's disease. *Amyloid Int. J. Exp. Clin. Investig.* 297, 353–357. doi: 10.1126/science.1072994
- Harmata, M. (2004). Chiral molecular tweezers. *Acc. Chem. Res.* 37, 862–873. doi: 10.1021/ar030164v
- Heid, C., Sowislok, A., Schaller, T., Niemeyer, F., Klärner, F.-G., and Schrader, T. (2018). Molecular tweezers with additional recognition sites. *Chem. Eur. J.* 24, 11332–11343. doi: 10.1002/chem.201801508
- Kirsch, M., Talbiersky, P., Polkowska, J., Bastkowski, F., Schaller, T., De Groot, H., et al. (2009). A Mechanism of efficient G6PD inhibition by a molecular clip. *Angew. Chem. Int. Ed.* 48, 2886–2890. doi: 10.1002/anie.200806175
- Klärner, F.-G., Benkhoff, J., Boese, R., Burkert, U., and Kamieth, M. (1996). Molecular tweezers as synthetic receptors in host-guest chemistry: inclusion of cyclohexane and self-assembly of aliphatic side chains. *Angew. Chem. Int. Ed. Engl.* 35, 4–7. doi: 10.1002/anie.199611301
- Klärner, F. G., Burkert, U., Kamieth, M., Boese, R., and Benet-Buchholz, J. (1999). Molecular tweezers as synthetic receptors: molecular recognition of electron-deficient aromatic and aliphatic substrates. *Chem. Eur. J.* 5, 1700–1707. doi: 10.1002/(SICI)1521-3765(19990604)5:6<1700::AID-CHEM1700>3.0.CO;2-9
- LeVine, H. (1999). Quantification of  $\beta$ -sheet amyloid fibril structures with thioflavin T. *Methods Enzymol.* 309, 274–284. doi: 10.1016/S0076-6879(99)09020-5
- Ma, D., Zhang, B., Hoffmann, U., Sundrup, M. G., Eikermann, M., Isaacs, L. (2012). Acyclic cucurbit[n]uril-type molecular containers bind neuromuscular blocking agents in vitro and reverse neuromuscular block *in vivo*. *Angew. Chem. Int. Ed.* 51, 11358–11362. doi: 10.1002/anie.201206031
- Malik, R., Di, J., Nair, G., Attar, A., Taylor, K., Teng, E., et al. (2018). Using molecular tweezers to remodel abnormal protein self-assembly and inhibit the toxicity of amyloidogenic proteins. *Methods Mol Biol.* 1777, 369–386. doi: 10.1007/978-1-4939-7811-3\_24
- Malik, R., Meng, H., Wongkongkathep, P., Corrales, C. I., Sepanj, N., Atlasi, R. S., et al. (2019). The molecular tweezer CLR01 inhibits aberrant superoxide dismutase 1 (SOD1) self-assembly in vitro and in the G93A-SOD1 mouse model of ALS. *J. Biol. Chem.* 294, 3501–3513. doi: 10.1074/jbc.RA118.005940
- McLaurin, J. A., Golomb, R., Jurewicz, A., Antel, J. P., and Fraser, P. E. (2000). Inositol stereoisomers stabilize an oligomeric aggregate of alzheimer amyloid  $\beta$  peptide and inhibit A $\beta$ -induced toxicity. *J. Biol. Chem.* 275, 18495–18502. doi: 10.1074/jbc.M906994199
- Necula, M., Breydo, L., Milton, S., Kaye, R., Van Der Veer, W. E., Tone, P., et al. (2007). Methylene blue inhibits amyloid A $\beta$  oligomerization by promoting fibrillization. *Biochemistry* 46, 8850–8860. doi: 10.1021/bi700411k
- Neri, P., Sessler, J. L., and Wang, M.-X. (2016). *Calixarenes and Beyond*. Cham: Springer International Publishing.
- Nshanian, M., Lantz, C., Wongkongkathep, P., Schrader, T., Klärner, F. G., Blümke, A., et al. (2018). Native top-down mass spectrometry and ion mobility spectrometry of the interaction of tau protein with a molecular tweezer assembly modulator. *J. Am. Soc. Mass. Spectrom.* 30, 16–23. doi: 10.1007/s13361-018-2027-6
- Paxton, R. J., Beatty, B. G., Hawthorne, M. F., et al. (1991). A transition metal complex (Venus flytrap cluster) for radioimmunodetection and radioimmunotherapy. *Proc. Natl. Acad. Sci. U.S.A.* 88, 3387–3391. doi: 10.1073/pnas.88.8.3387
- Podlisy, M. B., Walsh, D. M., Amarante, P., Ostaszewski, B. L., Stimson, E. R., Maggio, J. E., et al. (1998). Oligomerization of endogenous and synthetic amyloid  $\beta$ -protein at nanomolar levels in cell culture and stabilization of monomer by Congo red. *Biochemistry* 37, 3602–3611. doi: 10.1021/bi972029u
- Prabhudesai, S., Sinha, S., Attar, A., Kotagiri, A., Fitzmaurice, A. G., Lakshmanan, R., et al. (2012). A novel "Molecular Tweezer" inhibitor of  $\alpha$ -synuclein neurotoxicity *in vitro* and *in vivo*. *Neurotherapeutics* 9, 464–476. doi: 10.1007/s13311-012-0105-1
- Richter, F., Subramaniam, S. R., Magen, I., Lee, P., Hayes, J., Attar, A., et al. (2017). A molecular tweezer ameliorates motor deficits in mice overexpressing  $\alpha$ -synuclein. *Neurotherapeutics* 14, 1107–1119. doi: 10.1007/s13311-017-0544-9
- Roland, J. R., and Jacobsen, H. (2009). Alzheimer's disease: From pathology to therapeutic approaches. *Angew. Chem. Int. Ed.* 48, 3030–3059. doi: 10.1002/anie.200802808
- Schrader, T., Bitan, G., and Klärner, F. G. (2016). Molecular tweezers for lysine and arginine-powerful inhibitors of pathologic protein aggregation. *Chem. Commun.* 52, 11318–11334. doi: 10.1039/C6CC04640A
- Sengupta, U., Nilson, A. N., and Kaye, R. (2016). The role of amyloid- $\beta$  oligomers in toxicity, propagation, and immunotherapy. *EBioMedicine* 6, 42–49. doi: 10.1016/j.ebiom.2016.03.035
- Shankar, G. M., Li, S., Mehta, T. H., Garcia-Munoz, A., Shepardson, N. E., Imelda, S., et al. (2008). Amyloid  $\beta$ -protein dimers isolated directly from alzheimer brains impair synaptic plasticity and memory. *Nat. Med.* 14, 837–842. doi: 10.1038/nm1782
- Sinha, S., Lopes, D. H. J., and Bitan, G. (2012). A key role for lysine residues in amyloid  $\beta$ -protein folding.pdf. *ACS Chem. Neurosci.* 3, 473–481. doi: 10.1021/cn3000247
- Sinha, S., Lopes, D. H. J., Du, Z., Pang, E. S., Shanmugam, A., Lomakin, A., et al. (2011). Lysine-specific molecular tweezers are broad-spectrum inhibitors of assembly and toxicity of amyloid proteins. *J. Am. Chem. Soc.* 133, 16958–16969. doi: 10.1021/ja206279b
- Talbiersky, P., Bastkowski, F., Kla, F., and Schrader, T. (2008). Molecular clip and tweezer introduce new mechanisms of enzyme inhibition molecular clip and



- tweezer introduce new mechanisms of enzyme inhibition. *J. Am. Chem. Soc.* 130, 9824–9828. doi: 10.1021/ja801441j
- Usui, K., Hulleman, J. D., Paulsson, J. F., Siegel, S. J., Powers, E. T., and Kelly, J. W. (2009). Site-specific modification of Alzheimer's peptides by cholesterol oxidation products enhances aggregation energetics and neurotoxicity. *Proc. Natl. Acad. Sci. U.S.A.* 106, 18563–18568. doi: 10.1073/pnas.0804758106
- Wytenbach, T., Kemper, P. R., and Bowers, M. T. (2001). Design of a new electrospray ion mobility mass spectrometer. *Int. J. Mass Spectrom.* 212, 13–23. doi: 10.1016/S1387-3806(01)00517-6
- Xu, N., Bitan, G., Schrader, T., Klärner, F. G., Osinska, H., and Robbins, J. (2017). Inhibition of mutant  $\alpha$ B crystallin-induced protein aggregation by a molecular tweezer. *J. Am. Heart Assoc.* 6, 1–13. doi: 10.1161/JAHA.117.006182
- Zhao, L. N., Long, H. W., Mu, Y., and Chew, L. Y. (2012). The toxicity of amyloid  $\beta$  oligomers. *Int. J. Mol. Sci.* 13, 7303–7327. doi: 10.3390/ijms13067303
- Zheng, X., Liu, D., Klärner, F. G., Schrader, T., Bitan, G., and Bowers, M. T. (2015). Amyloid  $\beta$ -protein assembly: the effect of molecular tweezers CLR01 and CLR03. *J. Phys. Chem.* 119, 4831–4841. doi: 10.1021/acs.jpcc.5b00692
- Zimmerman, S. (1991). Molecular tweezers: synthetic receptors for  $\pi$ -sandwich complexation of aromatic substrates. *Bioorganic Chem. Front.* 199, 33–71. doi: 10.1007/978-3-642-76241-3\_2

**Conflict of Interest:** The authors declare that the research was conducted in the absence of any commercial or financial relationships that could be construed as a potential conflict of interest.

Copyright © 2019 Hadrovic, Rebmann, Klärner, Bitan and Schrader. This is an open-access article distributed under the terms of the Creative Commons Attribution License (CC BY). The use, distribution or reproduction in other forums is permitted, provided the original author(s) and the copyright owner(s) are credited and that the original publication in this journal is cited, in accordance with accepted academic practice. No use, distribution or reproduction is permitted which does not comply with these terms.

## **3.2 Publication II**

### **Supramolecular Enhancement of Natural 14-3-3 Protein Ligands**

Supramolecular chemistry has recently proven to be a promising approach to modulate protein functions. Indeed, the unique molecular features of supramolecular ligands allow specific recognition of protein residues or sites, enabling the modulation of their functions or assembly. However, supramolecular ligands, especially host molecules, often display poor target selectivity and a low affinity, which hinders their development and attractiveness. We report here that an engineered conjugation of lysine-specific molecular tweezers with a peptide-based inhibitor of the 14-3-3 family's protein-protein interactions led to a supramolecular ditopic ligand exhibiting 100-fold elevated protein affinity. The X-ray crystal structure obtained was astonishingly close to reference structures from our computer simulations. This finding indicates that the careful design of supramolecular ditopic protein ligands using host molecules may represent a promising approach for modulating protein-protein interactions and protein assembly process.

Reprinted with permission from *J. Am. Chem. Soc.* 2021, 143, 13495–13500. Copyright 2021 American Chemical Society. The publication can be found under: <https://pubs.acs.org/doi/full/10.1021/jacs.1c07095>

# Supramolecular Enhancement of a Natural 14–3–3 Protein Ligand

Xavier Guillory,<sup>||</sup> Inesa Hadrović,<sup>||</sup> Pim J. de Vink, Andrea Sowislok, Luc Brunsveld, Thomas Schrader,\* and Christian Ottmann\*

Cite This: *J. Am. Chem. Soc.* 2021, 143, 13495–13500

Read Online

ACCESS |

Metrics & More

Article Recommendations

Supporting Information

**ABSTRACT:** Rational design of protein–protein interaction (PPI) inhibitors is challenging. Connecting a general supramolecular protein binder with a specific peptidic ligand provides a novel conceptual approach. Thus, lysine-specific molecular tweezers were conjugated to a peptide-based 14–3–3 ligand and produced a strong PPI inhibitor with 100-fold elevated protein affinity. X-ray crystal structure elucidation of this supramolecular directed assembly provides unique molecular insight into the binding mode and fully aligns with Molecular Dynamics (MD) simulations. This new supramolecular chemical biology concept opens the path to novel chemical tools for studying PPIs.

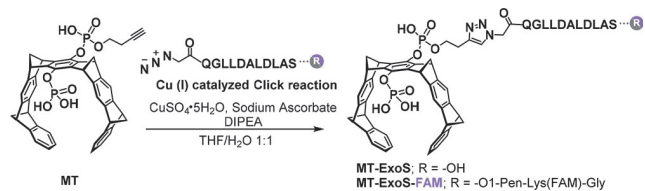
Selective recognition of proteins and modulation of their interactions represents an unprecedented opportunity for pharmacological innovation.<sup>1–3</sup> Despite the importance of protein–protein interactions (PPIs), the development of molecular tools for pharmacological intervention of PPIs has remained a challenge, mainly due to the different structural characteristics of protein interfaces compared to traditional drug targets. Supramolecular systems provide orthogonal molecular elements for enhancing affinity and selectivity in protein recognition and modulation.<sup>4</sup> Hence, synthetic supramolecular host–guest systems can recognize protein elements such as side chains<sup>5–9</sup> and peptide motifs,<sup>10,11</sup> even with selectivity within a specific protein context.<sup>12,13</sup> Achieving higher levels of affinity and selectivity in the supramolecular protein recognition process will be crucial in bringing this concept to the next level of application. Combining synthetic supramolecular elements with peptide recognition motifs would provide an elegant and unique entry for the development of such improved protein modulator tool compounds.

The biological function of the 14–3–3 adapter proteins hinges on PPIs with its clients.<sup>14–17</sup> Modulators of 14–3–3 are desired for mechanistic studies and for interference with pathology.<sup>2,18</sup> Inhibitory modulation of 14–3–3 PPIs is typically done with peptides and peptidomimetics derived from client partners.<sup>19–21</sup> Simultaneously, supramolecular systems have been brought forward as 14–3–3 recognition elements.<sup>7,11,22</sup> A prominent client protein for 14–3–3 is exoenzyme S (ExoS), a pathogenicity factor of the pneumonia-causing bacterium *Pseudomonas aeruginosa*, which uses human 14–3–3 as a host factor.<sup>23–25</sup> Here, we show for the first time the interfacing of a synthetic supramolecular element (molecular tweezers) with an ExoS peptide recognition motif to furnish a powerful ditopic 14–3–3 ligand.

Previously, we solved the crystal structure of molecular tweezers (MT) bound to 14–3–3σ.<sup>7</sup> The supramolecular ligand was threaded onto Lys214, located at the edge of the northern α-helix. This placed the spacious torus-shaped tweezers body at the rim of the central binding channel,

which is the primary docking region for the ExoS protein. The molecular tweezers were shown to displace ExoS from its 14–3–3 complex, with a moderate IC<sub>50</sub> value of 500 μM.<sup>7</sup> It occurred that the position of both 14–3–3 binders would offer enough space to be covalently connected while maintaining complementary binding. To this end, we equipped one of the tweezer's phosphates with a butynyl ester arm.<sup>26</sup> Subsequent “Click” reaction with an ExoS peptide featuring an N-terminal azide afforded the tweezers peptide conjugate (MT-ExoS) (Scheme 1).

## Scheme 1. Synthetic Strategy toward the Ditopic MT-ExoS Conjugate



NMR spectroscopy revealed the absence of upfield shifts in the peptide moiety signals, indicating that the peptide sequence was not self-complexed in the tweezers' cavity (Supporting Information (SI), section 3.6). To enable biophysical studies, the MT-ExoS ligand was also synthesized with an additional C-terminal fluorophore. Docking of this new ditopic ligand to 14–3–3σ was performed with Monte-Carlo calculations and MD simulations (SI, section 3.1). This resulted in a favorable complex structure (SI), which did not

Received: July 9, 2021

Published: August 24, 2021



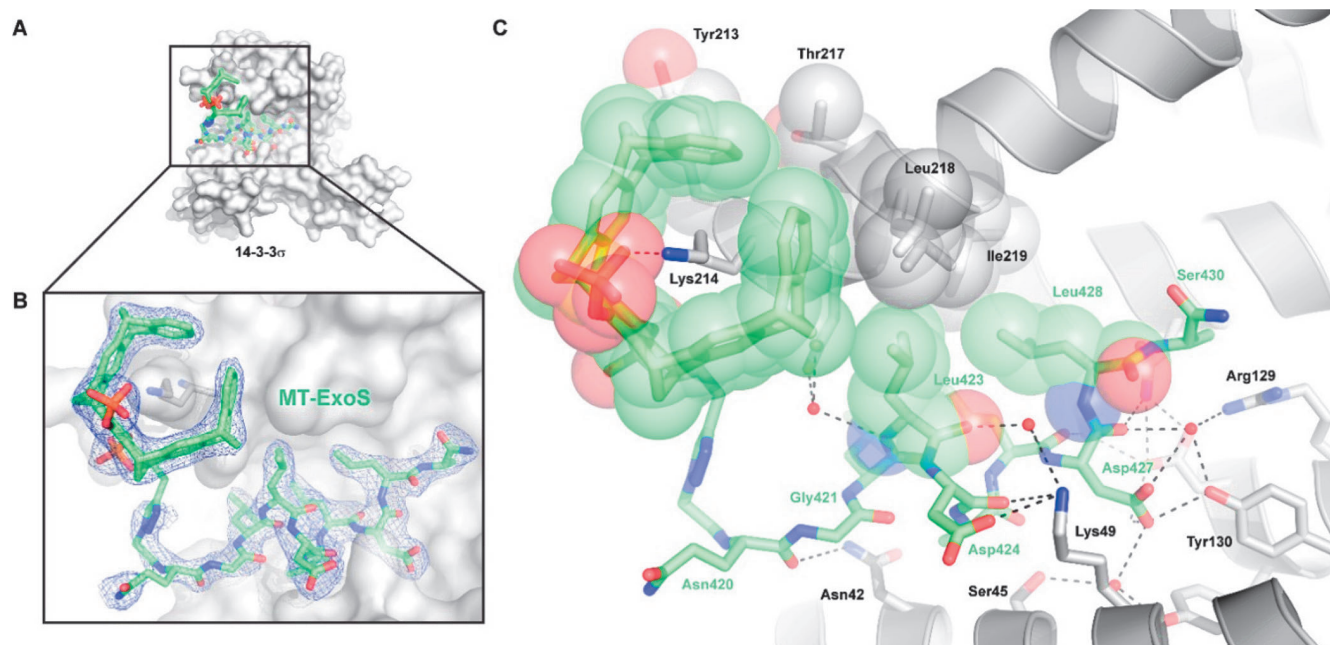


**Figure 1.** Crystal structure of the MT-ExoS ligand in complex with 14-3-3 $\sigma$ . (A) MT-ExoS ligand (green sticks) bound to one 14-3-3 $\sigma$  monomer (white surface). (B)  $2F_o - F_c$  electron density (blue mesh; contoured at  $1\sigma$ ) for MT-ExoS bound to 14-3-3 $\sigma$ . (C) Interaction network of the MT-ExoS ligand with 14-3-3 $\sigma$  and surrounding water molecules (small red spheres).

show any inner strain and placed both moieties very close to their locations in the isolated binary crystal structures (Figure S1).

Crystallography screening led to a highly informative crystal structure of the supramolecular MT-ExoS ligand in complex with 14-3-3 $\sigma$  (PDB ID 6Y7T, Figure 1). The *I*121 space group showed four 14-3-3 monomers in the asymmetric unit. In two of the four 14-3-3 monomers the unbiased  $F_o - F_c$  map, computed directly after the molecular replacement (Figure S10), showed electron density matching unambiguously with the supramolecular ligand. The ExoS short  $\alpha$ -helical backbone and the unique shape of the molecular tweezers bound to Lys214 were clearly recognizable. The final structure obtained after molecular refinement (Figure 1 and Figures S11–S13) also allowed a clear definition of the peptide side chains and the triazole linker.

This new supramolecular protein structure allowed for a direct comparison with the structures of the individual components<sup>7,11,20,27</sup> as well as computational prediction (Figure 2A–E). The MT and ExoS elements of the ditopic ligand display an excellent overlap (Figure 2D) with the reference structures of 14-3-3 in complex with MT or ExoS alone (Figure 2A,B). In the new structure, the asymmetric unit contains one typical W-shaped 14-3-3 dimer structure, and two monomers for which their dimerization partners belong to the symmetry related asymmetric unit (Figures S11, S12). Interestingly, the two MT-ExoS ligands visible in the new crystal structure are part of two different, adjacent dimers and position the ligands near each other at the interface (Figure S13). This phenomenon has already been observed in previous structures of the MT;<sup>7,11</sup> the surrounding of the MTs' moiety (Figure 1 and Figure S14) is mostly composed of hydrophobic residues from the target 14-3-3 $\sigma$  monomer (Tyr213, Thr217, Leu218), symmetry-related monomer (Thr217, Met220, Phe198, Met202), and ExoS peptide (Leu423). These apolar residues form a crescent shape with pronounced hydrophobic

interactions around the MT and shield its apolar exterior from the aqueous solvent.

Additional ionic interactions between the tweezers' upper phosphate moiety and the terminal Lys214's ammonium, as well as Arg224's guanidinium cation, further strengthen the MT-ExoS complex with 14-3-3 $\sigma$  (Figure S15). Of note and contrary to most other 14-3-3's protein partners, the ExoS sequence is not phosphorylated and cannot bind the preorganized cationic 14-3-3 groove, but uses a succession of hydrophobic interactions between its own leucine cluster and hydrophobic residues on the 14-3-3 roof instead.<sup>24,28</sup> This unique combination of extensive hydrophobic interactions and Coulomb attraction may explain the prominent contribution of favorable entropy changes determined by isothermal calorimetry (*vide infra*).

Examination of the ligand's peptide geometry compared to the reference ExoS structure (Figure 2D) shows how closely the main chain and side chains located in the 14-3-3 groove overlap (all atom RMSD<sub>ExoS</sub> 2.14 Å; *C $\alpha$*  RMSD<sub>ExoS</sub> 1.65 Å). A slightly different orientation can be seen for Gln420, and, to a smaller extent, for Gly421, most likely due to the introduction of the triazole linker. However, previous work on ExoS/14-3-3 complexes has shown that this residue can adopt distinct conformation and interaction patterns without altering the overall binding mode (Figure S16).<sup>7,28</sup> Ser430, located near  $\alpha$ -helix 9 and lacking hydrogen bonding interactions, also shows a small variation (RMSD 2.12 Å). The same excellent overlap is also found for the orientation of the tweezers torus on Lys214 (RMSD<sub>MT</sub> 1.95 Å). We believe that the superimposition between single elements and the combined hybrid tweezers in all three crystal structures demonstrates their generally preferred orientation and advocates for the use of X-ray structures in the rational design of ditopic protein ligands.

Comparison of the ligand geometry in the crystal with the MD simulations (Figure 2E and Figure S2) confirms the general trends observed, namely strong binding of the MT and

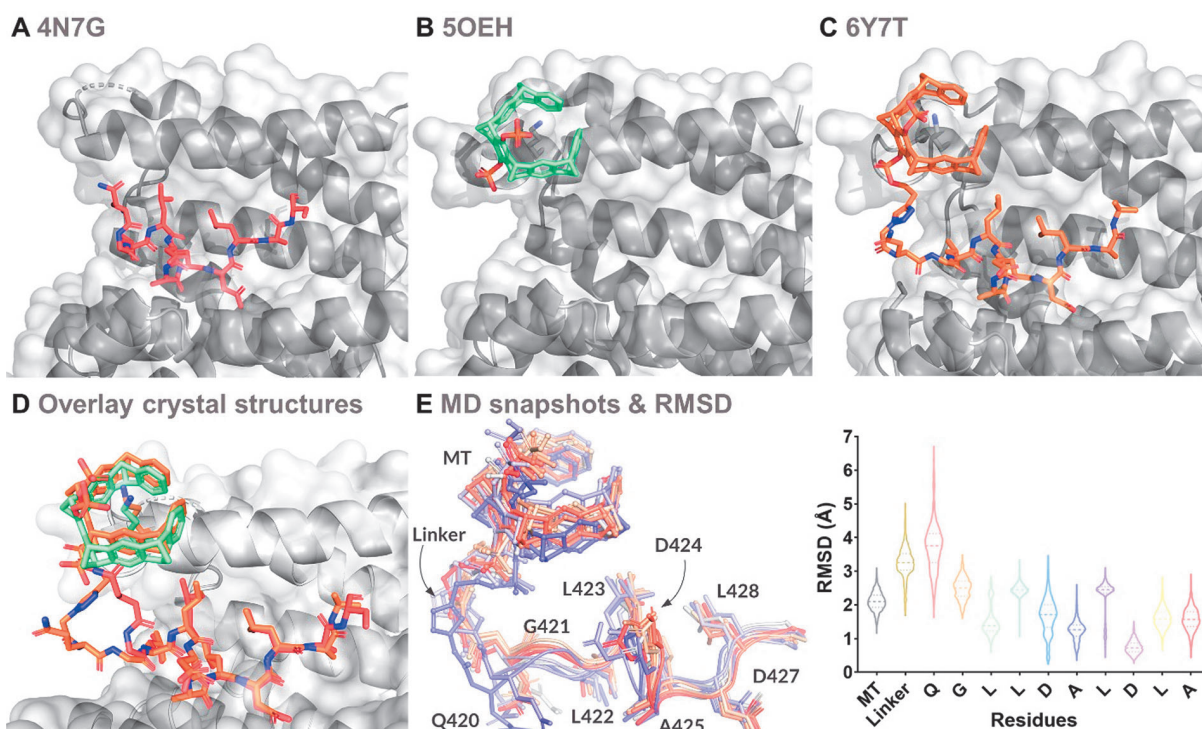


**Figure 2.** Crystal structures and molecular dynamics simulations. (A) Structure of the ExoS derived peptide (red sticks) bound to 14-3-3 $\zeta$  (white cartoon and transparent surface; PDB ID 4N7G). (B) Structure of the molecular tweezers (seafoam green sticks) bound to 14-3-3 $\sigma$  (PDB ID 5OEH). (C) Crystal structure of the new MT-ExoS ligand (orange sticks) bound to 14-3-3 $\sigma$  (PDB ID 6Y7T). (D) Overlay of the individual structures of the MT and ExoS peptide with the structure of the supramolecular ditopic MT-ExoS ligand (color code as in A, B, and D). (E) Left: overlay of 10 snapshots (10 ns interval, 100 ns total) of the MT-ExoS ligand MD simulation on 14-3-3 $\sigma$  (protein not shown for clarity). Right: Violin box plot of the all atoms RMSD per residue of the MT-ExoS construct extracted from 100 ns (2000 frames) of MD simulation. Note the relatively high flexibility of the linker region (see Figure S2 for replicates).

ExoS moieties showing very little variations, with the exception of Asp424, a solvent exposed residue displaying an increased range of motion. Again, the triazole linker and adjacent residues Gln420 and Gly421 displayed more conformational variation (Figure S2, Supplementary Movie 1). Flexibility was indeed an integral part of the linker design to allow enough degrees of freedom for the movement of both components. The resulting entropic gain during the binding event is in agreement with the ITC experiment.

Competitive Fluorescence Polarization (FP) experiments of the MT-ExoS against 14-3-3 $\sigma$  bound to the fluorescein-labeled tight binder TAZpS89<sup>29,30</sup> revealed displacement of this reference peptide by the supramolecular conjugate (Figure 3A). The MT-ExoS ligand displaces the TAZpS89 peptide at a lower concentration than the ExoS peptide alone ( $EC_{50}$  MT-ExoS  $\approx 70 \mu\text{M}$  vs  $EC_{50}$  ExoS  $\approx 134 \mu\text{M}$ ). Direct 14-3-3 $\sigma$  binding assays were performed with FAM-labeled versions of the three different ligands (Figure 3B). Full sigmoidal curves were obtained allowing determination of  $K_D$  values. Control experiments with fluorescein ruled out a potential binding of the fluorophore to 14-3-3 $\sigma$  (Figure S3). Of note, this is the first report on direct binding of the parent molecular tweezers to 14-3-3 $\sigma$  as measured by FP; the obtained  $K_D$  of  $8 \mu\text{M}$  is comparable to their known affinity toward free and peptidic lysines ( $10\text{--}20 \mu\text{M}$ ).<sup>7</sup> The ExoS peptide affinity toward the 14-3-3 $\sigma$  isoform was measured at  $46 \mu\text{M}$ . The combination of both ligands in the ditopic MT-ExoS ligand shifts the  $K_D$  into the nanomolar regime ( $K_D$   $0.4 \mu\text{M}$ ), indicating a 100-fold stronger binding as compared to the native peptide. Such a dramatic enhancement in binding energy corresponds well to

the effect induced by an increased valency<sup>31–34</sup> and confirms that both units find their own binding site on the 14-3-3 protein surface.

Further insight into the ditopic binding mode of the tweezer peptide conjugate was obtained from competitive back-titrations: an excess of nonfluorescent ExoS peptide, MT, or MT-ExoS was added to a preformed saturated complex between 14-3-3 $\sigma$  and the fluorescent binders. Both monotopic binders had only moderate effects, whereas the ditopic ExoS tweezer completely displaced its fluorescent counterpart (Figure S4).

It is known that other 14-3-3 isoforms accommodate their client-derived peptides even better in their cleft than 14-3-3 $\sigma$ .<sup>35–37</sup> We reasoned that this might also be reflected in elevated affinities for the tweezer conjugate. Direct FP titrations confirmed this assumption and produced  $IC_{50}$  values of 1 (14-3-3 $\zeta$ ) and even 2 orders of magnitude (14-3-3 $\gamma$ ) below 14-3-3 $\sigma$ . The respective binding curves depicted in Figure S5 reveal a plateau, perhaps indicating a two-step event of protein interaction with the tweezers.

Isothermal titration calorimetry (ITC) studies provided thermodynamic information on the binding events (Figure 3C and Figures S6, S7). The ExoS peptide bound with a  $K_D$  of  $41 \mu\text{M}$  to 14-3-3 $\sigma$ , very similar to the FP value. Fusion with the MT moiety greatly strengthened the interaction, but produced a biphasic titration curve indicating two binding events of different affinity. Careful optimization of the experimental setup allowed independent titrations at three different concentrations whose evaluation by nonlinear regression according to a two-set-of-sites model gave very similar results:

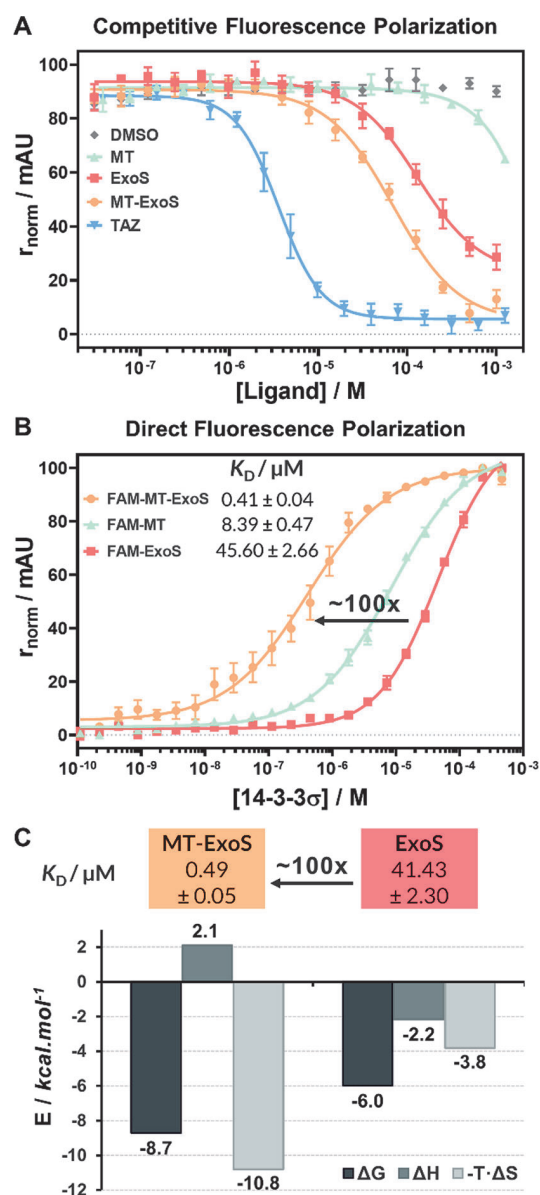


**Figure 3.** Biophysical characterization of the 14–3–3 ditopic ligand interaction. (A) Competitive Fluorescence Polarization titrations to 14–3–3 $\sigma$  in complex with the fluorescently labeled FITC-TAZpS89 peptide ( $K_D$ , 1.3  $\mu\text{M}$ ). (B) Fluorescence Polarization titrations of 14–3–3 $\sigma$  to 10 nM FAM-MT-ExoS, FAM-ExoS, and FAM-MT. (C) Thermodynamic footprints of ExoS and MT-ExoS binding to 14–3–3 $\sigma$ .

in all cases a very strong first binding event was documented with a 1:1 stoichiometry and a submicromolar  $K_D$  between 0.3 and 0.5  $\mu\text{M}$ . A second tweezer conjugate was found to bind to the protein much more weakly with submillimolar affinity. No interaction was found between the Lys(FAM) derivative and 14–3–3 $\sigma$  in a control ITC titration (Figure S9). Thus, tweezer peptide conjugation leads to 100-fold improved affinity in the first powerful binding step, in good agreement with the FP result. This corresponds to a lowered Gibb's free energy  $\Delta G$  from  $-6.0$  to  $-8.7$  kcal mol<sup>-1</sup>.

Interestingly, the thermodynamic footprint changes from the free peptide to the supramolecular MT-ExoS: while the peptide alone displays favorable entropy and enthalpy changes when binding to the 14–3–3 cleft, the binding event becomes

endothermic ( $\Delta H = 2.1$  kcal mol<sup>-1</sup>) for the MT-ExoS conjugate and is largely driven by a favorable entropy gain ( $T\Delta S = 10.8$  kcal mol<sup>-1</sup>). We tentatively explain this behavior by a pronounced hydrophobic effect of the tweezers conjugate which finds a large surface area for contacts between apolar moieties of ligand and protein, leading to the release of ordered water molecules. In addition, MD simulations, as well as crystal structures (*vide supra*), point to a significant flexibility of the spacer region between both binding sites, a large degree of mobility being also entropically favorable. Large entropy and enthalpy changes in opposite directions are frequently observed in protein recognition events and are known as enthalpy–entropy compensation.<sup>38–40</sup>

With this report, a new conceptual approach for the rational design of advanced tool compounds for the interference with PPIs is brought forward. The fusion of a peptidic recognition motif with a supramolecular binder of surface-exposed lysines led to a site-selective 14–3–3 inhibitor with 100-fold improved affinity. The design of this tailored supramolecular conjugate was greatly facilitated by crystal structures of complexes from both subcomponents and the support from MD simulations. Together with the structural data of the protein-bound novel ditopic ligand, this highlights that a short but flexible linker maintains enough degrees of freedom for favorable entropy contributions, while allowing both elements to occupy their respective binding site with retained orientation. The supramolecular approach described here could, therefore, represent a general concept for the design of selective and potent ligands with a ditopic mode of action. Incorporation of supramolecular elements could also be used to improve existing PPI modulators as well as to develop new molecular tools capable of modulating protein assemblies through multitopic binding with several partner proteins.

## ASSOCIATED CONTENT

### Supporting Information

The Supporting Information is available free of charge at <https://pubs.acs.org/doi/10.1021/jacs.1c07095>.

Full wwPDB X-ray structure validation report; structures (ZIP)

Simulation interactions diagram report; protein-ligand RMSD; Protein RMSF (PDF)

MD movie (ZIP)

Detailed description of materials and methods, supplementary data and figures (PDF)

### Accession Codes

Crystal structure of MT-ExoS in complex with 14–3–3, PDB ID 6Y7T.

## AUTHOR INFORMATION

### Corresponding Authors

Thomas Schrader – Department of Chemistry, University of Duisburg-Essen, 45117 Essen, Germany; [orcid.org/0000-0002-7003-6362](https://orcid.org/0000-0002-7003-6362); Email: [thomas.schrader@uni-due.de](mailto:thomas.schrader@uni-due.de)

Christian Ottmann – Laboratory of Chemical Biology, Department of Biomedical Engineering and Institute for Complex Molecular System, Eindhoven University of Technology, 5612 AZ Eindhoven, The Netherlands; Department of Chemistry, University of Duisburg-Essen, 45117 Essen, Germany; [orcid.org/0000-0001-7315-0315](https://orcid.org/0000-0001-7315-0315); Email: [C.Ottmann@tue.nl](mailto:C.Ottmann@tue.nl)

## Authors

Xavier Guillory – Laboratory of Chemical Biology, Department of Biomedical Engineering and Institute for Complex Molecular System, Eindhoven University of Technology, 5612 AZ Eindhoven, The Netherlands; Department of Chemistry, University of Duisburg-Essen, 45117 Essen, Germany; Present Address: Inserm U1242 & Univ Rennes, CNRS, ISCR (Institut des Sciences Chimiques de Rennes) – UMR 6226, F-35000 Rennes, France

Inesa Hadrović – Department of Chemistry, University of Duisburg-Essen, 45117 Essen, Germany

Pim J. de Vink – Laboratory of Chemical Biology, Department of Biomedical Engineering and Institute for Complex Molecular System, Eindhoven University of Technology, 5612 AZ Eindhoven, The Netherlands

Andrea Sowislok – University Clinics Essen, Experimental Orthopedics and Trauma Surgery, 45147 Essen, Germany

Luc Brunsveld – Laboratory of Chemical Biology, Department of Biomedical Engineering and Institute for Complex Molecular System, Eindhoven University of Technology, 5612 AZ Eindhoven, The Netherlands; [orcid.org/0000-0001-5675-511X](https://orcid.org/0000-0001-5675-511X)

Complete contact information is available at: <https://pubs.acs.org/10.1021/jacs.1c07095>

## Author Contributions

<sup>||</sup>These authors contributed equally.

## Funding

Funded by the Deutsche Forschungsgemeinschaft (CRC 1093, Projects A3 and B4) and The Netherlands Organization for Scientific Research (NWO) (Gravity Program 024.001.035 and Vici grant 016.150.366).

## Notes

The authors declare the following competing financial interest(s): L.B. and C.O. are founders and shareholders of Ambagon Therapeutics.

## ACKNOWLEDGMENTS

We thank Dr. Christian Heid for initial MD simulations and Dr. Torsten Schaller for help with characterization of 2D NMR spectra.

## REFERENCES

- (1) Milroy, L.-G.; Grossmann, T. N.; Hennig, S.; Brunsveld, L.; Ottmann, C. Modulators of protein-protein interactions. *Chem. Rev.* **2014**, *114*, 4695–4748.
- (2) Scott, D. E.; Bayly, A. R.; Abell, C.; Skidmore, J. Small molecules, big targets: drug discovery faces the protein-protein interaction challenge. *Nat. Rev. Drug Discovery* **2016**, *15*, 533–550.
- (3) Kubota, R.; Hamachi, I. Protein recognition using synthetic small-molecular binders toward optical protein sensing in vitro and in live cells. *Chem. Soc. Rev.* **2015**, *44*, 4454–4471.
- (4) van Dun, S.; Ottmann, C.; Milroy, L.-G.; Brunsveld, L. Supramolecular Chemistry Targeting Proteins. *J. Am. Chem. Soc.* **2017**, *139*, 13960–13968.
- (5) Hof, F. Host-guest chemistry that directly targets lysine methylation: synthetic host molecules as alternatives to bio-reagents. *Chem. Commun. (Cambridge, U. K.)* **2016**, *52*, 10093–10108.
- (6) McGovern, R. E.; Fernandes, H.; Khan, A. R.; Power, N. P.; Crowley, P. B. Protein camouflage in cytochrome c-calixarene complexes. *Nat. Chem.* **2012**, *4*, 527–533.
- (7) Bier, D.; Rose, R.; Bravo-Rodriguez, K.; Bartel, M.; Ramirez-Angueta, J. M.; Dutt, S.; Wilch, C.; Klärner, F.-G.; Sanchez-Garcia, E.;

Schrader, T.; et al. Molecular tweezers modulate 14–3–3 protein-protein interactions. *Nat. Chem.* **2013**, *5*, 234–239.

(8) Chinai, J. M.; Taylor, A. B.; Ryno, L. M.; Hargreaves, N. D.; Morris, C. A.; Hart, P. J.; Urbach, A. R. Molecular recognition of insulin by a synthetic receptor. *J. Am. Chem. Soc.* **2011**, *133*, 8810–8813.

(9) Hatai, J.; Schmuck, C. Diverse Properties of Guanidiniocarbonyl Pyrrole-Based Molecules: Artificial Analogues of Arginine. *Acc. Chem. Res.* **2019**, *52*, 1709–1720.

(10) Smith, L. C.; Leach, D. G.; Blaylock, B. E.; Ali, O. A.; Urbach, A. R. Sequence-specific, nanomolar peptide binding via cucurbit[8]uril-induced folding and inclusion of neighboring side chains. *J. Am. Chem. Soc.* **2015**, *137*, 3663–3669.

(11) Bier, D.; Mittal, S.; Bravo-Rodriguez, K.; Sowislok, A.; Guillory, X.; Briels, J.; Heid, C.; Bartel, M.; Wettig, B.; Brunsveld, L.; et al. The Molecular Tweezer CLR01 Stabilizes a Disordered Protein-Protein Interface. *J. Am. Chem. Soc.* **2017**, *139*, 16256–16263.

(12) McGovern, R. E.; Snarr, B. D.; Lyons, J. A.; McFarlane, J.; Whiting, A. L.; Paci, I.; Hof, F.; Crowley, P. B. Structural study of a small molecule receptor bound to dimethyllysine in lysozyme. *Chem. Sci.* **2015**, *6*, 442–449.

(13) Sonzini, S.; Marcozzi, A.; Gubeli, R. J.; van der Walle, C. F.; Ravn, P.; Herrmann, A.; Scherman, O. A. High Affinity Recognition of a Selected Amino Acid Epitope within a Protein by Cucurbit[8]uril Complexation. *Angew. Chem., Int. Ed.* **2016**, *55*, 14000–14004.

(14) Pennington, K. L.; Chan, T. Y.; Torres, M. P.; Andersen, J. L. The dynamic and stress-adaptive signaling hub of 14–3–3: emerging mechanisms of regulation and context-dependent protein-protein interactions. *Oncogene* **2018**, *37*, 5587–5604.

(15) Aghazadeh, Y.; Papadopoulos, V. The role of the 14–3–3 protein family in health, disease, and drug development. *Drug Discovery Today* **2016**, *21*, 278–287.

(16) Yang, X.; Lee, W. H.; Sobott, F.; Papagrigoriou, E.; Robinson, C. V.; Grossmann, J. G.; Sundström, M.; Doyle, D. A.; Elkins, J. M. Structural basis for protein-protein interactions in the 14–3–3 protein family. *Proc. Natl. Acad. Sci. U. S. A.* **2006**, *103*, 17237–17242.

(17) Milroy, L.-G.; Brunsveld, L.; Ottmann, C. Stabilization and inhibition of protein-protein interactions: the 14–3–3 case study. *ACS Chem. Biol.* **2013**, *8*, 27–35.

(18) Stevers, L. M.; Sijbesma, E.; Botta, M.; MacKintosh, C.; Obsil, T.; Landrieu, I.; Cau, Y.; Wilson, A. J.; Karawajczyk, A.; Eickhoff, J.; et al. Modulators of 14–3–3 Protein-Protein Interactions. *J. Med. Chem.* **2018**, *61*, 3755–3778.

(19) Krüger, D. M.; Glas, A.; Bier, D.; Pospiech, N.; Wallraven, K.; Dietrich, L.; Ottmann, C.; Koch, O.; Hennig, S.; Grossmann, T. N. Structure-Based Design of Non-natural Macrocyclic Peptides That Inhibit Protein-Protein Interactions. *J. Med. Chem.* **2017**, *60*, 8982–8988.

(20) Glas, A.; Bier, D.; Hahne, G.; Rademacher, C.; Ottmann, C.; Grossmann, T. N. Constrained peptides with target-adapted cross-links as inhibitors of a pathogenic protein-protein interaction. *Angew. Chem., Int. Ed.* **2014**, *53*, 2489–2493.

(21) Andrei, S. A.; Thijssen, V.; Brunsveld, L.; Ottmann, C.; Milroy, L.-G. A study on the effect of synthetic  $\alpha$ -to- $\beta$ -amino acid mutations on the binding of phosphopeptides to 14–3–3 proteins. *Chem. Commun. (Cambridge, U. K.)* **2019**, *55*, 14809–14812.

(22) de Vink, P. J.; de Briels, J. M.; Schrader, T.; Milroy, L.-G.; Brunsveld, L.; Ottmann, C. A Binary Bivalent Supramolecular Assembly Platform Based on Cucurbit[8]uril and Dimeric Adapter Protein 14–3–3. *Angew. Chem., Int. Ed.* **2017**, *56*, 8998–9002.

(23) Fu, H.; Coburn, J.; Collier, R. J. The eukaryotic host factor that activates exoenzyme S of *Pseudomonas aeruginosa* is a member of the 14–3–3 protein family. *Proc. Natl. Acad. Sci. U. S. A.* **1993**, *90*, 2320–2324.

(24) Ottmann, C.; Yasmin, L.; Weyand, M.; Veessenmeyer, J. L.; Diaz, M. H.; Palmer, R. H.; Francis, M. S.; Hauser, A. R.; Wittinghofer, A.; Hallberg, B. Phosphorylation-independent interaction between 14–3–3 and exoenzyme S: from structure to pathogenesis. *EMBO J.* **2007**, *26*, 902–913.

- (25) Karlberg, T.; Hornyak, P.; Pinto, A. F.; Milanova, S.; Ebrahimi, M.; Lindberg, M.; Püllen, N.; Nordström, A.; Löverli, E.; Caraballo, R.; et al. 14–3–3 proteins activate *Pseudomonas* exotoxins-S and -T by chaperoning a hydrophobic surface. *Nat. Commun.* **2018**, *9*, 3785.
- (26) Heid, C.; Sowislok, A.; Schaller, T.; Niemeyer, F.; Klärner, F.-G.; Schrader, T. Molecular Tweezers with Additional Recognition Sites. *Chem. - Eur. J.* **2018**, *24*, 11332–11343.
- (27) Bier, D.; Glas, A.; Hahne, G.; Grossmann, T.; Ottmann, C. Crystal structure of 14–3–3zeta in complex with a peptide derived from ExoS: DOI: [10.2210/pdb4N7G/pdb](https://doi.org/10.2210/pdb4N7G/pdb).
- (28) Yasmin, L.; Veessenmeyer, J. L.; Diaz, M. H.; Francis, M. S.; Ottmann, C.; Palmer, R. H.; Hauser, A. R.; Hallberg, B. Electrostatic interactions play a minor role in the binding of ExoS to 14–3–3 proteins. *Biochem. J.* **2010**, *427*, 217–224.
- (29) Guillory, X.; Wolter, M.; Leysen, S.; Neves, J. F.; Kuusk, A.; Genet, S.; Somsen, B.; Morrow, J. K.; Rivers, E.; van Beek, L.; et al. Fragment-based Differential Targeting of PPI Stabilizer Interfaces. *J. Med. Chem.* **2020**, *63*, 6694–6707.
- (30) Sijbesma, E.; Skora, L.; Leysen, S.; Brunsveld, L.; Koch, U.; Nussbaumer, P.; Jahnke, W.; Ottmann, C. Identification of Two Secondary Ligand Binding Sites in 14–3–3 Proteins Using Fragment Screening. *Biochemistry* **2017**, *56*, 3972–3982.
- (31) Magdalena Estirado, E.; Aleman Garcia, M. A.; Schill, J.; Brunsveld, L. Multivalent Ultrasensitive Interfacing of Supramolecular 1D Nanoplatfoms. *J. Am. Chem. Soc.* **2019**, *141*, 18030–18037.
- (32) Fasting, C.; Schalley, C. A.; Weber, M.; Seitz, O.; Hecht, S.; Koks, B.; Dermedde, J.; Graf, C.; Knapp, E.-W.; Haag, R. Multivalency as a chemical organization and action principle. *Angew. Chem., Int. Ed.* **2012**, *51*, 10472–10498.
- (33) Gestwicki, J. E.; Cairo, C. W.; Strong, L. E.; Oetjen, K. A.; Kiessling, L. L. Influencing receptor-ligand binding mechanisms with multivalent ligand architecture. *J. Am. Chem. Soc.* **2002**, *124*, 14922–14933.
- (34) Kostecky, B.; Saurin, A. T.; Purkiss, A.; Parker, P. J.; McDonald, N. Q. Recognition of an intra-chain tandem 14–3–3 binding site within PKCepsilon. *EMBO Rep.* **2009**, *10*, 983–989.
- (35) Gogl, G.; Tugaeva, K. V.; Eberling, P.; Kostmann, C.; Trave, G.; Sluchanko, N. N. Hierarchized phosphotarget binding by the seven human 14–3–3 isoforms. *Nat. Commun.* **2021**, *12*, 1677.
- (36) Centorrino, F.; Ballone, A.; Wolter, M.; Ottmann, C. Biophysical and structural insight into the USP8/14–3–3 interaction. *FEBS Lett.* **2018**, *592*, 1211–1220.
- (37) Soini, L.; Leysen, S.; Davis, J.; Ottmann, C. A biophysical and structural analysis of the interaction of BLNK with 14–3–3 proteins. *J. Struct. Biol.* **2020**, *212*, 107662.
- (38) Olsson, T. S. G.; Ladbury, J. E.; Pitt, W. R.; Williams, M. A. Extent of enthalpy-entropy compensation in protein-ligand interactions. *Protein Sci.* **2011**, *20*, 1607–1618.
- (39) Reynolds, C. H.; Holloway, M. K. Thermodynamics of ligand binding and efficiency. *ACS Med. Chem. Lett.* **2011**, *2*, 433–437.
- (40) Du, X.; Li, Y.; Xia, Y.-L.; Ai, S.-M.; Liang, J.; Sang, P.; Ji, X.-L.; Liu, S.-Q. Insights into Protein-Ligand Interactions: Mechanisms, Models, and Methods. *Int. J. Mol. Sci.* **2016**, *17*, 144.












### 3.3 Publication III

#### **Targeting a protein epitope: Specific inhibition of the Survivin-CRM1-interaction by peptide-modified Molecular Tweezers**

Survivin's dual function as an apoptosis inhibitor and a regulator of cell proliferation is mediated via its interaction with the export receptor CRM1. Thus, this protein-protein interaction represents an attractive target in cancer research and therapies. Here we report a novel strategy to inhibit this PPI by addressing specific supramolecular tweezers towards Survivin's nuclear export signal, the binding site of CRM1. We used docking guided design to develop peptides enhancing the tweezer's ability to shield the NES. Binding of the tweezer molecules to Survivin and interference on the PPI were shown via ITC and pull-down experiments. Detailed information of the tweezer's binding site was gained by NMR titration experiments, strongly supported by MD and QM/MM calculations, and further substantiated by fluorescence anisotropy. Hence, with the newly developed peptide-modified tweezers a supramolecular inhibitor of the CRM1-Survivin interaction is available which is of great interest since it might lead to a loss of both functions in apoptosis and mitosis.

Material from: Meiners, A., Bäcker, S., Hadrović, I. et al. Specific inhibition of the Survivin–CRM1 interaction by peptide-modified molecular tweezers. *Nature Communications*, published 2021. Copyright 2021 Springer Nature (CC BY). Available at: <https://www.nature.com/articles/s41467-021-21753-9>

# Specific inhibition of the Survivin–CRM1 interaction by peptide-modified molecular tweezers

Annika Meiners<sup>1,6</sup>, Sandra Bäcker <sup>1,6</sup>, Inesa Hadrović<sup>2,6</sup>, Christian Heid<sup>2,6</sup>, Christine Beuck <sup>3</sup>, Yasser B. Ruiz-Blanco<sup>4</sup>, Joel Mieres-Perez <sup>4</sup>, Marius Pörschke <sup>3</sup>, Jean-Noël Grad<sup>5</sup>, Cecilia Vallet<sup>1</sup>, Daniel Hoffmann <sup>5</sup>, Peter Bayer <sup>3</sup>, Elsa Sánchez-García <sup>4,7</sup>✉, Thomas Schrader <sup>2,7</sup>✉ & Shirley K. Knauer <sup>1,7</sup>✉

Survivin's dual function as apoptosis inhibitor and regulator of cell proliferation is mediated via its interaction with the export receptor CRM1. This protein–protein interaction represents an attractive target in cancer research and therapy. Here, we report a sophisticated strategy addressing Survivin's nuclear export signal (NES), the binding site of CRM1, with advanced supramolecular tweezers for lysine and arginine. These were covalently connected to small peptides resembling the natural, self-complementary dimer interface which largely overlaps with the NES. Several biochemical methods demonstrated sequence-selective NES recognition and interference with the critical receptor interaction. These data were strongly supported by molecular dynamics simulations and multiscale computational studies. Rational design of lysine tweezers equipped with a peptidic recognition element thus allowed to address a previously unapproachable protein surface area. As an experimental proof-of-principle for specific transport signal interference, this concept should be transferable to any protein epitope with a flanking well-accessible lysine.

<sup>1</sup>Department of Molecular Biology II, Centre for Medical Biotechnology (ZMB), University of Duisburg-Essen, Essen, Germany. <sup>2</sup>Institute of Organic Chemistry I, Faculty of Chemistry, University of Duisburg-Essen, Essen, Germany. <sup>3</sup>Department of Structural and Medicinal Biology, Centre for Medical Biotechnology (ZMB), University of Duisburg-Essen, Essen, Germany. <sup>4</sup>Department of Computational Biochemistry, Centre for Medical Biotechnology (ZMB), University of Duisburg-Essen, Essen, Germany. <sup>5</sup>Department of Bioinformatics and Computational Biophysics, Centre for Medical Biotechnology (ZMB), University of Duisburg-Essen, Essen, Germany. <sup>6</sup>These authors contributed equally: Annika Meiners, Sandra Bäcker, Inesa Hadrović, Christian Heid. <sup>7</sup>These authors jointly supervised this work: Elsa Sánchez-García, Thomas Schrader, Shirley K. Knauer. ✉email: [elsa.sanchez-garcia@uni-due.de](mailto:elsa.sanchez-garcia@uni-due.de); [thomas.schrader@uni-due.de](mailto:thomas.schrader@uni-due.de); [shirley.knauer@uni-due.de](mailto:shirley.knauer@uni-due.de)

Protein–protein interactions (PPIs) have enormous importance for numerous biological processes, and are relevant to understand protein function, assembly, and communication. Today, large efforts and resources are focused on unveiling the wide interactome between more than 200,000 human proteins encoded in our genome<sup>1</sup>. The deliberate modulation of PPIs with external agents opens opportunities to study biological mechanisms and to interfere with pathological processes<sup>1,2</sup>.

However, interfaces between proteins are very difficult targets for molecular recognition since such interfaces are usually large (>1000 Å<sup>2</sup>), well solvated, and display a rugged topology<sup>3</sup>. Thus, until today interfering molecules have in most cases been identified by extensive library screening.

Supramolecular chemistry provides orthogonal artificial elements for protein recognition and, in combination with computational modeling, allows a deeper understanding of the underlying non-covalent interactions<sup>4</sup>. Inter alia, calixarenes<sup>5</sup>, cucurbiturils<sup>6</sup>, molecular tweezers<sup>7</sup>, and GCP motifs<sup>8</sup> recognize well-solvated amino acid residues on protein surfaces and have been successfully used to target protein surfaces and to interfere with PPIs<sup>9–13</sup>. On the same protein, i.e., ubiquitin, a recent comparative study revealed that these host molecules occupy different areas and seem to exhibit complementary recognition profiles<sup>14</sup>.

Despite these promising features and first applications in cells and animals, the selective recognition of protein elements by supramolecular host systems remains highly challenging. A few recent examples include synthetic ligands for peptide motifs on proteins<sup>15</sup> and for a specific protein context<sup>16,17</sup>.

We here present an advanced approach by combination of a supramolecular host molecule with a well-defined biomolecular interaction. This ditopic hybrid allows us to complex a single critical amino acid together with its direct environment on the protein surface, which leads to powerful competition with the natural binding partner. Specifically, we generate a covalent conjugate between a lysine-selective molecular tweezer and a self-complementary peptide and target a critical interface important for the survival of cancer cells, i.e., the nuclear export signal (NES), located on an ordered but somewhat dynamic loop on the Survivin surface.

Survivin is mostly absent in normal resting adult tissues, but highly upregulated in almost all cancer types<sup>18,19</sup>. Its overexpression is associated with resistance against chemo- and radiotherapy, frequent recurrences, and a decreased patient survival<sup>20–23</sup>. Despite its small size (142 aa, 16.5 Da) and its lack of enzymatic activity, Survivin is fulfilling a well characterized dual role within the cell<sup>24</sup>. As the smallest member of the inhibitor of apoptosis protein family, Survivin on the one hand plays a role in counteracting programmed cell death. As part of the chromosomal passenger complex (CPC), Survivin is on the other hand crucial for mitotic regulation promoting cell proliferation<sup>25</sup>. For both functions, an interaction with the nuclear export receptor CRM1 mediated by Survivin's highly conserved, leucine-rich NES is pivotal<sup>26–28</sup>. Thus, interference with the Survivin–CRM1 interaction can inhibit cancer cell proliferation.

The development of a small molecule, which specifically binds to the NES on Survivin's surface, would represent a valuable approach to inhibit the Survivin–CRM1 interaction. This is a challenge for supramolecular chemistry: can we direct an amino acid-selective host molecule to the functionally relevant epitope on Survivin by combining it with a recognition unit for the NES? This key region is located on an ordered loop and flanked by well-accessible basic amino acids, K90/91 and K103/R106. We therefore designed supramolecular tweezers that only target lysine (Lys) and arginine (Arg) residues and that are equipped with a compact binder to the natural dimer interface overlapping with the NES.

Molecular tweezers possess a torus-shaped arrangement of alternating benzene and norbornadiene rings, which form an

electron-rich unpolar cavity—ideally suited to pull the cationic side chains of Lys and Arg inside. Two (hydrogen)phosphate groups lock the included side chain in an ion pair<sup>29</sup>. This unique binding mechanism operates well under physiological conditions and has already been exploited for protease inhibition<sup>30,31</sup>, prevention of protein aggregation<sup>32,33</sup>, and modulation of PPIs on shallow grooves<sup>7,34</sup>. In order to turn these molecular tools into specific Survivin ligands, it was necessary to identify a binding motif for the NES region and to develop a synthesis for efficient tweezer monofunctionalization. This would allow us to attach the NES binder covalently to the tweezer and generate the desired ditopic ligand.

In this work, we thus rationally equipped molecular tweezers for lysine and arginine with small peptides resembling the natural dimer interface in order to shield the NES from binding of cognate receptor CRM1. We demonstrate and rationalize the binding of the tweezers to Survivin and the interference with this critical PPI via several biochemical methods combined with molecular dynamics (MD) simulations and multiscale computational studies. Indeed, conjugation of an elongated peptide sequence (ELTLGEFL) outmatched a shorter and a scrambled, unselective peptide with regard to binding and inhibition potential. As such, with our rationally developed peptide-modified tweezers, specific supramolecular inhibitors of so far not easily targetable protein surface structures are now available.

## Results

**Development of peptide-modified molecular tweezers.** In the absence of other binding partners, the monomer–dimer equilibrium of Survivin lies on the dimer side; the functional interface (<sup>93</sup>FEELTLGEFL<sup>102</sup>) between both protomers is self-complementary with the hydrophobic interactions of entangled leucines playing a crucial role<sup>35,36</sup>. Intriguingly, this interface largely overlaps with Survivin's NES (<sup>89</sup>VKKQFEELTL<sup>98</sup>). Hence, peptide fragments from the dimer interface (Fig. 1 a) are ideal candidates for the desired additional recognition unit. We therefore selected a short (<sup>95</sup>ELTL<sup>98</sup>) and an elongated peptide (<sup>95</sup>ELTLGEFL<sup>102</sup>) taken directly from this dimer interface (Fig. 1b–e). A synthetic strategy employing click chemistry was envisaged for monovalent tweezer functionalization, involving the esterification of one tweezer phosphate with a butynyl ester and introduction of an N-terminal azidoglycine into the peptide (Fig. 2). Using computational modeling, we identified K103 at the beginning of Survivin's C-terminal α-helix as a well-suited anchor for the tweezers with K90/91 as potential alternatives.

**Synthesis of peptide-modified molecular tweezers.** The peptide tweezer hybrid molecules became synthetically accessible by a sophisticated general strategy: first, an alkyne ester group was introduced to only one phosphate in the parent tweezer (TW, formerly named CLR01)<sup>37</sup>. This monofunctionalization relies on activation of the free phosphoric acid by trichloroacetonitrile followed by nucleophilic attack of butynol, which occurs only once if the reaction is carried out in pyridine. Second, an N-terminal azide group is attached to the peptide with azidoglycine. After cleavage of the peptide from the resin, both components are finally subjected to the standard conditions of a click reaction under Cu-I catalysis (water/THF). No protecting groups are needed on tweezer or peptide, so that the reaction product may be directly purified by preparative HPLC (Fig. 2).

For NES recognition, the peptide ELTL and the elongated peptide ELTLGEFL, which are resembling the natural dimer interface and thus are complementary to the partially overlapping NES of Survivin, were both synthesized by solid phase peptide synthesis (SPPS) with an N-terminal azidoglycine (Azac-peptides,

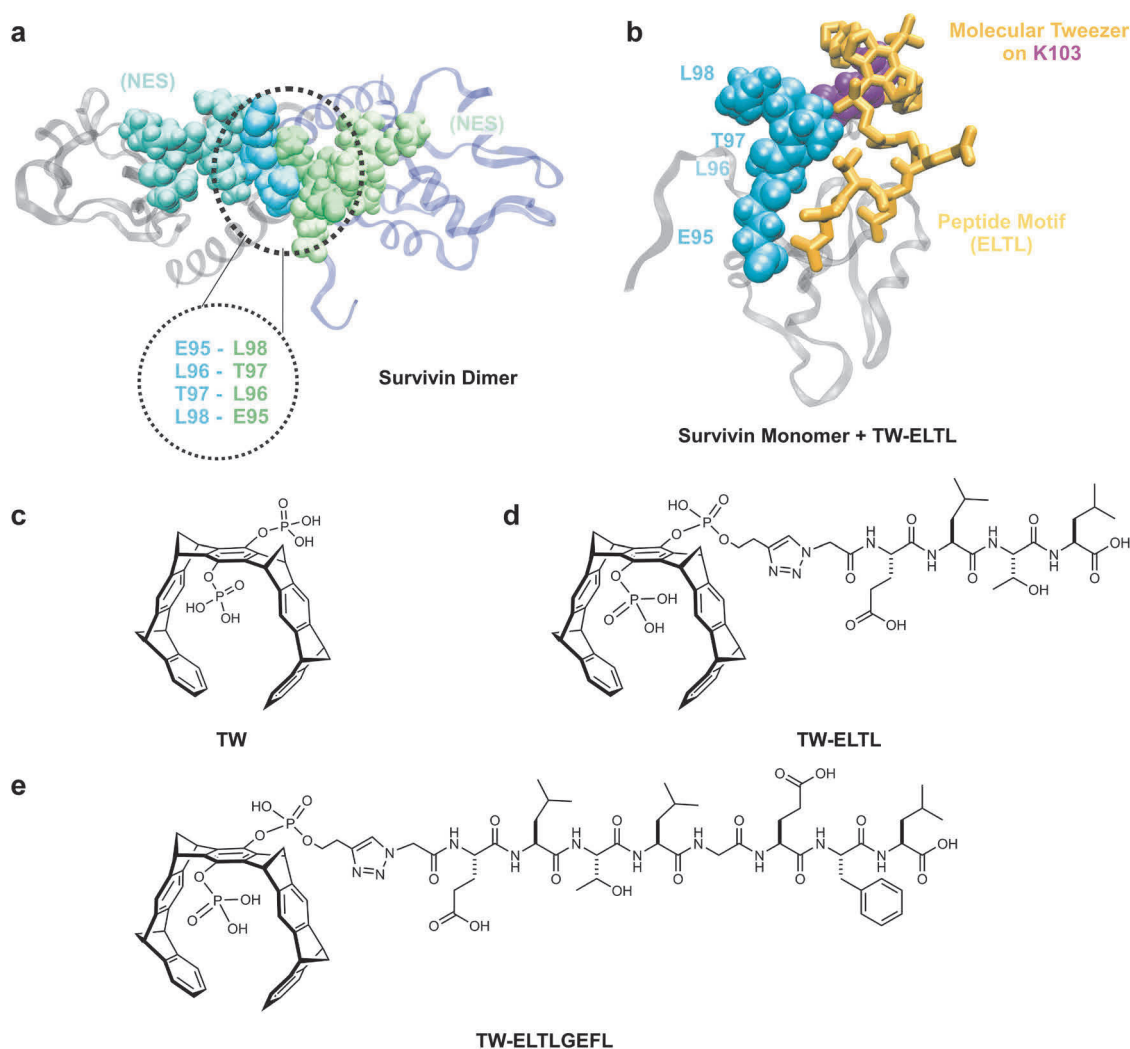


**Fig. 1** Design of peptide-modified supramolecular tweezers. **a** Representation of Survivin's dimer interface based on PDB-ID: 1XOX [<https://www.rcsb.org/structure/1xox>]<sup>38</sup>. Both monomers, depicted in blue and gray, mainly interact via the ETLT sequence (contact region of both monomers overlapping with the NES, represented in cyan and green). This sequence was chosen as second binding motif for the peptide-modified tweezer molecules. **b** Representation of TW-ELTL (shown in **d**) bound to Survivin. TW-ELTL (yellow) binds the anchor lysine residue K103 (violet) on Survivin's surface while the peptide motif ETLT (yellow) interacts with the ETLT region of the Survivin monomer (cyan). This is the same region of the dimer interface represented in Fig. 1a, overlapping with the NES (cyan). The chemical structures of the unmodified tweezer molecule TW (**c**), an asymmetrical tweezer molecule linked to the short peptide ETLT (TW-ELTL) (**d**), and an asymmetrical tweezer molecule linked to the elongated peptide ETLTGEFL (TW-ELTLGEFL) (**e**) are depicted.

SI1). Subsequently, peptide and monobutynyl tweezer were coupled in a THF/water solvent mixture with ascorbic acid and  $\text{CuSO}_4 \cdot 5 \text{H}_2\text{O}$ . Both click reactions proceeded smoothly and gave the coupling products in good yields and excellent purity after HPLC purification (SI2). In addition, FAM-labels were introduced into the peptide-modified tweezers via a C-terminal (Fluorescein-labeled lysine)-glycine dipeptide fragment (SI3).

Reaction monitoring was facilitated by the appearance of additional  $^1\text{H}$  NMR signals at 5.2 ppm ( $\text{CH}_2$ -triazole) and 8.0 ppm ( $\text{CH}_{\text{arom}}$ ) indicative of triazole formation. The final peptide tweezers displayed very good water solubility, because they carry multiple negative charges both in the tweezer and in the peptidic part. No self-inclusion of the tweezer moieties was observed in the form of potential upfield shifts in the  $^1\text{H}$  NMR spectra, also ruling out the formation of unproductive tweezer dimers (SI2).

**Characterization of binding by isothermal titration calorimetry.** The interaction between the tweezers and Survivin was studied by isothermal titration calorimetry (ITC) and NMR

spectroscopy. So far, the only published NMR structure originated from a truncated Survivin (aa 1-120) with improved solubility<sup>38</sup>. Indeed, MD simulations of full-length Survivin revealed a highly flexible C-terminal  $\alpha$ -helix fragment around residue 120 (SI4), which might explain poor expression of the full-length protein. Since the truncated construct still contains all relevant parts of the protein and gives excellent NMR spectra (SI5), we chose it for all our in vitro experiments and denote it as Survivin120 in the following results.

ITC titration of Survivin120 to the tweezers resulted in exothermic binding isotherms (Fig. 3) with dissociation constants  $K_D$  of 38  $\mu\text{M}$  for the unmodified tweezer TW, 24  $\mu\text{M}$  for TW-ELTL as well as a  $K_D$  of 19  $\mu\text{M}$  for TW-ELTLGEFL. These values are in good agreement with the unmodified tweezer TW (formerly CLR01) affinity toward lysine ( $K_D$  17  $\mu\text{M}$ )<sup>39</sup>. Fitting the ITC titrations with Survivin120 to a one set of sites model allowed us to derive all relevant thermodynamic data including stoichiometries and changes in Gibbs free energy (G), enthalpy (H), and entropy (S) as summarized in a supplementary table (SI7). Importantly, the unmodified tweezer produced a

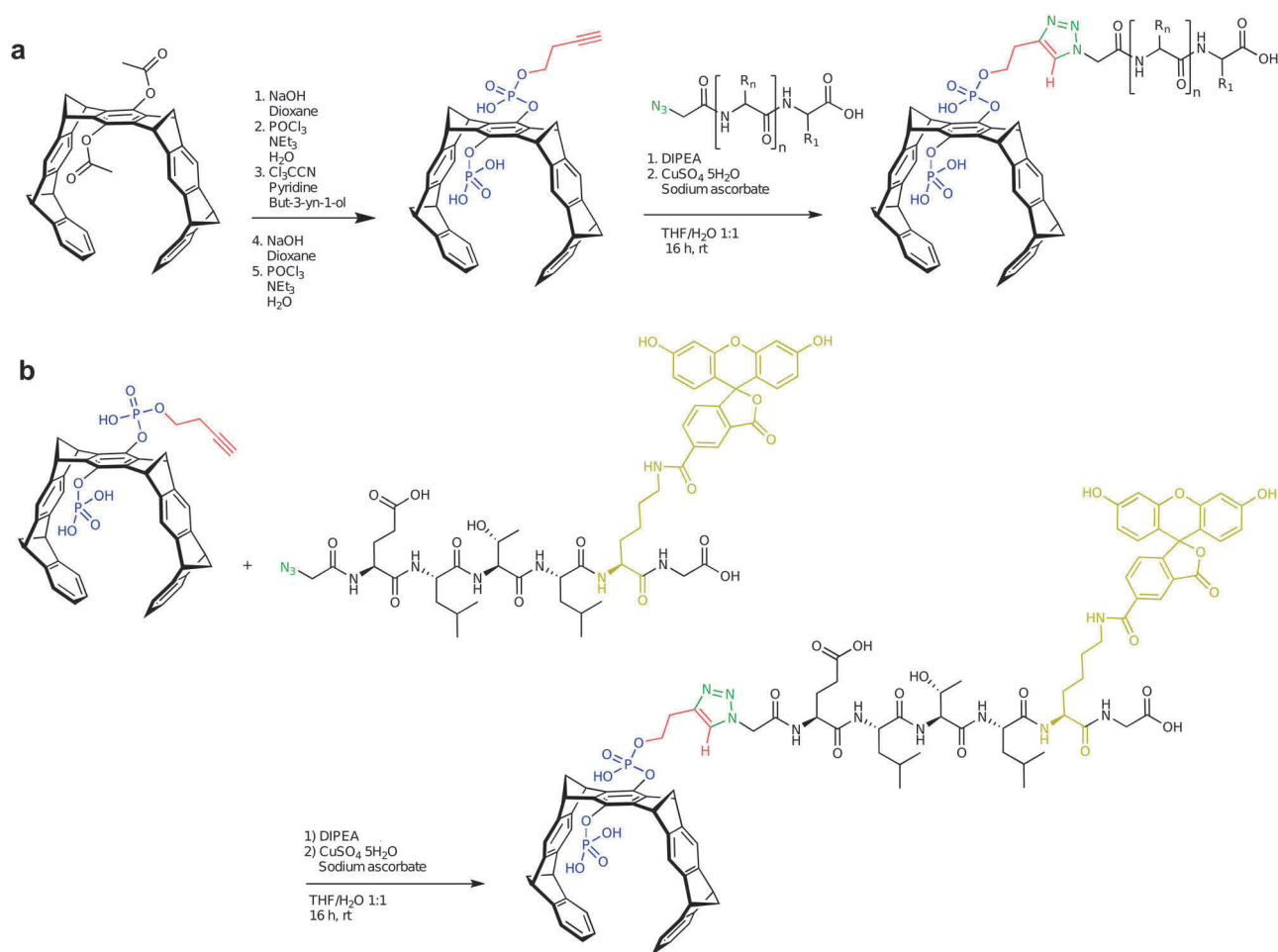


**Fig. 2 Synthetic strategy leading to monofunctionalized molecular tweezers.** **a** Introduction of one butynyl phosphate ester arm on the parent diacetox tweezers (TCA coupling) followed by click chemistry with N-terminal azidopeptide; **b** additional introduction of a fluorescence label by adding a C-terminal Lys<sup>FAM</sup>-Gly sequence to the clicked peptide. Blue: phosphate; red: alkyne/triazole; green: azide/triazole; olive: FAM label. DIPEA N,N-diisopropylethylamine, THF tetrahydrofuran.

20:1 stoichiometry (correlating well with 16 accessible lysine and arginine residues in Survivin120), whereas the modified tweezers displayed 2:1 ligand/protein ratios. This stoichiometry might be plausible with regard to the antiparallel orientation of the Survivin monomers in the respective homodimer, probably allowing the conjugated peptides to also align in both directions with the tweezers either binding to one or the other neighboring anchor lysine. In addition, we carried out reverse titrations by adding increasing amounts of unmodified tweezers TW vs. TW-ELTL into a constant concentration of Survivin (SI8). Interestingly, a sharp kink was produced at a 4–5-fold tweezers excess in both cases, indicating that 4–5 tweezers molecules can be accommodated on the protein surface. However, further addition of unmodified tweezers produced a second substantial exothermic titration step, indicating further unspecific binding to accessible lysine and arginine residues, while the peptide tweezers had already almost reached saturation. Due to the biphasic character these binding curves do not allow the determination of binding constants. However, our data indicate that the introduction of a peptide mimicking Survivin's natural dimer interface enhanced the tweezers affinity toward Survivin only slightly, but greatly increased its regioselectivity. Although the dimer stability of Survivin120 is not known, it likely represents the binding partner for all tweezers, because apart from the NES region V89-L102 some remote residues P4-W10 contribute additional, mostly aromatic, interactions. Even in the dimer, however, the self-

complementary peptide loops (V89-L102) are dynamic and can be expected to expose the NES region temporarily (see discussion of the simulations below).

**Mapping tweezers binding sites by NMR.** To map tweezers binding to distinct amino acid residues of Survivin, we performed NMR titrations adding tweezers up to equimolar amounts to <sup>15</sup>N-labeled Survivin120 (SI5). Binding of a ligand causes signal shifts and often reduced signal intensities for the residues involved in the interaction (Fig. 4). Titration of the unmodified tweezers resulted in reduced signal intensities and shifts around the basic amino acids K91, K103, and R106 (Fig. 4a, b). K90 also lies in the regions identified; however, it is not assigned in the spectrum. In addition, signal intensities decrease in the same regions (Fig. 4d) confirming these as potential tweezers binding sites. Unfortunately, the applied NMR method does not allow us to differentiate between tweezers binding to residues K90 vs. K91 and K103 vs. R106 since they are in too close proximity. Titration of TW-ELTL (Fig. 4c, d) as well as TW-ELTLGEFL (Fig. 4e, f) decreased signal intensities in this region even more and enhanced signal shifts for the same basic residues. In addition, the NES residues between K91 and K103 experienced an intensity loss and significant signal shift when the peptide-linked tweezers were binding in contrast to the unmodified tweezers. This shows that the peptides indeed contact the NES region and confirms the desired regioselectivity of the tweezers

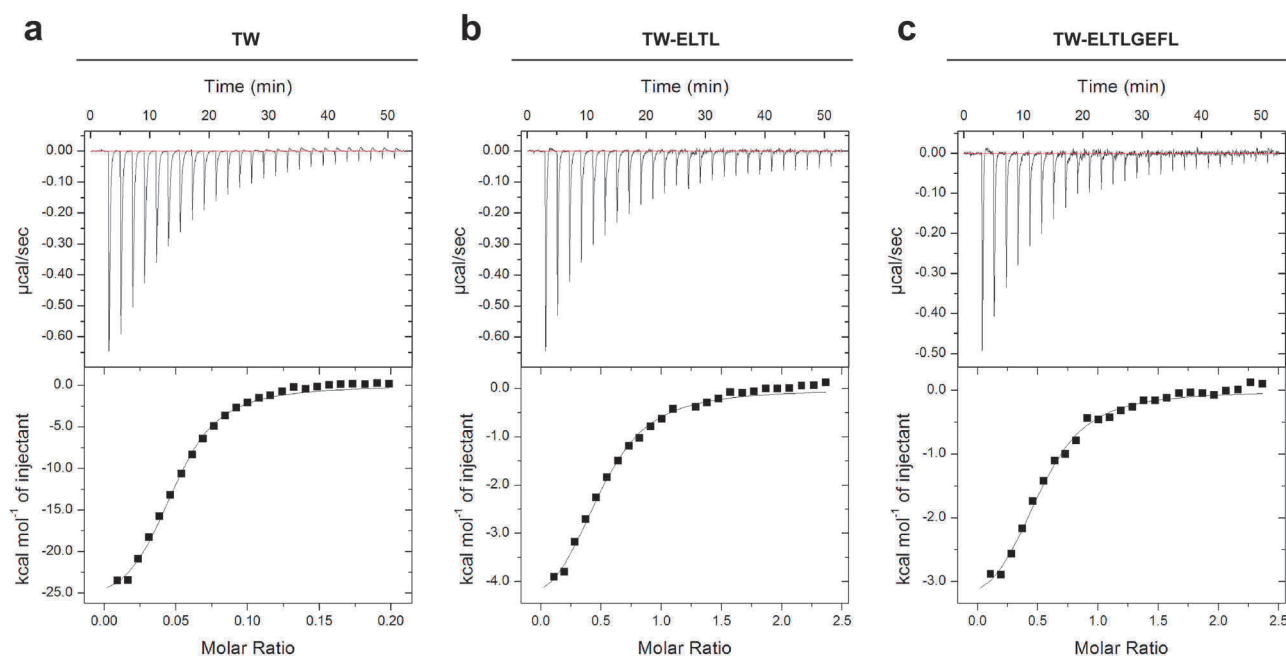


**Fig. 3 Evidence for tweezer binding to Survivin120 from ITC measurements.** Titration of 300  $\mu\text{M}$  TW (a) in the cell with 300  $\mu\text{M}$  Survivin120 in the syringe. Titration of 100  $\mu\text{M}$  TW-ELTL (b) and TW-ELTLGEFL (c) in the cell with 1.2 mM Survivin120 in the syringe. All titrations were performed in PBS, pH 7.4 at 25  $^{\circ}\text{C}$ . The black lines in the bottom panels are the best fit of the data to a one set of sites model. The heat of dilution was subtracted as constant. Dissociation constants were determined to be  $38 \pm 4 \mu\text{M}$  for TW,  $24 \pm 4 \mu\text{M}$  for TW-ELTL and  $19 \pm 3 \mu\text{M}$  for TW-ELTLGEFL. Values reported are the mean  $\pm$  SEM of the fit. For thermodynamic parameters see SI7. Source data are provided as a Source Data file.

conjugate on Survivin's surface. The overall line shape of the HSQC spectra indicates that Survivin120 likely remains dimeric upon tweezer binding. If the dimer would dissociate upon ligand binding, a sharpening of the signals and thus an intensity increase would occur due to slower T2 relaxation. Rather the contrary is observed, especially at ligand:protein ratios  $>1:1$ , which indicates beginning aggregation. Nevertheless, anchoring the peptide-tweezers nearby the NES with direct peptide-NES interactions is expected to shield the natural binding site and significantly weaken the Survivin-CRM1 interaction.

For a better understanding of the complexation process, we performed MD and Gaussian accelerated molecular dynamics (GaMD) simulations as well as quantum mechanics/molecular mechanics (QM/MM) calculations (see SI10 for computational details). TW-lysine interactions were calculated in the Survivin120 monomer (protomer A, structure with PDB-ID 1XOX [<https://www.rcsb.org/structure/1xox>])<sup>38</sup>. The monomer, unlike the dimer structure, displays an exposed NES region, which is a key feature for the activity of Survivin. Thus, it represents the most suitable model to study the interactions of the tweezers with the lysine residues in this region. Four well-accessible lysine residues (K23, K90, K91, and K103) were selected on the monomeric protein for an in-depth characterization of their binding mode with TW as well as TW-ELTL. MD and GaMD simulations evidenced interactions of the peptide-modified tweezers with Survivin120 via the peptide moieties (SI12, Table 1, and Fig. 5). Due to the lack of the peptide motif, such interactions cannot be established by the bishydrogenphosphate-substituted tweezer TW. Since the inclusion complexes of lysine with TW and TW-ELTL otherwise display remarkably similar structural features (SI13), we can assume that the additional interactions found in the peptide-modified tweezers contribute to their improved selectivity toward K103/K91. We quote these interactions as dynamic because of the lack of a highly conserved binding pose of the peptide fragment.

Interestingly, a conserved interaction between the peptide tail of TW-ELTL and the homologous segment in the protein (<sup>95</sup>ELTL<sup>98</sup>) occurred only when TW-ELTL was encapsulating K103 (SI12). This particular site allows for the antiparallel pairing found in the naturally occurring dimer structure. According to the QM/MM calculations, this site also produced a very stable complex (Table 1 and SI13), which is further stabilized by a salt bridge with R106 (SI14). Therefore, we also performed GaMD simulations of the monomer of Survivin120 and a modified tweezer with the elongated peptide, TW-ELTLGEFL, on K103. At this point, it is important to notice that the above-discussed structural details are in very good agreement with the shift and intensity changes observed by NMR experiments, with one exception: they require an exposed NES region such as in monomeric Survivin. This apparent discrepancy can be rationalized by the conformational flexibility at the weakly associated dimeric NES region. We therefore also performed GaMD simulations of the Survivin120 dimer in an explicit solvent box. The frequency of hydrogen bond formation during the simulation within the dimer interface was analyzed (Fig. 5a, b). The results show that the strongest interaction at the <sup>95</sup>ELTL<sup>98</sup>-region of the dimer interface (involving two hydrogen bonds) has a very low prevalence along the simulation. In the most frequent scenario, no hydrogen bonds are formed, indicating weak and labile interactions between the interface fragments <sup>95</sup>ELTL<sup>98</sup> in both monomers. Not surprisingly, the GaMD simulations also showed that TW-ELTLGEFL is able to form more noncovalent interactions with the NES region than the shorter TW-ELTL. This difference becomes most apparent in the ELTL region of the interface (<sup>95</sup>ELTL<sup>98</sup>) (Fig. 5c). The peptide substituents of the modified tweezers are rather flexible, allowing for frequent interactions with the NES. It seems that the rigid triazole linker acts as an anchor point and facilitates these interactions (SI15)—a synergistic effect between the peptide motif and the (otherwise inactive) linker fragment. As expected, the longer, more flexible

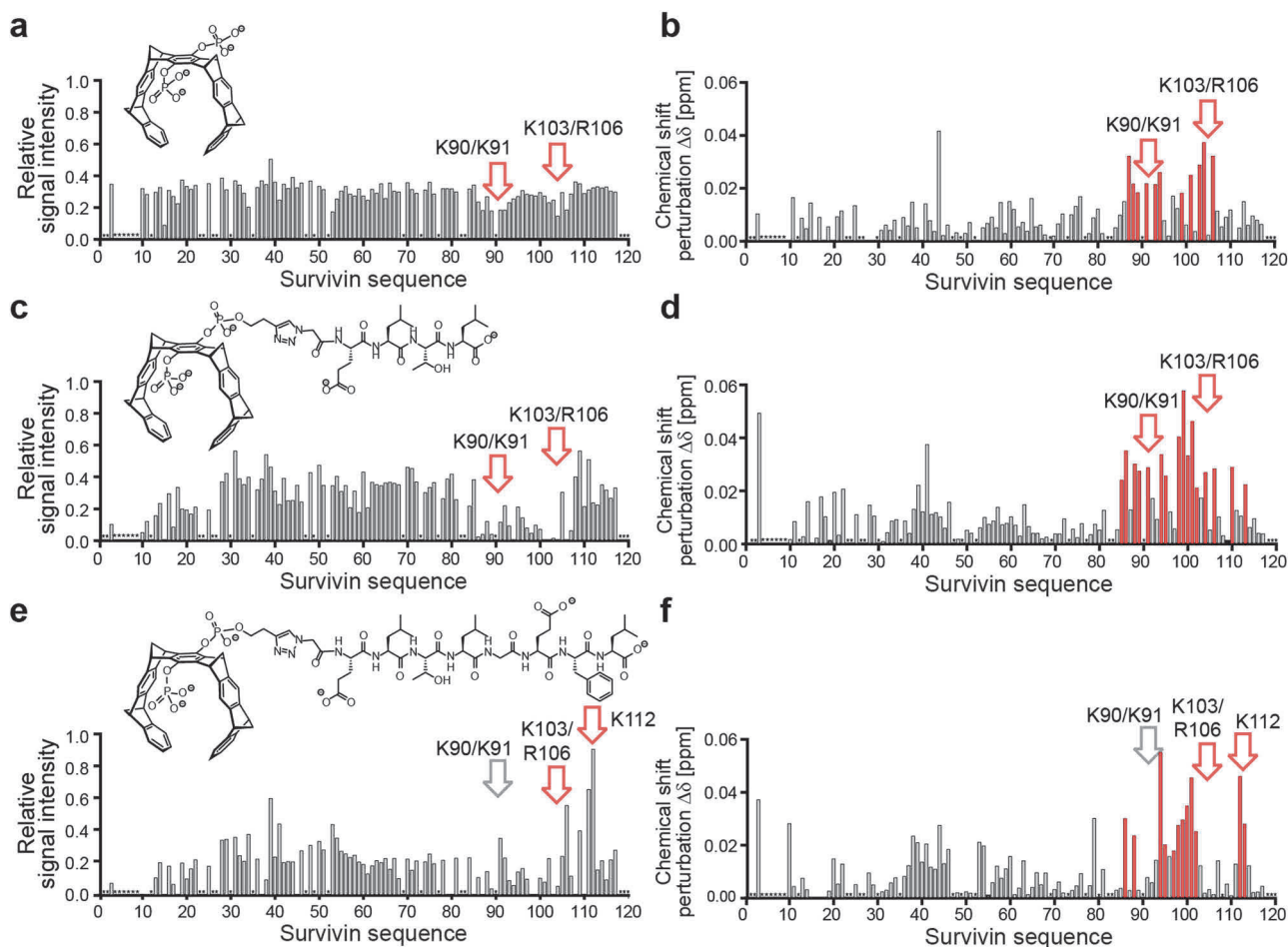


**Fig. 4** NMR chemical shift perturbation and signal intensity analyses allow us to map binding of molecular tweezers to Survivin120. NMR intensity changes and signal shifts of Survivin120 in complex with one equivalent of tweezers compared to Survivin alone plotted against the amino acid sequence. Normalized signal intensities as well as signal shifts for the unmodified tweezer TW (**a**, **b**), TW-ELTL (**c**, **d**), and TW-ELTLGEFL (**e**, **f**) were identified for each signal and plotted against the Survivin sequence (residues 2–117 as assigned in the BMRB data-base). Residues that were excluded from analysis because they are not visible in the spectra or suffer from signal overlap are marked with an asterisk. Residues with a prominent shift or reduced signal intensity (red) are clustered around Survivin’s NES, and lysine and arginine residues are additionally marked with an arrow. Upon titration with TW-ELTL and TW-ELTLGEFL, signal intensities collapse around the NES region. Source data are provided as a Source Data file.

**Table 1** The relative energies of the QM region indicate that the tweezer–lysine complexes are most stable in positions 103 and 91.

TW-ELTL	Relative energy QM region (kcal/mol)
K103	0 ± 1
K91	1 ± 14
K90	27 ± 6
K23	68 ± 3

peptide chain of TW-ELTLGEFL explores a larger conformational space and establishes more attractive interactions with the NES, explaining its superior performance in binding experiments. Our calculations show weak and dynamic interactions at the dimer interface. Such features might be leveraged by the TW-anchored peptide to form contacts with one of the Survivin protomers and, hence, shield the corresponding NES region. Without further structural information we cannot exclude that the peptide might also bind in a way that stabilizes the dimer interface and thus prevents CRM1 from binding a Survivin monomer.

**Tweezer interference with the export complex assembly in vitro.** We next investigated whether tweezers inhibit the Survivin–CRM1 complex formation in vitro. The effects of the unmodified and peptide-linked tweezers were analyzed via pull-down experiments with 293T lysates containing overexpressed HA-tagged Survivin142, recombinant GST-CRM1 as bait protein, and tweezers (Fig. 6). The parent and ELTL-linked tweezer required 10–50 μM to disrupt the Survivin–CRM1 complex. TW-ELTLGEFL was already effective at 1–10 μM and thus turned out to be more potent. In order to provide experimental evidence for the sequence selectivity of the TW-ELTLGEFL ligand, a scrambled analog was synthesized and clicked to the tweezer, resulting in the hybrid molecule TW-LFEEGLLT (S11, S12, and S110). Intriguingly, this ligand was about one order of magnitude less effective than the one bearing the original NES-derived sequence and rather comparable to the unconjugated tweezer TW with regard to the pull-down analyses (Fig. 6a and S118). Moreover, ITC titrations with TW-LFEEGLLT revealed much lower heat changes, and the corresponding  $K_D$  value dropped from  $19 \pm 3$  for TW-ELTLGEFL to  $68 \pm 22$  μM for the scrambled peptide conjugate (S116 and S17). Thus, it displays significantly (~three times) lower affinity toward the wildtype protein, indicating that the correct self-complementary NES sequence is indeed essential

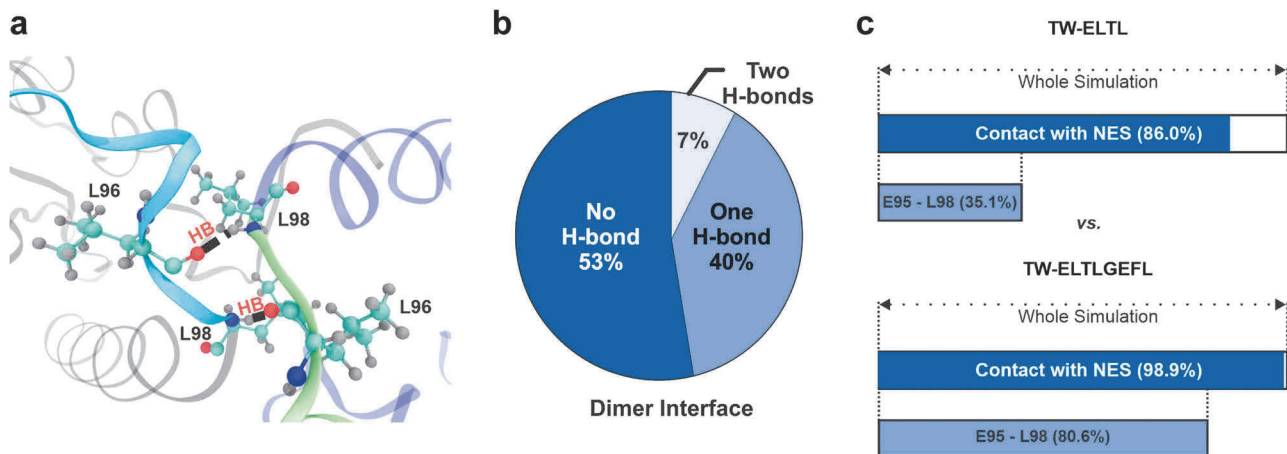


**Fig. 5** GaMD simulations and QM/MM calculations on the tweezers-Survivin interaction provide deeper insights into the binding event. **a** Main hydrogen bonds (HB, red) established between Survivin monomers (gray, violet) at the ETLT interface (contact region of both monomers overlapping with the NES, represented in cyan and green). The leucine residues engaged in these interactions are shown in CPK representation. **b** Occurrence of hydrogen bonds at the dimer interface. **c** Frequency of noncovalent contacts between the tweezers, bound to K103, and the NES as well as with the ETLT region ( $^{95}$ ETLT $^{98}$ ) of the dimer interface.

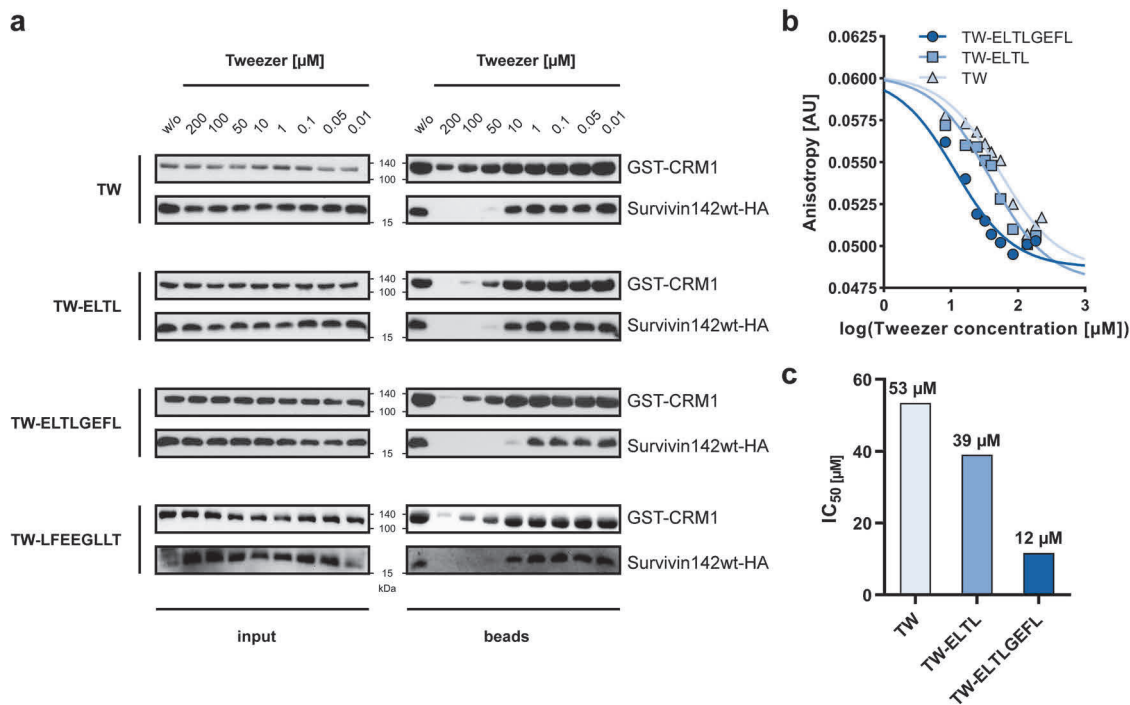


**Fig. 6** The assembly of the export complex is disturbed by unmodified and peptide-linked tweezer molecules. **a** 293T cell lysate with overexpressed Survivin142-HA was preincubated with either unmodified tweezer (TW), TW-ELTL, TW-ELTLGEFL, or a scrambled peptide-modified tweezer, TW-LFEEGLLT, at concentrations ranging from 0.01 to 200  $\mu$ M. GST-CRM1 was mixed with either non- or preincubated cell lysates in the presence of recombinant RanQ69L and dGTP to allow complex assembly. GST-CRM1 and interacting proteins were pulled by GSH-Sepharose beads. Proteins in input and beads samples were analyzed via immunoblotting with antibodies specific for GST or HA. For each tweezer, samples derive from the same experiment and gels/blots were processed in parallel. Direct comparison for this exact concentration range was performed once for TW, TW-ELTL, and TW-ELTLGEFL and for TW-LFEEGLLT in three technical replicates. **b, c** Atto488-labeled Survivin120 was preincubated with CRM1 $_1$ -1062VLV430AAA mutant in a ratio of 1:5 and titrated with supramolecular tweezers up to approx. 180  $\mu$ M. Fluorescence anisotropy was measured ( $n = 1$ ) (**b**), and IC $_{50}$  values were determined from the resulting curves (**c**). TW light blue/ triangles, TW-ELTL blue/squares, TW-ELTLGEFL dark blue/circles. Source data are provided as a Source Data file.

for efficient ditopic recognition. Additional NMR studies demonstrated that the tweezer with the scrambled peptide sequence is still able to bind to the two sites K90/K91 and K103/R106 like the unmodified TW (SI17). However, no large perturbations as for TW-ELTL or TW-ELTLGEFL are observed between residues 91–103, indicating that the peptide moiety does

not form specific contacts with Survivin. Instead, the slight chemical shift perturbations might be due to the spatial proximity of the peptide moiety to the anchoring residue. All those results strongly indicate that the additional binding energy from the NES interface was lost due to scrambling and thus point toward specific recognition as the reason for increased selectivity and



interference with the Survivin–CRM1 interaction. Of note, very high tweezer concentrations (100–200  $\mu\text{M}$ ) also weakened GST–CRM1 binding to GSH-Sepharose beads, most likely by low-affinity binding to the GST protein. However, direct ITC titrations gave only small heat changes and revealed that this interaction is endothermic (SI9).

We also used fluorescence anisotropy experiments to investigate the ability of the tweezer molecules to disrupt the Survivin–CRM1 complex. Atto488-labeled Survivin120 was preincubated with the CRM1\_1-1062VLV430AAA mutant<sup>40</sup> that binds Survivin irrespective of RanGTP and titrated with tweezers. The presence of all tweezers significantly lowered the fluorescence anisotropy, indicating a potent disruption of the Survivin–CRM1 complex (Fig. 6b, c).  $\text{IC}_{50}$  values were determined at 53  $\mu\text{M}$  for the unmodified tweezer, 39  $\mu\text{M}$  for TW-ELTL, and 12  $\mu\text{M}$  for TW-ELTLGEFL. Thus, pull-down and fluorescence anisotropy experiments both indicated that the peptide modification increases the inhibitory potential of the tweezers for the Survivin–CRM1 interaction.

**Confirmation of the tweezer binding site.** If the tweezer-based inhibitors indeed bind to lysines/arginines flanking the NES (K90, K91, K103, R106), their mutation to, e.g., threonine, should abolish the observed effects. For this reason, we generated double and triple Survivin120 mutants lacking these putative tweezer anchor points. Unfortunately, most double mutants and especially the triple mutants were unfolded as evidenced by 1D  $^1\text{H}$  NMR (SI6); finally, the correctly folded double threonine mutant Survivin120 K90/103T was chosen for further investigation. Indeed, ITC titrations with this mutant revealed lower tweezer affinities (dissociation constants  $K_D$  of  $49 \pm 5 \mu\text{M}$  for the unmodified tweezer TW,  $50 \pm 10 \mu\text{M}$  for TW-ELTL, and  $36 \pm 10 \mu\text{M}$  for TW-ELTLGEFL) and 1:1 stoichiometries for the peptide-modified tweezers (Fig. 7a–c and SI7). Next, binding of FAM-labeled tweezers (SI3) to either Survivin120 wildtype or the K90/103T mutant was studied by fluorescence anisotropy (Fig. 7d–f). For Survivin120 wildtype, the affinities correspond well to those values obtained from the initial ITC titrations: TW-FAM  $K_D$  of  $27 \pm 2 \mu\text{M}$ , TW-ELTL-FAM  $K_D$  of  $26 \pm 2 \mu\text{M}$ , and TW-ELTLGEFL-FAM  $K_D$  of  $5 \pm 0.5 \mu\text{M}$  (potential stabilizing influence of the FAM unit). Binding to the Survivin120 K90/103T mutant, however, was strongly impaired ( $K_D$  values of  $240 \pm 20$ ,  $240 \pm 20$  and,  $92 \pm 5 \mu\text{M}$ ). We conclude that lysines 90 and 103 are indeed essential for efficient tweezer binding.

Next, we investigated whether tweezer inhibition of the export complex assembly is compromised upon lysine mutations near the NES. Therefore, pull-down experiments were performed with recombinant GST-tagged Survivin120 wildtype and K90/103T as bait proteins, tweezers, recombinant CRM1 and RanQ69L (Fig. 7g). Controls lacking the Survivin baits were included, as well as isolated peptides without tweezer (Fig. 7h). In these experiments, both tweezer peptide conjugates potentially inhibited the interaction between CRM1 and GST–Survivin120; in sharp contrast, the parent tweezer TW and uncoupled peptides were all inactive. However, for the double lysine mutant GST–Survivin120–K90/103T even the tweezer conjugates lost most of their inhibitory power toward the essential Survivin–CRM1 interaction. This is an important control: it indicates that the tweezer conjugates address specific lysine residues in Survivin’s NES and thus shield it against CRM1.

## Discussion

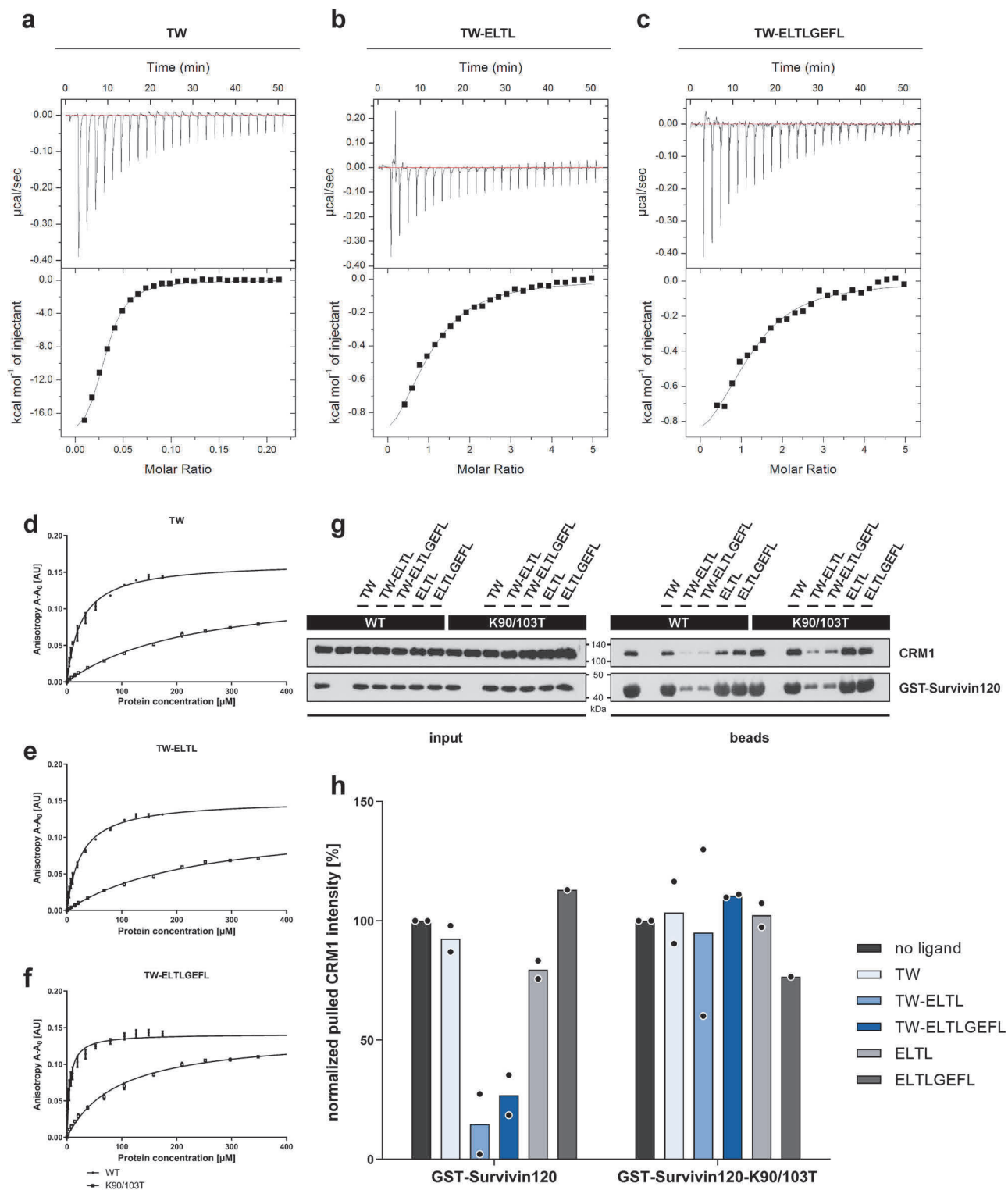
Inhibition of the essential Survivin–CRM1 interaction is of great interest because it regulates cell proliferation and mediates a cytoprotective function<sup>27,30</sup>. However, the development of CRM1 binders bears the disadvantage that it affects a large number of cargo

proteins and is therefore not specific for Survivin. Here, we present prototypes for an alternative strategy: to address Survivin’s NES with specific supramolecular tweezer conjugates, which dock onto the overlapping natural dimer interface on Survivin’s protein surface with low micromolar affinities. This alternative is now accessible by click reactions from an alkyne-modified parent tweezer. We emphasize that this synthetic strategy greatly expands the design of modified tweezers, because it can be applied to tweezers with one or two phosphate arms and is not restricted to peptides. Virtually any additional functional unit can now be attached to the tweezers by click chemistry: fluorescence labels, chemically reactive groups, peptidic and other recognition units, Au nanoparticles (via C-terminal cysteines), and scaffolds with various alkynes for multivalency have already been introduced<sup>37,41</sup>. This functionalization synthetic strategy now opens up a pioneering class of advanced tweezer derivatives with two or more functions.

Moreover, as a proof-of-principle, our experiments confirm that binding of peptide-equipped tweezers occurs in Survivin’s NES region overlapping with the dimer interface and therefore impairs the interaction with CRM1. To the best of our knowledge, this is the so far sole successful example that an amino acid binder (lysine tweezer) is directed to a specific epitope of a protein—in our case by conjugation to the self-complementary dimer interface comprising the NES sequence. The underlying rational design was supported by ITC titrations and NMR spectroscopy that produced maximum chemical shift perturbations on four lysine/arginine residues flanking the NES. Detailed MD and GaMD simulations complemented with QM/MM calculations revealed K103 as a preferred binding site and supported that even in the dynamic dimer the NES signal is partially exposed to approaching ligands. Pull-down experiments and fluorescence anisotropy titrations both indicated that the peptide modification indeed increases the inhibitory potential and specificity of the tweezers for the Survivin–CRM1 interaction. Importantly, a tweezer molecule equipped with a scrambled peptide motif was significantly less effective with regard to binding and inhibition of the relevant Survivin–CRM1 interaction. Again, this points toward a specific recognition as the origin for increased selectivity of our hybrid ligand. Finally, a double lysine mutant of Survivin (K90/103T) further substantiated the identified binding sites, because here the potent tweezer conjugates lost most of their inhibitory potential (ITC, pull-down, FT). Our sophisticated synthetic approach allows the formation of labeled tweezer peptide conjugates for advanced binding experiments, which may also find applications in fluorescence imaging.

Even though the peptide modification increased the ability of the tweezers to shield the NES, it had only moderate impact on the binding affinity. Obviously, additional binding energy must be generated by tailored recognition units incorporated into the tweezer conjugates. A second tweezer unit at the opposed end of the peptide may serve this purpose, or alternatively more powerful supramolecular NES binders of synthetic or natural origin.

In this study, we established that a supramolecular amino acid binder can be designed for an exposed surface epitope on a given protein target. Our strategy involves the combination of a lysine-selective tweezer with a peptidic recognition element for the desired binding epitope. This was accomplished by trichloroacetone nitrile-assisted monoesterification of a single tweezer phosphate with butynol and subsequent click reaction with an azide-modified peptide without the need of any protecting group. Attachment of a single peptide arm renders the hybrid tweezer selective for the peptide loop representing the NES in Survivin which is self-complementary and flanked by well-accessible lysine residues. The design was guided by MD and GaMD simulations as well as QM/MM calculations of the putative tweezer–protein complexes. Structural evidence was provided by 2D NMR



spectroscopy, affinities were determined by ITC titrations. The hybrid tweezers were able to disrupt the essential complex between Survivin and its export receptor CRM1 in cell lysates as demonstrated with pull-down assays and in vitro as shown by fluorescence anisotropy measurements. Labeled tweezer hybrids revealed strongly diminished affinities to a Survivin double mutant that lacked the NES-flanking lysines and confirmed the selectivity for the respective epitope on Survivin. We thus accomplished the proof-of-principle of epitope targeting by supramolecular binders. Further optimization should improve the

performance of our ligands by, e.g., by replacing the peptide unit resembling the natural dimer interface of Survivin with much more powerful interaction partners from the CPC, such as Borealin fragments. Alternatively, we plan to employ dimeric tweezers with an internal peptide unit—in order to exploit two attachment sites to the NES region. Lysine 90 and 103 have been proven very well suited for this purpose and work into this direction is underway in our laboratory.

In the future, supramolecular inhibition of the CRM1–Survivin interaction should be transferred into the cellular context in order

**Fig. 7 Lysine to threonine mutations near Survivin's NES and dimer interface reduce tweezer affinity and impair its inhibitory effect on the Survivin-CRM1 interaction.** Titration of 300  $\mu\text{M}$  TW (a) in the cell with 321  $\mu\text{M}$  Survivin120 K90/103T in the syringe. Titration of 100  $\mu\text{M}$  TW-ELTL (b) and TW-ELTLGEFL (c) in the cell with 2.5 mM Survivin120 K90/103T in the syringe. All titrations were performed in PBS, pH 7.4 at 25 °C. Graphs represent one representative example each from three independent experiments ( $n = 3$ ). The black lines in the bottom panels are the best fit of the data to a one set of sites model. The heat of dilution was subtracted as constant. For thermodynamic data derived from the graphs see SI7. FAM-labeled unmodified tweezer molecule (d), TW-ELTL (e), and TW-ELTLGEFL (f) (0.2  $\mu\text{M}$ ) were titrated with either Survivin120 (200  $\mu\text{M}$ , circles) or Survivin120 K90/103T (400  $\mu\text{M}$ , squares). Survivin120 K90/103T showed greatly reduced tweezer affinities (lower curves). **d-f** Data are presented as mean values  $\pm$  SD with  $n = 3$  independent experiments. **g** Pull-down results after immunostaining. GST-Survivin120-WT or GST-Survivin120-K90/103T were incubated with 50  $\mu\text{M}$  respective tweezer molecule or ELTL/ELTLGEFL peptides w/o tweezer. GST-Survivin120- or GST-Survivin120-K90/103T-loaded beads were mixed with CRM1 and RanQ69L prey proteins as well as dGTP to allow export complex assembly. Proteins in input and bead samples were analyzed via immunoblotting with antibodies specific for CRM1 or GST. WT, wildtype. One representative example of two independent biological replicates is shown. Samples derive from the same experiment and gels/blots were processed in parallel. **h** Quantification of two independent pull-down experiments. After subtraction of the CRM1 negative control from the pulled CRM1 intensity, the latter is normalized by the GST-Survivin intensity and afterwards normalized by the CRM1 intensity without tweezer incubation. Export complex assembly is only compromised by peptide tweezers in the wildtype Survivin120, but not in the mutant. No ligand: black; TW: light blue; TW-ELTL: blue; TW-ELTLGEFL: dark blue; ELTL peptide: light gray; ELTLGEFL peptide: dark gray. Source data are provided as a Source Data file.

to further probe Survivin's biological functions and to gain control over its export activity. The introduction of fluorescence labels into the next generation of tailored tweezer conjugates via click chemistry will facilitate their detailed monitoring by confocal microscopy. Our study is an experimental proof-of-principle that specific shielding of intracellular transport signals can indeed be accomplished by supramolecular ligands. In the past, inhibition of nucleocytoplasmic transport, including nuclear export and import processes, was only achieved in a rather unspecific manner targeting the respective receptors instead of the bound signals, exemplified by the drug Leptomycin B binding to Crm1. As the activity of several disease-driving proteins besides Survivin is based on selective nuclear transport and protein interactions, our results could indeed set the stage for a broad future exploitation of the developed principles in basic and applied biomedical research.

## Methods

**Synthesis of tweezer conjugates.** Due to its excellent biocompatibility and very good tolerance toward peptidic side chains<sup>42</sup> the copper-catalyzed Huisgen cycloaddition was employed to couple an alkyne tweezer with an azidopeptide<sup>43</sup>. To this end the unsymmetrical monophosphate monobutynylphosphate tweezer was synthesized according to our recently published protocol for the synthesis of unsymmetrical diphosphate monoesters via the trichloroacetonitrile method<sup>37</sup>. All peptides were prepared with a final coupling of azidoacetic acid to their N-terminus. Cleavage from the resin and purification by preparative HPLC yielded pure peptides. Subsequent click reactions between free azido peptides and alkyne tweezers were carried out in a mixture of water and THF (1:1). The catalyst was prepared in situ by reaction of copper sulfate with sodium ascorbate in the presence of DIPEA base. The resulting hybrid molecules were precipitated by acidification with HCl, followed by removal of THF in vacuo and filtration. Unreacted starting materials could be separated from the products by RP-18 column chromatography or preparative HPLC.

**Peptide synthesis.** All peptides were synthesized using automated, microwave assisted, SPPS. The synthesis was carried out on a CEM peptide synthesizer using a Wang resin (4-hydroxybenzyl alcohol (PHB) on polystyrene) already equipped with the C-terminal amino acid. Coupling was effected with HCTU. In the final step, 2-azidoacetic acid was coupled to the free N-terminus of the peptide; then the entire peptide was cleaved off the resin with TFA, TIS, and water. The peptide in the cleavage solution was poured onto ice-cooled diethyl ether and stored in the freezer for 1 h to precipitate. Each peptide was pre-purified by centrifugation and washed again with diethyl ether. Subsequently, preparative purification was carried out by means of HPLC. Purification was performed on a preparative HPLC system from Jasco with UV/Vis detector (UV-975, DG-2080-53 solvent degasser, LG-980-02S 3-channel solvent mixer, peak-detection at 210 nm). The instrument is equipped with a reverse-phase column from Macherey-Nagel (Modell EC 250/4 Nucleosil 100-3 C18). Linear gradients of acetonitrile and water with presence of 0.1 TFA were applied.

**Click coupling.** Monophosphate monobutynylphosphate tweezer (5.0 mg, 6.4  $\mu\text{mol}$ ) was dissolved in 2 mL THF/H<sub>2</sub>O (1:1) in a 5-mL round-bottom flask together with the respective N-terminal Azac peptide (23  $\mu\text{mol}$ ). Fresh distilled DIPEA (11.3  $\mu\text{L}$ ) was added to the previously degassed solution. Subsequently, the copper sulfate solution (8.3 mg CuSO<sub>4</sub>·5H<sub>2</sub>O, 33  $\mu\text{mol}$  in 1 mL water) was mixed

with the sodium ascorbate solution (13 mg C<sub>6</sub>H<sub>7</sub>NaO<sub>6</sub>, 66  $\mu\text{mol}$  in 1 mL water) and the catalytic brew was immediately added to the reaction solution. The reaction mixture was stirred for 16 h at room temperature and subsequently quenched by addition of 1 M HCl (5 mL), resulting in formation of a colorless (yellow in the case of FAM-labeled derivatives) precipitate, followed by removal of THF in vacuo. The suspension was extracted with chloroform (3  $\times$  5 L). The aqueous phase was filtered and the collected solid was washed with water (2  $\times$  1 mL). The crude product was rinsed with distilled THF from the fritted funnel and the desired TW-peptide conjugate was obtained as a colorless (or yellow) solid after evaporation to dryness (6  $\mu\text{mol}$ , 94 %). LC traces of all final products (peptides, FAM-labeled peptides, tweezer molecules) can be found in the supplementary information (SI19).

**Plasmids.** Bacterial expression vectors encoding Survivin120 variants, CRM1, and RanQ69L were constructed by polymerase chain reaction (PCR) amplification using appropriate templates and primers containing ApaI/BamHI restriction sites (SI20). PCR products were cloned into the vector pET41-GST-PreSc as an N-terminal fusion with GST and a PreScission protease cleavage site as described (SI20)<sup>26</sup>. To generate Survivin point mutants, critical lysines were changed by site-directed mutagenesis with the Q5<sup>®</sup> Site-Directed Mutagenesis Kit from New England BioLabs<sup>®</sup>. The eukaryotic expression vector pc3-Survivin142-HA was analogously constructed by PCR amplification using an appropriate template and primers containing BamHI/NheI restriction sites (SI20). The PCR product was cloned into the vector pcDNA3.1 as a C-terminal fusion with an HA expression tag and transfected as described<sup>26</sup>.

**Protein expression and purification.** GST-tagged proteins were expressed in *Escherichia coli* soluBL21 cultivated in LB media containing 50  $\mu\text{g}/\text{mL}$  kanamycin. The expression was induced with 1 mM IPTG at an OD<sub>600</sub> of 0.6–0.8. Bacteria were pelleted, lysed with lysozyme, and subsequent sonication in TRIS/NaCl (pH 7.4) supplemented with 1 mM PMSF. The GST-tagged proteins were then immobilized on GSTrap 4B columns. The GST-Tag was optionally cleaved with PreScission protease on column, depending on the experiments performed afterwards. The protein was then loaded on a HiTrap Q HP column and eluted with a 0.025–1 M NaCl gradient in 50 mM Tris-HCl buffer, pH 7.5, containing 1 mM DTT.

His-tagged CRM1<sub>1-1062VLV430AAA</sub> was expressed in *E. coli* BL21-CodonPlus-RIL from Agilent Technologies using a pTGA20 vector obtained from Dr. Sonia Banuelos (Department of Biochemistry and Molecular Biology, Biofisika Institute, University of the Basque Country, Leioa, Spain). Bacteria were cultivated in LB media containing 100  $\mu\text{g}/\text{mL}$  carbenicillin for the pTGA20 vector and 50  $\mu\text{g}/\text{mL}$  chloramphenicol for maintaining the pACYC plasmid in the BL21-Codon Plus strain. The expression was induced with 0.1 mM IPTG at an OD<sub>600</sub> of 0.5. Bacteria were pelleted and lysed with lysozyme and subsequent sonication in TRIS/NaCl (pH 7.4) supplemented with 1 mM PMSF. The lysates were then immobilized on HisTrap FF columns and eluted using 50 mM NaH<sub>2</sub>PO<sub>4</sub>, 300 mM NaCl, and 500 mM imidazole, pH 8.0. Afterwards the His-Tag was cleaved with TEV protease from Sigma-Aldrich overnight at 4 °C. The protein was dialyzed against 50 mM Tris-HCl and 25 mM NaCl, pH 7.5 and passed over another HisTrap FF column to remove the cleaved His-Tag. The protein was then loaded on a HiTrap Q HP column and eluted with a 0.025–1 M NaCl gradient in 50 mM Tris-HCl buffer, pH 7.5, containing 1 mM DTT.

Isotopically <sup>15</sup>N-labeled GST-tagged Survivin120 was expressed in *E. coli* SoluBL21 by growing a culture in 4 L LB medium at 37 °C. At an OD<sub>600</sub> of 1.0–1.2, the bacteria were pelleted and resuspended in 1 L M9 minimal medium supplemented with 1 g/L <sup>15</sup>N-ammonium chloride. After incubation for 30 min at 37 °C, expression was induced with 0.2 mM IPTG and the protein was expressed for 20 h at 30 °C. The cells were harvested and lysed by sonication in PBS (pH 7.4) supplemented with 1 mM PMSF. <sup>15</sup>N-GST-Survivin120 was purified via a GSTrap 4B affinity column. The GST-tag was cleaved with PreScission protease for 6 h at 4 °C. Subsequent preparative size exclusion chromatography was performed with a HiLoad 26/60 Superdex 75  $\mu\text{g}$  column and a

downstream mounted GSH-column from GE Healthcare in 50 mM KPi pH 7.4 with 150 mM KCl and 2 mM DTT. The pure protein was concentrated, and the buffer was exchanged to NMR buffer (50 mM KPi pH 6.5, 90 mM KCl, 2 mM DTT) using Vivaspin Ultracentrifugation filters with a molecular weight cutoff of 10 kDa.

**Isothermal titration calorimetry (ITC).** ITC was performed with a MicroCal iTC200 from Malvern Panalytical in PBS, pH 7.4 at 25 °C with molecular tweezers in the cell and Survivin120 in the titration syringe. The protein was dialyzed overnight at 4 °C against the PBS buffer. Ligands were dissolved in the respective dialysis buffer. Then, 300 μM TW were titrated with 300 μM Survivin120 WT or 321 μM Survivin120 K90/103T. Then, 100 μM TW-ELTL, TW-ELTLGEFL, or TW-LFEEGLT was titrated with 1.2 mM Survivin120 WT or 2.5 mM Survivin120 K90/103T. For reverse titrations, either 33.3 or 34.4 μM Survivin120 in the cell was titrated with 5 mM TW or TW-ELTL in the syringe, respectively. All titrations were performed in PBS, pH 7.4 at 25 °C. Then, 1.5 μL injections were used with 120 s spacing time between injections. The injection rate was set to 0.5 μL/s and the reference power was 5 μcal/s. ITC thermograms were fitted to a one set of sites model with the software Origin (v7.0552) provided with the instrument. Heat of dilution was subtracted as constant from each data point.

**Pull-down experiments.** All pull-down assays were performed at room temperature in pull-down buffer (PBS, pH 7.4, 1 mM DTT, 0.02 Triton X-100). GST fusion proteins were immobilized on 50 μL GSH-coated Sepharose 4B beads from GE Healthcare. The beads were prior equilibrated and blocked with 500 μL pull-down blocking buffer (PBS, pH 7.4, 1 (w/v) BSA, 1 mM DTT, 0.02 (v/v) Triton X-100) for 1 h to prevent unspecific binding.

For analysis of the effective inhibitory tweezer concentration, 200 μg 293T lysate with overexpressed Survivin142-HA was preincubated without ligand or with different concentrations (10 nM to 200 μM) of unmodified tweezer TW, TW-ELTL, TW-ELTLGEFL, or TW-LFEEGLT for 1 h and then mixed with 35 μg GST-CRM1, 55 μg RanQ69L, and 2 mM dGTP. GSH-beads were incubated with this protein mixture for 2 h under rotation. For analysis of tweezer specificity, 40 μg GST-Survivin120 or GST-Survivin120-K90/103T point mutant was pre-bound to equilibrated GSH-beads in 500 μL pull-down buffer, containing additionally either no ligand or 50 μM unmodified tweezer TW, TW-ELTL, TW-ELTLGEFL, or peptides ELTL and ELTLGEFL for 1 h under rotation. After washing and blocking, GSH-beads were incubated with a protein mixture consisting of 2 mM dGTP, 50 μg CRM1, and 50 μg RanQ69L for 2 h under rotation.

Samples of input and beads taken during pull-down experiments were ran on 12.5 SDS gels and transferred onto 0.2 μM PVDF membranes (Amersham Hybond P 0.2) using a PerfectBlue™ tank electro blotter (Peqlab) at 350 mA for 150 min. Membranes were blocked for 1 h using 5% milk powder in TBS buffer containing 0.1% Tween-20. Next, membranes were incubated in primary antibodies against HA (anti-HA, mouse monoclonal, BioLegend, Covance MMS-101R, 1:1,000), GST (anti-GST, mouse monoclonal, Santa Cruz Biotechnology Inc., sc-57753, 1:1000) or CRM1 (anti-CRM1, rabbit polyclonal, Novus Biologicals Ltd., NB100-79802, 1:10,000) overnight at 4 °C. Secondary horseradish peroxidase (HRP)-conjugated antibody (anti-mouse IgG-HRP, sheep, GE Healthcare, NXA931 or anti-rabbit IgG-HRP, donkey, GE Healthcare, NA934) was then added (1:10,000) for 1 h at room temperature. Chemiluminescence was detected and imaged using the Pierce ECL Plus Western Blotting Substrate kit (Thermo Fisher Scientific) and Chemidoc system (Bio-Rad) or film processor Cawomat 2000 IR (CAWO). Western blots were analyzed by densitometric analysis with ImageJ version 1.52p (U.S. National Institutes of Health), measuring the mean gray intensity of protein bands. Uncropped and unprocessed scans of western blots are deposited in the Source Data file.

**NMR experiments.** NMR experiments were performed on a Bruker 700 MHz Avance Ultrashield NMR spectrometer (Bruker, Germany) equipped with a 5 mm CPTCI <sup>1</sup>H-<sup>13</sup>C/<sup>15</sup>N/D cryoprobe with z-gradient at 25 °C. The pulse program for the <sup>1</sup>H-<sup>15</sup>N-BEST-TROSY-HSQC is part of the NMRlib 2.0 pulse sequence tools library from IBS (Grenoble, France) available at <http://www.ibs.fr/research/scientific-output/software/pulse-sequence-tools/>. Spectra were processed with Topspin 3.5 and analyzed in CARA<sup>44</sup>. Histograms plotting chemical shift perturbation or signal intensities against the protein sequence were generated in GraphPad Prism 5. The assignments for the Survivin120 construct were obtained from BMRB entry # 6342.

Protein NMR samples for <sup>15</sup>N-HSQC titrations contained 400–600 μM <sup>15</sup>N-labeled Survivin120 in NMR buffer (50 mM KPi pH 6.5, 90 mM KCl, 2 mM DTT with 10% D<sub>2</sub>O). A 10 mM (TW) or 5 mM (TW-ELTL, TW-ELTLGEFL, TW-LFEEGLT) stock solution of ligand in water was added stepwise to the protein samples. Tweezers were titrated stepwise up to a 1:1 ratio, and <sup>1</sup>H-<sup>15</sup>N-BEST-TROSY-HSQC NMR spectra were recorded for each titration step. General line broadening was observed in the NMR spectra once the ligand:protein ratio exceeds 1:1; therefore, titration points are only analyzed up to this ratio.

The chemical shift perturbation Δδ for the <sup>1</sup>H,<sup>15</sup>N-BEST-TROSY-HSQC was calculated from the <sup>1</sup>H- and <sup>15</sup>N-shifts according to Eq. 1<sup>40</sup> using the spectra with 0 and 1 equivalent of tweezers, where Δδ<sub>N</sub> and Δδ<sub>H</sub> represent the chemical shift perturbation values of the amide nitrogen and proton, respectively:

$$\Delta\delta = \sqrt{\Delta\delta_H^2 + (0.154 \cdot \Delta\delta_N)^2} \quad (1)$$

Relative signal intensities  $I/I_0$  were obtained by dividing the intensities in the presence of 1 equivalent of each tweezer by the intensities in the absence of tweezers. Residues L6 and W10 whose signals overlap with other signals at the end of the titration were excluded from the intensity analysis. Spectra were processed with Topspin 3.5 (Bruker) and analyzed in CARA (version 1.9.1.7). Chemical shift perturbation and relative signal intensities were calculated from the raw chemical shift data and peak intensities using Excel 2016 (Microsoft) and plotted with GraphPad Prism 5.0.

NMR samples of Survivin120 mutants to assess proper folding contained 100–500 μM unlabeled Survivin120 mutants in NMR buffer (50 mM KPi pH 6.5, 90 mM KCl, 2 mM DTT with 10% D<sub>2</sub>O). 1D proton spectra with water suppression were recorded and protein folding was evaluated based on the dispersion of amide, aromatic, and methyl signals. Folded proteins show a wide signal dispersion in the amide/aromatic range (6–10 ppm) and the presence of methyl signals at <1 ppm. By reason of the high demand for isotope-labeled protein, all NMR experiments were by default performed only once.

**Fluorescence anisotropy measurements.** Fluorescence anisotropy was measured with a Jasco Spectrofluorometer FP-8300 in PBS buffer, pH 7.4, at 25 °C and data were collected with the software Spectra Manager™.

For the quantitative analysis of the Survivin120/CRM1 complex, Survivin120 was labeled with ATTO488-maleimide from Jenabioscience according to the manufacturer's instructions and mixed with CRM1<sub>1-1062VLV430AAA</sub> in a ratio of 1:5. The protein complex was then titrated with tweezers in several steps until a final concentration of approximately 180 μM tweezers was reached. Data were transformed to logarithmic scale and IC<sub>50</sub> was fitted using the equation in GraphPad Prism 8:

$$y = A_{\min} + \frac{(A_{\max} - A_{\min})}{1 + 10^{x - \log(IC_{50})}} \quad (2)$$

where  $A_{\max}$  is the anisotropy in the absence of tweezer,  $A_{\min}$  is the anisotropy at the end titration, and  $x$  is the concentration of tweezer.  $A_{\max}$  was constrained for each data set, whereas  $A_{\min}$  and IC<sub>50</sub> were fitted.

For binding studies, FAM-labeled molecular tweezers (200 nM) were titrated with Survivin120 wildtype or K90/103T mutant until a final concentration of 180 μM (wildtype) or 350 μM (K90/103T) was reached. Data were normalized to the measured anisotropy  $A_0$  in the absence of protein. Using a single-site binding model, the fluorescence anisotropy data were fitted to the equation:

$$y = A \cdot \frac{(L + x + K_D) - \sqrt{(L + x + K_D)^2 - 4 \cdot x \cdot L}}{2 \cdot L} \quad (3)$$

where  $A$  is the anisotropy at saturation,  $L$  is the concentration of the fluorescent ligand,  $x$  is the concentration of protein titrated, and  $K_D$  is the dissociation constant.

**Statistical analysis.** ITC thermograms were fitted to a one set of sites model with the software Origin provided with the instrument. Heat of dilution was subtracted as constant from each data point. From three independent experiments ( $n = 3$ ), one representative example was depicted, and thermodynamic data were derived thereof. For pull-down experiments, only the representative quantification of the depicted western blot is shown. Of note, low protein yields of the mutant CRM1<sub>1-1062VLV430AAA</sub> did not allow replicates of the respective experiment. Fluorescence anisotropy graphs were generated with GraphPad Prism 5.0. Depicted error bars represent the standard deviation of three independent titrations.

**Computational details.** For MD simulations of full-length Survivin, an initial structure for Survivin was generated in Modeller v9.17<sup>45</sup> using the Uniprot protein sequence O15392-1 [<https://www.uniprot.org/uniprot/O15392>] (human BIRC5 isoform alpha) as target and PDB entries 1E31 [<https://www.rcsb.org/structure/1E31>]<sup>46</sup>, 1F3H [<https://www.rcsb.org/structure/1F3H>]<sup>47</sup>, 3UEG [<https://www.rcsb.org/structure/3UEG>], 3UEH [<https://www.rcsb.org/structure/3UEH>], 3UEI [<https://www.rcsb.org/structure/3UEI>]<sup>48</sup>, and 1XOX [<https://www.rcsb.org/structure/1XOX>]<sup>38</sup> as templates. The best model was selected to minimize the DOPE and molpdf scores and was validated with PROCHECK (v.3.5.4)<sup>49</sup> from the online Swiss-Model Workspace<sup>50</sup>. The root-mean-square deviation (RMSD) between the model and templates is less than 0.7 Å for the crystal structures (1E31, 1F3H, 3UEG, 3UEH, 3UEI) and 2.0 Å for the NMR solution (1XOX).

MD simulations were run with Gromacs 4.6.7<sup>51</sup> using the Amber ff99SB force field<sup>52</sup> extended with ZAFF to model the zinc finger<sup>53</sup>. Topology files were created with the TLEaP module of Amber v12.21<sup>54</sup> and converted to Gromacs topologies by ACPype<sup>55</sup>. Proteins were solvated in a dodecahedron box of SPC/E water molecules<sup>56</sup> with a 10 Å minimum separation between the protein and the box boundaries. The system was neutralized by addition of Na<sup>+</sup> and Cl<sup>-</sup> ions to a final ionic strength of 0.15 mol/L. The system was energy-minimized by steepest-descent to a total force of 2000, equilibrated for 5 ns in the NVT ensemble with restrained heavy atoms, and for 5 ns in the NPT ensemble without restraints. Production simulations were run in the NPT ensemble for a total of 310 ns (3 × 50 ns, 2 × 80 ns). Temperature was stabilized at 300 K in the NVT and NPT ensembles by the V-rescale thermostat<sup>57</sup>, while the pressure was stabilized at 1 atm in the NPT ensemble by the Berendsen barostat (equilibration) or Parrinello-Rahman barostat (data production)<sup>58</sup>. Simulations were carried out on a GPU (GeForce 970 and GeForce 1070, CUDA 6.5) using a time step of 2 fs, the Verlet

scheme<sup>59</sup> for neighbor search with a 10 Å cutoff, the Particle Mesh Ewald method<sup>60</sup> for electrostatic calculations, and the LINCS algorithm<sup>61</sup> for bond constraints.

Representative structures were extracted from trajectories based on mutual RMSDs of the backbone atoms, using the *g\_rms* tool in Gromacs to produce 2D RMSD plots, the PAM (partition around medoids)<sup>62</sup> tool from R package cluster, version 2.0.6, in R v3.3.1<sup>63</sup> to find clusters, and the *cluster.stats* function of R package *fpc*, version 2.1.10, to validate the clustering based on silhouette coefficients<sup>64</sup>. For each cluster, the MD frame that minimized the RMSD with all other frames in the cluster was selected as the representative pose of that cluster. Root-mean-square fluctuations were calculated residue-wise on the concatenated MD trajectories using the *g\_rms* tool in Gromacs.

For MD simulations of monomeric and dimeric Survivin120, NAMD<sup>65</sup> was used to perform 80 ns ( $2 \times 40$  ns) MD simulations of 1:1 protein-tweezer complexes with the ligand (TW and TW-ELTL) on K23, K90, K91, and K103 (SI11). The simulations were performed in the NPT ensemble at 1 atm and 300 K<sup>74</sup> with the CHARMM36m force field<sup>66,67</sup>. The system was placed in a TIP3P<sup>68</sup> water box built with a padding of 20 Å and neutralized with sodium ions. A cutoff of 12 Å was used for Van der Waals interactions. Long-range electrostatic contributions were evaluated using the Particle Mesh Ewald method<sup>60</sup>. The systems were initially minimized and equilibrated at 300 K by performing 150 ps each of NVT and NPT simulations with a time step of 2 fs. Harmonic constraints on the collective variables representing distances and angles were used to maintain the geometry of the tetrahedral zinc finger. As in previous studies, the conformational features of the lysine-tweezers complexes are conserved (Table SI12).

QM/MM optimizations were performed using ChemShell<sup>69</sup> with the DL-FIND geometry optimizer<sup>70</sup> and Turbomole<sup>71</sup> to handle the QM region. The QM region was formed by the tweezer as well as the ammonium and the methylene groups in positions  $\delta$  and  $\epsilon$  of the lysine's sidechain. The MM region comprised the remaining protein atoms, solvent and ions. An electrostatic embedding scheme<sup>72,73</sup> was used. The MM region was calculated with the CHARMM36m force field and the QM region at the DFT(B3LYP-D3)/Def2SVP level of theory<sup>74</sup>. Five snapshots from the MD simulations were used as initial geometries for QM/MM optimizations. The snapshots correspond to geometries around the centroid of the largest cluster from the MD simulations. The cluster analysis was performed using a quality-threshold-based algorithm implemented in VMD<sup>75</sup>, with a RMSD cutoff of 3 Å.

Additional information and computational details can be found in the supplementary information (SI10).

GaMD<sup>76</sup> simulations were performed with NAMD using an analogous setup to the standard MDs. The statistics for the biasing potential were collected during 50 ns of equilibration prior to the production run, which was then extended to 100 ns. The threshold value for the biasing potential was fixed at the maximum potential energy sampled during the equilibration step. The standard deviation of the biasing potential was controlled by allowing a maximum value of 10 kT.

**Reporting Summary.** Further information on research design is available in the Nature Research Reporting Summary linked to this article.

## Data availability

Data supporting the findings of this manuscript are available from the corresponding authors upon reasonable request. A reporting summary for this article is available as a Supplementary Information file. Source data are provided with this paper.

Received: 3 February 2020; Accepted: 2 February 2021;

Published online: 08 March 2021

## References

- Keskin, O., Tuncbag, N. & Gursesoy, A. Predicting protein-protein interactions from the molecular to the proteome level. *Chem. Rev.* **116**, 4884–4909 (2016).
- Kubota, R. & Hamachi, I. Protein recognition using synthetic small-molecular binders toward optical protein sensing in vitro and in live cells. *Chem. Soc. Rev.* **44**, 4454–4471 (2015).
- Scott, D. E., Bayly, A. R., Abell, C. & Skidmore, J. Small molecules, big targets: drug discovery faces the protein-protein interaction challenge. *Nat. Rev. Drug Discov.* **15**, 533–550 (2016).
- van Dun, S., Ottmann, C., Milroy, L. G. & Brunsveld, L. Supramolecular chemistry targeting proteins. *J. Am. Chem. Soc.* **139**, 13960–13968 (2017).
- McGovern, R. E., Fernandes, H., Khan, A. R., Power, N. P. & Crowley, P. B. Protein camouflage in cytochrome *c*-calixarene complexes. *Nat. Chem.* **4**, 527–533 (2012).
- Chinai, J. M. et al. Molecular recognition of insulin by a synthetic receptor. *J. Am. Chem. Soc.* **133**, 8810–8813 (2011).
- Bier, D. et al. Molecular tweezers modulate 14-3-3 protein-protein interactions. *Nat. Chem.* **5**, 234–239 (2013).
- Hatai, J. & Schmuck, C. Diverse properties of guanidiniocarbonyl pyrrole-based molecules: artificial analogues of arginine. *Acc. Chem. Res.* **52**, 1709–1720 (2019).
- Bier, D. et al. The molecular tweezer CLR01 stabilizes a disordered protein-protein interface. *J. Am. Chem. Soc.* **139**, 16256–16263 (2017).
- de Vink, P. J. et al. A binary bivalent supramolecular assembly platform based on cucurbit[8]uril and dimeric adapter protein 14-3-3. *Angew. Chem. Int. Ed. Engl.* **56**, 8998–9002 (2017).
- Nguyen, H. D., Dang, D. T., van Dongen, J. L. & Brunsveld, L. Protein dimerization induced by supramolecular interactions with cucurbit[8]uril. *Angew. Chem. Int. Ed. Engl.* **49**, 895–898 (2010).
- Trusch, F. et al. Cell entry of a host-targeting protein of oomycetes requires gp96. *Nat. Commun.* **9**, 2347 (2018).
- Vallet, C. et al. Functional disruption of the cancer-relevant interaction between survivin and histone H3 with a guanidiniocarbonyl pyrrole ligand. *Angew. Chem. Int. Ed. Engl.* **59**, 5567–5571 (2020).
- Mallon, A. I., Dutt, S., Schrader, T. & Crowley, P. B. Protein camouflage: a supramolecular anion recognition by ubiquitin. *ChemBioChem* **17**, 774–783 (2016).
- Smith, L. C., Leach, D. G., Blaylock, B. E., Ali, O. A. & Urbach, A. R. Sequence-specific, nanomolar peptide binding via cucurbit[8]uril-induced folding and inclusion of neighboring side chains. *J. Am. Chem. Soc.* **137**, 3663–3669 (2015).
- McGovern, R. E. et al. Structural study of a small molecule receptor bound to dimethyllysine in lysozyme. *Chem. Sci.* **6**, 442–449 (2015).
- Sonzini, S. et al. High affinity recognition of a selected amino acid epitope within a protein by cucurbit[8]uril complexation. *Angew. Chem. Int. Ed. Engl.* **55**, 14000–14004 (2016).
- Ambrosini, G., Adida, C. & Altieri, D. C. A novel anti-apoptosis gene, survivin, expressed in cancer and lymphoma. *Nat. Med.* **3**, 917–921 (1997).
- Adida, C. et al. Prognostic significance of survivin expression in diffuse large B-cell lymphomas. *Blood* **96**, 1921–1925 (2000).
- Capalbo, G. et al. The role of survivin for radiation therapy. Prognostic and predictive factor and therapeutic target. *Strahlenther. Onkol.* **183**, 593–599 (2007).
- Chen, P. et al. Over-expression of survivin and VEGF in small-cell lung cancer may predict the poorer prognosis. *Med Oncol.* **31**, 775 (2014).
- Engels, K. et al. Dynamic intracellular survivin in oral squamous cell carcinoma: underlying molecular mechanism and potential as an early prognostic marker. *J. Pathol.* **211**, 532–540 (2007).
- Xu, C. et al. High survivin mRNA expression is a predictor of poor prognosis in breast cancer: a comparative study at the mRNA and protein level. *Breast Cancer* **21**, 482–490 (2014).
- Knauer, S. K., Mann, W. & Stauber, R. H. Survivin's dual role: an export's view. *Cell Cycle* **6**, 518–521 (2007).
- Li, F. et al. Control of apoptosis and mitotic spindle checkpoint by survivin. *Nature* **396**, 580–584 (1998).
- Knauer, S. K., Bier, C., Habtemichael, N. & Stauber, R. H. The Survivin-Crm1 interaction is essential for chromosomal passenger complex localization and function. *EMBO Rep.* **7**, 1259–1265 (2006).
- Knauer, S. K. et al. The survivin isoform survivin-3B is cytoprotective and can function as a chromosomal passenger complex protein. *Cell Cycle* **6**, 1502–1509 (2007).
- Knauer, S. K. et al. Nuclear export is essential for the tumor-promoting activity of survivin. *FASEB J.* **21**, 207–216 (2007).
- Fokkens, M., Schrader, T. & Klarner, F. G. A molecular tweezer for lysine and arginine. *J. Am. Chem. Soc.* **127**, 14415–14421 (2005).
- Talibersky, P., Bastkowski, F., Klarner, F. G. & Schrader, T. Molecular clip and tweezer introduce new mechanisms of enzyme inhibition. *J. Am. Chem. Soc.* **130**, 9824–9828 (2008).
- Wilch, C. et al. Molecular tweezers inhibit PARP-1 by a new mechanism. *Eur. J. Org. Chem.* **2017**, 2223–2229 (2017).
- Schrader, T., Bitan, G. & Klarner, F. G. Molecular tweezers for lysine and arginine—powerful inhibitors of pathologic protein aggregation. *Chem. Commun. (Camb.)* **52**, 11318–11334 (2016).
- Vopel, T. et al. Inhibition of huntingtin exon-1 aggregation by the molecular tweezer CLR01. *J. Am. Chem. Soc.* **139**, 5640–5643 (2017).
- Trusch, F. et al. Molecular tweezers target a protein-protein interface and thereby modulate complex formation. *Chem. Commun. (Camb.)* **52**, 14141–14144 (2016).
- Engelsma, D., Rodriguez, J. A., Fish, A., Giaccone, G. & Fornerod, M. Homodimerization antagonizes nuclear export of survivin. *Traffic* **8**, 1495–1502 (2007).
- Pavlyukov, M. S. et al. Survivin monomer plays an essential role in apoptosis regulation. *J. Biol. Chem.* **286**, 23296–23307 (2011).
- Heid, C. et al. Molecular tweezers with additional recognition sites. *Chemistry* **24**, 11332–11343 (2018).
- Sun, C., Nettesheim, D., Liu, Z. & Olejniczak, E. T. Solution structure of human survivin and its binding interface with Smac/Diablo. *Biochemistry* **44**, 11–17 (2005).
- Dutt, S. et al. Molecular tweezers with varying anions: a comparative study. *J. Org. Chem.* **78**, 6721–6734 (2013).
- García-Santisteban, I., et al. A cellular reporter to evaluate CRM1 nuclear export activity: functional analysis of the cancer-related mutant E571K. *Cell. Mol. Life Sci.* **73**, 4685–4699 (2016).
- Sowislok, A. A. Ein neuer Weg zu asymmetrischen Klammern und Pinzetten mit Phosphoramiditen. Universität Duisburg-Essen (2019).

42. Li, H., Aneja, R. & Chaiken, I. Click chemistry in peptide-based drug design. *Molecules* **18**, 9797–9817 (2013).
43. Lallana, E., Riguera, R. & Fernandez-Megia, E. Reliable and efficient procedures for the conjugation of biomolecules through Huisgen azide–alkyne cycloadditions. *Angew. Chem. Int. Ed. Engl.* **50**, 8794–8804 (2011).
44. Keller, R. L. The computer aided resonance assignment tutorial. CANTINA Verlag 1st ed. (2004).
45. Sali, A. & Blundell, T. L. Comparative protein modelling by satisfaction of spatial restraints. *J. Mol. Biol.* **234**, 779–815 (1993).
46. Chantalat, L. et al. Crystal structure of human survivin reveals a bow tie-shaped dimer with two unusual alpha-helical extensions. *Mol. Cell* **6**, 183–189 (2000).
47. Verdecia, M. A. et al. Structure of the human anti-apoptotic protein survivin reveals a dimeric arrangement. *Nat. Struct. Biol.* **7**, 602–608 (2000).
48. Niedzialkowska, E. et al. Molecular basis for phosphospecific recognition of histone H3 tails by Survivin paralogues at inner centromeres. *Mol. Biol. Cell* **23**, 1457–1466 (2012).
49. Laskowski, R. A., MacArthur, M. W., Moss, D. S. & Thornton, J. M. PROCHECK: a program to check the stereochemical quality of protein structures. *J. Appl. Crystallogr.* **26**, 283–291 (1993).
50. Arnold, K., Bordoli, L., Kopp, J. & Schwede, T. The SWISS-MODEL workspace: a web-based environment for protein structure homology modelling. *Bioinformatics* **22**, 195–201 (2006).
51. Pronk, S. et al. GROMACS 4.5: a high-throughput and highly parallel open source molecular simulation toolkit. *Bioinformatics* **29**, 845–854 (2013).
52. Hornak, V. et al. Comparison of multiple Amber force fields and development of improved protein backbone parameters. *Proteins* **65**, 712–725 (2006).
53. Peters, M. B. et al. Structural survey of zinc containing proteins and the development of the Zinc AMBER Force Field (ZAFF). *J. Chem. Theory Comput* **6**, 2935–2947 (2010).
54. Case, D. A. et al. AMBER 12. University of California, San Francisco (2012).
55. Sousa da Silva, A. W. & Vranken, W. F. ACPYPE - AnteChamber PYthon Parser interface. *BMC Res Notes* **5**, 367 (2012).
56. Berendsen, H. J. C., Grigera, J. R. & Straatsma, T. P. The missing term in effective pair potentials. *J. Phys. Chem.* **91**, 6269–6271 (1987).
57. Bussi, G., Donadio, D. & Parrinello, M. Canonical sampling through velocity rescaling. *J. Chem. Phys.* **126**, 014101 (2007).
58. Parrinello, M. & Rahman, A. Polymorphic transitions in single crystals: a new molecular dynamics method. *J. Appl. Phys.* **52**, 7182–7190 (1981).
59. Páll, S. & Hess, B. A flexible algorithm for calculating pair interactions on SIMD architectures. *Computer Phys. Commun.* **184**, 2641–2650 (2013).
60. Darden, T., York, D. & Pedersen, L. Particle mesh Ewald: an N log(N) method for Ewald sums in large systems. *J. Chem. Phys.* **98**, 10089–10092 (1993).
61. Hess, B., Bekker, H., Berendsen, H. J. C. & Fraaije, J. G. E. M. LINCS: a linear constraint solver for molecular simulations. *J. Computational Chem.* **18**, 1463–1472 (1997).
62. Kaufman L., Rousseeuw P. J. Clustering by means of medoids. 405–416 (1987).
63. R Core Team. R: a language and environment for statistical computing. Available at [www.R-project.org](http://www.R-project.org) (2016).
64. Rousseeuw, P. Silhouettes: a graphical aid to the interpretation and validation of cluster analysis. *J. Computational Appl. Math.* **20**, 53–65 (1987).
65. Phillips, J. C. et al. Scalable molecular dynamics with NAMD. *J. Comput Chem.* **26**, 1781–1802 (2005).
66. Klauda, J. B. et al. Update of the CHARMM all-atom additive force field for lipids: validation on six lipid types. *J. Phys. Chem. B* **114**, 7830–7843 (2010).
67. Vanommeslaeghe, K. et al. CHARMM general force field: a force field for drug-like molecules compatible with the CHARMM all-atom additive biological force fields. *J. Comput Chem.* **31**, 671–690 (2010).
68. Mark, P. & Nilsson, L. Structure and dynamics of the TIP3P, SPC, and SPC/E water models at 298 K. *J. Phys. Chem. A* **105**, 9954–9960 (2001).
69. Sherwood, P. et al. QUASI: a general purpose implementation of the QM/MM approach and its application to problems in catalysis. *J. Mol. Struct-Theochem.* **632**, 1–28 (2003).
70. Kastner, J. et al. DL-FIND: an open-source geometry optimizer for atomistic simulations. *J. Phys. Chem. A* **113**, 11856–11865 (2009).
71. Ahlrichs, R., Bär, M., Häser, M., Horn, H. & Kölmel, C. Electronic structure calculations on workstation computers: the program system turbomole. *Chem. Phys. Lett.* **162**, 165–169 (1989).
72. Lin, H. & Truhlar, D. G. QM/MM: what have we learned, where are we, and where do we go from here? *Theor. Chem. Acc.* **117**, 185 (2006).
73. Cisneros, G. A., Piquemal, J. P. & Darden, T. A. Quantum mechanics/molecular mechanics electrostatic embedding with continuous and discrete functions. *J. Phys. Chem. B* **110**, 13682–13684 (2006).
74. Grimme, S. Density functional theory with London dispersion corrections. *WIREs Computational Mol. Sci.* **1**, 211–228 (2011).
75. Humphrey, W., Dalke, A. & Schulten, K. VMD: Visual molecular dynamics. *J. Mol. Graph.* **14**, 33–38 (1996).
76. Pang, Y. T., Miao, Y., Wang, Y. & McCammon, J. A. Gaussian accelerated molecular dynamics in NAMD. *J. Chem. Theory Comput* **13**, 9–19 (2017).

## Acknowledgements

The pTGA vector for the expression of the CRM1\_1-1062VLV430AAA mutant was a gift from Dr. Sonia Banuelos (Department of Biochemistry and Molecular Biology, Biofisika Institute, University of the Basque Country, Leioa, Spain). This work was supported by the Collaborative Research Centre 1093 Supramolecular Chemistry on Proteins (T. S., P. B., D. H., S. K. K., E. S.-G.) and funded by the German Research Foundation (DFG), E. S.-G. acknowledges support from the DFG under Germany's Excellence Strategy (EXC-2033; project no. 390677874) and a Plus-3 grant from the Boehringer Ingelheim Foundation. E. S.-G. acknowledges computational time provided by the Computing and Data Facility of the Max Planck Society and the supercomputer magnitUDE of the University of Duisburg-Essen. We also thank Lisa Oelschläger for performing supporting experiments.

## Author contributions

Knauer group: A. M. and S. B. cloned, expressed, and purified proteins, and performed ITC titrations as well as pull-down experiments. S. B. developed the protocols for protein expression and purification as well as for pull-down and initial ITC experiments. A. M. developed, optimized, and performed fluorescence anisotropy experiments, optimized the ITC protocols, and analyzed the ITC data together with I. H. A. M. and S. B. wrote the manuscript together with T. S., E. S.-G. and S. K. K., who designed the study and supervised the experiments together with C. V. Schrader group: C. H. designed the modified tweezer constructs from computational visualization; he also developed the synthetic protocol for the generation of tweezer conjugates by click chemistry and synthesized the first generation tweezer conjugates. I. H. synthesized FAM-labeled tweezers, modified the tweezer with the scrambled peptide, and determined affinities by ITC titrations. T. S. wrote the paper together with S. K. K. and E. S.-G. Sánchez-García group: Y. B. R.-B. and J. M.-P. carried out the QM/MM calculations, the classical MD simulations, and GaMD simulations of Survivin dimer and Survivin monomer with and without tweezers, processed the data, and analyzed the results together with E. S.-G., who designed the computational work and wrote the paper together with S. K. K. and T. S. Hoffmann group: J.-N. Grad carried out MD simulations on the full-length Survivin dimer and interpreted the data together with D. H. Bayer group: M. P. expressed and purified <sup>15</sup>N-labeled Survivin. C. B. and M. P. performed the NMR titrations. P. B. and C. B. supervised the NMR experiments and interpreted the NMR data.

## Funding

Open Access funding enabled and organized by Projekt DEAL.

## Competing interests

The authors declare no competing interests.

## Additional information

**Supplementary information** The online version contains supplementary material available at <https://doi.org/10.1038/s41467-021-21753-9>.

**Correspondence** and requests for materials should be addressed to E.S.-G., T.S. or S.K.K.

**Peer review information** *Nature Communications* thanks the anonymous reviewers for their contribution to the peer review of this work.

**Reprints and permission information** is available at <http://www.nature.com/reprints>

**Publisher's note** Springer Nature remains neutral with regard to jurisdictional claims in published maps and institutional affiliations.



**Open Access** This article is licensed under a Creative Commons Attribution 4.0 International License, which permits use, sharing, adaptation, distribution and reproduction in any medium or format, as long as you give appropriate credit to the original author(s) and the source, provide a link to the Creative Commons license, and indicate if changes were made. The images or other third party material in this article are included in the article's Creative Commons license, unless indicated otherwise in a credit line to the material. If material is not included in the article's Creative Commons license and your intended use is not permitted by statutory regulation or exceeds the permitted use, you will need to obtain permission directly from the copyright holder. To view a copy of this license, visit <http://creativecommons.org/licenses/by/4.0/>.

© The Author(s) 2021

### 3.4 Publication IV

#### **New tools to probe the protein surface: Ultrasmall gold nanoparticles carry amino acid binders**

Ultrasmall gold nanoparticles (diameter of the metallic core about 2 nm) equipped with azide functionalities were covalently fused with molecular tweezers as supramolecular host molecules selective for lysine and arginine. Attachment of molecular tweezer to the surface of gold nanoparticles was done utilizing copper-catalyzed azide-alkyne cycloaddition. Different instrumental techniques have been used to characterize the novel, nanoparticle-conjugated tweezers, such as high-resolution transmission electron microscopy (HRTEM), differential centrifugal sedimentation (DCS), and <sup>1</sup>H-NMR spectroscopy (diffusion-ordered spectroscopy DOSY, and surface composition). It has been found that each nanoparticle carries between 11 and 30 tweezer molecules. The resulting constructs represents the first multivalent tweezer conjugates suitable for simultaneous targeting of multiple lysines and arginings located in hot regions of different proteins.

The ability of the novel constructs to interact with protein surfaces was probed with the model proteins hPin1 (WW domain; hPin1-WW) and Survivin. Isothermal titration calorimetry (ITC) was used to determine the binding affinities and NMR titration to gain information on the binding specificity. The nanoparticle-conjugated tweezers exhibited binding affinity of  $41 \pm 2 \mu\text{M}$  to the WW domain of hPin1, and  $8 \pm 1 \mu\text{M}$  to the larger protein Survivin, both with negative enthalpies as shown by ITC. According to the <sup>15</sup>N-HCSQ data collected from NMR titrations, the nanoparticle-conjugated tweezers targeted cationic amino acids G3 and R17 with the highest preference. The collected experimental data offer a promising base for further biophysical investigations and employment of nanoparticle-conjugated tweezers as multivalent receptors to target rather large protein flanks and thus modulate their PPI.

Reprinted with permission from *J. Phys. Chem. B* 2021, 125, 115–127. Copyright 2020 American Chemical Society. The publication can be found under:

<https://pubs.acs.org/doi/full/10.1021/acs.jpcc.0c09846>

# New Tools to Probe the Protein Surface: Ultrasmall Gold Nanoparticles Carry Amino Acid Binders

Selina Beatrice van der Meer, Inesa Hadrovic, Annika Meiners, Kateryna Loza, Marc Heggen, Shirley K. Knauer, Peter Bayer, Thomas Schrader, Christine Beuck,\* and Matthias Epple\*



Cite This: *J. Phys. Chem. B* 2021, 125, 115–127



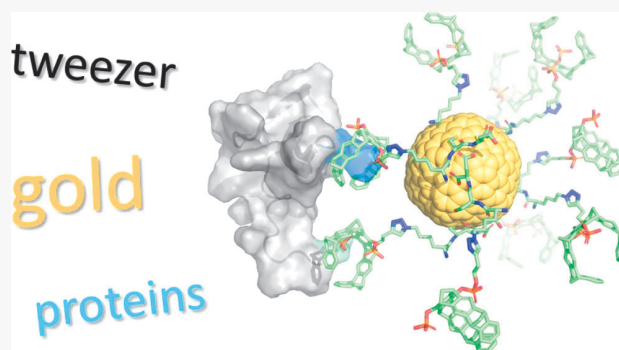
Read Online

ACCESS |

Metrics & More

Article Recommendations

**ABSTRACT:** A strategy toward epitope-selective functionalized nanoparticles is introduced in the following: ultrasmall gold nanoparticles (diameter of the metallic core about 2 nm) were functionalized with molecular tweezers that selectively attach lysine and arginine residues on protein surfaces. Between 11 and 30 tweezer molecules were covalently attached to the surface of each nanoparticle by copper-catalyzed azide alkyne cycloaddition (CuAAC), giving multiavid agents to target proteins. The nanoparticles were characterized by high-resolution transmission electron microscopy, differential centrifugal sedimentation, and  $^1\text{H}$  NMR spectroscopy (diffusion-ordered spectroscopy, DOSY, and surface composition). The interaction of these nanoparticles with the model proteins hPin1 (WW domain; hPin1-WW) and Survivin was probed by NMR titration and by isothermal titration calorimetry (ITC). The binding to the WW domain of hPin1 occurred with a  $K_D$  of  $41 \pm 2 \mu\text{M}$ , as shown by ITC. The nanoparticle-conjugated tweezers targeted cationic amino acids on the surface of hPin1-WW in the following order: N-terminus (G)  $\approx$  R17  $>$  R14  $\approx$  R21  $>$  K13  $>$  R36  $>$  K6, as shown by NMR spectroscopy. Nanoparticle recognition of the larger protein Survivin was even more efficient and occurred with a  $K_D$  of  $8 \pm 1 \mu\text{M}$ , as shown by ITC. We conclude that ultrasmall nanoparticles can act as versatile carriers for artificial protein ligands and strengthen their interaction with the complementary patches on the protein surface.



## INTRODUCTION

Selective targeting of protein epitopes is a promising way to influence a protein's function. This is frequently used in pharmaceutical chemistry to inhibit or activate proteins, typically with small molecules ("ligands"), where concepts from supramolecular chemistry have been applied as well.<sup>1–5</sup> Extending the field beyond molecules, nanoparticles have been proposed as selective binders for proteins, for example, for enzyme inhibition by binding to the active center.<sup>6–12</sup> This is especially interesting when ultrasmall nanoparticles (1–2 nm diameter) are used, which are small in comparison with proteins and meet the dimension of metal clusters.<sup>6,10,13,14</sup> They are also able to enter cells,<sup>13,15–17</sup> and in some cases, also the cell nucleus.<sup>14,18,19</sup> However, a viable strategy for covalent attachment of selective supramolecular ligands to ultrasmall nanoparticles is still missing. Such a strategy would lead to multiavid nanoparticles with increased protein binding affinity.

Specific targeting ligands can be covalently attached via copper-catalyzed azide–alkyne cycloaddition (CuAAC; a "click reaction") to the surface of gold nanoparticles.<sup>20–32</sup> If the nanoparticle is ultrasmall, its surface composition can be directly probed by solution NMR spectroscopy, giving both

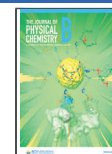
the amount and the chemical nature of the attached receptor molecules, an approach that is unfeasible for larger nanoparticles.<sup>32–37</sup> This surface functionalization allows a specific interaction between the immobilized ligands and the target protein.<sup>6</sup> The high local concentration of the ligand molecules can then lead to increased avidity that we denote as multiavidity in the following.<sup>6,32</sup> Entropically, this leads to a higher probability to target a given protein epitope.

Molecular tweezers developed by Klärner and Schrader have turned out to be selective and efficient binders for cationic amino acids, especially when exposed on the surface of proteins.<sup>38–40</sup> They are based on a specific three-dimensional structure where a defined cavity is formed by alternating units of benzene and norbornadiene. This forms a rigid host molecule with a negatively polarized cavity that can

**Received:** November 1, 2020

**Revised:** December 11, 2020

**Published:** December 23, 2020





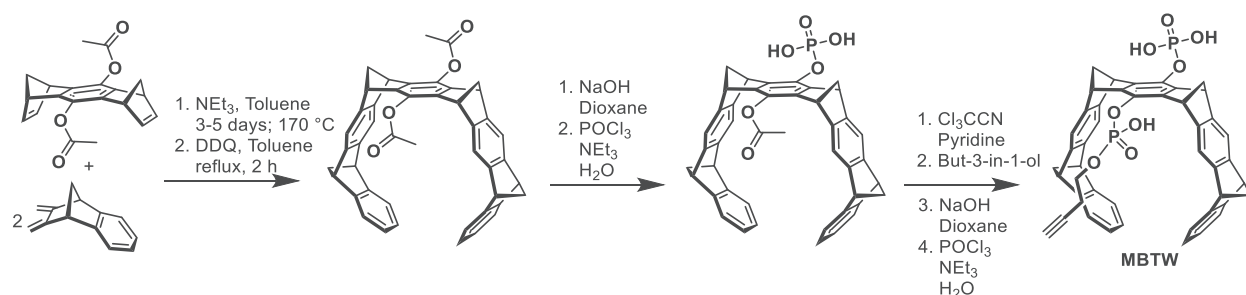


Figure 1. Synthesis of monophosphate monobutynyl phosphate tweezer.<sup>40</sup>

accommodate a guest molecule with aliphatic chains and cationic end groups. The positively charged group of a guest molecule is able to enter the cavity of the tweezer and interact with the phosphate anion in the central benzene unit. As a result, these molecular tweezers selectively bind to the side chains of lysine (K) and arginine (R) in amino acids, peptides, and proteins. Importantly, only the sterically accessible arginines and lysines of a protein are addressed.<sup>41,42</sup>

Herein, we demonstrate how the surface of ultrasmall gold nanoparticles can be covalently functionalized with molecular tweezers as selective ligands for different protein surfaces. The interaction of such multiavid agents with the model proteins hPin1 (WW domain)<sup>43–47</sup> and Survivin<sup>48–51</sup> is then quantitatively monitored on the molecular scale by NMR spectroscopy and isothermal titration calorimetry (ITC).

## METHODS

**Chemicals.** A solution of tetrachloroauric acid (HAuCl<sub>4</sub>) was prepared by dissolving elemental gold (≥99%) in *aqua regia*. Sodium borohydride (NaBH<sub>4</sub>, ≥96%), (+)sodium L-ascorbate (≥99%), copper(II)sulfate pentahydrate (≥99%), tris(3-hydroxypropyl)triazolylmethylamine (≥95%), and deuterium oxide (D<sub>2</sub>O, 99%) were obtained from Sigma-Aldrich. Dipotassium hydrogen phosphate (p.a.) and potassium dihydrogen phosphate (p.a.) were obtained from Panreac Applichem. Aminoguanidine hydrogen carbonate (≥98%) was obtained from Alfa Aesar. The tripeptide 6-azido-lysine-cysteine-asparagine K(N<sub>3</sub>)CD (≥95%) was obtained from EMC Microcollections (Tübingen, Germany). Ultrapure water (Purelab Ultra instrument from ELGA) was used for all syntheses and purifications unless otherwise noted. For all reactions involving nanoparticles, all glassware was cleaned with boiling *aqua regia* and thoroughly washed with water afterward. **Synthesis.** The ultrasmall gold nanoparticles were prepared by a modified one-phase Brust synthesis.<sup>32,52</sup> The cysteine- and azide-containing peptide K(N<sub>3</sub>)CD (4.5 μmol) was dissolved in 6 mL water. The pH was adjusted to 7 by addition of 0.1 M sodium hydroxide solution under continuous stirring. The solution was degassed with argon and 30 μL of 50 mM tetrachloroauric acid (1.5 μmol) was added. After the yellow color of tetrachloroauric acid had vanished, 22.5 μL of a 200 mM ice-cold aqueous sodium borohydride solution (4.5 μmol) was added. After the addition of sodium borohydride, the solution rapidly turned brown, and the dispersion was stirred for one more hour at room temperature. The nanoparticle dispersion was passed through an ultrafiltration spin column (molecular weight cut-off, 3 kDa; Amicon; Merck) for 20 min at 14,000g to remove all unreacted

compounds. The nanoparticles remained on the filter. After centrifugation, the filter was rinsed three times with potassium phosphate buffer (pH 8). By reverse centrifugation, the concentrated gold nanoparticles (~70 μL) with the K(N<sub>3</sub>)CD ligand covalently attached via the thiol group of cysteine<sup>53</sup> were recovered from the filter. Alkyne-functionalized tweezer molecules were conjugated to the azide-terminated gold nanoparticles by copper-catalyzed azide–alkyne cycloaddition (CuAAC) by analogy with the coupling of alkyne-functionalized dyes.<sup>52</sup> The tweezer-conjugated nanoparticles were thoroughly purified by ultrafiltration and reverse centrifugation in the same way as described above. Special care was given to remove any unbound tweezer.

A monophosphate monobutynyl phosphate tweezer was obtained in a 17-step total synthesis developed for unsymmetric diphosphate monoesters, as described by Heid et al.<sup>40</sup> The trichloroacetonitrile route was followed for the functionalization of the parent molecular tweezer with the clickable ester alcohol moiety. Figure 1 shows the basic reaction steps and the analytical characterization data.<sup>40</sup>

The concentration of the nanoparticle-conjugated tweezer molecules was determined by ultraviolet–visible (UV–vis) spectroscopy using an unbound tweezer as calibration standard. For quantification of the clicked amount of tweezers, the aromatic absorption band at 260–310 nm from a dilution series of pure tweezers was integrated and plotted against the concentration. From the slope of linear regression, the tweezer concentration was determined according to Lambert–Beer’s law. The number of tweezers attached to each nanoparticle varied between the synthetic batches and was therefore separately determined for each batch.

**Protein Expression and Purification.** The hPin1-WW domain (residues 3–39; hPin1-WW) was expressed as an N-terminal GST fusion protein with a PreScission protease cleavage site and purified as described earlier.<sup>54</sup> The <sup>13</sup>C, <sup>15</sup>N-, or <sup>15</sup>N-labeled protein for NMR titrations was expressed in *Escherichia coli* BL21 (DE3) T1r in M9 minimal medium containing <sup>15</sup>NH<sub>4</sub>Cl and <sup>13</sup>C- or <sup>12</sup>C-glucose, while unlabeled protein for ITC experiments was expressed in LB medium. The protein was purified by GSH affinity chromatography, followed by cleavage of the GST tag with a PreScission protease and subsequent size exclusion chromatography. Protein NMR samples contained 300 μM of the <sup>13</sup>C, <sup>15</sup>N-labeled protein or 50 μM of the <sup>15</sup>N-labeled protein in 50 mM KPi (pH 8.0) with 10% D<sub>2</sub>O.

GST-tagged truncated Survivin (amino acids 1–120) was expressed in *E. coli* SoluBL21 in 2 L LB medium supplemented with 25 μg mL<sup>-1</sup> kanamycin.<sup>1</sup> Bacteria were grown at 37 °C. Protein expression was induced with 0.2 mM IPTG at an OD<sub>600</sub> of 1.0–1.2 over 20 h at 30 °C. Cells were pelleted and

lysed by sonication in PBS (pH 7.4) supplemented with 1 mM phenylmethylsulfonyl fluoride and 50  $\mu\text{g mL}^{-1}$  lysozyme. GST-Survivin was purified with a GSTrap 4B affinity column, and the tag was cleaved by PreScission protease for 8 h at 4 °C. Subsequent size exclusion chromatography was performed with a HiLoad 26/600 Superdex 75 pg column and a GSTrap 4B column mounted beneath in 50 mM KPi pH 7.4 with 150 mM KCl and 2 mM DTT. Survivin was concentrated and dialyzed against PBS buffer with 10 kDa MWCO dialysis units.

**Nanoparticle Characterization.** The concentrations of gold and copper in the nanoparticle dispersion were determined by atomic absorption spectroscopy (AAS) with a Thermo Electron M-Series spectrometer (graphite tube furnace according to DIN EN ISO/IEC 17025:2005) after dissolving the nanoparticles in *aqua regia*. Analytical disc centrifugation (differential centrifugal sedimentation; DCS) was performed with a CPS Instruments DC 24000 disc centrifuge (24,000 rpm). Two sucrose solutions (8 and 24 wt %) formed a density gradient that was capped with 0.5 mL dodecane as a stabilizing agent. The calibration standard was a poly(vinyl chloride) latex in water with a particle size of 483 nm provided by CPS Instruments. This calibration was carried out before each run. A sample volume of 100  $\mu\text{L}$  of dispersed nanoparticles was used. The recording time was about 6 h at the given centrifugation speed. The density of elemental gold (19,300  $\text{kg m}^{-3}$ ) was used for the computations. UV-vis spectroscopy was performed with a Varian Cary 300 instrument from 200 to 800 nm after background solvent correction (water). Suprasil quartz glass cuvettes with a sample volume of 600  $\mu\text{L}$  were used. High-resolution transmission electron microscopy (HRTEM) was performed with an aberration-corrected FEI Titan transmission electron microscope equipped with a Cs-probe corrector (CEOS Company) operated at 300 kV.<sup>55</sup>

**NMR Spectroscopy.** The nanoparticle samples were dispersed in 600  $\mu\text{L}$   $\text{D}_2\text{O}$  for NMR spectroscopy.  $^1\text{H}$  NMR spectra were recorded with a Bruker AVANCE III 600 MHz spectrometer at room temperature.  $^1\text{H}$ -DOSY experiments (diffusion-ordered spectroscopy) were performed at 25 °C on a Bruker AVANCE III 700 MHz spectrometer equipped with a 5 mm TCI  $^1\text{H}/^{13}\text{C}/^{15}\text{N}/\text{D}$  cryoprobe with a z-gradient in nonspinning mode using a 3 mm NMR tube. A presaturation pulse was added to the  $^1\text{H}$ -DOSY pulse sequence from the Bruker library to suppress the remaining water signal. The diffusion time was set to  $\Delta = 100$  ms and the pulsed gradient duration to  $\delta = 4$  ms for tweezer-functionalized ultrasmall gold nanoparticles. The diffusion time was set to  $\Delta = 100$  ms and the pulsed gradient duration to  $\delta = 2.5$  ms for dissolved tweezer molecules. The gradient strength was incremented in 32 steps from 5 to 95% of the maximum gradient strength (50.4  $\text{G cm}^{-1}$  for a smoothed square gradient pulse) with a linear ramp. The spectra were Fourier-transformed, phased, and integrated using Topspin 3.5. Plotting and fitting of the linearized diffusion data according to the Stejskal–Tanner equation<sup>56,57</sup> were performed with Origin Pro 2017

$$\ln\left(\frac{I}{I_0}\right) = -\gamma^2\delta^2\left(\Delta - \frac{\delta}{3}\right) \cdot D \cdot G^2 \quad (1)$$

with  $I$  being the signal intensity,  $I_0$  the signal intensity without gradient,  $\gamma$  the gyromagnetic ratio of  $^1\text{H}$ ,  $\delta$  the diffusion gradient pulse length,  $\Delta$  the diffusion delay,  $G$  the gradient strength, and  $D$  the translational diffusion coefficient.

The Stejskal–Tanner plots of all nanoparticle signals were first analyzed separately. If the same diffusion coefficient, within the error margin, was obtained for all signals, the relative intensities  $I/I_0$  were averaged. Error bars of the averaged data points represent the standard deviation of this computation.

The hydrodynamic diameter of the functionalized nanoparticle was then calculated by the Stokes–Einstein equation

$$d_{\text{H}} = \frac{k \cdot T}{3\pi \cdot \eta \cdot D} \quad (2)$$

with  $d_{\text{H}}$  being the hydrodynamic diameter,  $k$  the Boltzmann constant,  $T$  the temperature in K,  $\eta$  the dynamic viscosity of  $\text{D}_2\text{O}$  at 25 °C, and  $D$  the translational diffusion coefficient.

The binding of the tweezer-functionalized nanoparticles to  $^{13}\text{C}$ ,  $^{15}\text{N}$ -lysine, or hPin1-WW ( $^{13}\text{C}$ ,  $^{15}\text{N}$ -, or  $^{15}\text{N}$ -labeled) was assessed by NMR titrations in a 3 mm NMR tube on a Bruker AVANCE III 700 MHz spectrometer with a 5 mm TCI cryoprobe. Tweezer-functionalized nanoparticles were added stepwise to 300  $\mu\text{M}$   $^{13}\text{C}$ ,  $^{15}\text{N}$ -lysine, or  $^{13}\text{C}$ ,  $^{15}\text{N}$ -labeled hPin1-WW, and lysine- and arginine-specific H2(C)N experiments<sup>54,58–60</sup> were recorded for each titration step. Relative signal intensities  $I/I_0$  were corrected for the dilution of the sample after nanoparticle addition, plotted against the nanoparticle concentration, and fitted with an exponential decay function to assess the rate of signal decay.<sup>54</sup>

Furthermore,  $^{15}\text{N}$ -HSQC titration experiments of tweezer-functionalized nanoparticles or free monobutynyl tweezer molecules with 50  $\mu\text{M}$   $^{15}\text{N}$ -labeled hPin1-WW were performed. The chemical shift perturbations  $\Delta\delta_{\text{total}}$  of the free tweezer were calculated from the  $^1\text{H}$  and  $^{15}\text{N}$  chemical shift differences ( $\Delta\delta_{\text{H}}$  and  $\Delta\delta_{\text{N}}$ ) as follows:<sup>61</sup>

$$\Delta\delta_{\text{total}} = \sqrt{(\Delta\delta_{\text{H}})^2 + (0.154 \cdot \Delta\delta_{\text{N}})^2} \quad (3)$$

For the nanoparticles, chemical shift perturbation analysis was not possible because the signals of residues involved in binding experienced strong line broadening and disappeared at low ligand concentrations, which made it impossible to track their positions. Instead, relative signal intensities (corrected for the dilution) were plotted against the ligand concentration, and the curves were fitted as described for the H2(C)N signal intensities. The signal decay rates of H2(C)N and HSQC experiments served to qualitatively assess the order of ligand binding but are not directly comparable between the two different experiments because the line broadening also depends on the relaxation rates of the involved nuclei.

**Isothermal Titration Calorimetry.** ITC was performed with a MicroCal iTC200 from Malvern Panalytical at 25 °C with tweezers (control) or nanoparticles in the cell and proteins in the syringe. The proteins were dialyzed overnight at 4 °C against the corresponding buffer using dialysis units with 3 kDa MWCO for hPin1-WW and 10 kDa MWCO for Survivin. ITC titrations with hPin1-WW were performed in 50 mM KPi/90 mM KCl at pH 8.0. Experiments with Survivin were performed in PBS at pH 7.4. Nanoparticles were dissolved in the corresponding dialysis buffer.  $\sim 150$   $\mu\text{M}$  tweezer molecules attached to gold nanoparticles [ $c(\text{Au}) = 250$   $\mu\text{g mL}^{-1}$ ] were titrated with a 3.5 mM solution of hPin1-WW.  $\sim 30$   $\mu\text{M}$  tweezer molecules attached to gold nanoparticles [ $c(\text{Au}) = 170$   $\mu\text{g mL}^{-1}$ ] were titrated with a 1.2 mM solution of Survivin. As control, azide-terminated nanoparticles [ $c(\text{Au}) = 170$   $\mu\text{g mL}^{-1}$ ] were titrated with the proteins at the given

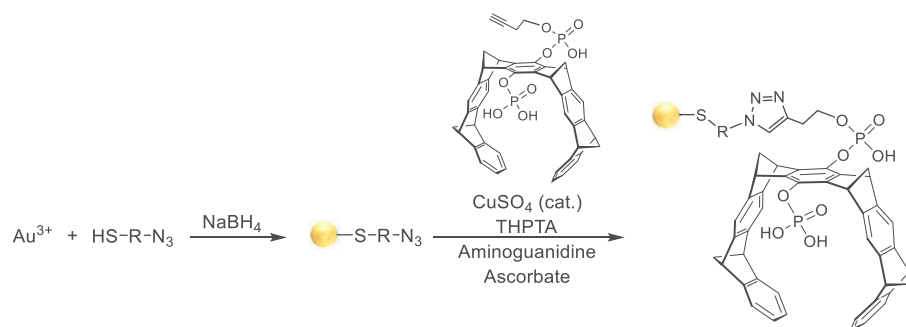


**Figure 2.** Synthetic pathway to tweezer-conjugated ultrasmall gold nanoparticles (Au-KCD-tweezer) by clicking a butynyl-functionalized tweezer to an azide-terminated ultrasmall gold nanoparticle (Au-N<sub>3</sub>). R = K(N<sub>3</sub>)CD.

concentrations. The cell was filled with 275  $\mu\text{L}$ . 38 injections (1  $\mu\text{L}$  each) were added with an equilibration time of 120–150 s between the injections. The injection rate was 2  $\mu\text{L s}^{-1}$ . The reference power was 5  $\mu\text{cal s}^{-1}$ . ITC thermograms were fitted with a stoichiometric equilibrium approach using software AFFINImeter.

## RESULTS AND DISCUSSION

Azide-terminated ultrasmall gold nanoparticles were surface-functionalized by a modified copper-catalyzed azide–alkyne cycloaddition (CuAAC click reaction)<sup>14,32</sup> of the surface-bound peptide 6-azido-lysine-cysteine-asparagine K(N<sub>3</sub>)CD with alkyne-functionalized molecular tweezers (Figure 2).

DCS gave a hydrodynamic diameter of  $1.5 \pm 0.6$  nm for azide-terminated (Au-N<sub>3</sub>) and of  $1.4 \pm 0.5$  nm for tweezer-conjugated gold nanoparticles (Au-KCD-tweezer; Figure 3).

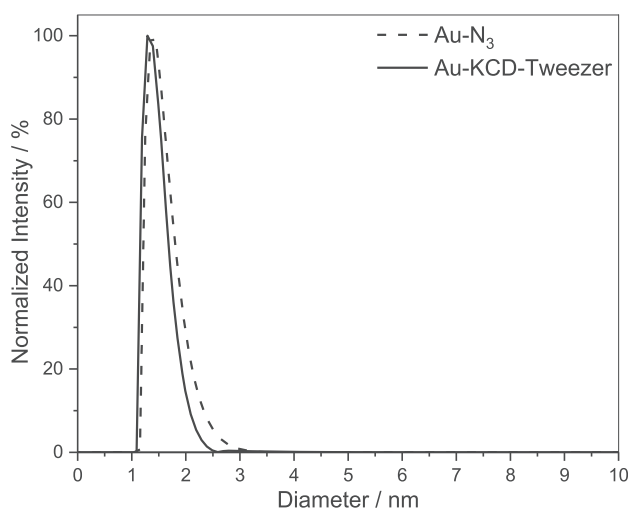


**Figure 3.** DCS curve of azide-terminated gold nanoparticles (Au-N<sub>3</sub>) and of tweezer-conjugated gold nanoparticles (Au-KCD-tweezer).

Note that the ligand shell on the particles generally has a considerable impact on the effective density, particularly, for ultrasmall nanoparticles: a decrease in the effective density leads to a lower sedimentation rate and a systematic underestimation of the hydrodynamic particle diameter.<sup>62</sup> Consequently, the nanoparticles appear considerably smaller in DCS than they actually are. The difference between azide-terminated and tweezer-conjugated gold nanoparticles was not statistically significant. Dynamic light scattering (DLS) did not give reliable results because of the very small particle size.

UV–vis spectroscopy confirmed the binding of the tweezer molecules to the gold nanoparticles and allowed their quantification (absorption band at 280 nm; Figure 4). Note that these nanoparticles are too small to show surface plasmon resonance,<sup>13,63</sup> therefore, we do not see an absorption peak around 500 nm.

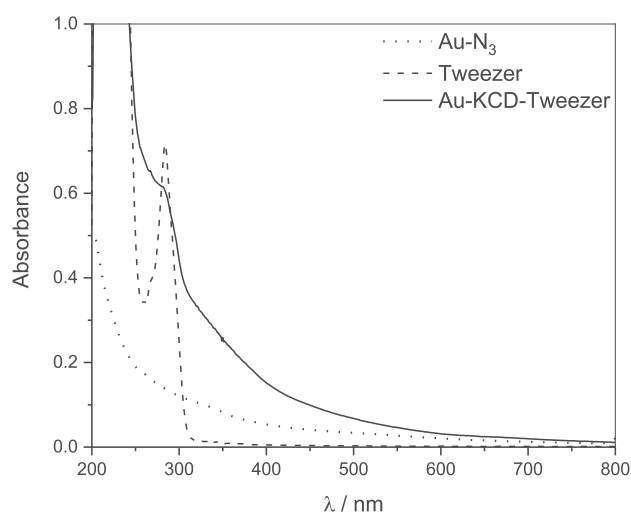


**Figure 4.** UV–vis spectra of azide-terminated gold nanoparticles [Au-N<sub>3</sub>,  $c(\text{Au}) = 22 \mu\text{g mL}^{-1}$ ], tweezer-conjugated gold nanoparticles [Au-KCD-tweezer,  $c(\text{Au}) = 47 \mu\text{g mL}^{-1}$ ], and the dissolved tweezer alone [ $c(\text{tweezer}) = 67 \mu\text{g mL}^{-1}$ ]. The solvent was water in all cases. The absorption band (shoulder) at 280 nm shows the successful attachment of the tweezer to the gold nanoparticle and permits its quantification.

The size of the gold core and its shape were assessed by HRTEM (Figure 5). TEM showed uniform particles with an average diameter of  $2.2 \pm 0.4$  nm, that is, larger than that observed by DCS, as expected because of the limitations of the DCS method (see above). The inset image shows an fcc polyhedron in the [110] zone axis orientation enclosed by (100) and (111) facets. Fourier transformation analysis gave the  $d$ -spacings of fcc elemental gold. The attached ligands were not visible in HRTEM due to the low scattering contrast of the organic ligands. For comparison, the HRTEM diameter of the azide-terminated gold nanoparticles was  $2.0 \pm 0.4$  nm,<sup>32</sup> that is, the click reaction did not significantly influence the metallic core.

The successful clicking of the monobutynyl tweezer to the gold nanoparticles was confirmed by <sup>1</sup>H NMR spectroscopy of

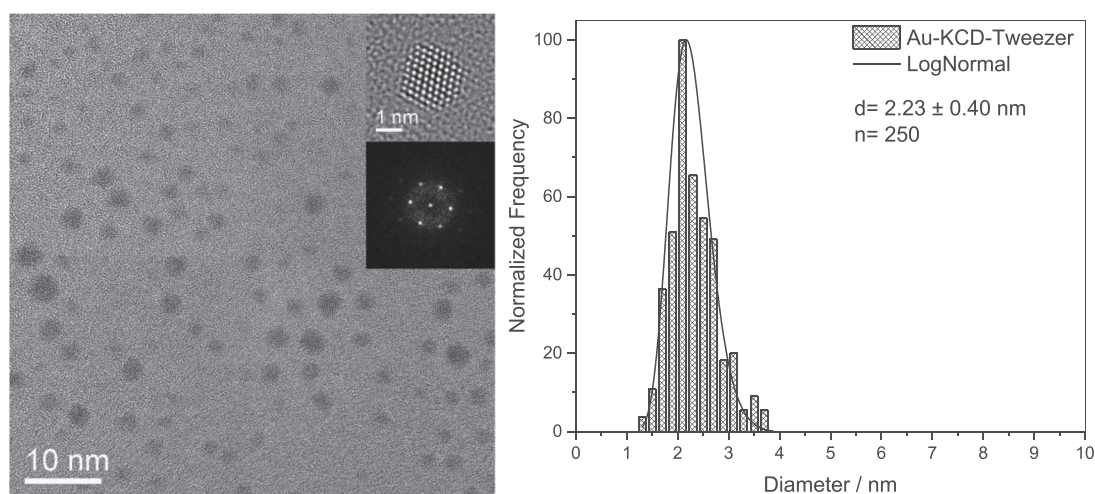


**Figure 5.** HRTEM image and Fourier-transform inset of tweezer-conjugated ultrasmall gold nanoparticles (Au-KCD-tweezer). The Fourier transformation clearly showed the [110] zone axis orientation of the single-crystalline fcc gold nanoparticle with  $d(111) = 2.31$  Å, in excellent agreement with the computed value of  $d(111) = 2.35$  Å (left). The analysis of 250 particles gave a narrow particle size distribution (right).

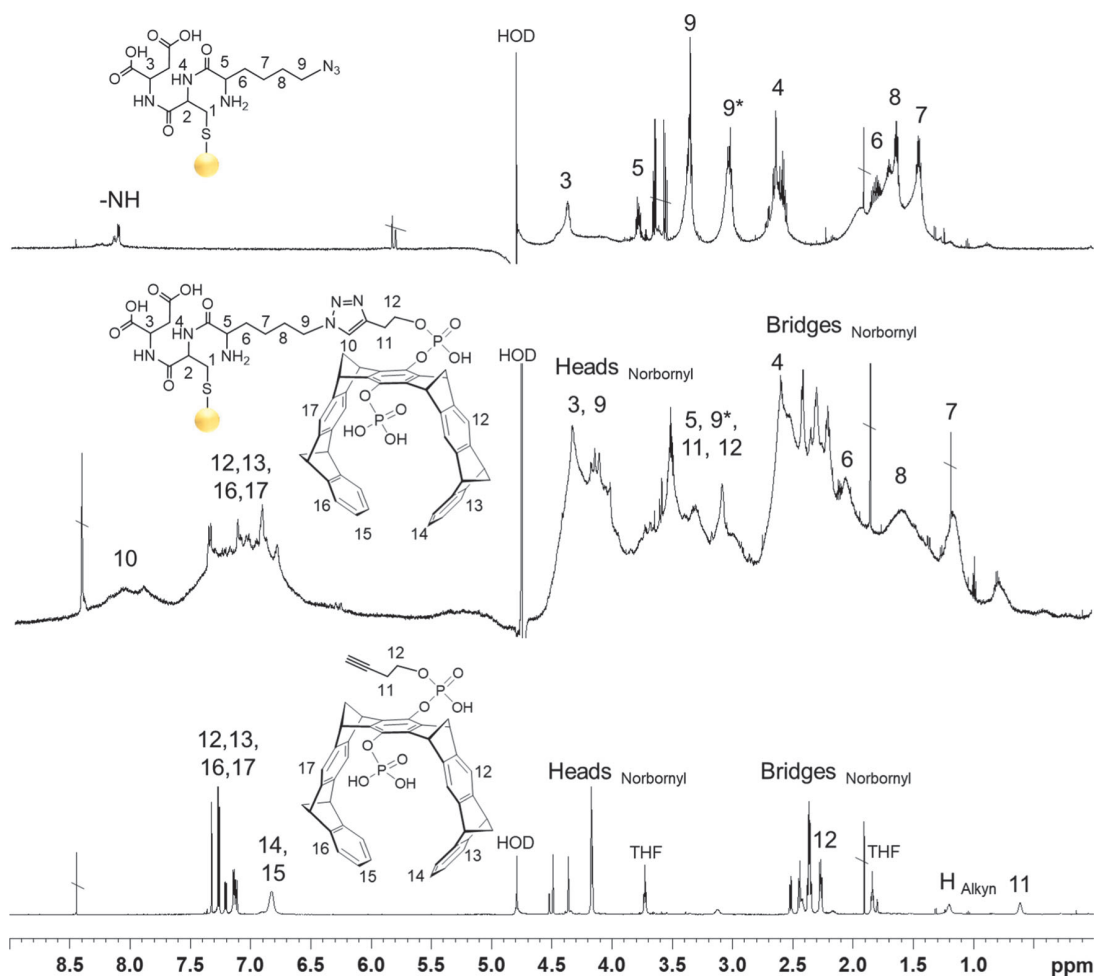


**Figure 6.** <sup>1</sup>H NMR spectra (700 MHz) of the azide-terminated gold nanoparticles (Au-N<sub>3</sub>; top), tweezer-conjugated ultrasmall gold nanoparticles (Au-KCD-tweezer; center), and the dissolved monobutynyl tweezer (bottom), all measured in 10% D<sub>2</sub>O/H<sub>2</sub>O at pH 8.

dispersed nanoparticles (Figure 6). The major aromatic peaks of the nanoparticle-conjugated tweezer (6.5–7.8 ppm) were well pronounced after attachment, including the aromatic

triazole proton from the click conjugation around 8 ppm. The observed strong line broadening compared to that of the free alkyne tweezer is consistent in the vicinity of the metallic

nanoparticle which broadens the NMR signals and has been observed previously for other ligands.<sup>32,33,35,36,64</sup> This analysis was only possible due to the ultrasmall nature of the nanoparticles; NMR spectroscopy of the ligand shell is not possible for larger nanoparticles at all. About 50% of the KCD-lysine residues carried an azide group (H9 at 3.35 ppm). The remaining fraction represents a regular KCD-lysine with a terminal  $\text{NH}_3^+$  group, giving a signal for H9\* at 3.0 ppm. The regular KCD peptide (i.e., lysine without an azide group) was already present in the K(N3)CD peptide batch obtained from the supplier prior to its covalent attachment to the gold core, which was evident in the  $^1\text{H}$  and TOCSY NMR spectra of the peptide (not shown). The intensity ratio, as determined by ERETIC,<sup>65</sup> showed that about 50% of the KCD peptide carried an azide group after conjugation with the gold nanoparticle, giving about 117 ligands with an azide group and the same number with an amino group. Note that the peak at 3.0 ppm was attributed to the  $\beta$ -proton of the cysteine (H1) in an earlier publication.<sup>32</sup> A detailed investigation has now shown that this interpretation was not correct, and this wrong assignment is therefore corrected here. The signals of cysteine experience severe line broadening because of their vicinity to the gold core. Therefore, they are not visible close to the sharper signals of the remaining residues that are not directly bound to the gold core and also experience more internal molecular motion, and therefore, yield a narrower linewidth. Furthermore, overlapping with signals from the other residues cannot be excluded.

$^1\text{H}$ -DOSY-NMR spectroscopy confirmed that the tweezer molecules were indeed attached to the gold nanoparticles as they diffused much more slowly than the free dissolved alkyne tweezer (Figure 7). The hydrodynamic diameter of the tweezer-conjugated nanoparticles was  $2.9 \pm 1.3$  nm. For comparison, the hydrodynamic diameter of the azide-terminated gold nanoparticles was  $2.2 \pm 0.2$  nm,<sup>32</sup> and the hydrodynamic diameter of dissolved tweezer molecules was  $1.4 \pm 0.3$  nm.

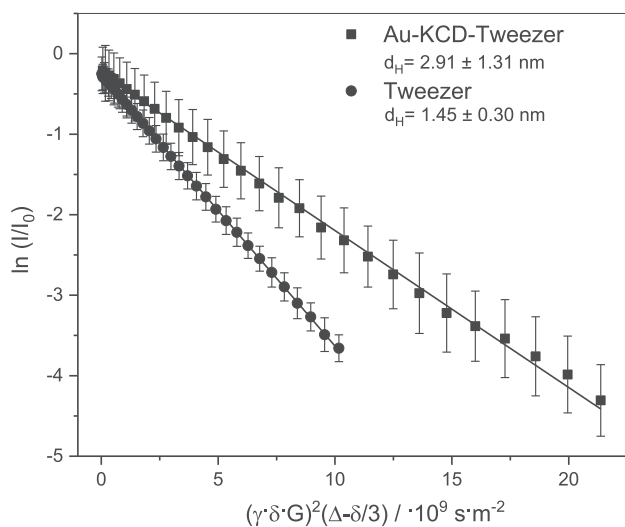


**Figure 7.** Stejskal–Tanner plots of dissolved tweezer molecules (dots) and tweezer-clicked gold nanoparticles (Au-KCD-tweezer; squares). The diffusion coefficients of dissolved tweezer molecules and tweezer-clicked gold nanoparticles, respectively, equal the absolute value of the slope.

The concentration of nanoparticles was determined by measuring the gold concentration by AAS, followed by computing the mass of one gold nanoparticle, based on an average diameter of 2 nm, containing the corresponding number of gold atoms.<sup>32</sup> No copper from the click reaction was detected by AAS, that is, the catalyst was completely removed by the washing steps after the click reaction. The tweezer concentration of the sample was measured by UV–vis spectroscopy. Together with the nanoparticle concentration calculated from the AAS data, we computed that between 11 and 30 tweezer molecules were attached to each gold nanoparticle (diameter 2 nm), depending on the synthesis batch. The reason for this variation is unknown and probably due to slight variations during the synthesis. Consequently, the surface density of tweezers on nanoparticles was determined separately for each synthetic batch.

A number of 11–30 tweezer molecules per nanoparticle (2 nm) gives a surface density between 0.9 and 2.4 tweezer molecules per  $\text{nm}^2$  (footprint,  $0.42\text{--}1.14$   $\text{nm}^2$  per tweezer). 117 azide molecules plus 117 lysine molecules were present on the surface of each nanoparticle (18.6 molecules per  $\text{nm}^2$ ; footprint, each  $0.053$   $\text{nm}^2$ ). This indicates that between 10 and 25% of the azide groups were accessed by the click reaction. This is in good agreement with the earlier results on ligands on ultrasmall nanoparticles, that is, clicked FAM (fluorescein; 8–9 molecules per 2 nm gold nanoparticle;  $0.6\text{--}0.7$  molecules per  $\text{nm}^2$ ; footprint,  $1.48$   $\text{nm}^2$ ),<sup>14,32</sup> clicked Cy3 (5 molecules per 2 nm gold nanoparticle; 0.4 molecules per  $\text{nm}^2$ ; footprint,  $2.5$   $\text{nm}^2$ ),<sup>14</sup> and cysteine (67 molecules per  $1.78$  nm gold nanoparticle; 6.7 molecules per  $\text{nm}^2$ ; footprint,  $0.15$   $\text{nm}^2$ ).<sup>36</sup> Table 1 summarizes all characterization data. These gold particle concentrations (all based on an average diameter of 2 nm) and the derived tweezer concentrations were used for the interpretation of the NMR and ITC experiments described in the following.

It is possible that the steric hindrance of multiple tweezers on the nanoparticle surface affects their recognition ability. Furthermore, the K(N<sub>3</sub>)CD peptide was only about 50% azide-functionalized, with the other half carrying unmodified lysine side chains, and thus, these unmodified peptides were also present on the nanoparticle surface, in addition to the tweezer-clicked peptides. In principle, this could lead to an intramolecular binding of a tweezer to a lysine on the same nanoparticle or a cross-linking between two nanoparticles (tweezer–lysine). To assess whether the surface-conjugated tweezers were still able to bind to lysine as a model compound, we monitored the binding of the tweezer-conjugated nanoparticles to dissolved  $^{13}\text{C}$ ,  $^{15}\text{N}$ -labeled lysine by NMR titration. In the following, we demonstrate that the nanoparticle-conjugated tweezers do not bind to one of these unmodified lysine side chains on the same or on another nanoparticle.

For supramolecular tweezers binding to lysine and arginine, the largest change in the chemical environment occurs for the atoms at the end of the side chain that are inserted into the electron-rich aromatic tweezer cavity. We previously established a lysine-selective H2(C)N experiment which correlates the terminal lysine  $\text{CH}_2$  group ( $\text{H}_e$ ) with the side chain nitrogen atom ( $\text{N}_c$ ) as a tool to distinguish and rank multiple tweezer binding sites within one protein in a semiquantitative way.<sup>54,58</sup> Here, we expand this technique to complex multiavid ligands such as the tweezer-functionalized nanoparticles. Binding of tweezers to lysine and arginine occurs on the intermediate-to-fast time scale which results in strong line

Table 1. Particle Size and Ligand Quantification Data of all Prepared Nanoparticles<sup>a</sup>

particle	diameter by DCS/nm	diameter by HRTEM/nm	diameter by <sup>1</sup> H NMR DOSY/nm	composition
dissolved K(N <sub>3</sub> )CD (free azide ligand) <sup>32</sup>			1.5 ± 0.2	
azide-terminated gold nanoparticles (Au-N <sub>3</sub> ) <sup>32</sup>	1.5 ± 0.6	2.0 ± 0.4	2.2 ± 0.2	117 azide groups and 117 lysine groups per nanoparticle (2 nm; by <sup>1</sup> H NMR spectroscopy)
tweezer-conjugated gold nanoparticles (Au-KCD-Tweezer)	1.4 ± 0.5	2.2 ± 0.4	2.9 ± 1.3	11–30 tweezer molecules per nanoparticle (2 nm; by UV–vis spectroscopy)
dissolved monobutynyl tweezer			1.5 ± 0.3	

<sup>a</sup>Note that DCS systematically underestimates the particle size. HRTEM gives the diameter of the metallic gold core and <sup>1</sup>H NMR DOSY gives the hydrodynamic diameter of water-dispersed nanoparticles. All results confirm the stability of the gold core during the surface functionalization reactions.

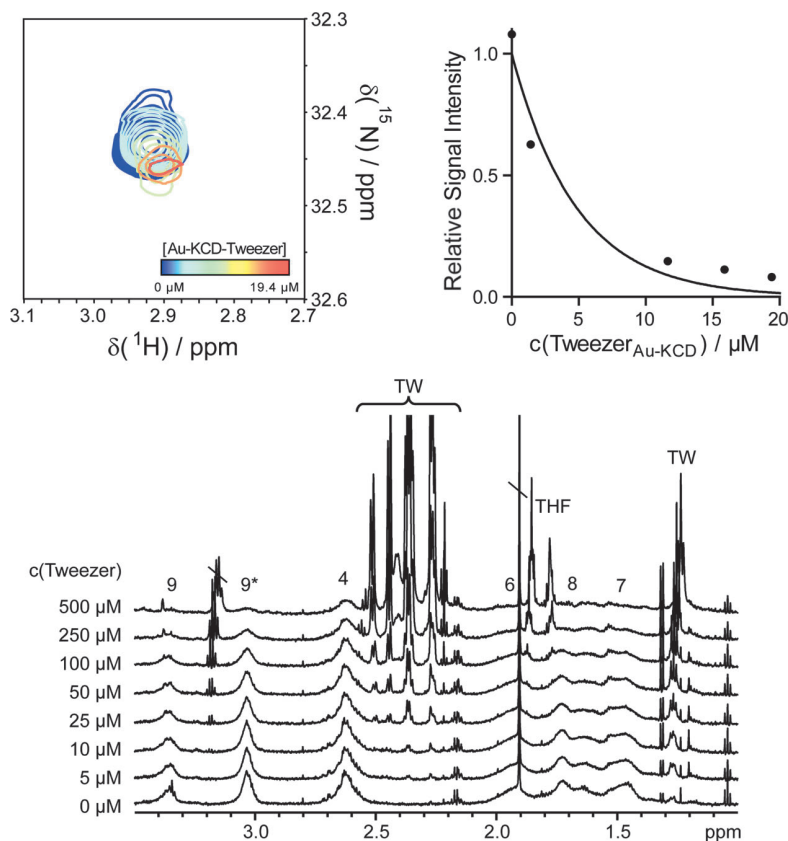


**Figure 8.** Top: H<sub>2</sub>(C)N NMR spectra of the titration of dissolved <sup>15</sup>N<sup>13</sup>C-labeled lysine (300 μM, 50 mM KPi buffer at pH 8) with tweezer-conjugated gold nanoparticles (Au-KCD-tweezer), recorded at 700 MHz. Spectral overlay (left) and plot of relative signal intensities against the tweezer concentration (on Au-KCD-tweezer nanoparticles) (right) are shown. The peak broadening and the resulting decay in the signal intensity are indicative of the tweezer binding to lysine. The final concentration of nanoparticle-bound tweezers (19.4 μM) corresponds to a 1:10 molar ratio of tweezers to lysine. Bottom: <sup>1</sup>H NMR titration of Au-N<sub>3</sub> nanoparticles with a monobutynyl tweezer. Some line broadening is observed at much higher concentrations compared to that of a tweezer binding to free lysine. All signals broaden and no signal shifts are observed, indicating a nonspecific electrostatic interaction of the tweezer with the nanoparticle at high concentrations but little to no encapsulation of a lysine side chain in the tweezer cavity.

broadening and thus a loss of signal intensity, even at very low tweezer concentrations and before a significant signal shift takes place.<sup>54</sup> Consequently, the lysine NMR signal has already broadened to disappear well below a molar 1:1 ratio of tweezer to lysine (Figure 8). A similar signal broadening was observed when titrating dissolved diphosphate tweezers to lysine.<sup>54</sup> If the unreacted lysines present on the nanoparticle surface (which are invisible in this NMR experiment) would significantly compete with the visible, isotope labeled-lysine, the line broadening would be expected to be much less pronounced and to occur at much higher ligand concen-

trations. As this is not the case, we conclude that the clicked tweezers on the gold nanoparticle surface were able to act as lysine binders and that the remaining lysine residues on the nanoparticle surface from the K(N<sub>3</sub>)CD ligand did not interfere with this binding process. In addition, the free monobutynyl tweezer was added to the Au-N<sub>3</sub> nanoparticles in a control <sup>1</sup>H NMR titration to test whether the tweezer can bind the lysine side chains to the nanoparticle. Line broadening of the nanoparticle signals occurred only at tweezer concentrations that are much higher compared to that of the titrating tweezer with free lysine,<sup>41</sup> without shifting

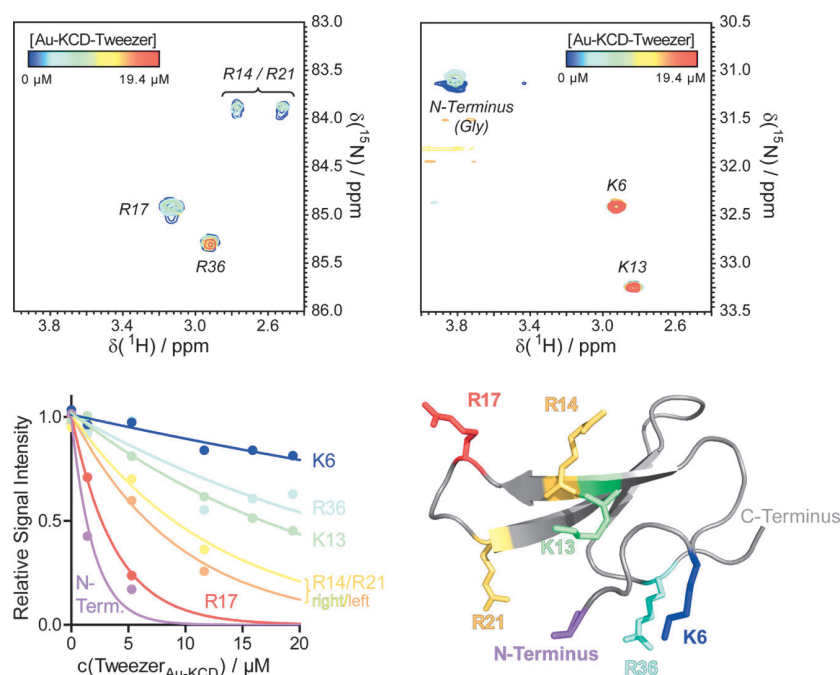


**Figure 9.** H2(C)N spectra of the arginine residues R14, R17, R24, and R36 (top left; signals of R14 and R21 are both split and overlapped) and the lysine residues K6 and K13 (top right) of the  $^{13}\text{C}$ ,  $^{15}\text{N}$ -labeled hPin1-WW domain ( $300\ \mu\text{M}$ ) at increasing concentrations of tweezer-conjugated ultrasmall gold nanoparticles (Au-KCD-tweezer). The final concentration of nanoparticle-bound tweezers ( $19.4\ \mu\text{M}$ ) corresponds to a 1:10 molar ratio of tweezer to protein. A decrease in signal intensity indicated binding, with preferred binding sites showing a faster decay. The plot of signal intensities versus the nanoparticle-bound tweezer concentration (bottom left) showed the fastest intensity decay for the N-terminus and for R17, indicating a preferred binding at these sites. Bottom right: Binding sites mapped onto the hPin1-WW domain structure (PDB no. 2M81) with the same color code as in the intensity plot; lysine and arginine residues are shown as sticks.

of the signals. This is probably due to nonspecific electrostatic interactions and “walking” of the tweezer on the nanoparticle surface like it was observed for proteins with many lysines on the surface.<sup>66</sup> As on nanoparticles with covalently attached tweezers, the tweezers cannot walk and still bind to external lysines, these effects on the Au-N<sub>3</sub> nanoparticles are not a concern for the subsequent protein binding studies.

After having confirmed the targeting ability of the tweezers bound to the nanoparticles, the binding to lysine and arginine on the surface of proteins was investigated. We chose the WW domain of the human peptidyl prolyl cis–trans isomerase (PPIase) hPin1 as a first model system. The hPin1-WW domain (4.5 kDa; hPin1-WW) consists of 36 amino acids, including two lysines and four arginines. Its interaction with free diphosphate tweezers has been thoroughly investigated by NMR.<sup>54</sup> In addition to the two lysines, the N-terminal glycine H $\alpha$ /N correlation is also visible in the lysine H2(C)N spectrum.<sup>54</sup> Tweezer-functionalized gold nanoparticles were titrated with  $^{13}\text{C}$ ,  $^{15}\text{N}$ -labeled hPin1-WW, recording both lysine- and arginine-specific H2(C)N spectra of the protein (Figure 9).

Because these experiments are so sensitive even at substoichiometric ligand concentrations, they are well suited to monitor the binding event of the Au-KCD-tweezer nanoparticles, although a stoichiometric ratio could not be achieved due to the high protein concentrations needed. In earlier experiments with dissolved phosphate tweezers and hPin1, a distinct binding order was obtained from the rates of signal decay in the H2(C)N spectra: the signal of R17 broadened and disappeared at very low tweezer concentrations, while the R36 and the N-terminal glycine signals remained

nearly unchanged, giving a binding order of  $\text{R17} \gg \text{K6} \approx \text{R14} \approx \text{R21} > \text{K13} \gg \text{R36}$ .<sup>54</sup>

Interestingly, a considerably different binding order was observed with the tweezer-conjugated nanoparticles: N-terminus (G)  $\approx$  R17 > R21/R14 > K13 > R36 > K6. The R17 signal in the H2(C)N spectrum broadened first as with free tweezers, but the N-terminus (which was not bound by the free tweezers at all) showed a strong line broadening at low ligand concentrations as well. The mechanism by which the N-terminal glycine residue is bound remains open. It is unlikely that it can be inserted into the tweezer cavity because it is too short, but the observed changes may result from a hydrogen bond to the KCD peptide scaffold in the vicinity of the covalently attached tweezers. It is unlikely that this behavior is caused by allosteric changes as the N-terminus is flexible and unstructured (pdb 2M81). Furthermore, K6 was affected least by the nanoparticles, although it was well bound by free tweezer molecules.<sup>54</sup>

Only substoichiometric tweezer concentrations could be investigated because the H2(C)N experiments required a high protein concentration and the available amounts of nanoparticles were limited. Therefore, we performed an  $^{15}\text{N}$ -HSQC titration of  $^{15}\text{N}$ -labeled hPin1-WW which required a lower protein concentration, so that an excess of tweezers to protein was achieved. The  $^{15}\text{N}$ -HSQC spectra show the correlation of the amide H and N, as well as some side-chain NH correlations. Ligand binding results in a signal shift and also some line broadening for residues close to the binding site.

Titration of the free monobutynyl tweezer with  $^{15}\text{N}$ -hPin1-WW (Figure 10) resulted in a shift of signals in the region between residues 15–22, including the two arginine residues R17 and

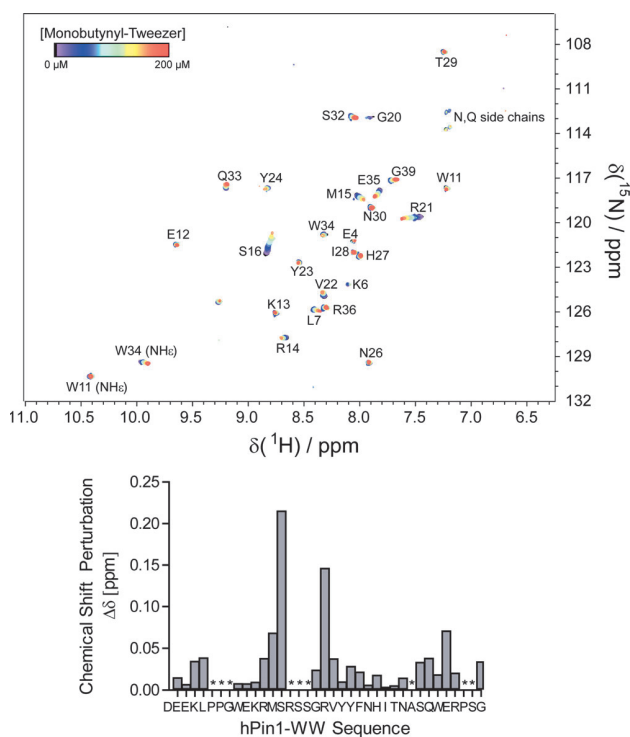


**Figure 10.**  $^{15}\text{N}$ -HSQC titration of  $^{15}\text{N}$ -hPin1-WW (50  $\mu\text{M}$ , 50 mM KPi buffer at pH 8) with a dissolved monobutynyl tweezer. Spectral overlay (top) and chemical shift perturbations (bottom) plotted against the protein sequence for a 150  $\mu\text{M}$  tweezer. Amino acids that are not visible in the HSQC spectrum are labeled with \*.

R21. For the Au-KCD-tweezer nanoparticles, shifts were observed for the same signals, which confirmed the preference for R17 observed in the H2(C)N experiments (Figure 11). The most striking difference compared to the free monobutynyl tweezer was a strong intensity loss due to line broadening of multiple signals, which led to their complete disappearance. Therefore, chemical shift perturbations could only be qualitatively assessed. The signal decay curves for the lysine and arginine residues (Figure 11, bottom left) and the ligand concentration at which each signal disappeared completely (Figure 11, bottom right) showed that the region between R17 and R21 responded to very low nanoparticle concentrations, confirming it as the preferred binding site. The observed line broadening could point to a shift of the binding equilibrium from fast to intermediate exchange, which implies a tighter binding of the nanoparticle compared to that of free tweezers. An exchange between different tweezer molecules of the same nanoparticle (“walking” or “rolling”) could also account for the low signal intensities at the preferred binding sites.

In summary, the H2(C)N and HSQC NMR experiments point to R17 as a preferred binding site for both nanoparticle-conjugated tweezers and free tweezers. Interestingly, the order of binding observed in the H2(C)N spectra is different between nanoparticles and free tweezers, which likely reflects an increased multiavid binding in favor of lysine and arginine residues in the vicinity of R17. K6, which ranks lower in the preferred binding hierarchy of the nanoparticles, lies on the opposite side of the protein. While free tweezers can bind K6 in addition to other sites without steric hindrance, tweezers on the same particle that binds to R17 cannot reach K6, and the

size of the tweezer-decorated nanoparticle might be too large to accommodate a second one binding on the K6 side of hPin1-WW. The line broadening in the HSQC titration of the nanoparticles can also be attributed to their multiavid nature, but more structural details of this interaction cannot be derived from the collected data. We tentatively attribute the observed differences to the fact that the tweezers clicked to a nanoparticle surface show a distinct binding pattern with potential multiavidity (more than one tweezer on a given nanoparticle binds to the same protein molecule) and also to steric hindrance due to the larger size of the nanoparticle compared to that of free tweezers.

For a more quantitative assessment of binding, an ITC titration of hPin1-WW to tweezer-conjugated nanoparticles was performed. However, data analysis of such a complex system involving a multiavid ligand binding to a protein with multiple potential binding sites with possibly different binding constants, is challenging. Because of the lack of a good model describing the binding equilibria and the risk of overfitting, the titrations were fitted with the simplest model that provided a good fit of the data (stoichiometric equilibria approach/simple model by AFFINImeter). This model assumes that the protein and the tweezer form a 1:1 complex. We opted to use the concentration of the tweezer units rather than gold cores because this yielded reasonably well-fitted binding curves. This in turn implies 11–30 tweezers on each nanoparticle independently binding to a protein, which appears unlikely due to steric hindrance. Therefore, the observed  $K_D$  values reflect the correct order of magnitude, but the absolute value has to be taken with care and experimental stoichiometries could not be determined.

Binding of hPin1-WW to tweezer-conjugated nanoparticles resulted in an exothermic binding reaction with a dissociation constant of  $K_D = 41 \pm 2 \mu\text{M}$  (Figure 12). A control titration of the hPin1-WW domain with azide-terminated gold nanoparticles caused only small endothermic peaks (Figure 13). Hence, an unspecific binding of the protein to the nanoparticles can be excluded. For comparison, a  $K_D$  of  $12 \pm 2 \mu\text{M}$  was determined for the interaction of free phosphate tweezers with hPin1-WW with a multiple-site binding model by ITC.<sup>54</sup>

Finally, binding of the tweezer-conjugated nanoparticles to the larger protein Survivin, an interesting cancer target, was measured by ITC (Figure 14). The tweezer-conjugated gold nanoparticles gave much larger exothermic peaks compared to those of azide-terminated gold nanoparticles, which indicates a stronger interaction with Survivin and underscores that an unspecific nanoparticle–protein binding is not present (Figure 13). The ITC titration of Survivin with the tweezer-conjugated nanoparticles resulted in a dissociation constant  $K_D = 8 \pm 1 \mu\text{M}$  with a fixed 1:1 stoichiometry of protein to tweezer. For comparison, the dissociation constant of unconjugated phosphate tweezers to Survivin was  $38 \pm 4 \mu\text{M}$  (unpublished). These values were in contrast with higher affinities determined earlier for single tweezer molecules on the surface of p97’s N domain (6  $\mu\text{M}$ )<sup>39</sup> and 14-3-3 proteins (30  $\mu\text{M}$ ).<sup>42</sup> However, especially, the biphasic curves obtained from the 14-3-3 titration with tweezers document that their affinity to any given lysine or arginine on a protein surface is strongly affected by topographical factors such as steric accessibility, local surface potential, positively charged neighbor residues, and hydrophobic or aromatic interactions.<sup>39,42,54</sup> Thus, tweezer affinities not only vary between different proteins but also between basic residues of the same protein.



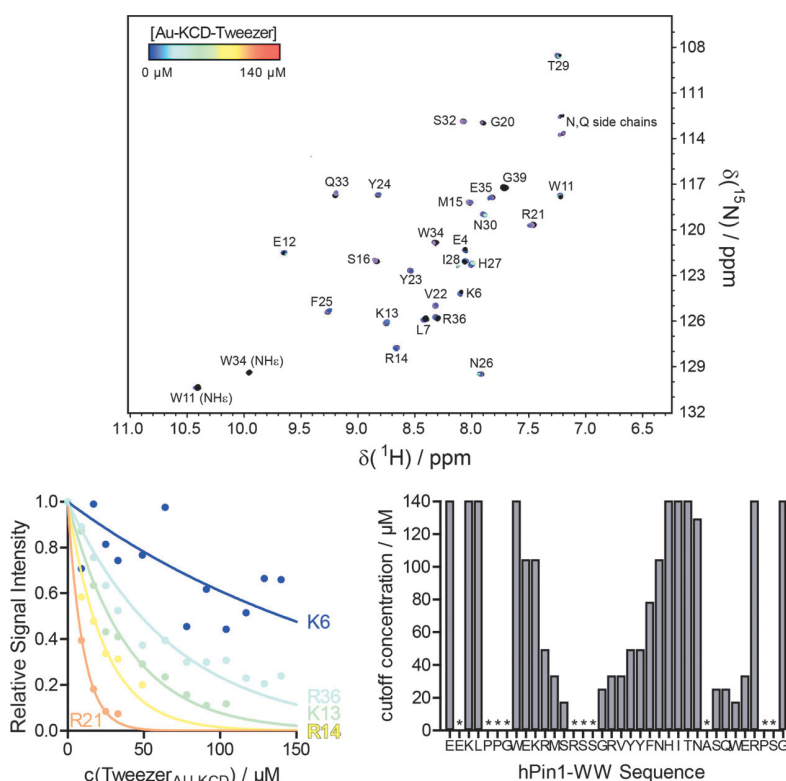


**Figure 11.**  $^{15}\text{N}$ -HSQC NMR titration of the hPin1-WW domain (50  $\mu\text{M}$ , 50 mM KPi buffer at pH 8) with tweezer-conjugated ultrasmall gold nanoparticles (Au-KCD-tweezer) recorded at 700 MHz (top). The signals of the two tryptophan indole NHs are labeled with NH $\epsilon$ . Signal shifts and reduced intensities indicate binding. The plot of signal intensities against the nanoparticle-bound tweezer concentration (bottom left, shown for lysine and arginine residues only) showed the same order of binding as in the H2(C)N experiments (Figure 9). R17 and the N-terminus were not visible in the HSQC spectrum. A plot of cutoff concentrations (bottom right, last concentration where a signal is still visible) against the hPin1-WW sequence indicated preferred binding to R17 and R21 as shown by the low cutoff concentrations. Amino acids that are not visible in the HSQC spectrum are labeled with an asterisk \*.

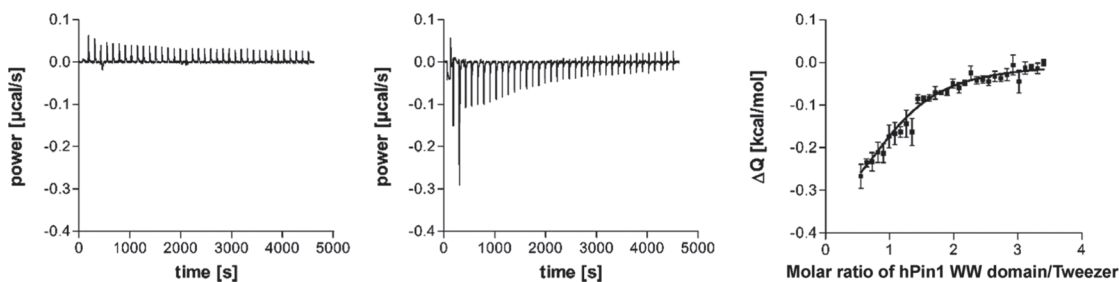


**Figure 12.** hPin1-WW binds to tweezer-conjugated gold nanoparticles (Au-KCD-tweezer), as shown by ITC. 3.5 mM hPin1-WW domain was titrated to tweezer-conjugated or azide-terminated nanoparticles (Au-N $_3$ ) in 50 mM KPi, 90 mM KCl, pH 8.0 at 25  $^{\circ}\text{C}$ . Left: Processed heating power over time from hPin1-WW titration to azide-terminated gold nanoparticles (Au-N $_3$ ; control). Center: Processed heating power over time from hPin1-WW domain titration with tweezer-conjugated gold nanoparticles (Au-KCD-tweezer). Right: Integrated energy values over the molar ratio of protein and tweezer. All data were processed and fitted with the simple model stoichiometric approach with software AFFINImeter. The first three data points were excluded from the analysis.

## CONCLUSIONS

In this work, we demonstrated how multiple selective supramolecular ligands can be covalently attached to ultrasmall nanoparticles and investigated their unique binding behavior toward two model proteins. Employing click chemistry, alkyne-functionalized molecular tweezer molecules can be covalently attached to the surface of azide-containing ultrasmall gold nanoparticles (2 nm). Each nanoparticle carries about 11–30 tweezer molecules. NMR spectroscopic investigations with the model protein hPin1-WW show that molecular tweezers,

clicked onto the surface of the nanoparticles, are able to specifically interact with amino acids on the protein surface. A competition to protein binding by the remaining free lysine side chains on the nanoparticle surface could be excluded. Clearly, the binding properties of the tweezers to attach to lysine and arginine, both free and on a protein surface, are still present after attaching them to a nanoparticle.

The specific interaction of the new nanoparticle tweezer conjugates with proteins was quantitatively assessed by NMR spectroscopy and ITC with hPin1 and Survivin. In contrast to dissolved tweezer molecules, the particle-bound tweezers not

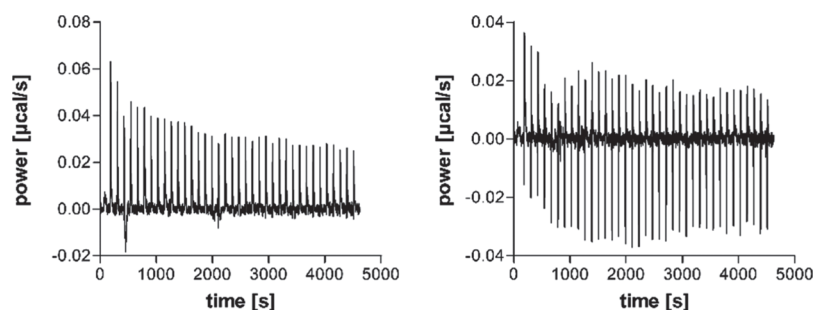


Figure 13. Magnification of the control experiments by ITC from Figure 12, showing the unspecific interaction between azide-terminated gold nanoparticles (Au-N<sub>3</sub>) with hPin1 WW (left) and Survivin (right).

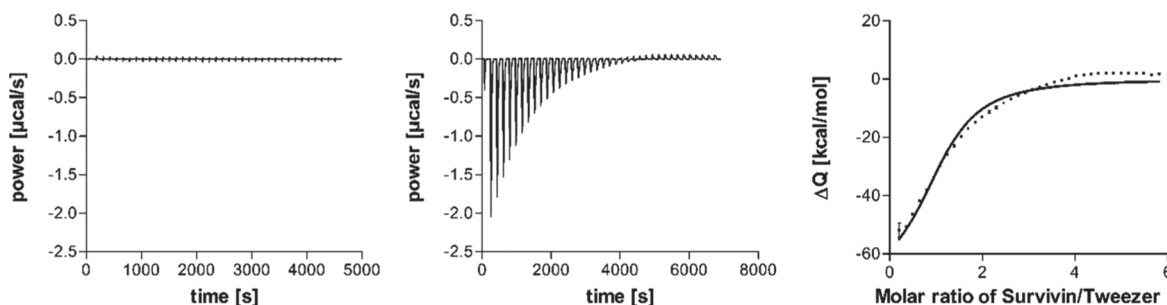


Figure 14. Survivin binds to tweezer-conjugated gold nanoparticles, as shown by ITC. 1.2 mM Survivin was titrated with tweezer-conjugated or azide-terminated nanoparticles in PBS, pH 7.4, at 25 °C. Left: Processed heating power over time from the ITC titration of Survivin with azide-terminated gold nanoparticles (Au-N<sub>3</sub>; control). Center: Processed heating power over time from Survivin titration with tweezer-conjugated gold nanoparticles (Au-KCD-tweezer). Right: Integrated energy values over the molar ratio of protein and tweezer. The data were processed and fitted using the simple model stoichiometric approach of software AFFINImeter. The deviation between data and fit indicates that multiple binding events are present, but as there is no clear plateau between the phases ( $K_D$ s are too similar), it was not possible to obtain reliable parameters from a multistep binding model.

only bind to the lysine and arginine residues within the hPin1-WW domain, but also interact strongly with the glycine residue of the N-terminus or in its immediate vicinity. For both model systems, the tweezer-conjugated nanoparticles bind to the protein with a comparable affinity with respect to the free tweezers. Generally, for a multiavid ligand, a tighter binding compared to its monoavid version is expected. However, this assumes that all ligands can reach their protein receptor site at the same time. For the nanoparticles, this is probably not the case because the tweezer ligands are distributed in a spherical geometry, and therefore, not all of them will be able to reach the protein surface at the same time.

A possible gain in binding affinity will therefore greatly depend on the topology and positioning of lysine and arginine residues on a specific target protein surface. While an advantage of the nanoparticle conjugate over free tweezers might not be obvious from the  $K_D$  values alone, there are two interesting features of the nanoparticles, which we will explore in the future: the size of a tweezer-conjugated nanoparticle is much larger compared to a single tweezer molecule. Therefore, it is possible to cover and thus block a larger epitope on the protein surface which can be favorable when aiming to inhibit protein–protein interactions. Furthermore, the multiavidity of the nanoparticle system offers the possibility to attach more than one ligand type on a single particle. The ligand density on the nanoparticle could also be varied by mixing tweezers with “space holder” ligands such as cysteine. This also opens up the possibility to improve the affinity and selectivity by combining different recognition units (heteroavidity).

Finally, covalently functionalized ultrasmall gold nanoparticles, decorated with supramolecular binders, may be well suited for target proteins both inside and outside cells, because they have the potential to enter cells, and in favorable cases, also the cell nucleus.

## AUTHOR INFORMATION

### Corresponding Authors

Christine Beuck – Department of Structural and Medicinal Biochemistry, Centre for Medical Biotechnology (ZMB), University of Duisburg-Essen, 45117 Essen, Germany; Email: [christine.beuck@uni-due.de](mailto:christine.beuck@uni-due.de)

Matthias Epple – Inorganic Chemistry and Center for Nanointegration Duisburg-Essen (CeNIDE), University of Duisburg-Essen, 45117 Essen, Germany; [orcid.org/0000-0002-1641-7068](https://orcid.org/0000-0002-1641-7068); Email: [matthias.epple@uni-due.de](mailto:matthias.epple@uni-due.de)

### Authors

Selina Beatrice van der Meer – Inorganic Chemistry and Center for Nanointegration Duisburg-Essen (CeNIDE), University of Duisburg-Essen, 45117 Essen, Germany

Inesa Hadrovic – Organic Chemistry, University of Duisburg-Essen, 45117 Essen, Germany

Annika Meiners – Department of Molecular Biology II, Centre for Medical Biotechnology (ZMB), University of Duisburg-Essen, 45117 Essen, Germany

Kateryna Loza – Inorganic Chemistry and Center for Nanointegration Duisburg-Essen (CeNIDE), University of Duisburg-Essen, 45117 Essen, Germany

Marc Heggen – Ernst Ruska-Centre for Microscopy and Spectroscopy with Electrons, Forschungszentrum Jülich GmbH, 52425 Jülich, Germany

Shirley K. Knauer – Department of Molecular Biology II, Centre for Medical Biotechnology (ZMB), University of Duisburg-Essen, 45117 Essen, Germany

Peter Bayer – Department of Structural and Medicinal Biochemistry, Centre for Medical Biotechnology (ZMB), University of Duisburg-Essen, 45117 Essen, Germany

Thomas Schrader – Organic Chemistry, University of Duisburg-Essen, 45117 Essen, Germany; [orcid.org/0000-0002-7003-6362](https://orcid.org/0000-0002-7003-6362)

Complete contact information is available at:  
<https://pubs.acs.org/10.1021/acs.jpccb.0c09846>

## Notes

The authors declare no competing financial interest.

## ACKNOWLEDGMENTS

The authors acknowledge financial support by the Deutsche Forschungsgemeinschaft (DFG) in the framework of the Collaborative Research Centre CRC 1093: Supramolecular Chemistry on Proteins. The authors thank Dr. Torsten Schaller and Dr. Felix Niemeyer for experimental assistance with NMR spectroscopy and Peter Binz for technical support. The authors thank Kerstin Brauner and Robin Meya for elemental analyses. The authors thank Anna-Lena Bunte for the experimental assistance and Alma Rute for the preparation of hPin1-WW. The authors thank Prof. Hemmo Meyer for providing access to the ITC equipment.

## REFERENCES

- (1) Vallet, C.; Aschmann, D.; Beuck, C.; Killa, M.; Meiners, A.; Mertel, M.; Ehlers, M.; Bayer, P.; Schmuck, C.; Giese, M.; et al. Functional disruption of the cancer-relevant interaction between survivin and histone H3 with a guanidiniocarbonyl pyrrole ligand. *Angew. Chem., Int. Ed. Engl.* **2020**, *59*, 5567–5571.
- (2) Hadrovic, I.; Rebmann, P.; Klärner, F. G.; Bitan, G.; Schrader, T. Molecular lysine tweezers counteract aberrant protein aggregation. *Front. Chem.* **2019**, *7*, 657.
- (3) Kubota, R.; Hamachi, I. Protein recognition using synthetic small-molecular binders toward optical protein sensing in vitro and in live cells. *Chem. Soc. Rev.* **2015**, *44*, 4454–4471.
- (4) Milroy, L.-G.; Grossmann, T. N.; Hennig, S.; Brunsveld, L.; Ottmann, C. Modulators of protein–protein interactions. *Chem. Rev.* **2014**, *114*, 4695–4748.
- (5) Peczuł, M. W.; Hamilton, A. D. Peptide and protein recognition by designed molecules. *Chem. Rev.* **2000**, *100*, 2479–2494.
- (6) Kopp, M.; Kollenda, S.; Epple, M. Nanoparticle–protein interactions: Therapeutic approaches and supramolecular chemistry. *Acc. Chem. Res.* **2017**, *50*, 1383–1390.
- (7) Algar, W. R.; Jeen, T.; Massey, M.; Peveler, W. J.; Asselin, J. Small surface, big effects, and big challenges: toward understanding enzymatic activity at the inorganic nanoparticle–substrate interface. *Langmuir* **2019**, *35*, 7067–7091.
- (8) Ferreira, R. S.; Lira, A. L.; Torquato, R. J. S.; Schuck, P.; Sousa, A. A. Mechanistic insights into ultrasmall gold nanoparticle–protein interactions through measurement of binding kinetics. *J. Phys. Chem. C* **2019**, *123*, 28450–28459.
- (9) Scaletti, F.; Hardie, J.; Lee, Y.-W.; Luther, D. C.; Ray, M.; Rotello, V. M. Protein delivery into cells using inorganic nanoparticle–protein supramolecular assemblies. *Chem. Soc. Rev.* **2018**, *47*, 3421–3432.
- (10) Boselli, L.; Polo, E.; Castagnola, V.; Dawson, K. A. Regimes of biomolecular ultrasmall nanoparticle interactions. *Angew. Chem., Int. Ed.* **2017**, *56*, 4215–4218.
- (11) Rotello, V. M. Organic chemistry meets polymers, nanoscience, therapeutics and diagnostics. *Beilstein J. Org. Chem.* **2016**, *12*, 1638–1646.
- (12) Jiang, Y.; Wang, M.; Hardie, J.; Tonga, G. Y.; Ray, M.; Xu, Q.; Rotello, V. M. Chemically engineered nanoparticle–protein interface for real-time cellular oxidative stress monitoring. *Small* **2016**, *12*, 3775–3779.
- (13) Zarschler, K.; Rocks, L.; Licciardello, N.; Boselli, L.; Polo, E.; Garcia, K. P.; De Cola, L.; Stephan, H.; Dawson, K. A. Ultrasmall inorganic nanoparticles: State-of-the-art and perspectives for biomedical applications. *Nanomedicine* **2016**, *12*, 1663–1701.
- (14) Sokolova, V.; Nzou, G.; van der Meer, S. B.; Ruks, T.; Heggen, M.; Loza, K.; Hagemann, N.; Murke, F.; Giebel, B.; Hermann, D. M.; et al. Ultrasmall gold nanoparticles (2 nm) can penetrate and enter cell nuclei in an in-vitro brain spheroid model. *Acta Biomater.* **2020**, *111*, 349–362.
- (15) Dzwonek, M.; Załubiniak, D.; Piątek, P.; Cichowicz, G.; Męczynska-Wielgosz, S.; Stępkowski, T.; Kruszewski, M.; Więckowska, A.; Bilewicz, R. Towards potent but less toxic nanopharmaceuticals - lipoic acid bioconjugates of ultrasmall gold nanoparticles with an anticancer drug and addressing unit. *RSC Adv.* **2018**, *8*, 14947–14957.
- (16) Yang, L.; Shang, L.; Nienhaus, G. U. Mechanistic aspects of fluorescent gold nanocluster internalization by live HeLa cells. *Nanoscale* **2013**, *5*, 1537–1543.
- (17) Leifert, A.; Pan-Bartnek, Y.; Simon, U.; Jahnen-Dechent, W. Molecularly stabilised ultrasmall gold nanoparticles: synthesis, characterization and bioactivity. *Nanoscale* **2013**, *5*, 6224–6242.
- (18) Huo, S.; Jin, S.; Ma, X.; Xue, X.; Yang, K.; Kumar, A.; Wang, P. C.; Zhang, J.; Hu, Z.; Liang, X.-J. Ultrasmall gold nanoparticles as carriers for nucleus-based gene therapy due to size-dependent nuclear entry. *ACS Nano* **2014**, *8*, 5852–5862.
- (19) Zhang, X.; Shastry, S.; Bradforth, S. E.; Nadeau, J. L. Nuclear uptake of ultrasmall gold-doxorubicin conjugates imaged by fluorescence lifetime imaging microscopy (FLIM) and electron microscopy. *Nanoscale* **2015**, *7*, 240–251.
- (20) Elliott, E. W.; Ginzburg, A. L.; Kennedy, Z. C.; Feng, Z.; Hutchison, J. E. Single-step synthesis of small, azide-functionalized gold nanoparticles: versatile, water-dispersible reagents for click chemistry. *Langmuir* **2017**, *33*, 5796–5802.
- (21) Chen, Y.; Xianyu, Y.; Jiang, X. Surface modification of gold nanoparticles with small molecules for biochemical analysis. *Acc. Chem. Res.* **2017**, *50*, 310–319.
- (22) Li, N.; Zhao, P.; Salmon, L.; Ruiz, J.; Zabawa, M.; Hosmane, N. S.; Astruc, D. “Click” star-shaped and dendritic PEGylated gold nanoparticle-carborane assemblies. *Inorg. Chem.* **2013**, *52*, 11146–11155.
- (23) Rousseau, G.; Fensterbank, H.; Bacsko, K.; Cano, M.; Allard, E.; Larpent, C. Azido-coated nanoparticles: a versatile clickable platform for the preparation of fluorescent polystyrene core–PAMAM shell nanoparticles. *Macromolecules* **2012**, *45*, 3513–3522.
- (24) Baranov, D.; Kadnikova, E. N. Synthesis and characterization of azidoalkyl-functionalized gold nanoparticles as scaffolds for “click”-chemistry derivatization. *J. Mater. Chem.* **2011**, *21*, 6152–6157.
- (25) Thode, C. J.; Williams, M. E. Kinetics of 1,3-dipolar cycloaddition on the surfaces of Au nanoparticles. *J. Colloid Interface Sci.* **2008**, *320*, 346–352.
- (26) Limapichat, W.; Basu, A. Reagentless functionalization of gold nanoparticles via a 3 + 2 Huisgen cycloaddition. *J. Colloid Interface Sci.* **2008**, *318*, 140–144.
- (27) Gole, A.; Murphy, C. J. Azide-derivatized gold nanorods: Functional materials for “Click” chemistry. *Langmuir* **2008**, *24*, 266–272.
- (28) Fischler, M.; Sologubenko, A.; Mayer, J.; Clever, G.; Burley, G.; Gierlich, J.; Carell, T.; Simon, U. Chain-like assembly of gold

nanoparticles on artificial DNA templates via “click chemistry”. *Chem. Commun.* **2008**, 169–171.

(29) Boisselier, E.; Salmon, L.; Ruiz, J.; Astruc, D. How to very efficiently functionalize gold nanoparticles by “click” chemistry. *Chem. Commun.* **2008**, 44, 5788–5790.

(30) Fleming, D. A.; Thode, C. J.; Williams, M. E. Triazole cycloaddition as a general route for functionalization of Au nanoparticles. *Chem. Mater.* **2006**, 18, 2327–2334.

(31) Brennan, J. L.; Hatzakis, N. S.; Tshikhudo, T. R.; Razumas, V.; Patkar, S.; Vind, J.; Svendsen, A.; Nolte, R. J. M.; Rowan, A. E.; Brust, M. Bionanoconjugation via click chemistry: The creation of functional hybrids of lipases and gold nanoparticles. *Bioconjugate Chem.* **2006**, 17, 1373–1375.

(32) van der Meer, S. B.; Loza, K.; Wey, K.; Heggen, M.; Beuck, C.; Bayer, P.; Epple, M. Click chemistry on the surface of ultrasmall gold nanoparticles (2 nm) for covalent ligand attachment followed by NMR spectroscopy. *Langmuir* **2019**, 35, 7191–7204.

(33) Salassa, G.; Burgi, T. NMR spectroscopy: a potent tool for studying monolayer-protected metal nanoclusters. *Nanoscale Horiz.* **2018**, 3, 457.

(34) Konopka, C. J.; Wozniak, M.; Hedhli, J.; Ploska, A.; Schwartz-Duval, A.; Siekierzycka, A.; Pan, D.; Munirathinam, G.; Dobrucki, I. T.; Kalinowski, L.; et al. Multimodal imaging of the receptor for advanced glycation end-products with molecularly targeted nanoparticles. *Theranostics* **2018**, 8, 5012–5024.

(35) Marbella, L. E.; Millstone, J. E. NMR techniques for noble metal nanoparticles. *Chem. Mater.* **2015**, 27, 2721–2739.

(36) Ruks, T.; Beuck, C.; Schaller, T.; Niemeyer, F.; Zähres, M.; Loza, K.; Heggen, M.; Hagemann, U.; Mayer, C.; Bayer, P.; et al. Solution NMR spectroscopy with isotope-labelled cysteine ( $^{13}\text{C}$ ,  $^{15}\text{N}$ ) reveals the surface structure of L-cysteine-coated ultrasmall gold nanoparticles (1.8 nm). *Langmuir* **2019**, 35, 767–778.

(37) van der Meer, S. B.; Seiler, T.; Buchmann, C.; Patalidou, G.; Boden, S.; Loza, K.; Heggen, M.; Linders, J.; Prymak, O.; Hartmann, L.; et al. Controlling the surface functionalization of ultrasmall gold nanoparticles by sequence-defined macromolecules. *Chem.—Eur. J.* **2020**.

(38) Schrader, T.; Bitan, G.; Klärner, F.-G. Molecular tweezers for lysine and arginine – powerful inhibitors of pathologic protein aggregation. *Chem. Commun.* **2016**, 52, 11318–11334.

(39) Trusch, F.; Kowski, K.; Bravo-Rodriguez, K.; Beuck, C.; Sowislok, A.; Wettig, B.; Matena, A.; Sanchez-Garcia, E.; Meyer, H.; Schrader, T.; et al. Molecular tweezers target a protein–protein interface and thereby modulate complex formation. *Chem. Commun.* **2016**, 52, 14141–14144.

(40) Heid, C.; Sowislok, A.; Schaller, T.; Niemeyer, F.; Klärner, F.-G.; Schrader, T. Molecular tweezers with additional recognition sites. *Chem. Eur. J.* **2018**, 24, 11332–11343.

(41) Fokkens, M.; Schrader, T.; Klärner, F.-G. A molecular tweezer for lysine and arginine. *J. Am. Chem. Soc.* **2005**, 127, 14415–14421.

(42) Bier, D.; Rose, R.; Bravo-Rodriguez, K.; Bartel, M.; Ramirez-Anguita, J. M.; Dutt, S.; Wilch, C.; Klärner, F.-G.; Sanchez-Garcia, E.; Schrader, T.; et al. Molecular tweezers modulate 14-3-3 protein–protein interactions. *Nat. Chem.* **2013**, 5, 234–239.

(43) Kowalski, J. A.; Liu, K.; Kelly, J. W. NMR solution structure of the isolated Apo Pin1 WW domain: comparison to the x-ray crystal structures of Pin1. *Biopolymers* **2002**, 63, 111–121.

(44) Luh, L. M.; Hänsel, B.; Löhr, F.; Kirchner, D. K.; Krauskopf, K.; Pitzius, S.; Schäfer, B.; Tufar, P.; Corbeski, I.; Güntert, P.; et al. Molecular crowding drives active Pin1 into nonspecific complexes with endogenous proteins prior to substrate recognition. *J. Am. Chem. Soc.* **2013**, 135, 13796–13803.

(45) Schelhorn, C.; Martin-Malpartida, P.; Sunol, D.; Macias, M. J. Structural Analysis of the Pin1-CPEB1 interaction and its potential role in CPEB1 degradation. *Sci. Rep.* **2015**, 5, 14990.

(46) Sekerina, E.; Rahfeld, J. U.; Müller, J.; Fanghänel, J.; Rascher, C.; Fischer, G.; Bayer, P. NMR solution structure of hPar14 reveals similarity to the peptidyl prolyl cis/trans isomerase domain of the

mitotic regulator hPin1 but indicates a different functionality of the protein. *J. Mol. Biol.* **2000**, 301, 1003–1017.

(47) Wintjens, R.; Wieruszkeski, J.-M.; Drobecq, H.; Rousselot-Pailley, P.; Buée, L.; Lippens, G.; Landrieu, I. 1H NMR study on the binding of Pin1 Trp-Trp domain with phosphothreonine peptides. *J. Biol. Chem.* **2001**, 276, 25150–25156.

(48) Frassanito, M. A.; Saltarella, I.; Vinella, A.; Muzio, L. L.; Pannone, G.; Fumarulo, R.; Vacca, A.; Mariggiò, M. A. Survivin overexpression in head and neck squamous cell carcinomas as a new therapeutic target (Review). *Oncol. Rep.* **2019**, 41, 2615–2624.

(49) Martínez-García, D.; Manero-Rupérez, N.; Quesada, R.; Korrodi-Gregório, L.; Soto-Cerrato, V. Therapeutic strategies involving survivin inhibition in cancer. *Med. Res. Rev.* **2019**, 39, 887–909.

(50) Zafari, P.; Rafiei, A.; Esmaeili, S. A.; Moonesi, M.; Taghadosi, M. Survivin a pivotal antiapoptotic protein in rheumatoid arthritis. *J. Cell. Physiol.* **2019**, 234, 21575–21587.

(51) Rafatmanesh, A.; Behjati, M.; Mobasser, N.; Sarvizadeh, M.; Mazooghi, T.; Karimian, M. The survivin molecule as a double-edged sword in cellular physiologic and pathologic conditions and its role as a potential biomarker and therapeutic target in cancer. *J. Cell. Physiol.* **2020**, 235, 725–744.

(52) Brust, M.; Fink, J.; Bethell, D.; Schiffrin, D. J.; Kiely, C. Synthesis and reactions of functionalised gold nanoparticles. *Chem. Commun.* **1995**, 1655–1656.

(53) Häkkinen, H. The gold–sulfur interface at the nanoscale. *Nat. Chem.* **2012**, 4, 443–455.

(54) Hogeweg, A.; Sowislok, A.; Schrader, T.; Beuck, C. An NMR method to pinpoint supramolecular ligand binding to basic residues on proteins. *Angew. Chem., Int. Ed.* **2017**, 56, 14758–14762.

(55) Thust, A.; Barthel, J.; Tillmann, K. FEI Titan 80-300 TEM. *J. Large-scale Res. Fac.* **2016**, 2, A41.

(56) Altieri, A. S.; Hinton, D. P.; Byrd, R. A. Association of biomolecular systems via pulsed-field gradient NMR self-diffusion measurements. *J. Am. Chem. Soc.* **1995**, 117, 7566–7567.

(57) Stejskal, E. O.; Tanner, J. E. Spin diffusion measurements: Spin echoes in the presence of a time-dependent field gradient. *J. Chem. Phys.* **1965**, 42, 288.

(58) Esadze, A.; Zandarashvili, L.; Iwahara, J. Effective strategy to assign  $^1\text{H}$ - $^{15}\text{N}$  heteronuclear correlation NMR signals from lysine side-chain  $\text{NH}_3^+$  groups of proteins at low temperature. *J. Biomol. NMR* **2014**, 60, 23–27.

(59) Iwahara, J.; Jung, Y.-S.; Clore, G. M. Heteronuclear NMR spectroscopy for lysine  $\text{NH}(3)$  groups in proteins: unique effect of water exchange on  $(15)\text{N}$  transverse relaxation. *J. Am. Chem. Soc.* **2007**, 129, 2971–2980.

(60) Zandarashvili, L.; Esadze, A.; Iwahara, J. NMR studies on the dynamics of hydrogen bonds and ion pairs involving lysine side chains of proteins. *Adv. Protein Chem. Struct. Biol.* **2013**, 93, 37–80.

(61) Ayed, A.; Mulder, F. A. A.; Yi, G.-S.; Lu, Y.; Kay, L. E.; Arrowsmith, C. H. Latent and active p53 are identical in conformation. *Nat. Struct. Biol.* **2001**, 8, 756–760.

(62) Mahl, D.; Diendorf, J.; Meyer-Zaika, W.; Epple, M. Possibilities and limitations of different analytical methods for the size determination of a bimodal dispersion of metallic nanoparticles. *Colloids Surf., A* **2011**, 377, 386–392.

(63) Yu, R.; Liz-Marzán, L. M.; García de Abajo, F. J. Universal analytical modeling of plasmonic nanoparticles. *Chem. Soc. Rev.* **2017**, 46, 6710–6724.

(64) Salorinne, K.; Malola, S.; Wong, O. A.; Rithner, C. D.; Chen, X.; Ackerson, C. J.; Häkkinen, H. Conformation and dynamics of the ligand shell of a water-soluble  $\text{Au}_{102}$  nanoparticle. *Nat. Commun.* **2016**, 7, 10401.

(65) Akoka, S.; Barantin, L.; Trierweiler, M. Concentration measurement by proton NMR using the ERETIC method. *Anal. Chem.* **1999**, 71, 2554–2557.

(66) Mallon, M.; Dutt, S.; Schrader, T.; Crowley, P. B. Protein camouflage: Supramolecular anion recognition by Ubiquitin. *ChemBioChem* **2016**, 17, 774–783.

## 4 UNPUBLISHED WORK FROM THIS DISSERTATION

The work that has not been published or submitted yet will be elucidated in this section.

### 4.1 Trifluoromethoxy Molecular Tweezer as a Drug Candidate

This chapter is dedicated to another important implementation of molecular tweezers, namely inhibition of amyloid protein aggregation. As described previously, the molecular diphosphate tweezer, patented as CLR01, is well-known for its broad-spectrum inhibitory potential in the self-assembly of toxic and amyloidogenic proteins (Chapters 1.6.3 and 3.1). The explicit concepts of this project and developed blood-brain barrier targeting strategies are explained in chapter 1.6.3.1.1. The fluorinated derivatives could be the key to success for facilitated penetration of the blood-brain membrane. The synthetic challenges faced on the way to novel fluorinated molecular tweezer are thoroughly evaluated in the following sections.

#### 4.1.1 Background Information

To promote the prodrug project (Figure 32.) in a targeted manner, it is necessary to further improve tweezers' ability to penetrate the blood-brain barrier. This could be achieved by increasing the hydrophobicity of CLR01 derivatives. Qualitatively, drugs that passively diffuse through the BBB are generally lipophilic and have a molecular weight of less than 400-500 Da. Therefore, new molecular tweezers derivatives have been designed, in which biologically stable groups replace the second phosphate group.

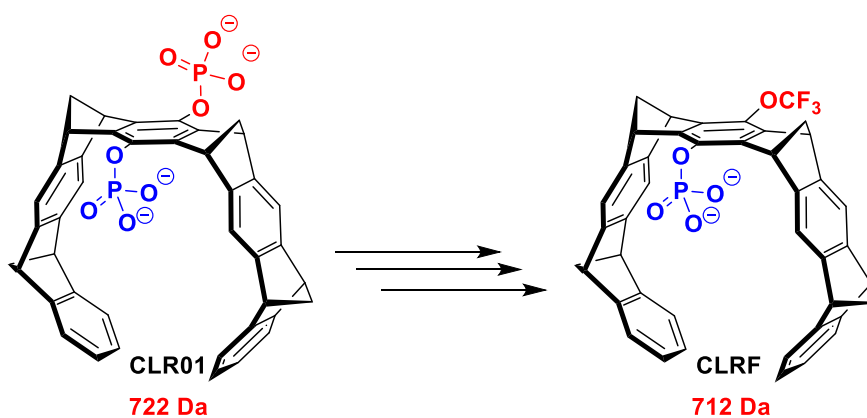


**Figure 59.** Desired synthetic transformation of parent molecular tweezer **CLR01** to trifluoromethoxy tweezer CLRF.

Here, in an attempt to tune the pharmacokinetics of CLR01 and enhance its hydrophobicity, the trifluoromethoxy group  $-OCF_3$  was chosen to substitute the second phosphate moiety (Figure 59). The presence of  $-OCF_3$  group directly attached to the tweezer skeleton would not only improve the overall construct's lipophilicity but also contribute to the lowering of its molecular weight compared to CLR01.

#### 4.1.2 Silver-mediated Oxidative Trifluoromethylation

Even if the phenol alkylation with electrophilic reagents could generally be considered trivial, knowing that there are several available, “user-friendly  $-CF_3$ ” electrophilic sources, this reaction has been elusive until 2015. The solution to this synthetical challenge was offered recently, when Liu *et al.* at the Shanghai Institute of Organic Chemistry, reported a method for successful trifluoromethylation of both electron-rich and electron-deficient phenols.<sup>[175]</sup> The described key to successful transformation implies using what can only be described as “witches’ brew of fluorine”.<sup>[176]</sup> The reaction mixture comprises silver(I) triflate ( $AgOTf$ ) and 2-fluoropyridine (which is presumed to be a ligand) with an optimal oxidant mixture of N-fluoro-benzenesulfonimide (NFSI), Selectfluor, cesium fluoride ( $CsF$ ), and a blend of toluene and trifluorotoluene as the solvent.

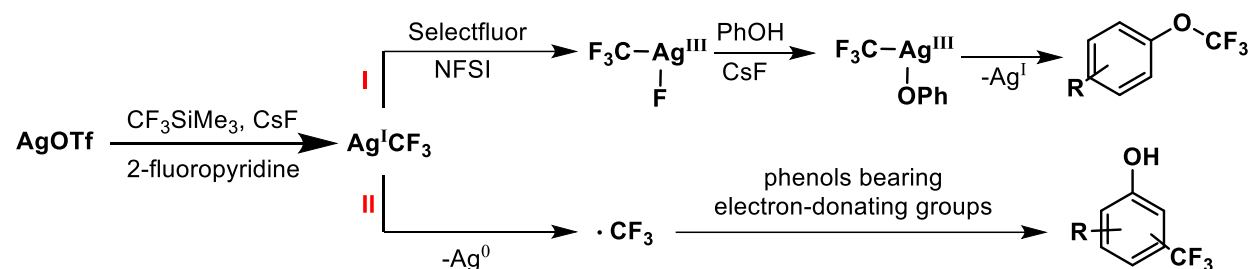


**Figure 60.** Proposed mechanisms for the silver-mediated oxidative trifluoromethylation of phenols.<sup>[175]</sup>

To avoid the harsh conditions needed to generate highly unstable  $-CF_3$  cations when using electrophilic  $-CF_3$  sources, the nucleophilic source (Ruppert-Prakash reagent- $CF_3SiMe_3$ ) was used instead. Excluding the solvents, a remarkable 53 molar equivalents of fluorine atoms are present in one single-pot reaction. The reaction has been reported to give the product in a 77 % yield at room temperature. The possible reaction mechanism was suggested in which catalytically active species  $Ag^I-CF_3$  are generated *in situ* in the reaction between  $AgOTf$  and  $CF_3SiMe_3$  and  $CsF$ . Due to the  $\sigma$ -donating nature of the  $CF_3$

group in  $\text{Ag}^{\text{I}}\text{CF}_3$ , active species further undergo oxidative addition with Selectfluor or NFSI to form  $\text{Ag}^{\text{III}}(\text{CF}_3)(\text{F})$ , followed by fluoride to phenoxide exchange to afford the critical intermediate  $\text{Ag}^{\text{III}}(\text{CF}_3)(\text{OPh})$ . Subsequent reductive elimination from the  $\text{Ag}^{\text{III}}$  to furnish the reaction product (pathway I in Figure 60). The proposed mechanism must be taken with precaution due to the complexity of the described reaction. Speculatively, the radical mechanism, where the  $\text{Ag}-\text{CF}_3$  is homolytic cleaved, seems to be possible as well, yielding trifluoromethylated arenes and electron-rich phenols shown as pathway II in Figure 60.

#### 4.1.3 Synthesis of Novel Fluorinated Molecular Tweezer

Since the tweezer skeleton can be synthetically transformed into the phenol-like structure, the synthetic procedure from the Liu group was applied to achieve the novel functionalization. The complete synthetic procedure to obtain the novel fluorinated CLR01 derivate is described in Figure 61.

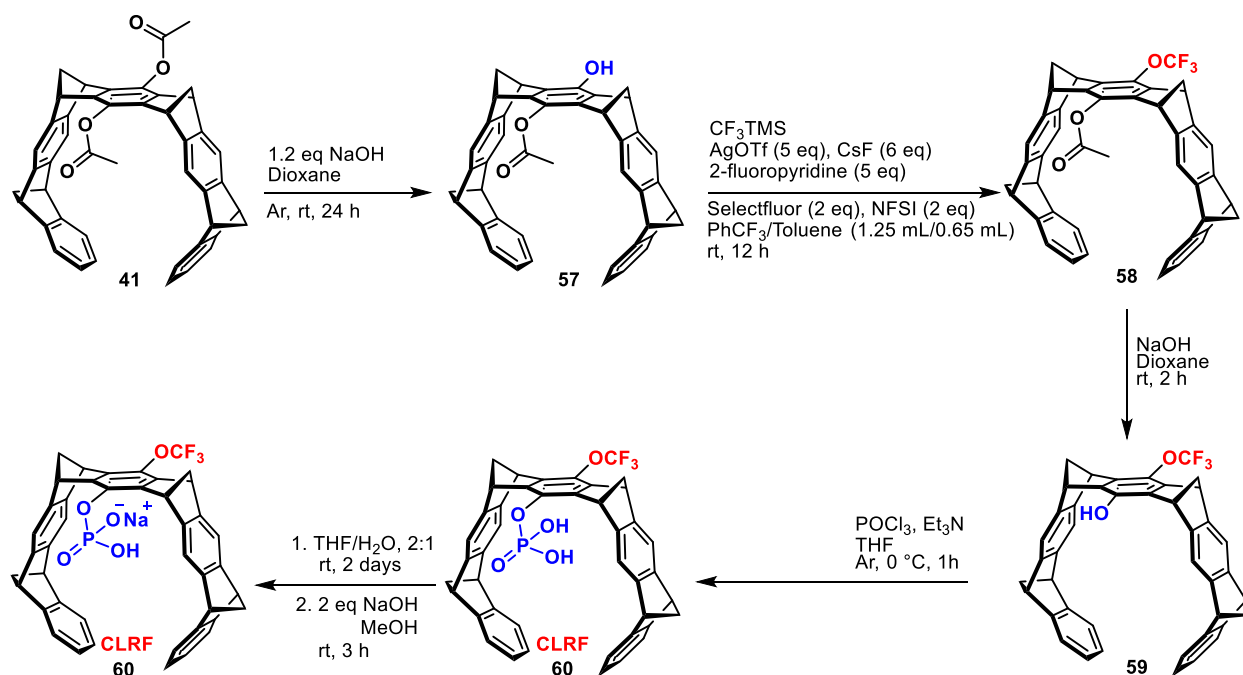


**Figure 61.** The complete synthetic procedure to obtain the phosphorylated trifluoromethoxy tweezer CLR01.

First, the diacetoxy tweezer **41** is deprotected to obtain phenol-like tweezer derivate **57**. Under light and oxygen exclusion, using glow box and Schlenk techniques, the silver-mediated oxidative trifluoromethylation strategy of phenol-like molecules, described in the

previous chapter, was applied to monohydroxy molecular tweezer **57**, leading to fluorinated product **58**.

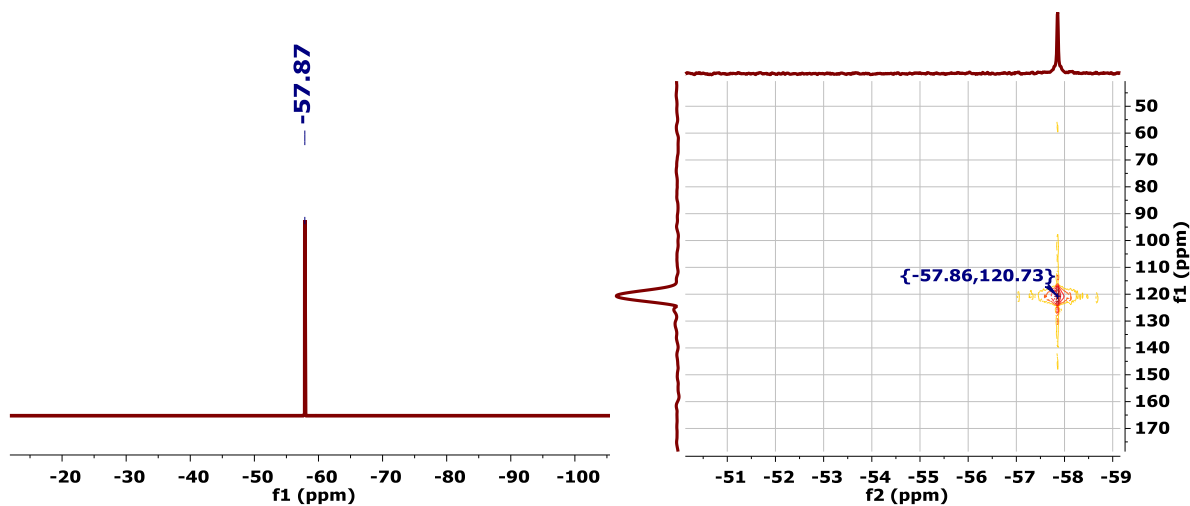


**Figure 62.**  $^{19}\text{F}$  NMR spectra of **58** (left) and two dimensional  $^{19}\text{F}$  –  $^{13}\text{C}$  correlation NMR of **58** (right).

After several purification steps described in the experimental part (Chapter 7.1.3.2.1), the first fluorinated tweezer derivative was isolated in a pure form, yielding a single fluorine signal in NMR (Figure 62). Besides the full NMR characterisation, LC-MS and HRMS techniques have confirmed the success of this crucial synthetic conversion step (Chapter 7.1.3.2). Subsequently, **58** was deacylated to yield **59** soluble in chloroform. After the second deprotection, an excess of  $\text{POCl}_3$  was used for phosphorylation of **59** to give monophosphorylated CLRf. In the final step, the phosphate moiety in **60** was deprotonated with two equivalents of the base to facilitate the solubility of the final product CLRf in aqueous solutions.

#### 4.1.4 Conclusion and Outlook

Silver-mediated, oxidative trifluoromethylation of phenol derivatives presented in chapter 4.1.3 was successfully applied to phenol-like molecular tweezers. It served as a tool to introduce  $-\text{OCF}_3$  group on the place of the second phosphate moiety. Until now, the reported procedure was only applied to the simple model of phenol molecules. Nevertheless, this reaction proved useful in functionalizing more complex molecular systems than simple phenols, such as molecular tweezer. The obtained CLR01 derivate is lower in weight than CLR01 itself and is supposed to exhibit increased lipophilicity. We



hope to improve blood-brain barrier penetration with this CLR01 derivate and prevent aberrant protein agglomeration more effectively. The group of Dr. Gal Bitan at UCLA is the performing pharmacokinetic studies.

The direct esterification of the phosphoric acid groups of CLR01 with fluorinated alcohols as well as a click reaction of the monobutynyl and bis-monobutynyl tweezers with fluorinated amino acids are reliable chemical approaches for obtaining the further fluorinated derivates. Moreover, a chemical method of modifying molecular tweezers by attaching fluorophores and signal peptides has been successfully established and might be beneficial also in the pro-drug project.

## 4.2 Design of Divalent Molecular Tweezer Constructs of Defined Geometries

Besides the design of molecular tweezers equipped with peptides as additional recognition units (Chapter 2.1) and its utilization evaluated in the published work (Chapter 3.2 and 3.3), this chapter describes the first steps made in the implementation of the second strategic approach, i.e., design of multivalent tweezers with defined geometries (Chapter 2.3). Multivalent constructs are hypothesized to enhance affinity in binding and specificity in recognition of proteins that contain two or more easily accessible Lys or Arg either in their hot regions or in their vicinities. Here, the design, synthesis, and preliminary biophysical findings of the first divalent molecular tweezers skeletons are described as still unpublished results. Based on the information collected about Survivins' hot region, we designed divalent tweezer constructs of defined lengths to bridge Survivin's binding interface and influence its further PPI. The double tweezer-oligomer constructs represent the first divalent tweezer skeletons tailored for modulation of PPI.

### 4.2.1 Background Information

The group of Dr. Hartmann from Düsseldorf came up with a solid-phase assembly of functional and spacer building blocks whose length can be manipulated through Fmoc-based peptide coupling protocols, known as precision oligomers (Figure 63).

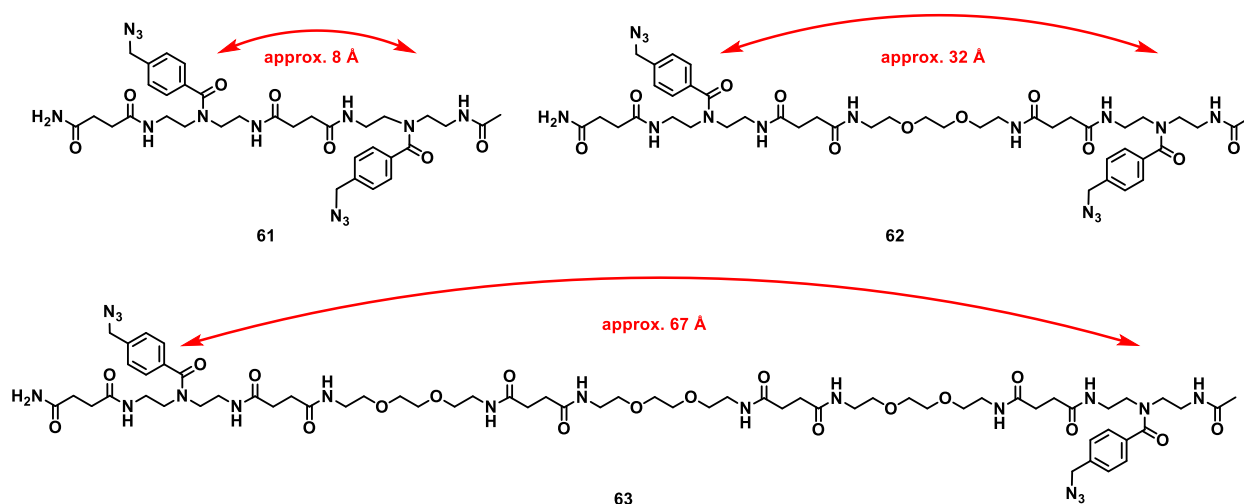


**Figure 63.** The precision oligomer molecules **61**, **62** and **63** in three different lengths, used as scaffolds for the synthesis of divalent molecular tweezers

Chemically, the precision oligomers represent sequence-controlled chains of oligo/amido amines. The molecules used for this project were synthesized on a solid surface in analogy to Baier *et al.* at Heinrich-Heine-Universität in Düsseldorf within the frame of CRC1093.<sup>[177]</sup> The stepwise addition of building blocks is realized by repetitive coupling upon activation of the carboxyl group followed by deprotection of the N-terminal Fmoc-group. In every additional step, a different building block can be applied to lead to the desired monomer sequence, and after cleavage from the support gives the final precision macromolecule. Oligomeric building blocks of defined length containing azides at desired distances, served as the connectors between the two tweezer molecules

#### 4.2.2 Tailormade Divalent Tweezer Constructs for Targeting Survivin

Since the precision macromolecular templates equipped with recognition motifs may be especially useful for the recognition of dimeric protein surfaces, we decided to start with targeting Survivin's NES region with a divalent tweezer-oligomer construct. The protein's monomer is characterized by two well-exposed critical lysines, K90/K91 located within the NES region and K103, located in the close vicinity of the binding interface on the distance of 20 Å. Both Lys should serve as two anchors for the two tweezer molecules interconnected with a proper length linker.

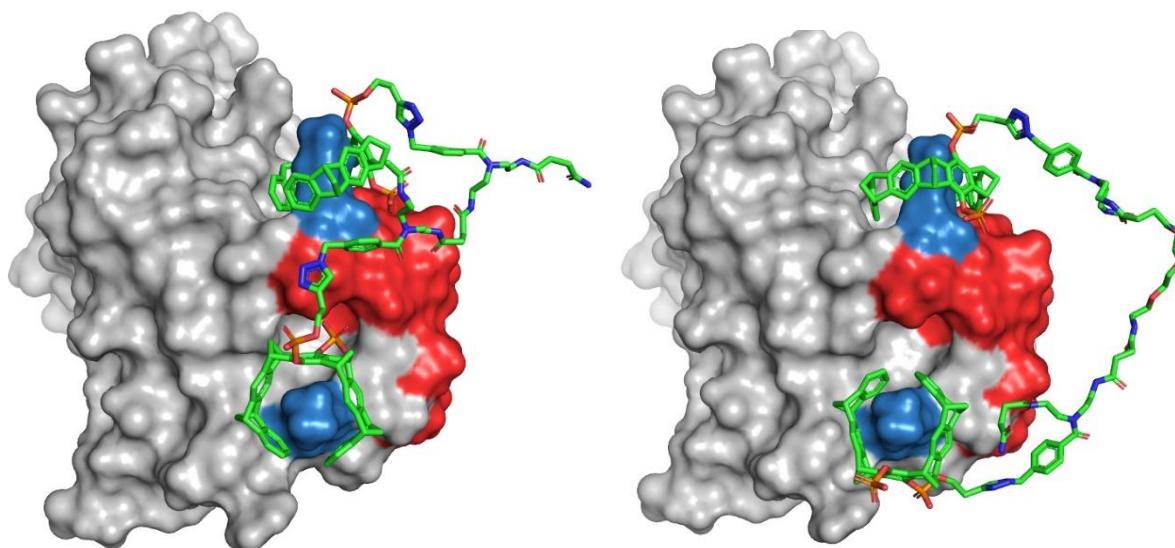


**Figure 64.** 1000 ns MD simulation of double tweezer-short oligomer conjugate **65** (left) and double tweezer-middle oligomer conjugate **64** (right). Survivin's monomer is shown as a gray surface. NES region is highlighted as a red surface. Critical Lys K90 and K103 are shown as blue spheres.

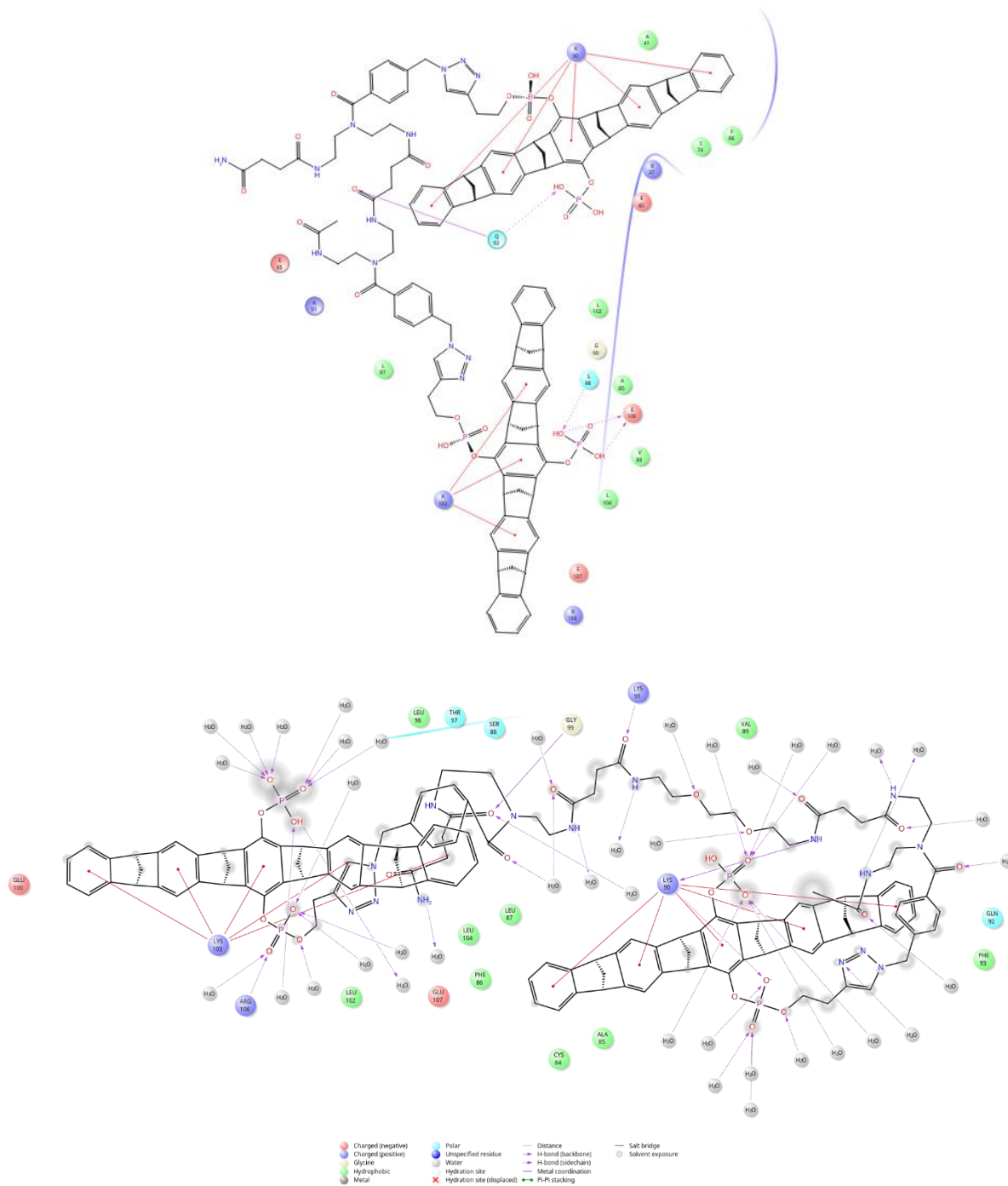


**Figure 65.** 1000 ns MD simulation interaction diagrams of double tweezer-short oligomer conjugate **65** (top) and double tweezer-middle oligomer conjugate **64** (bottom).

Since we were offered three linkers of different lengths from the Hartmann group, as shown in Figure 80, the first MD simulation was done with the hybrid molecule of the most favorable length **65** (molecular tweezer-middle length oligomer **62**) (Figure 64. right).

The construct remained docked to Lys K90/K103 during the entire trajectory, showing stable  $\pi$ -cation interactions during 98 % simulation time. Beside docked K103, R106 contributes to the stability of the assembly building an H-bond with the central unsubstituted phosphate-oxygen atom. Two noticeable H-bonds form between K91 and G99 (side chain) and carbonyl oxygens during 35 % simulation time and on H-bond between K90 (backbone) and an amide. Nevertheless, the linker loop freely swam in the solution and exhibited a high level of freedom with very few contacts with the protein backbone, as shown in the simulation interaction diagram (Figure 65. bottom).

Due to the outcome after the first MD simulation of **65**, where the linker loop exhibited a high level of flexibility, the MD simulation of the hybrid molecule – double tweezer-long oligomer conjugate **66** was not performed. Nevertheless, the molecule is going to be synthesized for comparison purposes with the other two shorter molecules in instrumental measurements and biological assays.

The next MD simulation was done with the daughter molecule **61**, which is around three times shorter in length. Again, the MD simulation job performed successfully and gave an insight into possible events in case of a lack of flexibility. However, the Survivin's NES region is left almost naked, and the linker seemed to favor the vertical space between critical Lys (Figure 64. left). This time, the linker part was quite restricted in movement due to its shortness with almost no interactions with the protein surface (Figure 65. top).

## 4.2.3 Synthesis of Double Tweezer-precision Oligomer Conjugates

### 4.2.3.1 Cu(I)-Catalyzed Azide-Alkyne Cycloadditions

The CuAAC click-type chemistry approach was utilized to covalently fuse unsymmetric tweezer molecules equipped with an alkyne moiety with precision oligomers *via* triazole rings into bulkier divalent constructs.<sup>[178]</sup> The 1,4-substituted triazoles are obtained only with the presence of Cu(I) catalysts. Nevertheless, the most frequently used catalysts are Cu(II), which can be reduced *in situ* to Cu(I) active catalysts in the presence of ascorbic acid. This reaction proceeds mechanistically *via* Cu(I) coordination of alkyne's triple bond (Figure 66. a).<sup>[179]</sup> Through coordination, the alkyne hydrogen becomes very acidic and can easily be deprotonated with a weak base and subsequently exchanged with Cu(I) (b). Then, the cycloaddition (c) occurs and leads to an unusual six-membered intermediate (Figure 66. d). Subsequent ring constriction (d), followed by protolysis (e), finally yields the 1,4-substituted triazole.

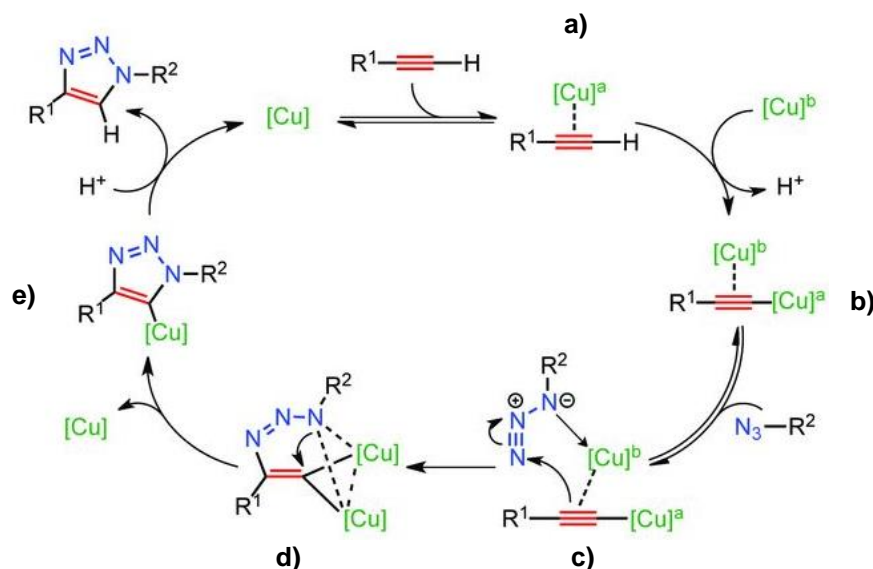


**Figure 66.** Proposed mechanism of click reaction catalyzed with two copper atoms.<sup>[179]</sup>

### 4.2.3.2 Synthesis

The three azido-functionalized linkers obtained from Hartmann's group, **61**, **62**, and **63** (Figure 63), are used as educts. The CuAAC reaction proceeded in THF/H<sub>2</sub>O at room temperature in the presence of sodium ascorbate as a reducing agent and DIPEA

as the base (Figure 67). The reaction mixture was stirred overnight at room temperature with restricted air contact. The appearance of the blue color after 16 hours of reaction time indicates the presence of Cu (II). Instead of repeated reduction Cu (II) to Cu (I) *in situ*, a new amount of freshly prepared catalytic brew was added, and the reaction mixture was left on stirring for additional 8 hours at room temperature. After the aqueous workup, to enhance the overall construct's solubility, it was necessary to deprotonate the product in the presence of 6 equivalents of the base. Unreacted material was removed utilizing RP-18 column chromatography. The reaction proceeded in ~ 60 % crude yield.

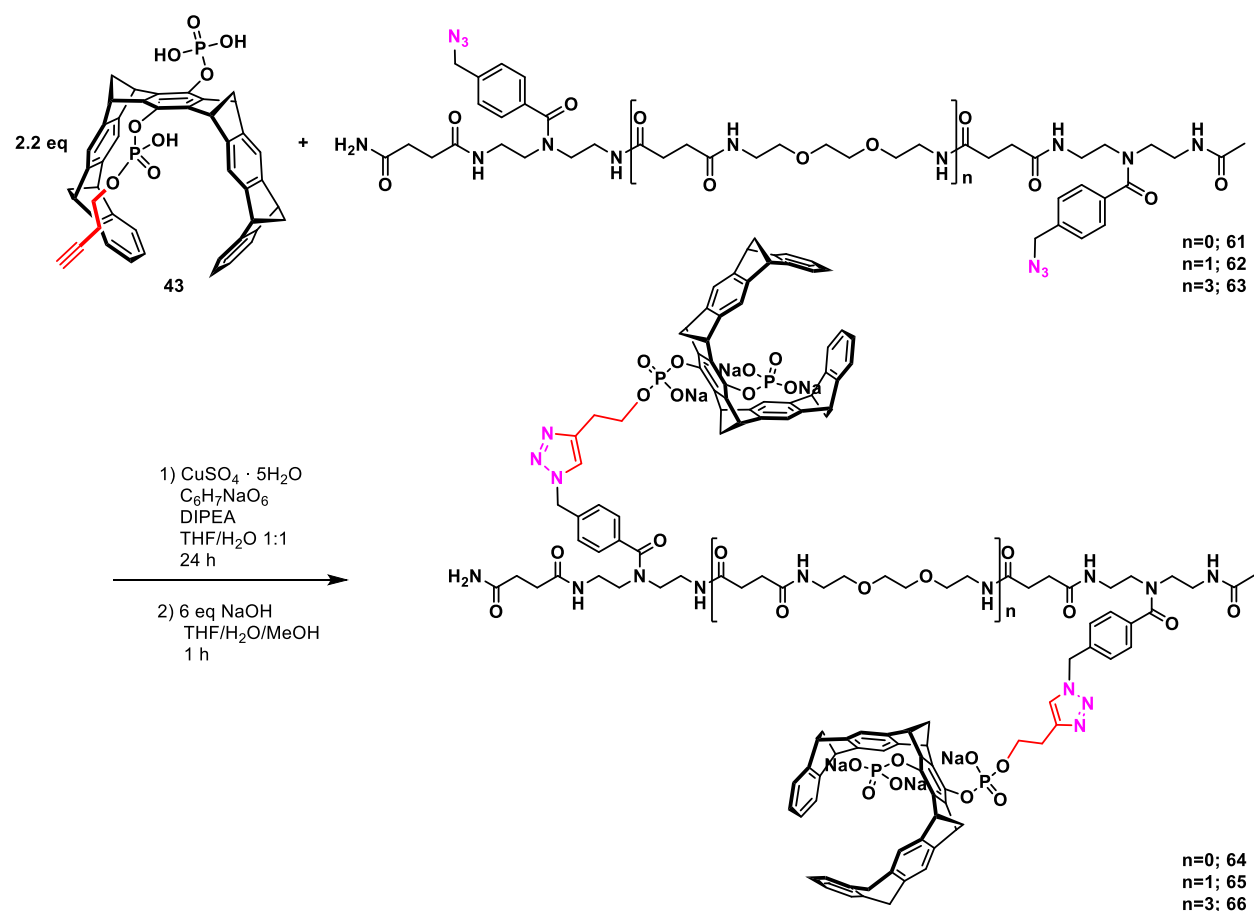


**Figure 67.** Synthesis of double tweezer-precision oligomer conjugates **64**, **65**, and **66**.

The success of the click reaction can be easily monitored *via* NMR as well as with IR spectroscopy. When comparing the NMR spectra of educts with the NMR spectra obtained from the product, two obvious characteristic features can be observed (Figure 67). Firstly, the triplet signal at 3.00 ppm characteristic for the clickable butynyl ester

moiety  $-CH$  (red box in Figure 67. a) is disappearing since it is directly involved in 1,4-dipolar cycloaddition and the triazole ring formation. The triazole  $-H$  from the final product can be found shifted to 8 ppm (red box in c). Downfield shifts are observed in the case of the azido-educt as well, as the second characteristic feature. Thus, the singlet characteristic for  $-CH_2-N_3$  (purple box in b) is shifted to higher ppm values (mostly around 5.60 – 5.70 ppm).

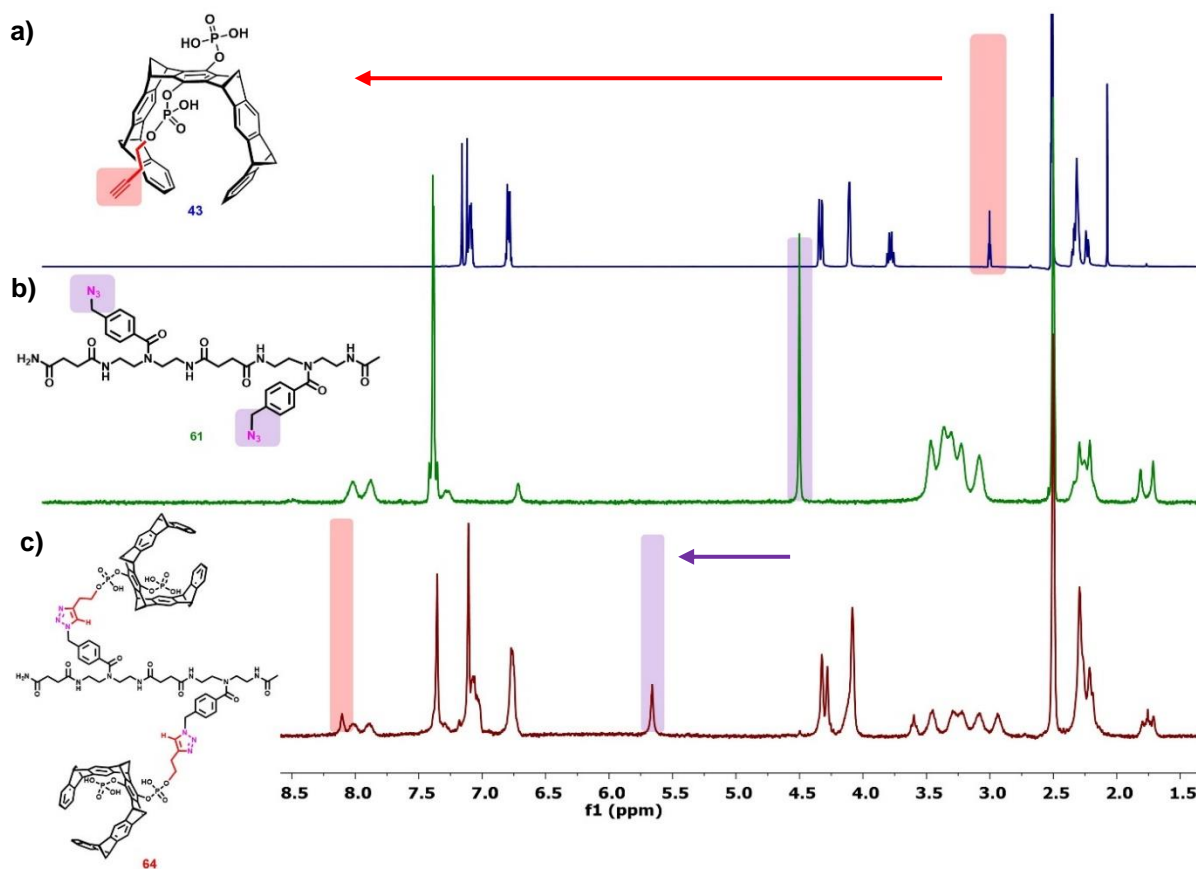


**Figure 68.** Characteristic NMR shifts useful for monitoring click reactions between educts **43** and **61** to yield the final product **64**.

The IR band characteristic for the azide group is shown in the purple box, and the expected lack of this band in the product is indicated with the red box in the IR spectrum below (Figure 67).



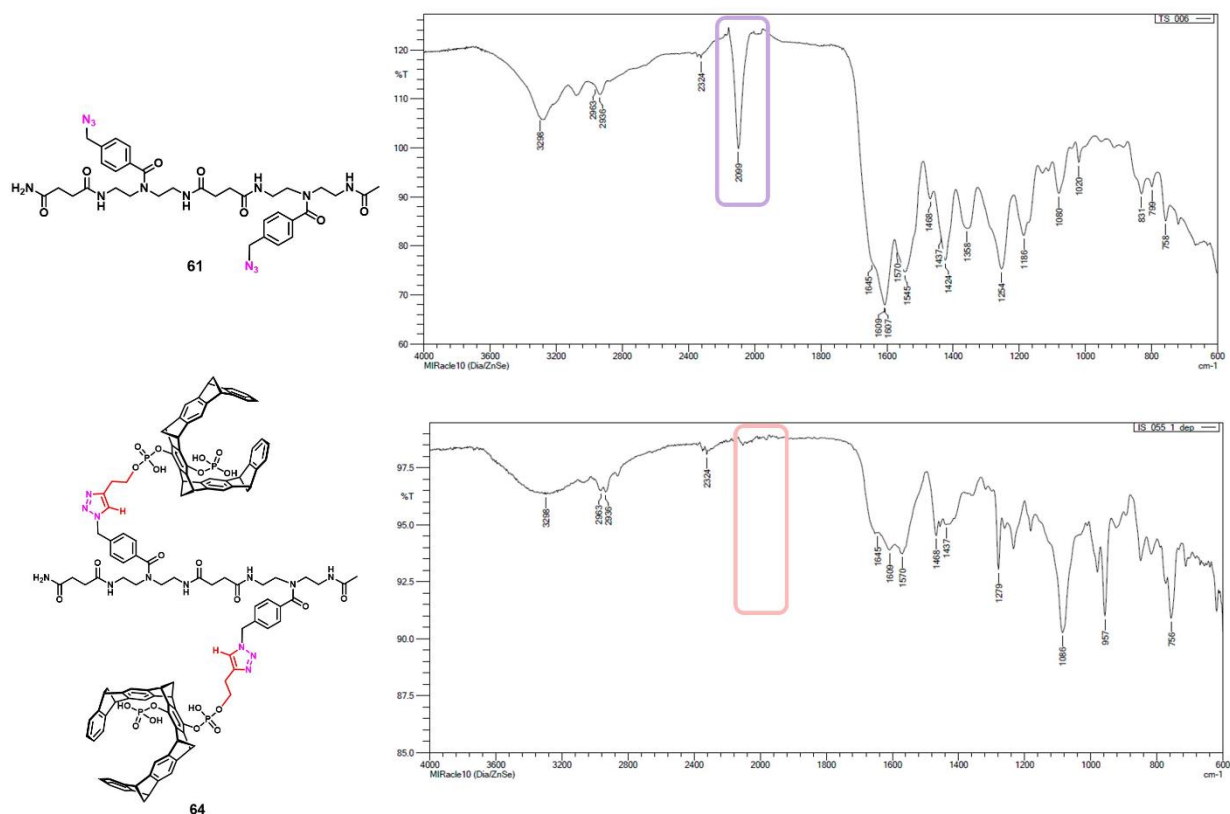


**Figure 69.** Characteristic IR band useful for monitoring click reactions between educts **43** and **61** to yield the final product **64**.

## 4.2.4 Results and Discussion

### 4.2.4.1 Pull-down Assays

Pull-down assays were done in the group of Prof. Dr. Knauer by Annika Meiners to analyze the effects of the tweezers on the Survivin-CRM1 interaction. GST-tagged CRM1 was used as bait protein for HA-tagged Survivin in 293T cell lysates, which were pre-incubated with the tweezers in different concentrations, respectively. It has been shown that all tested constructs influence this PPI – concentration dependently (Figure 70). The short double tweezer-oligomer conjugate **64** inhibits the Survivin-CRM1 interaction at lower concentrations than the unmodified single molecular tweezer CLR01. The concentration of CLR01 required to inhibit Survivin-CRM1 complex assembly is found to be between 10 and 50  $\mu\text{M}$ , while **64** exhibits inhibitory characteristics already at 1 to 5  $\mu\text{M}$ , which represents ten times stronger effects. The same inhibitory concentration was

observed for **65**, while the Survivin-CRM1 complex was still detectable at a concentration of 25  $\mu\text{M}$  for **66**.

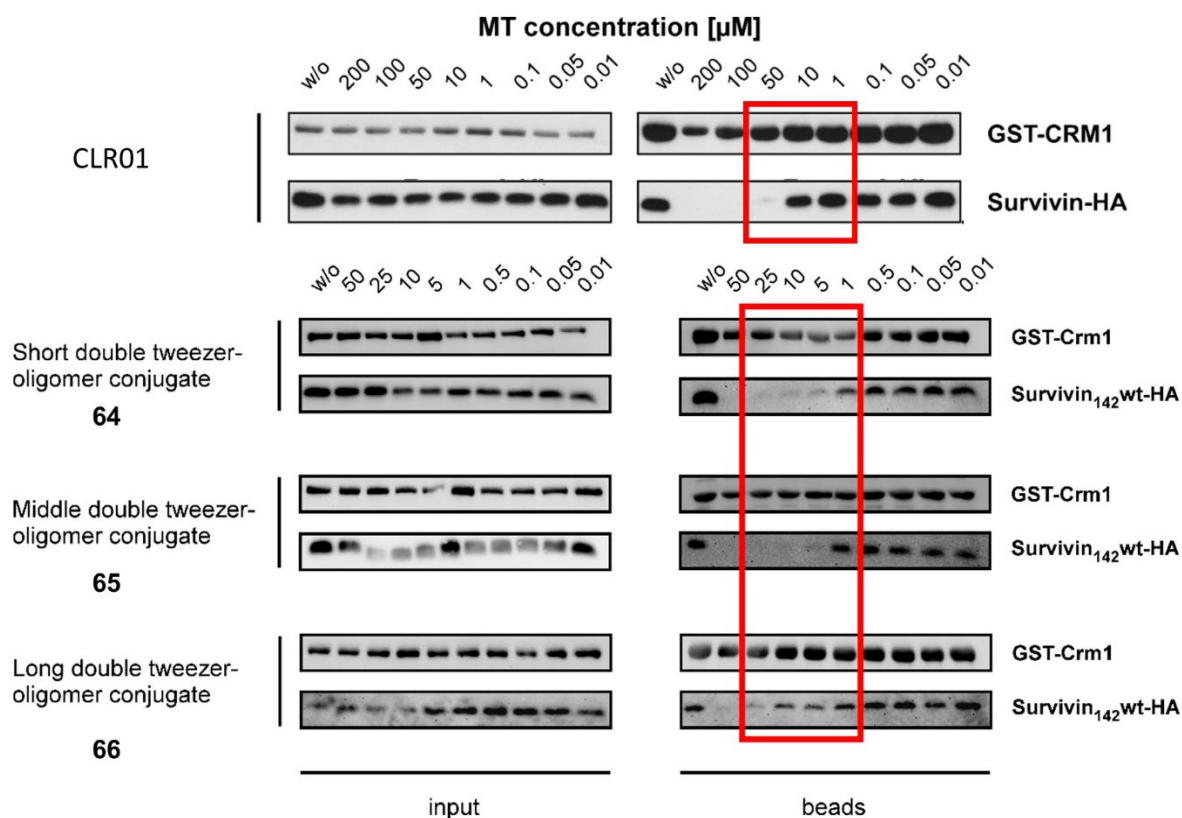


**Figure 70.** Pull-down assays to assess the Survivin-CRM1 interaction.

#### 4.2.4.2 ITC Titrations

ITC-measurements were done using Malvern MicroCal 200 VP-ITC calorimeter. The reversed titrations were performed first (Figure 71). Survivin placed in the syringe was titrated to the ligands **64**, **65**, and **66**, respectively. Strong binding events and significant response are evident from the obtained exothermic peaks (Figure 71). A sequential binding effect can be elucidated from the curve profile, but unfortunately, the reasonable fit could not be obtained, and therefore the actual thermodynamic data are missing. Then, the direct titrations were done, where the **64**, **65**, and **66** were titrated to Survivin in the cell. The curves were fitted with independent sites model, applying two independent sets of sites (Figure 72). Obtained thermodynamic data (TD) shown in Table 3. were interpreted using Affinimeter software (Cloud-version).

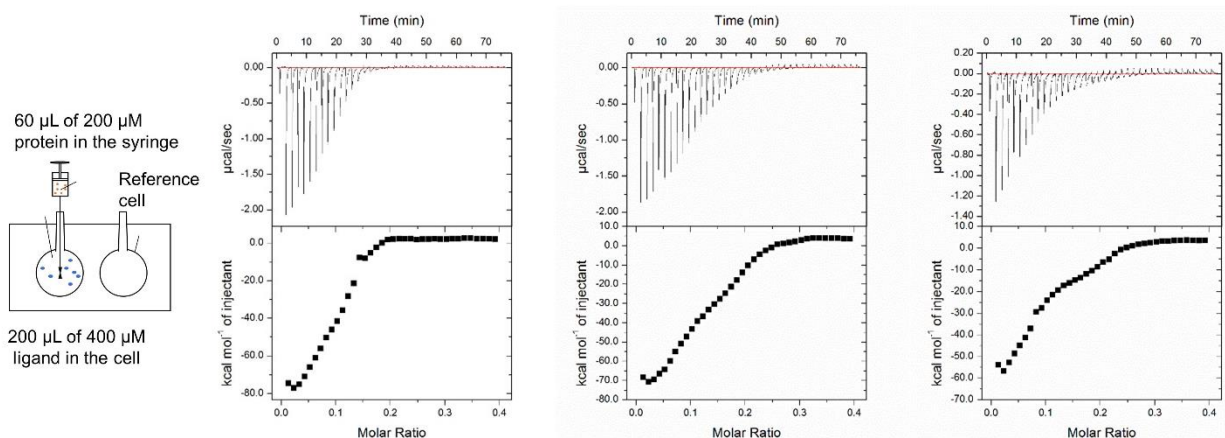


**Figure 71.** Reverse ITC titrations.

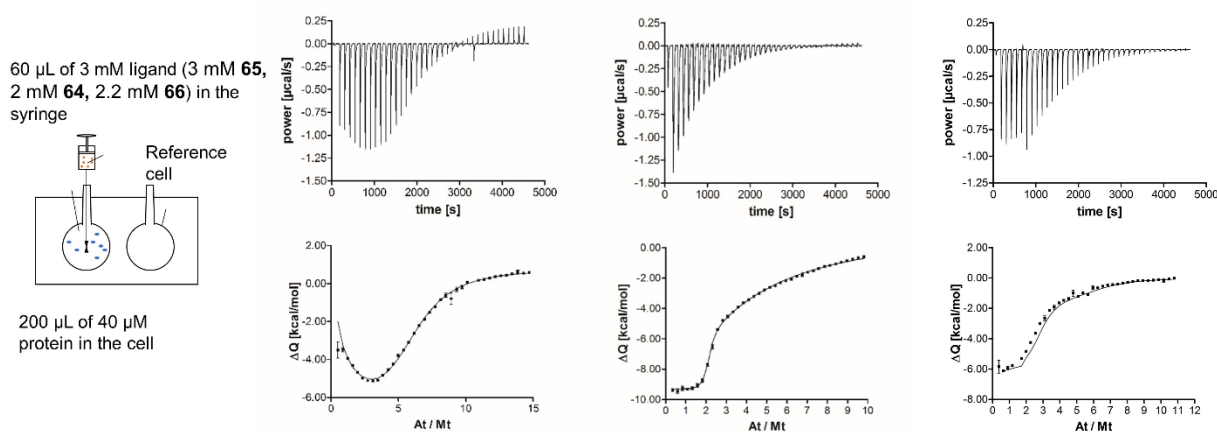


**Figure 72.** Direct ITC titrations.

**Table 3.** Thermodynamic data from direct ITC titrations, obtained after applying the independent sites fit.

MT	$K_a(1,1)$ [M <sup>-1</sup> ]	$K_a(1,2)$ [M <sup>-1</sup> ]	$\Delta H(1,1)$ [kcal/mol]	$\Delta H(1,2)$ [kcal/mol]
64	$(0.1802 \pm 4.5380)e+06$	$(1.0000 \pm 0.0375)e+08$	$(2.0299 \pm 0.1064)$	$(-5.9296 \pm 5.6341)$
65	$(6.7470 \pm 2.6965)e+06$	$(9.2266 \pm 3.6548)e+03$	$(-20.670 \pm 1.2137)$	$(-51.022 \pm 3.2418)$
66	$(2.1206 \pm 0.3842)e+06$	$(1.2923 \pm 0.0413)e+04$	$(-5.1952 \pm 0.1071)$	$(-22.608 \pm 0.0426)$

The TD data suggest that the binding site with more affinity has a lower enthalpy. The given analysis must be taken with precaution due to the complexity of the examined system and the variety of possible side events that can take place. For this purpose, we

developed the tailor-made model that considers major possible outcomes of the system in which divalent ligand A reacts with multivalent receptor MB (Figure 73).

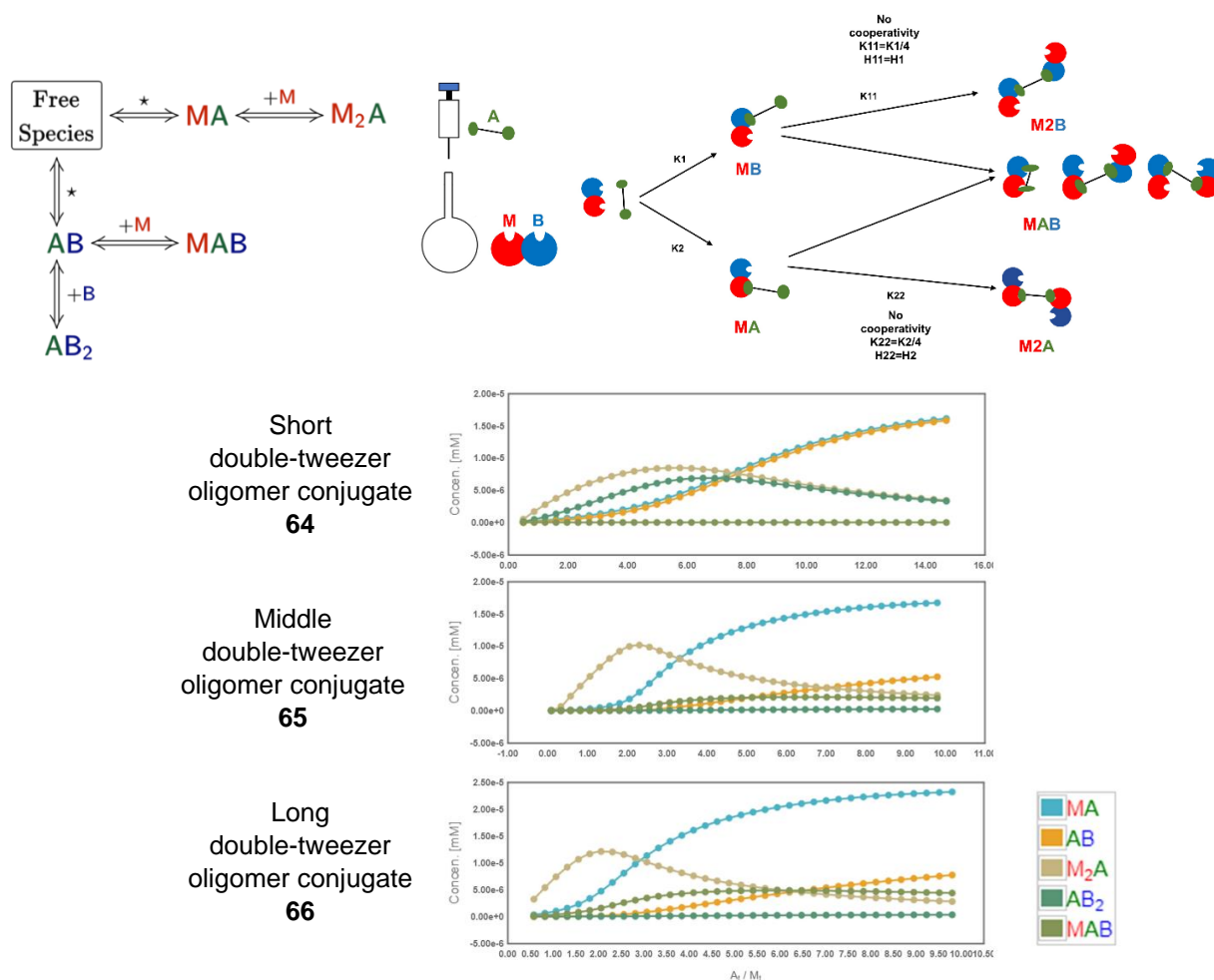


**Figure 73.** Possible binding events in case of divalent ligand A and multivalent receptor MB (top) and the species distribution plot of direct titration of **64**, **65**, and **66** to Survivin, where the concentrations of all possible species were plotted against the titrant to titrate molar ratio ( $A_i/M_i$ ) (bottom).

The species distribution plot obtained from Affinimeter (Figure 73. bottom) for **64** shows that in excess of ligand A at the end of the titration, MA, and MB are preferred species. Whereas, in excess of the protein, at the beginning of titration M<sub>2</sub>A and M<sub>2</sub>B are preferred species. The existence of MAB is not registered from this experimental data. Nevertheless, in the next two cases of **65** and **66**, the occurrence of MAB is evident. The interaction of the long and middle tweezer-oligomer conjugate seems to be stronger with one of the protein's binding sites. The species distribution plot suggests that the binding site with higher affinity is initially filled, and then, a second binding site with large enthalpy

occurs. Further mathematical approaches on obtained thermodynamic data (based on the tailor-made model for the described system) suggest that the observed system tends to minimize the overall entropy. The construct where two ligands are bound to a single receptor is entropically favorable than the corresponding 1:1 assembly (Figure 74). On the left side in Figure 74. is the desired binding outcome, resulting in an assembly where a divalent ligand recognizes the targeted epitope on the protein surface. The shown assembly on the right is a speculated outcome suggested by the above presented ITC approach.<sup>[180]</sup>

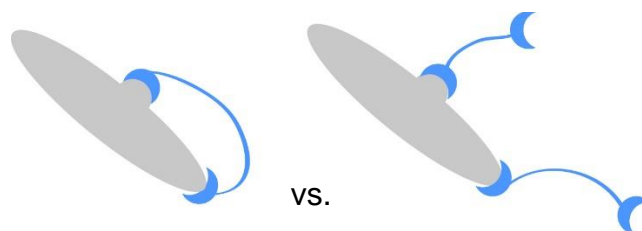


**Figure 74.** Expected vs. suggested binding (entropically favorable) model of Survivin monomer with double tweezer-oligomer conjugates.

#### 4.2.4.3 Protein NMR Titrations

Protein NMR titrations were performed in the group of Prof. Dr. Bayer by Dr. Christine Beuck to probe the specificity of the binding event and eventually determine the binding affinities. Chemical shift perturbation and relative signal intensities obtained from NMR titrations of double tweezer-oligomer conjugates to <sup>15</sup>N-labeled Survivin (1-120) reveal binding events that could not have been specified due to the existence of a mixture of different binding modes on the dimer, that are resulting in aggregated oligomers (Figure 75).

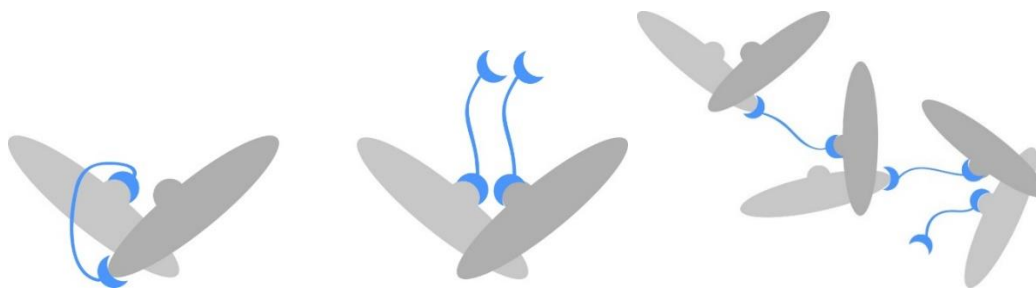


**Figure 75.** Possible binding models suggested after analysis of NMR data.

Therefore, the findings from NMR titrations and collected ITC data correlate with each other.

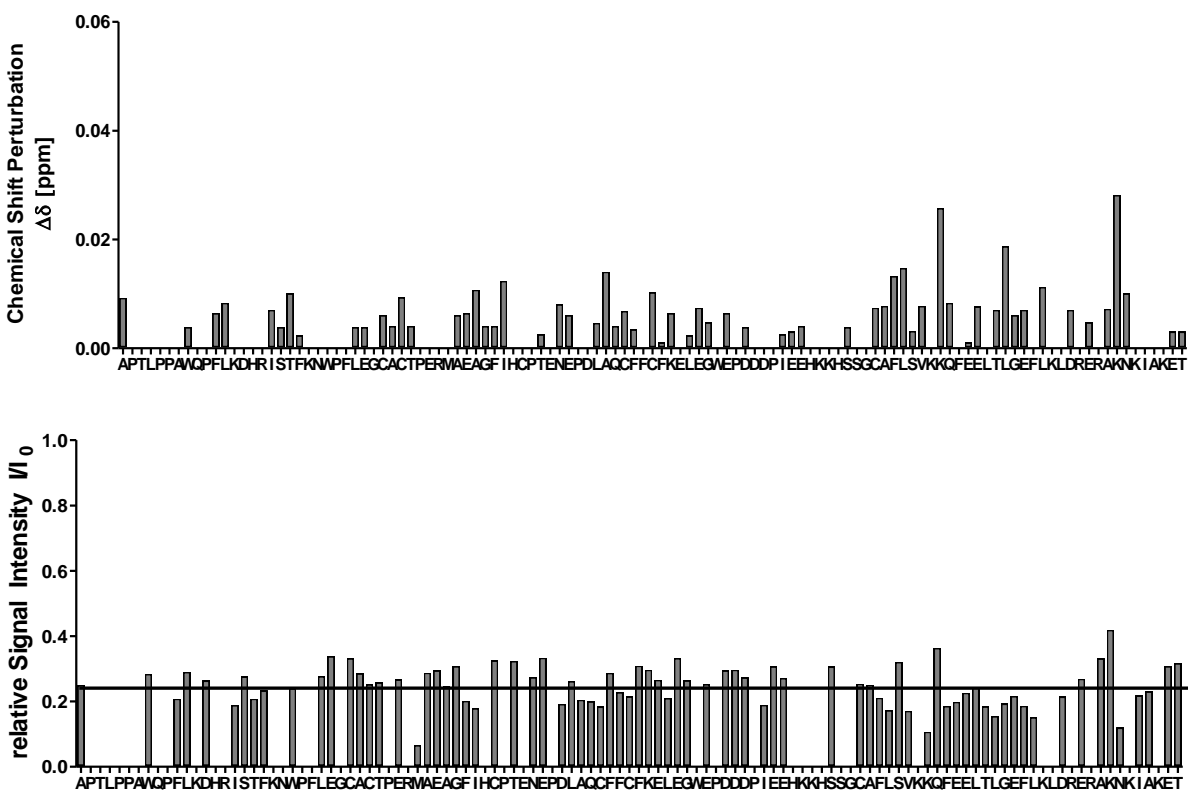


**Figure 76.** Signal shifts and signal intensities were recorded between **64** and  $^{15}\text{N}$ -labeled Survivin. Shifts (top) and relative intensities (bottom) were plotted against the protein sequence.

Furthermore, no major shifts were observed upon the titration. Additionally, the signal intensity did not decrease for a certain protein region but was strongly reduced for the whole protein, indicating its aggregation. Therefore, a specific binding site could not be identified. There are most likely multiple binding sites without a strong preference (Figure 76).

## 5 CONCLUSION AND OUTLOOK

This chapter summarizes the achievements and findings from individual subparts of this dissertation in a scientifically coherent manner. The achieved results are presented with a reflection on the existing literature sources given at the beginning of the dissertation, i.e., state of knowledge before starting the experimental work. However, the remaining challenges and further possibilities for improving molecular tweezers' features are given in the outlook.

### 5.1 Conclusion

The common focus of subtasks discussed in previous chapters is on the host-guest chemistry and its application for biological purposes. The introduction part already highlights the challenges in modern supramolecular chemistry. One of those is creating water-soluble supramolecules capable of protein recognition. Water is the only environmentally benign solvent that allows biological applications.<sup>[50,181]</sup> So far, numerous natural and synthetic macrocyclic host molecules have been reported, but their applications under physiological conditions are still rare. To reach high affinity and specificity for its biological target, the ligand molecule must not only compete with, e.g., solvent but also recognize large binding sites on a protein's surface.

Here, we present a novel generation of molecular tweezers designed individually for interaction with different proteins' flanks. The rational design and visualization of ligands with desired properties at the molecular level were feasible by employing computational skills gained within CRC 1093 and available modeling software within the Schrader group. All presented ligand molecules are soluble in both aqueous buffer solutions and water in a millimolar concentration range (up to 5 mM). However, the novel molecular tweezers were derived from Klärner's and Schrader's molecular tweezers discussed in Chapter 1.4.<sup>[45,60–63,66]</sup> By introducing the polar anionic functional groups into the rigid molecular tweezers' spacer units, Schrader and co-workers made a revolutionary step in constructing water-soluble molecular tweezers.<sup>[45]</sup> Further functionalization of the diphosphate tweezer by an alkyne moiety, accomplished by Heid *et al.*, served as the milestone in synthesizing the new hybrid tweezer molecules presented in this work.<sup>[66]</sup> Here, the click chemistry approach was utilized for the first time to covalently fuse a

supramolecular host scaffold carrying alkyne functionality with various predefined rigid or flexible skeletons, such as ultrasmall gold nanoparticles, precision oligomers, peptides, and novel fluorophores. Besides offering versatile synthetic possibilities, the CuAAC click chemistry's distinguishes with mild reaction conditions. The reaction proceeds at room temperature in water solutions, yielding no side products.

The two main strategic approaches were designed to advance known tweezer's features, such as binding specificity and affinity (described in Chapters 2.1 and 2.2). We introduced peptidic motifs of choice and fluorophores in the first approach. Different peptides provided an additional recognition pattern and were used to promote the molecular tweezers' specificity. The presence of fluorophores (attached either directly on to a tweezer skeleton or indirectly as a label on a recognition unit) facilitated the direct readout in cell culture experiments and performing the binding studies such as fluorescent polarization assays. Following the second strategic approach, we generated divalent tweezer skeletons of defined lengths. We also achieved the multiple attachments of molecular tweezers on to a gold nanoparticle and obtained the first multivalent tweezer skeleton of defined geometry and size.

The new concept of molecular tweezer for protein specificity has been proven through various performed biophysical experiments. X-ray structure of the complex between hybrid tweezer and 14-3-3 protein and NMR titrations performed with Survivin, respectively, are the strong experimental evidence for the binding of peptide-modified tweezers in a specific manner to the desired proteins' hot-regions. Furthermore, from ITC and FP measurements, we learned that unmodified molecular tweezer (CLR01) binds with significantly lower affinities than the corresponding tweezer-peptide hybrid molecule. Pull-down assays were done to prove the novel molecular tweezers' capability to inhibit the Survivin-CRM1 complex formation *in vitro*. For example, the tweezer-ELTLGEFL conjugate was already effective at 1-10  $\mu\text{M}$ , while its parent molecule tweezer-ELTL showed the same inhibitory effect only at a higher concentration range (10-50  $\mu\text{M}$ ). Information collected from pull-down assays and other instrumental measurements allowed us to discriminate between the examined ligands and proclaim the most effective ones. The new generation of molecular tweezers presented is shown to be able to recognize a specific region on a rugged protein surface and therewith influence Survivin's



PPI with CRM1. The functional applications and *in vitro* studies of tailor-made novel binders for the 14-3-3 protein case still need to be examined.

However, the first divalent, tailor-made molecular tweezers constructs are currently investigated to answer whether they may efficiently modulate and probe complex systems' protein functions. So far, we know that the short double tweezer-oligomer conjugate inhibits the Survivin-CRM1 interaction at ten times lower concentrations than the unmodified single molecular tweezer CLR01 as discussed in 4.2.5.2. Besides speculated improvement in binding affinities towards Survivin, we could not confirm the achievement of target specificity in NMR titrations. NMR results, as well as thermodynamic data collected from ITC measurements, are referring to cross-binding effects.

## 5.2 Outlook

This work describes the strategic approaches and tools used to create a novel generation of molecular tweezers. Nevertheless, the same strategy can be further implemented in many different variations to obtain even more powerful binders than those already described. This chapter outlines some of the ideas born while exploring further possibilities to improve tweezers' specificity and binding affinity.

Thinking of ways to advance the first strategic approach (Chapter 2.1), we designed a peptidic skeleton, equipped with the azide-ornithines on the N and C terminus (N<sub>3</sub>-ornithine-ELTLG-ornithine-N<sub>3</sub>). Utilizing the previously described click chemistry approach, both azido-functionalities should allow further functionalization with two tweezer molecules carrying alkyne moieties to give a divalent tweezer-peptide conjugate (**67**). Using computational chemistry, **67** was found to address the Survivin's NES region in an optimal manner (Figure 77). Besides the usual non-covalent interaction between two tweezer molecules and addressed lysines, the protein-ligand interaction diagram suggests several hydrogen bonds between the peptidic linker and the protein backbone. Importantly, the selected peptidic part maintains contact with the protein interface region during the entire simulation time.

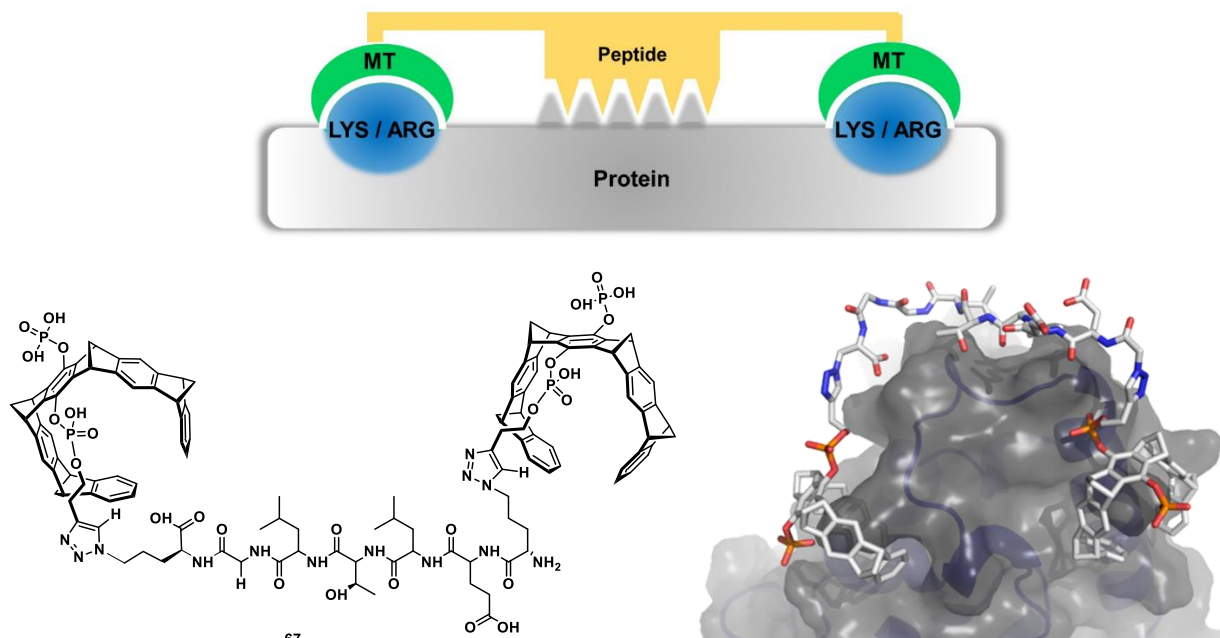


**Figure 77.** The next step in the improvement of the first strategic approach (Chapter 2.1). MD simulation of divalent tweezer-recognition peptide conjugate shielding Survivin's NES region.

The lack of specificity in the second strategical approach (Chapter 2.2) evaluated previously in the conclusion section can be overcome by introducing an additional binding motif (Figure 78).

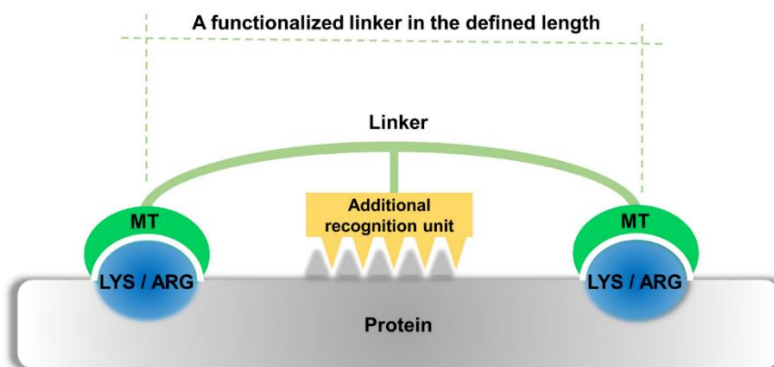


**Figure 78.** The next step in the improvement of the second strategic approach (Chapter 2.2). A functionalized linker of the defined length is carrying an additional recognition unit.

To improve Lys/Arg recognition specificity and enhance binding affinities towards targeted versatile protein regions of designed constructs, one must carefully inspect the

targeted protein regions and employ only those linkers that do not exhibit a large degree of freedom. However, the multivalent tweezer skeletons of defined geometries could be the key to successfully modulating the protein functions in complex systems. This concept is presented in Figure 79, which illustrates a multivalent tweezer skeleton targeting the four different lysines simultaneously in the Ndc80 microtubule. Rationally designed multivalent recognition units for synergistic binding to a protein's hot regions could dramatically contribute to the given challenges of modern supramolecular chemistry.

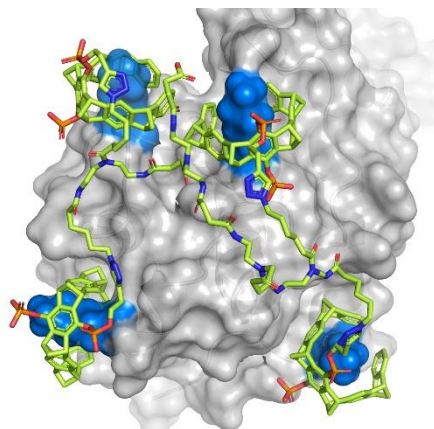


**Figure 79.** A multivalent tweezer skeleton (green sticks) of defined geometry targeting the four different lysines (marine blue spheres) simultaneously in the Ndc80 microtubule hot-region (gray surface).

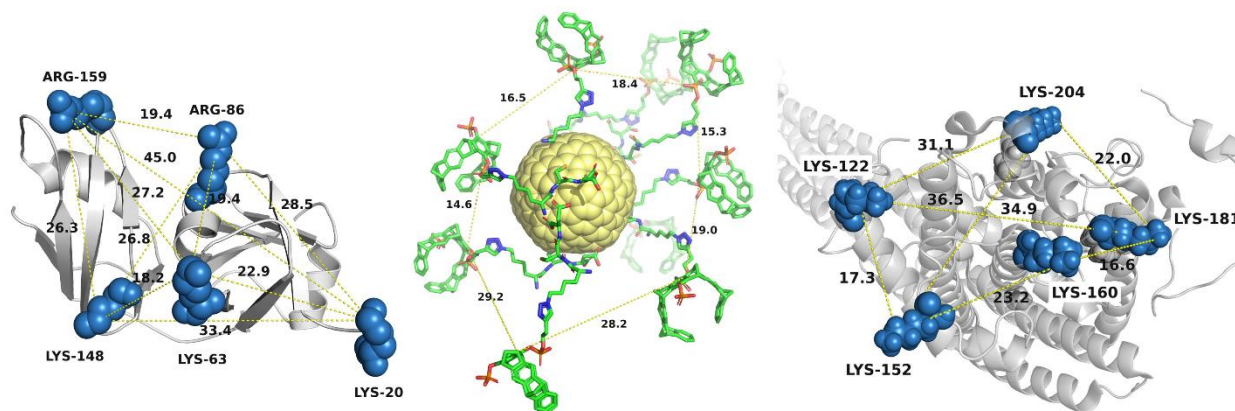


**Figure 80.** p-97 N-terminal domain (left) gold nanoparticle decorated with multiple molecular tweezer molecules (middle) and Ndc80 microtubule with the well-accessible lysines in the hot region (marine blue spheres).

Furthermore, the synthesized ultrasmall gold nanoparticle equipped with multiple tweezers in Epple's group can be probed to target proteins containing several well-accessible Lys/Arg, such as the N-terminal domain of p-97 and the head of

microtubule Ndc80 (Figure 80). The distances between the given amino acids correspond to those found between the tweezer molecules on the gold nanoparticle. Besides targeting the N-domain of protein p-97, the presented multivalent construct could eventually be applied to block the protein pore as well.

As shown in Chapter 1.6, intermolecular forces govern protein folding, assembly, and PPI. The specific inhibition or support of these non-covalent interactions represents a very promising area for external interference, with profound mechanistic and therapeutic implications. For example, the hydrophobic interface between the exotoxins and 14-3-3 proteins might be a useful target for the development of ExoS inhibitors. Given its roles in cell division, proliferation, and survival, the Survivin signaling pathway's exploitation may provide important predictive and prognostic clues to cancer diagnosis and offer new therapeutic alternatives for cancer treatment.

Besides the very broad scope of the possible application of novel molecular tweezers in protein recognition listed above, a last suggested application related to this work will target the SARS-CoV2 Spike protein-ACE2 Interface. The research group of Dr. Chunyu Wang at Rensselaer Polytechnic Institute found that SARS-CoV2 cell entry is facilitated by viral protein interaction with the human ACE2 Receptor.<sup>[182]</sup> Together with the Wang group, we became curious if the novel molecular tweezers can interfere with the PPI between the Spike protein and the human ACE2 Receptor. The first useful insights on the interaction of a novel generation of molecular tweezers were gained again utilizing computational chemistry.

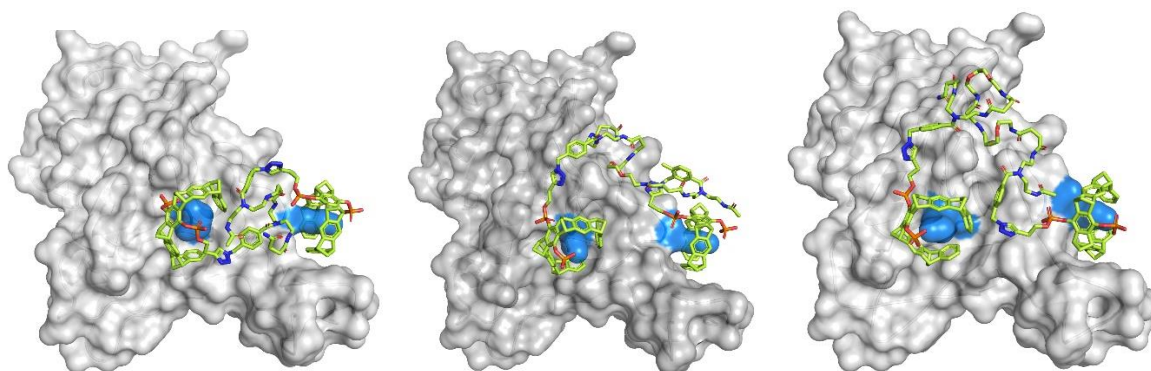


**Figure 81.** The novel coronavirus Spike receptor-binding domain (gray surface) and the critical lysines (K417 located in the vicinity of the interface with ACE2 and K458 located at the interface with ACE2) docked with **64**, **65**, and **67**, respectively. (PDB ID: 6LZG)

Dylan Mah from the Wang group modeled double tweezers constructs offered by our group. The chemical structures of four different constructs were inspected, among which **64**, **65**, and **66**. Double tweezer precision-oligomer conjugates exhibited many intramolecular interactions and, therefore, may behave like foldamers. Nevertheless, it has been found that all three inspected molecules are capable of capturing both critical lysines in the host cavity, with favorable hydrophobic and electrostatic interactions (Figure 81). The fourth inspected molecule is double tweezer derivate with a minimal peptidic linker length, also showed stable interactions with K417 and K458. The newly designed divalent tweezer molecule captured the protein-protein interface even more efficiently than it has been the case with previous three molecules. The peptidic linker connecting two tweezer molecules has the perfect length and does not inter-fold like the case with previously shown oligomeric linkers (Figure 82).

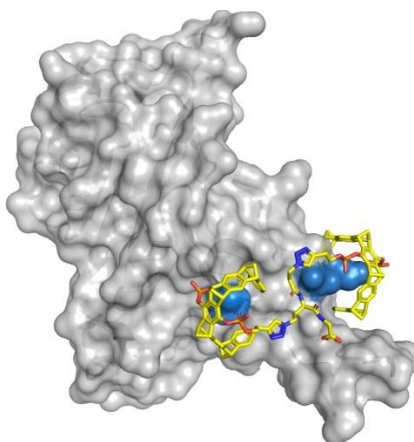


**Figure 82.** The novel coronavirus Spike receptor-binding domain (gray surface) and the critical lysines (K417 located in the vicinity of the interface with ACE2 and K458 located at the interface with ACE2) (marine blue spheres) docked with the double tweezer derivate with the shortest possible peptidic linker. (PDB ID: 6LZG)

This molecule is yet to be synthesized. It represents the double tweezer derivate connected with the shortest possible peptidic linker according to safety instructions. Since the peptidic linker carries two azide-functionalities within a relatively small molecule, it is recommendable to handle it with caution. The linker needs to be stored below room temperature, at a not higher concentration than 1 M, and the maximal amount of 5 g. The synthetic strategy for obtaining this molecule could be based on the solid phase peptide

synthesis (Figure 83). After cleaving the peptide **68** from the resin, a subsequential double click reaction is expected to yield the desired product.

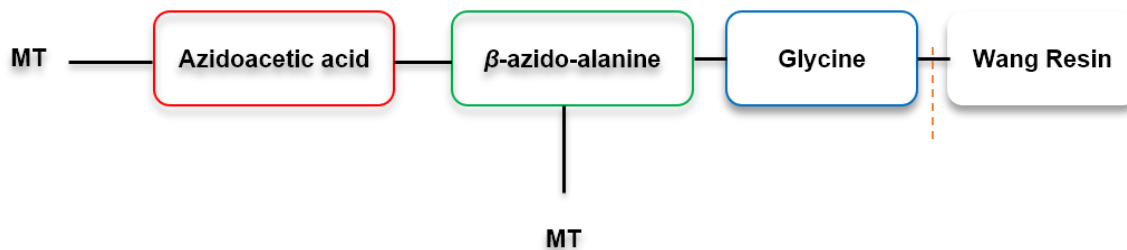


**Figure 83.** SPPS plan for the shortest double azide-peptide, subsequent cleavage from the resin, and two click reactions.

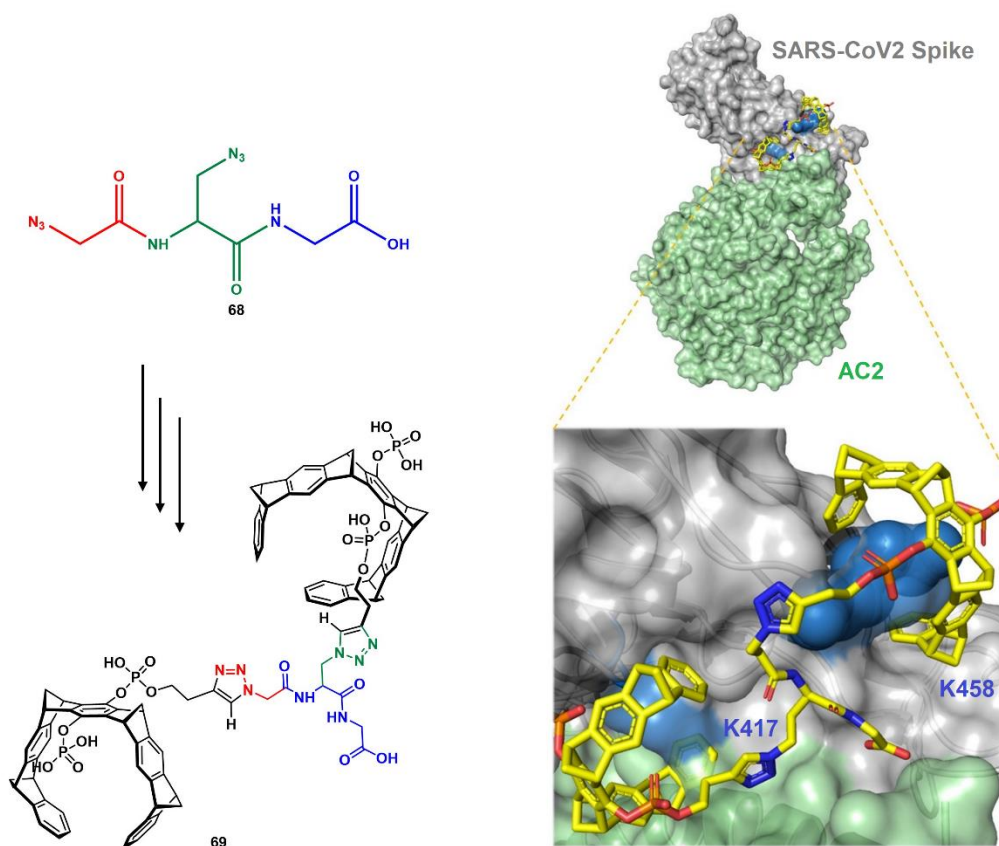


**Figure 84.** The shortest "safe" double azido-peptide **68** functionalized into novel divalent molecular tweezer **69** (left). SARS-CoV2 Spike protein (gray surface) complexed with its receptor ACE2 (green surface) and **69** binding in their interface. (PDB ID: 6LZG)

The four above shown molecules can be tested experimentally to determine the binding affinities to SARS-CoV2 Spike protein with SPR. To test inhibition of viral cellular

entry, one could examine the disruption of SARS-CoV2 Spike protein-ACE2 interaction with AlphaScreen assay.

## 6 AUTHOR'S CONTRIBUTIONS TO PRESENTED PUBLICATIONS

### Publication I

**Hadrović, I.**, Rebmann, P., Klärner, F.-G., Bitan, G., Schrader, T. *Molecular Lysine Tweezers Counteract Aberrant Protein Aggregation*. *Frontiers in Chemistry* 7, 657, **2019**. DOI: 10.3389/fchem.2019.00657

**IH** wrote chapters about the prevention of pathologic protein aggregation by molecular tweezers, summarized the novel findings of instrumental methods for determining the binding mode and interaction mechanism of amyloid proteins and molecular tweezers (Thioflavin T-ThT Fluorescence, Electron Microscopy-EM, Circular Dichroism-CD Spectroscopy, Dynamic Light Scattering-DLS, and Mass Spectrometry-MS).

### Publication II

Guillory, X., **Hadrović, I.**, de Vink, P., Brunsveld, L., Schrader, T., Ottmann, C. *Supramolecular Enhancement of Natural 14-3-3 Protein Ligands*. *J. Am. Chem. Soc.*, 143, 13495–13500, **2021**. DOI: org/10.1021/jacs.1c07095

**IH** contributed to the rational design of the ligands performing MD simulations, carried out all syntheses and characterizations of the ligands and subsequent ITC measurements. **IH** and **PdV** performed the direct FP titrations with the fluorescently labeled ligands (SPR and MST measurements as well, but they are not published). **IH** wrote the first SI draft. All authors contributed to the final version of the manuscript.

### Publication III

Meiners, A., Bäcker, S., **Hadrović, I.**, Heid, C., Beuck, C., Ruiz-Blanco, Y., Mieres-Perez, J., Pörschke, M., Grad, J.-N., Vallet, C., Hoffmann, D., Bayer, P., Sanchez-Garcia, E., Schrader, T., Knauer, S. *Targeting a protein epitope: Specific inhibition of the Survivin-CRM1-interaction by peptide-modified Molecular Tweezers*. *Nature Commun.* 12, 1505, **2021**. DOI: org/10.1038/s41467-021-21753-9



**IH** provided all 10 ligands for biological assays, made fluorescently labeled conjugates that allowed direct FP titrations, and determined affinities by ITC titrations with AM.

#### **Publication IV**

van der Meer, S.-B., **Hadrovic, I.**, Meiners, A., Loza, K., Heggen, M., Knauer, S., Bayer, P., Schrader, T., Beuck, C., Epple, M. *New tools to probe the protein surface: Ultrasmall gold nanoparticles carry amino acid binders*. J. Phys. Chem. B, 125, 115-127, **2021**.

DOI: [doi.org/10.1021/acs.jpccb.0c09846](https://doi.org/10.1021/acs.jpccb.0c09846)

**IH** synthesized and characterized monobutynyl tweezer used for functionalization of ultrasmall gold nanoparticles, contributed to the interpretation of ITC data, and modeled the graphical abstract.

## 7 THE EXPERIMENTAL PART RELEVANT FOR UNPUBLISHED WORK

The experimental part relevant for published work can be found within supporting information. This chapter describes only the experimental work that has not been published yet.

### 7.1 Materials and methods

#### 7.1.1 Reagents

All reagents needed are commercially available and were purchased from various suppliers at the highest purity grade available. The reagents were further used as received without further purification unless otherwise stated. CsF was dried before use for 12 h at 180 °C under high vacuum. The commercially available reagents for click reactions (copper sulfate pentahydrate –  $\text{CuSO}_4 \cdot 5\text{H}_2\text{O}$ , sodium ascorbate solution –  $\text{C}_6\text{H}_7\text{NaO}_6$ , and sodium hydroxide – NaOH) were purchased from Sigma Aldrich, each at the highest purity grade available and were used as received without further purification.

#### 7.1.2 Solvents

Toluene was distilled under argon and dry over activated molecular sieves type 4A in a Schlenk tube. For the performance of column- and thin layer chromatography solvents of technical quality, distilled over sodium were used exclusively. P.a. grade solvents for chromatographic and spectroscopic purposes were used without further purification, under an argon stream. The deuterated solvents were purchased and stored over molecular sieves under an inert atmosphere. Tetrahydrofuran (THF) and *N,N*-diisopropylethylamine (DIPEA) were freshly distilled before the use, according to the standard procedures under an argon stream. Deionized water was further purified over PURELAB classic to deliver 18.2 M $\Omega$ .cm type I ultrapure water. Evaporation of bulk solvents was done under reduced pressure using Heidolph rotary evaporators.

#### 7.1.3 Freeze-drying

Lyophilization of all final products was done by Christ des Models Alpha 2-4 LSC freeze dryer.

#### 7.1.4 Chromatography

The reactions were monitored by standard and reversed-phase thin-layer chromatography (RP-TLC), respectively, using Merck Kieselgel RP-18 fluorescent treated silica aluminum plates, which were visualized under UV light (254 nm and 366 nm) or by staining with a solution of potassium permanganate in ethanol. TLC chromatography was utilized for the semi-preparative purification of the fluorinated molecular tweezer as well, using pre-coated glass TLC plates SIL G-50 with fluorescent indicator UV<sub>254</sub> and 0.5 mm layer thickness. The gradient of cyclohexane (Cy) and ethyl acetate (EtOAc) 3:1 was used as the eluent.

Click reactions were monitored by reversed-phase thin-layer chromatography (RP-TLC) when practical, using Merck Kieselgel RP-18 fluorescent treated silica aluminum plates, which were visualized under UV light (254 nm and 366 nm) or by staining with a solution of potassium permanganate in ethanol.

#### 7.1.5 Oxygen-free Techniques

The fluorination reaction was carried out under an inert atmosphere using the glovebox techniques (4 MBRAUN glovebox filled with argon with water and oxygen presence level under 0.5 ppm) as well as the Schlenk techniques for the rest of the conversions.

#### 7.1.6 NMR Spectrometry

The <sup>1</sup>H- and <sup>31</sup>P-NMR-spectra were primarily recorded with Bruker DMX 300 instrument (300 MHz). The Advance-III-HD 600-instrument (600 MHz) from the same company was used to obtain <sup>13</sup>C-, DEPT 90-, DEPT 135-NMR data as well as for the more precise <sup>1</sup>H-NMR analysis. Furthermore, 600-instrument has been used for 2D-measurements (HMBC, HSQC, <sup>1</sup>H, <sup>1</sup>H-COSY, <sup>13</sup>C-COSY, TOCSY, NOESY, ROESY). All measurements were performed at room temperature using CDCl<sub>3</sub> and DMSO-d<sub>6</sub> as a solvent, respectively. Chemical shifts ( $\delta$ ) are given in parts per million (ppm), and coupling constants (J) are given in Hertz (Hz), rounded to the nearest 0.1 Hz. The chemical shifts are relative to the signals of DMSO-d<sub>6</sub> ( $\delta$  <sup>1</sup>H = 2.50 ppm and  $\delta$  <sup>13</sup>C = 39.5 ppm). NMR assignments are made according to spin systems, using two-dimensional (COSY, HSQC, HMBC) NMR spectroscopy to assist the assignment when possible. The <sup>1</sup>H NMR spectra

are reported as follows: ppm (multiplicity, coupling constants, number of protons). The spectra were evaluated using the MestReNova and TopSpin software.

### **7.1.7 Mass Spectrometry**

HRMS analyses were performed using Bruker BioTOF III mass spectrometer with electrospray ionization (ESI), electron impact ionization (EI), or atmospheric pressure chemical ionization (APCI). GC-MS was performed on an Agilent 6890 Series GC and 5973 detectors using an HP-5MS UI column (15 m x 0.25 mm x 0.25  $\mu$ m).

### **7.1.8 Molecular Modeling**

Maestro Software (Schrödinger Release 2019-1: Schrödinger, LLC, New York, NY, 2019) was used for visualization, necessary molecular modeling steps (protein preparation, and energy minimization), as well as for the molecular dynamic (MD) simulation trajectory using Desmond. The crystal structure of Survivin protein (PDB ID: 1XOX) in complex with double tweezer-oligomer ligands, addressing the two critical lysines K90/103 in the NES region, served as the starting point for all molecular modeling. Finally, the protein-ligand complexes were subjected to geometry refinements using the OPLS\_2005 force field in restrained minimizations. The PyMOL Molecular Graphics System, Version 2.0 Schrödinger, LLC was used for visualization of structures generated in Maestro.

#### **7.1.8.1 Ligand Preparation and 3D Docking**

Ligands were prepared using LigPrep in the Schrödinger suite. The molecular tweezer molecules were docked to the well accessible lysines 90 and 103 in the vicinity of the Survivin binding groove in a 3D manner. After the minimization of molecular tweezers, and subsequent optimization using the LigPrep module, the final ligand structure was generated by utilizing the builder panel in Maestro. This tool allowed the creation of bridging linkers in the form of triazole rings between the alkyne moiety on the tweezer and the two azide moieties on the oligomer.

### **7.1.8.2 Molecular Dynamics Simulation**

The OPLS\_2005 force field was used for optimization and production of low energy conformer of the ligands (Force Field: OPLS\_2005; Monte Carlo: 1000 steps, GBA solvation). The resulting structure was then chosen for performing molecular dynamics simulations using Desmond-GPU (MD: Desmond-GPU, 100 ns, NPT, 150 mM NaCl, explicit water, 300 K).

### **7.1.9 Isothermal Titration Calorimetry**

ITC-measurements were done using Malvern MicroCal 200 VP-ITC calorimeter. The titrations consisted of a series of 18 times injections, each 2- $\mu$ L volume (0.4  $\mu$ L being the first injection volume only). All measurements are performed at 25 °C with cell reference power of 5  $\mu$ Cal/s, initial delay of 180 s, stirring speed of 750 rpm, and spacing of 200 s. Obtained thermodynamic data were interpreted using Affinimeter software (Cloud-version).

### **7.1.10 Pull-down assays and Western Blotting Analysis**

Pull-down assays were performed in the group of Prof. Dr. Shirley Knauer within CRC 1093. The experiments were carried out by Annika Meiners at room temperature in a pull-down buffer (PBS, pH 7.4, 1 mM DTT, 0.02 % Triton X-100). GST fusion proteins were immobilized on 50  $\mu$ l GSH-coated Sepharose 4B beads from GE Healthcare. The beads were prior equilibrated and blocked with pull-down blocking buffer (PBS, pH 7.4, 1 % (w/v) BSA, 1mM DTT, 0.02 % (v/v) Triton X-100) for 1 h to prevent unspecific binding. For analysis of the inhibitory tweezer concentration, 200  $\mu$ g 293T lysate with overexpressed Survivin142-HA were pre-incubated without ligand or with different concentrations (10 nM to 200  $\mu$ M) of the oligomer double tweezers for one hour and then mixed with 35  $\mu$ g GST-CRM1 and 55  $\mu$ g RanQ69L and 2 mM dGTP. GSH-beads were incubated with the protein mixture for two hours under rotation. Input and bead samples were analyzed by Western blotting.

## 7.2 Synthesis

### 7.2.1 Synthesis of **57**

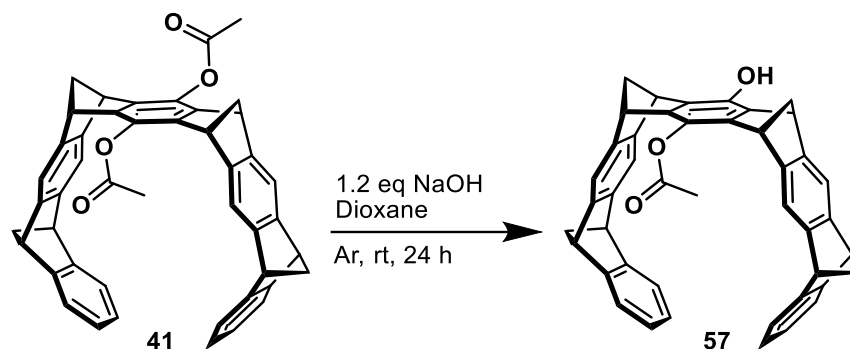
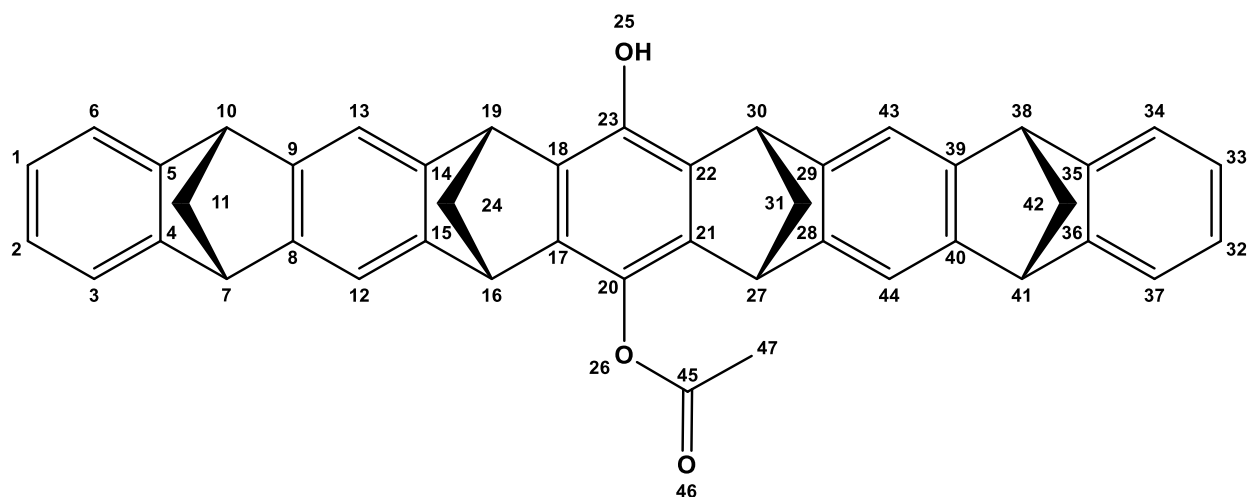
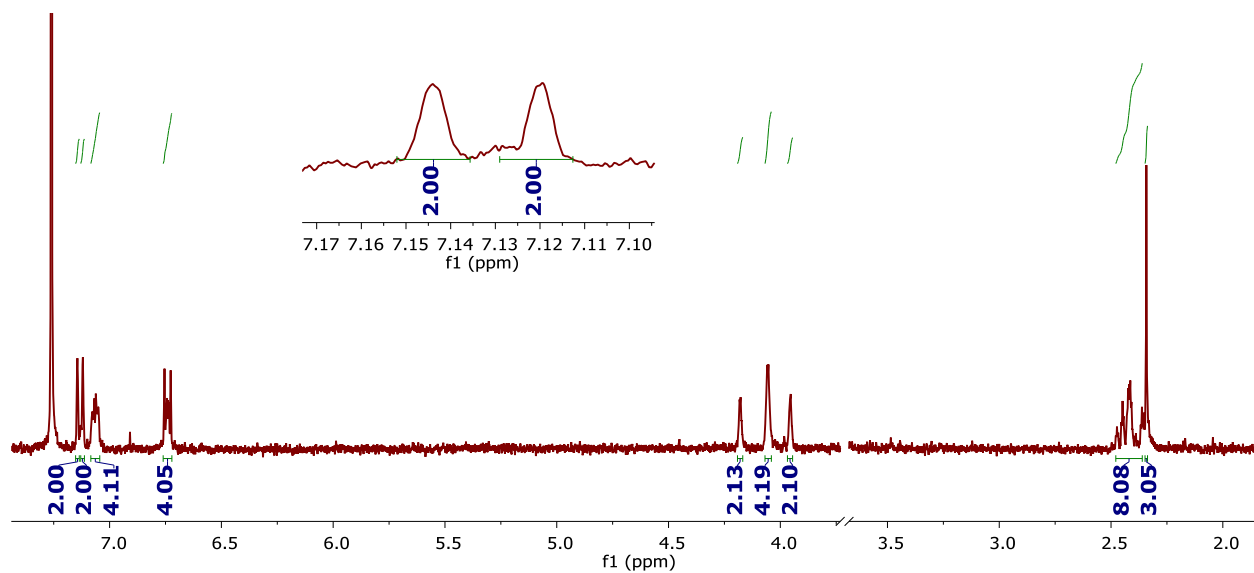


**Figure 85.** Synthesis of **57**.

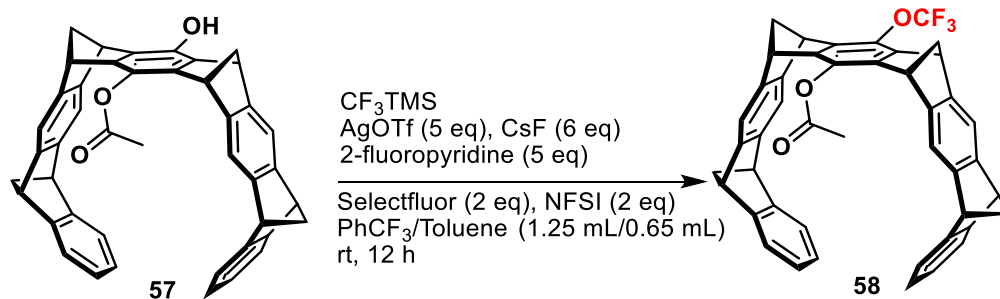
To a dry, round bottom Schlenk flask of 250 mL diacetoxy tweezer, **41** (600 mg, 0.92 mmol) was added under the flush of argon. Argon stream and high vacuum were applied alternately three times to eliminate the presence of oxygen. Vigorously stirring dioxane and freshly prepared NaOH<sub>aq</sub> were degassed separately for three hours. Under argon, 50 mL of degassed dioxane was added to the **41** using the three-needle technique. Once the **41** was completely dissolved, 1.4 equivalents of NaOH<sub>aq</sub> (1 M, 1.23 mL, 1.23 mmol) were added dropwise, again avoiding the air contact. The solution immediately turned to bright-yellow. The reaction was left to stir under argon at room temperature. After 24 hours, quenching proceeded with 150 mL 1:1 mixture of saturated NH<sub>4</sub>Cl and 6 M HCl. Subsequently, the resulted aqueous solution was extracted with dichloromethane (DCM) 3 x 70 mL. The collected organic layers were washed with distilled water, then brine, and finally dried over Na<sub>2</sub>SO<sub>4</sub>. Evaporation of DCM and dioxane was done under reduced pressure using a rotary evaporator, leaving the yellowish solid on the walls of the flask. The product was purified by column chromatography (Cy:EtOAc = 3:1), giving **57** as colorless solid in almost quantitative yield (550 mg, 0.905 mmol, **98 % yield**).



**$^1\text{H NMR}$**  (300 MHz, Chloroform-*d*)  $\delta$  [ppm] = 2.34 (s, 3H, H-47), 2.36 – 2.50 (m, 8H, H-11, H-24, H-31, H-42), 3.93 – 3.98 (m, 2H, H-16, H-27), 4.02 – 4.08 (m, 4H, H-7, H-10, H-38, H-41), 4.15 – 4.20 (m, 2H, H-19, H-30), 6.67 – 6.80 (m, 4H, H-1, H-2, H-32, H-33), 7.02 – 7.10 (m, 4H, H-3, H-6, H-34, H-37), 7.12 (s, 2H, H-12, H-44), 7.14 (s, 2H, H-13, H-43).

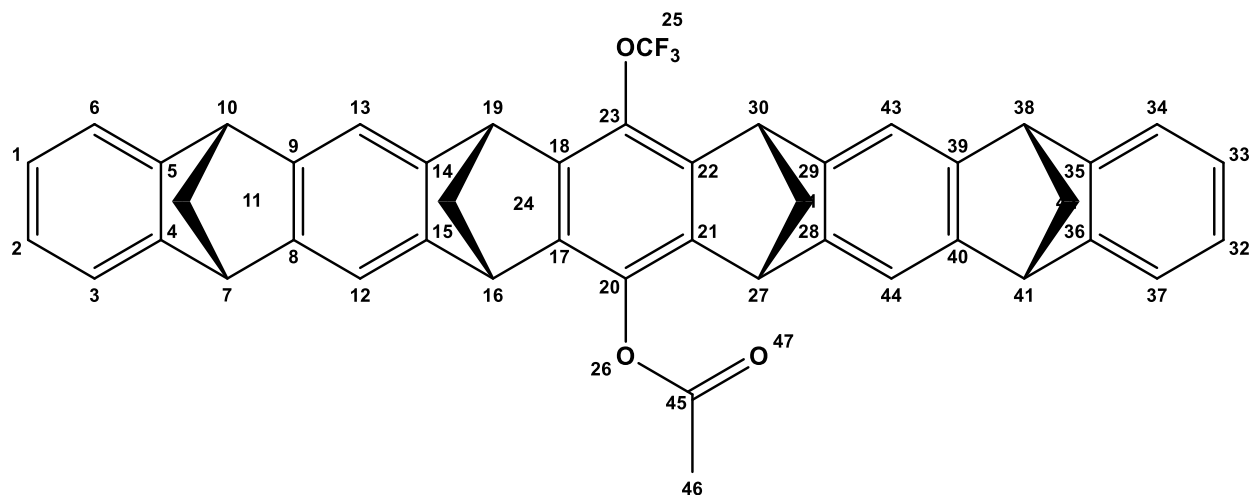


**Figure 86.**  $^1\text{H NMR}$  spectra of **57**.

7.2.2 Synthesis of **58****Figure 87.** Synthesis of **58**.

To a dried reaction Schlenk tube that was equipped with a stirring bar, AgOTf (160.4 mg, 0.62 mmol, 5.0 eq), Selectfluor (87.15 mg, 0.25 mmol, 2.0 eq), NFSI (77.57 mg, 0.25 mmol, 2.0 eq), CsF (121.10 mg, 0.74 mmol, 6.0 eq), phenol (monohydroxy-tweezer) (76.00 mg, 0.12 mmol, 1.0 eq) were added successively in a argon-filled glovebox. After that, the flask was taken out of the glovebox, and toluene (0.62 mL), benzotrifluoride (1.25 mL), 2-fluoropyridine (60.00 mg, 2.5 mmol, 5.0 eq), and CF<sub>3</sub>TMS (88 mg, 2.5 mmol, 5.0 eq) were added successively under Ar atmosphere using the Schlenk line. The reaction mixture was stirred at room temperature, wrapped in aluminum foil overnight. After 12 h, the reaction mixture was filtered through a plug of silica (eluted with ethyl acetate). The filtrate was concentrated by evaporating the solvent leaving the aryl trifluoromethyl ether in the form of yellow solid (80 mg crude yield). Further, the obtained product was purified, first using the column chromatography applying the gradient of Cy:EtOAc = 15:1→3:1. Seven fractions with different retention times were collected. Since the obtained product has shown the presence of impurities in NMR, two subsequent semi-preparative TLCs were used in the next purification step to obtain the pure product **58** as colorless solid (28 mg, 0.04 mmol, **33 % yield**).





**$^1\text{H NMR}$**  (300 MHz, Chloroform-*d*)  $\delta$  [ppm] = 2.31 – 2.53 (m, 11H, H-11, H-24, H-31, H-42, H-46), 3.96 – 4.03 (m, 2H, H-16, H-27), 4.03 – 4.10 (m, 4H, H-7, H-10, H-38, H-41), 4.24 – 4.32 (m, 2H, H-19, H-30), 6.70 – 6.79 (m, 4H, H-1, H-2, H-32, H-33), 7.10 – 7.14 (m, 4H, H-3, H-6, H-34, H-37), 7.11 – 7.14 (m, 2H, H-12, H-44), 7.15 (s, 2H, H-13, H-43).

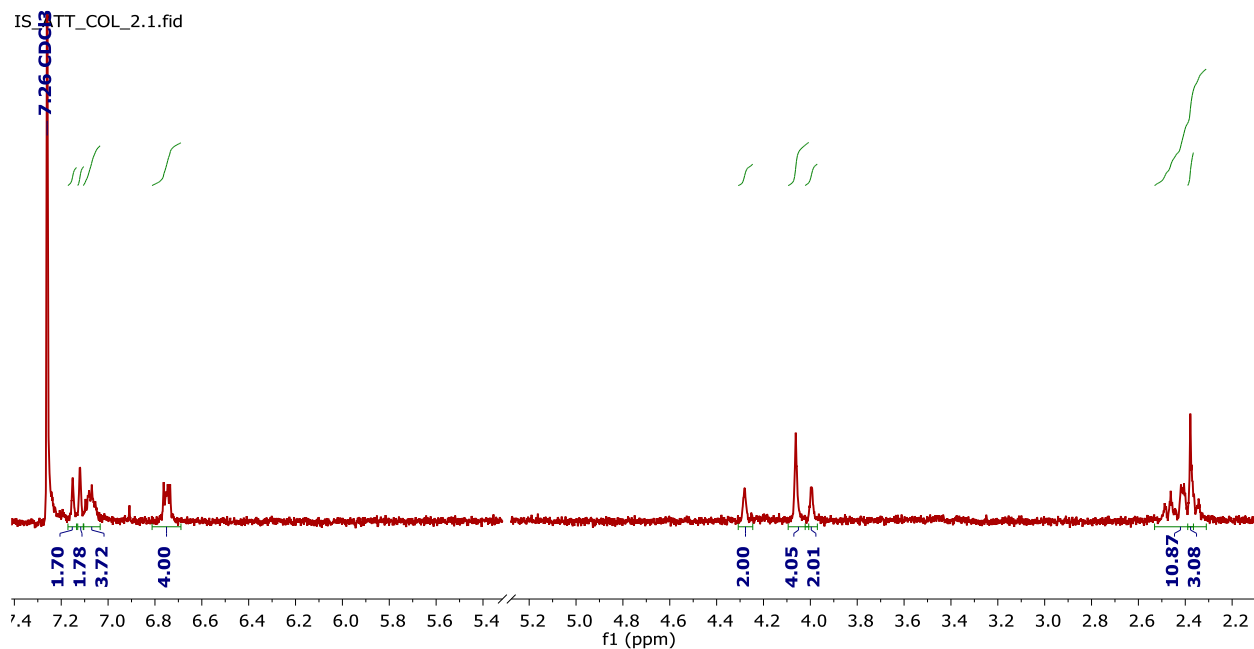


**Figure 88.**  $^1\text{H NMR}$  spectra of **58**.

**$^{19}\text{F NMR}$**  (565 MHz, Chloroform-*d*)  $\delta$  [ppm] = -57.87

**HPLC-MS (ESI<sup>+</sup>):** [H<sub>2</sub>O/MeCN, 15→95 %], Retention time: 0.707 min [M+Na]<sup>+</sup>: calcd. for C<sub>45</sub>H<sub>31</sub>F<sub>3</sub>O<sub>3</sub>, 699.220; found 699.206.

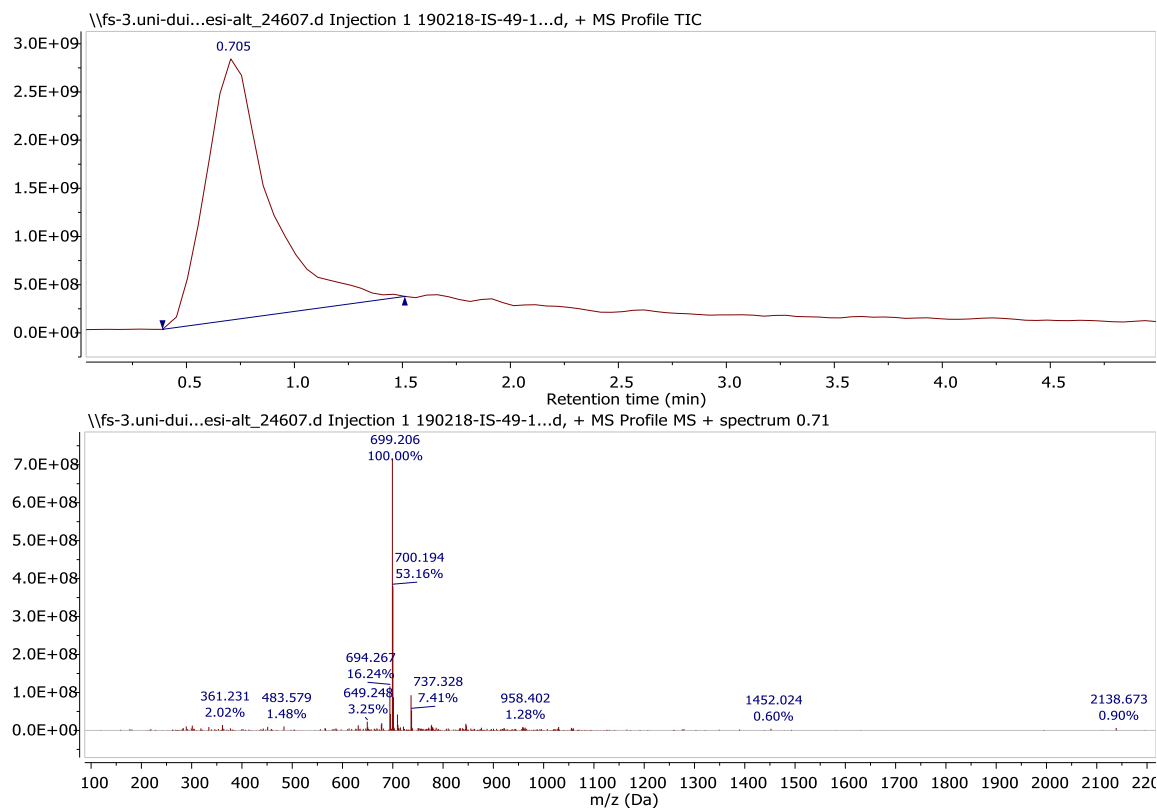


**Figure 89.** HPLC-MS of **58**.

**HRMS (m/z):** [M+H]<sup>+</sup>: calcd. for C<sub>45</sub>H<sub>31</sub>F<sub>3</sub>O<sub>3</sub> 677.2298; found 677.2297.

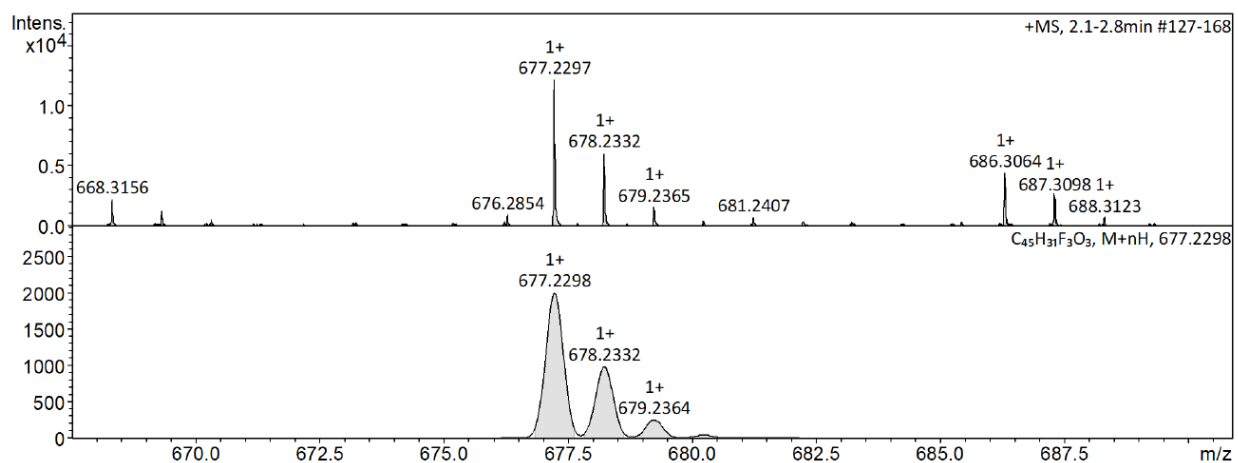


**Figure 90.** HRMS of **58**.

### 7.2.2.1 Purification of 58

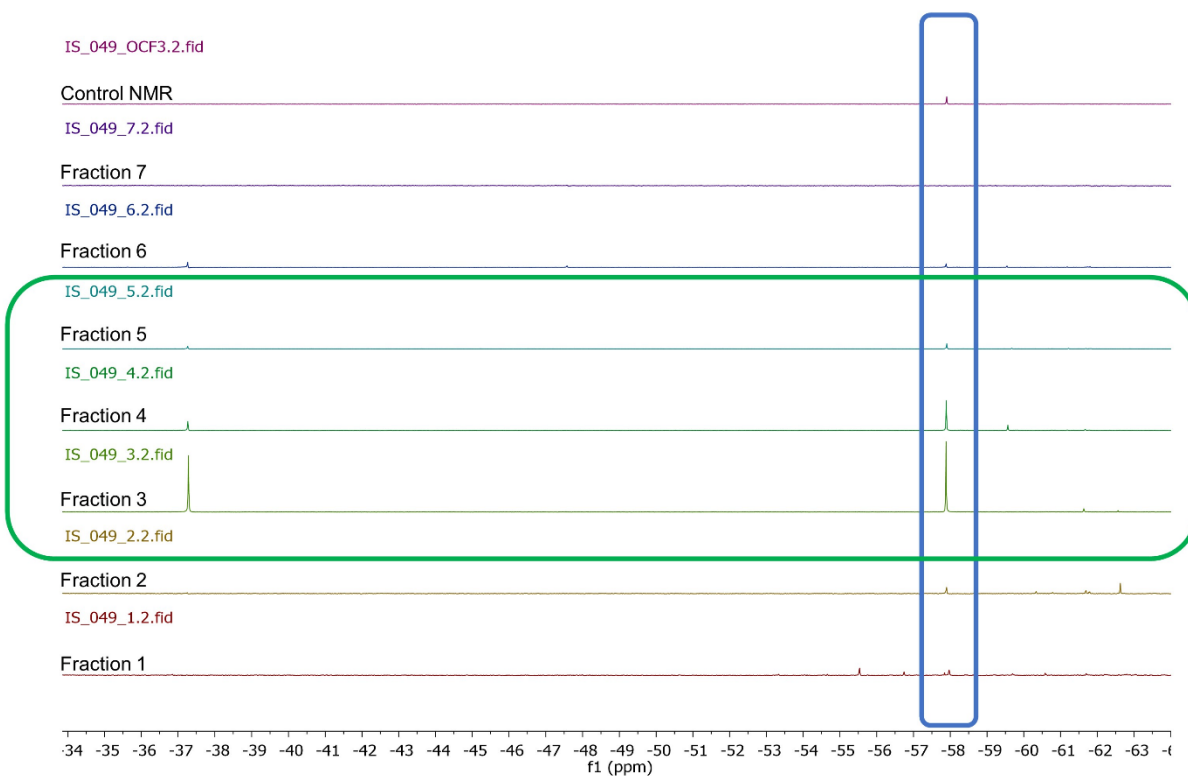


**Figure 91.**  $^{19}\text{F}$  NMR of seven collected fractions after the first column compared to the control probe. The signal labeled with the blue box is the desired one, and the green box comprised fraction that were united and purified further *via* semi-preparative TLC.

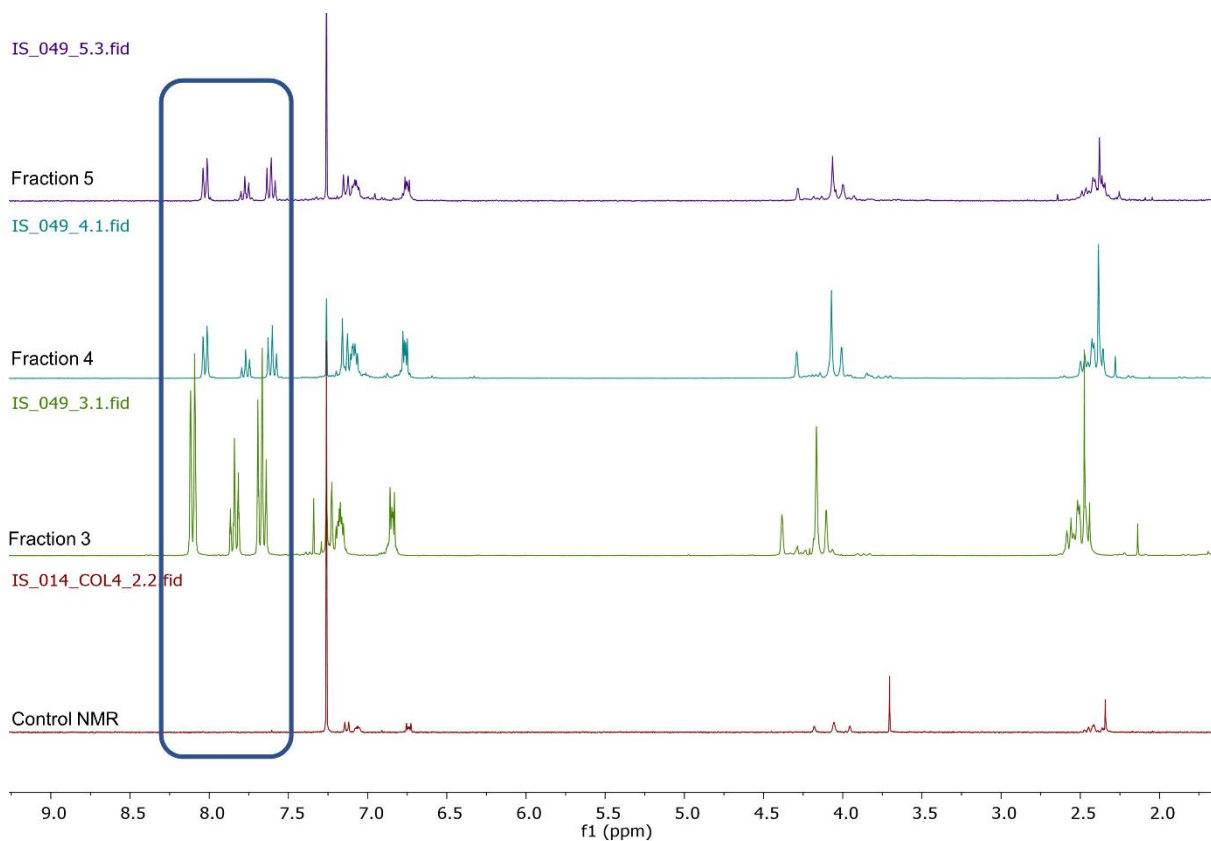


**Figure 92.**  $^1\text{H}$  NMR of three united fractions after the first column compared to the control probe. The blue box illustrates the main impurities that were still presented in the three fractions in comparison to the control probe after the column chromatography.

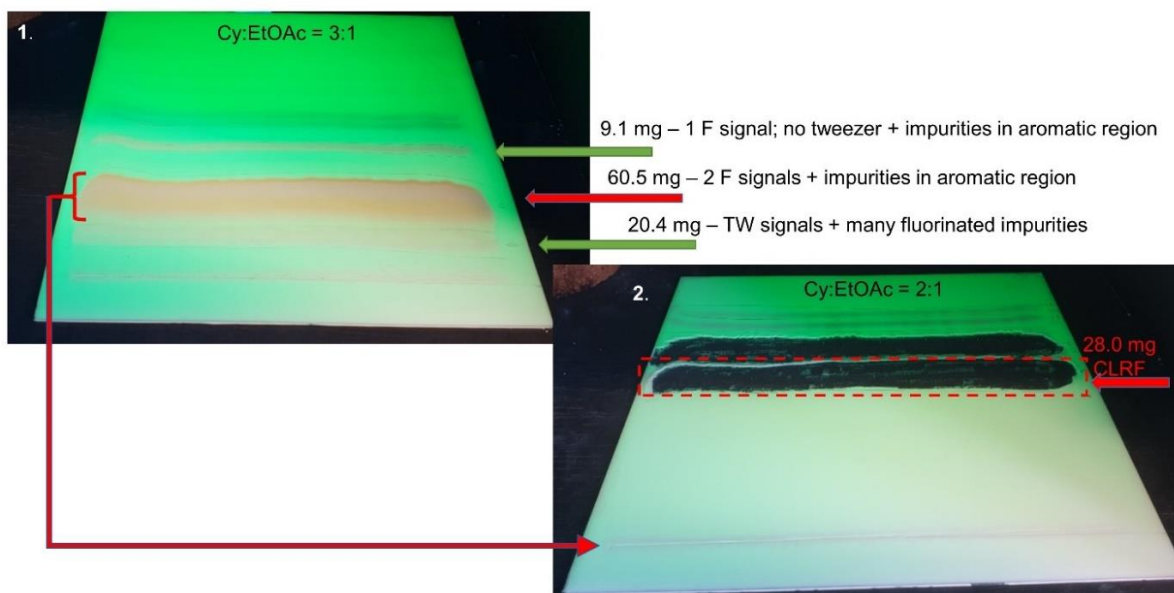


**Figure 93.** Semi-preparative TLC. In the 1. step, the three most promising fractions shown in Figure 57. are applied together on the baseline of the glass plate. Using the solvent mixture of Cy:EtOAc = 3:1, the plate was let to develop in the chamber for 1.5 hours. Three bands were separated, and the middle one

was used as crude in the 2. semi-preparative TLC. As eluent, the mixture of Cy:EtOAc = 2:1 was used to yield pure CLRF.

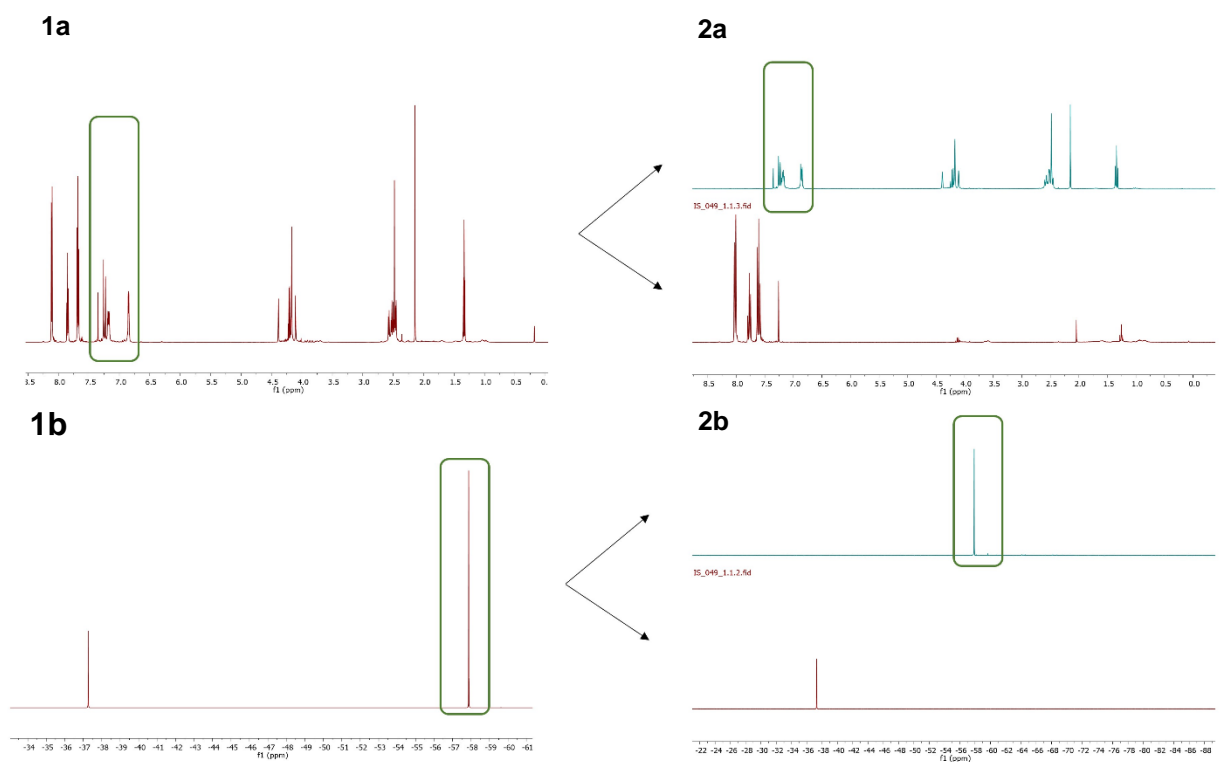


**Figure 94.** The  $^1\text{H}$  NMR (1a) and  $^{19}\text{F}$  NMR (1b) of the isolated crude product after the first semi-preparative TLC (green boxes are including the signals of the desired product). In 2a and 2b,  $^1\text{H}$  NMR and  $^{19}\text{F}$  NMR of the two obtained fractions after the final semi-preparative TLC are shown, respectively, where the upper spectra are the spectra of the CLRF.

## 7.2.3 Synthesis of 59

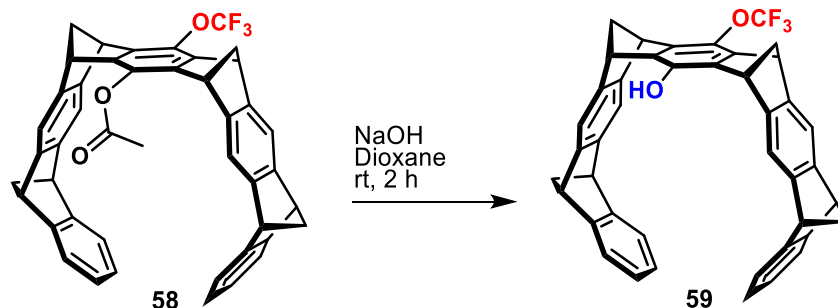
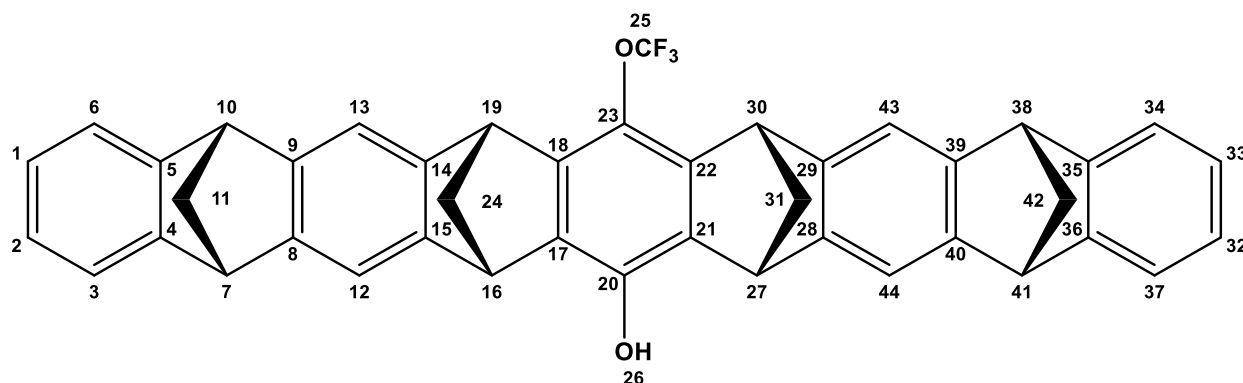


Figure 95. Synthesis of 59.

In a 50 mL one neck round bottom flask equipped with a stirring bar, **58** (25 mg, 0.036 mmol) was dissolved in 10 mL dioxane, after which 1.2 equivalents of 0.1 M NaOH (440  $\mu$ L, 0.044 mmol) were added dropwise and stirred continued for additional 2 h at room temperature. The quenching proceeded with 150 mL 1:1 mixture of saturated  $\text{NH}_4\text{Cl}$  and 6 M HCl. The aqueous solution was extracted with dichloromethane (3 x 15 mL). The collected organic layers were washed with distilled water and brine and dried over  $\text{Na}_2\text{SO}_4$ . Evaporation of DCM and dioxane was done under reduced pressure using a rotary evaporator, giving a beige solid (22 mg, 0.034 mmol, **96 % yield**).



$^1\text{H NMR}$  (300 MHz, Chloroform-*d*)  $\delta$  [ppm] = 2.32 – 2.50 (m, 8H H-11, H-24, H-31, H-42), 4.07 (m, 4H, H-7, H-10, H-38, H-41), 4.19 – 4.25 (m, 2H, H-19, H-30), 4.23 – 4.30 (m, 2H, H-16, H-27), 6.70 – 6.81 (m, 4H, H-1, H-2, H-32, H-33), 7.05 – 7.11 (m, 4H, H-3, H-6, H-34, H-37), 7.13 (s, 2H, H-12, H-44), 7.17 (s, 2H, H-13, H-43).

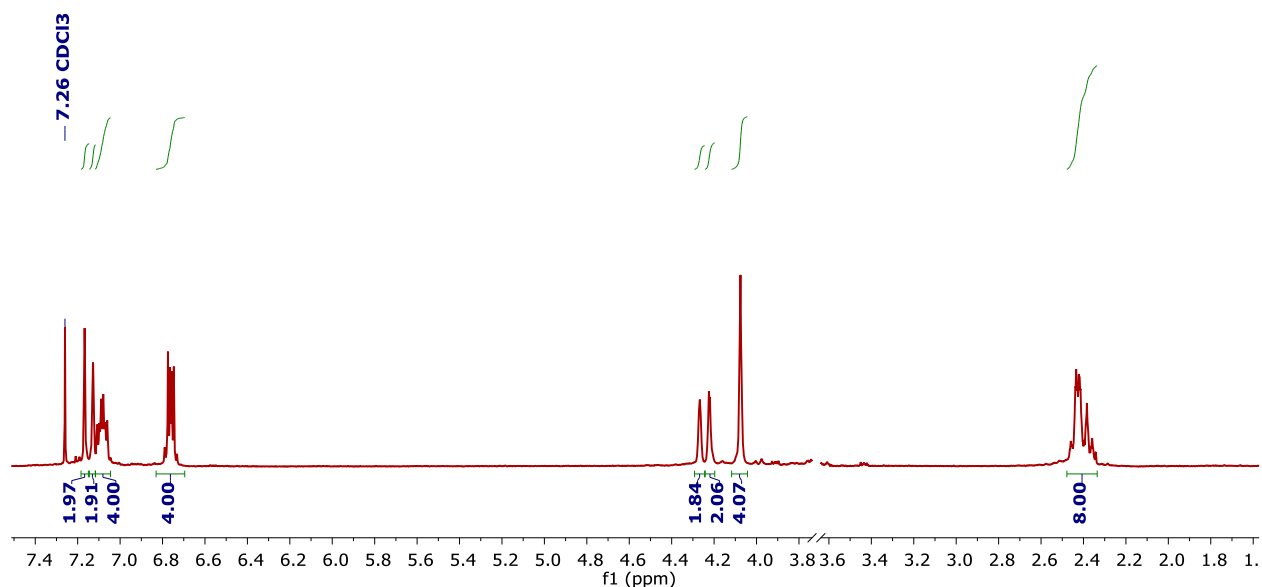


Figure 96.  $^1\text{H}$  NMR spectra of **59**.

$^{19}\text{F}$  NMR (565 MHz, Chloroform-*d*)  $\delta$  [ppm] = -57.87

#### 7.2.4 Synthesis of **60**

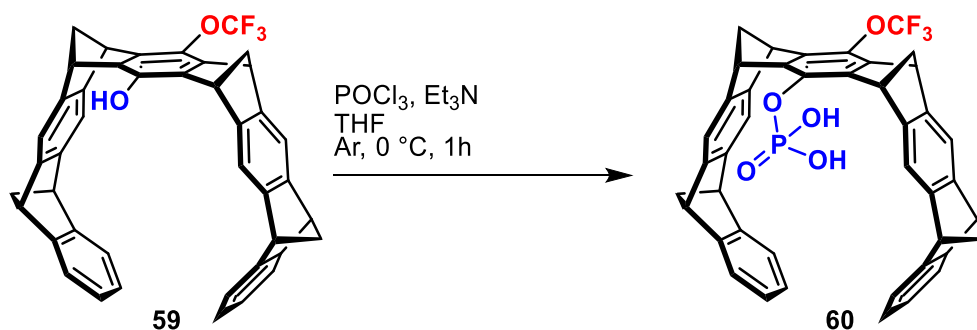
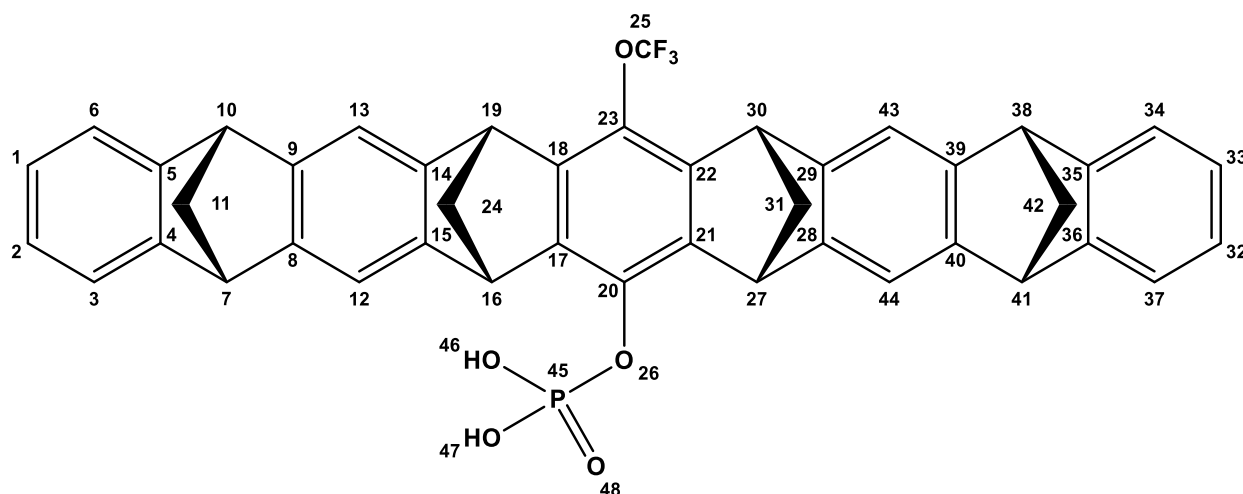


Figure 97. Synthesis of **60**.

To a 0 °C cooled, stirring solution of **59** (20 mg, 0.031 mmol) in 5 mL distilled anhydrous THF under argon atmosphere, 32  $\mu\text{L}$  freshly distilled phosphoryl chloride and 75  $\mu\text{L}$  triethylamine, one after another, were added dropwise. The resulting mixture was stirred at 0 °C for an additional hour. The solution was allowed to warm up to room temperature under argon, after which it was distilled utilizing the static vacuum Schlenk techniques. Work-up of the resulting solid proceeded by the addition of 20 mL of 1 M HCl and subsequent ultrasound treatment of 10 minutes. The solution was filtered through the

D4 fritted funnel, and the collected solid was rinsed with an additional 5 mL of diluted HCl and finally with 5 mL distilled water. Using the distilled THF, the crude product was rinsed from the funnel into a 50 mL round-bottom flask, mixed with 15 mL water, and left to stir overnight. After removing the solvent on a rotary evaporator and the lyophilizer, the brownish residue was purified by reversed-phase column chromatography (MeCN:H<sub>2</sub>O = 10:1 → 5:1), yielding a beige solid (12 mg, 0.017 mmol, **54 % yield**).



**<sup>1</sup>H NMR** (600 MHz, DMSO-d<sub>6</sub>) δ [ppm] = 2.22 – 2.39 (m, 8H, H-11, H-24, H-31, H-42), 4.06 – 4.17 (m, 4H, H-7, H-10, H-38, H-41), 4.21 – 4.26 (m, 2H, H-19, H-30), 4.29 – 4.44 (m, 2H, H-16, H-27), 6.71 – 6.83 (m, 4H, H-1, H-2, H-32, H-33), 7.05 – 7.15 (m, 6H, H-3, H-6, H-34, H-37, H-12, H-44), 7.15 – 7.21 (s, 2H, H-13, H-43)

IS\_058\_1.1.fid

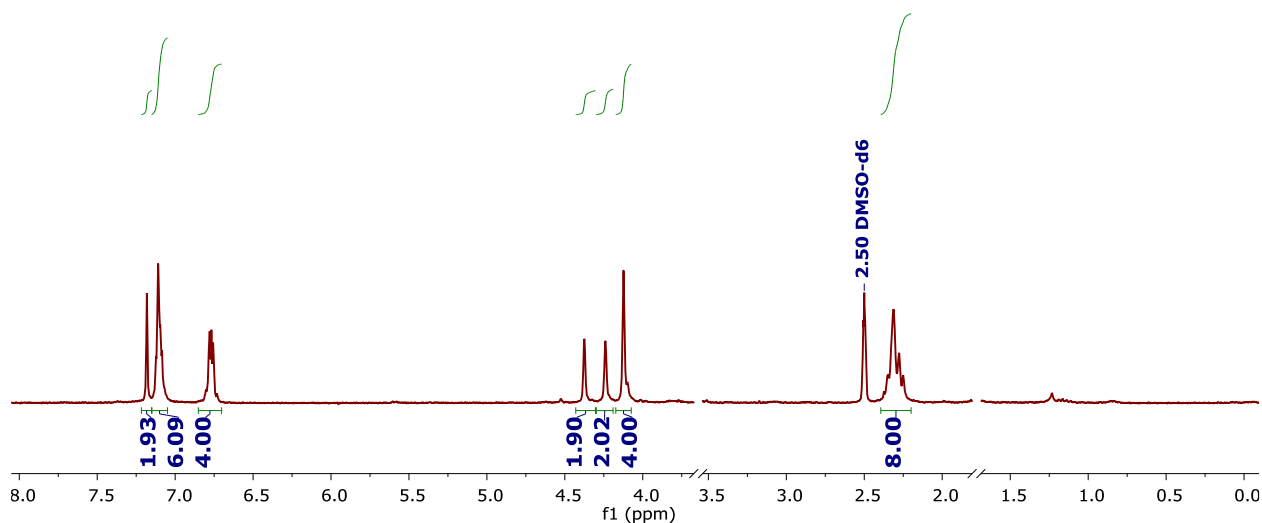


**Figure 98.** <sup>1</sup>H NMR spectra of **60**.



**$^{19}\text{F}$  NMR** (565 MHz, Chloroform-*d*)  $\delta$  [ppm] = -57.87

IS\_058\_1.3.fid

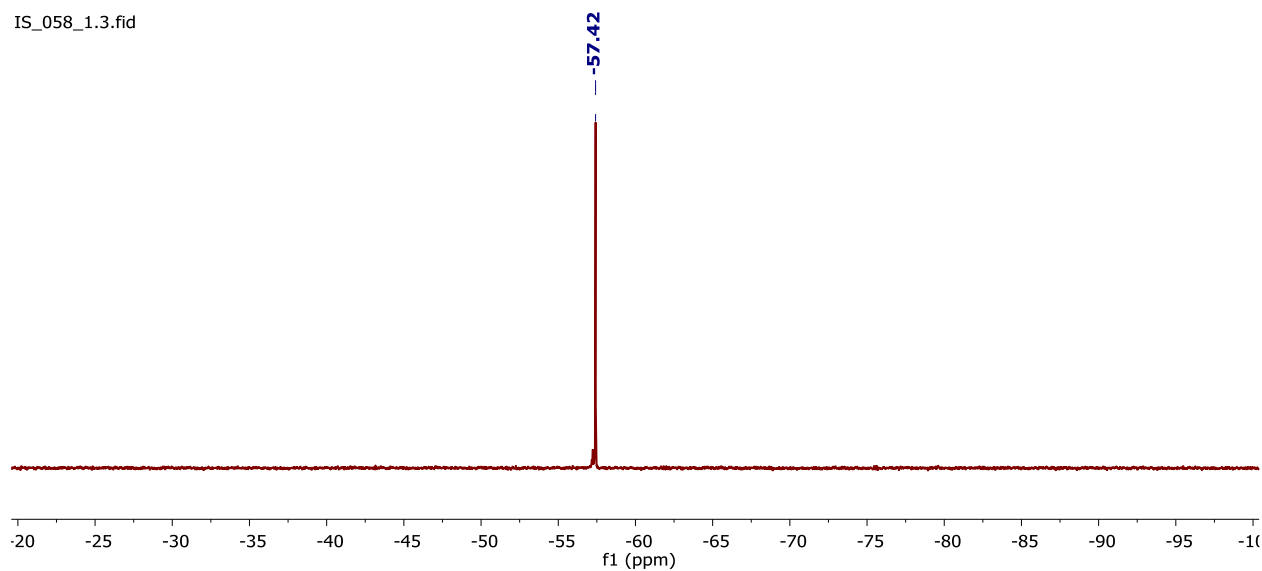


**Figure 99.**  $^{19}\text{F}$  NMR spectra of **60**.

**$^{31}\text{P}$  NMR** (122 MHz, DMSO-*d*<sub>6</sub>)  $\delta$  [ppm] = -5.82

IS\_058\_1.2.fid

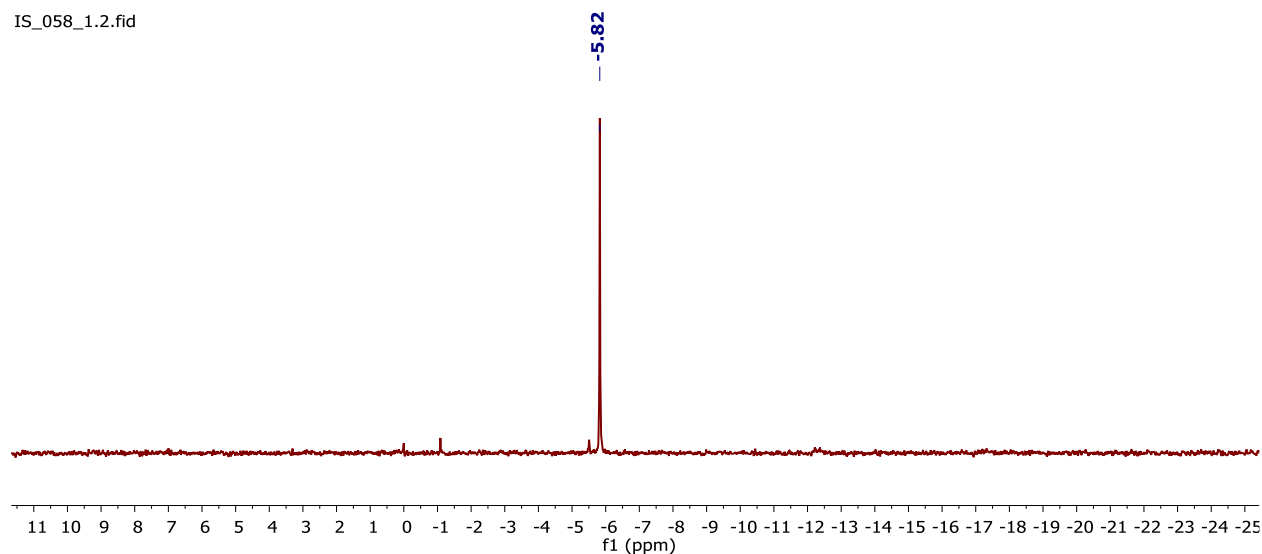


**Figure 100.**  $^{31}\text{P}$  NMR spectra of **60**.

**HRMS** (m/z): [M+H]<sup>+</sup>: calcd. for  $\text{C}_{43}\text{H}_{30}\text{F}_3\text{O}_5\text{P}_1$  715.1856; found 715.1853.

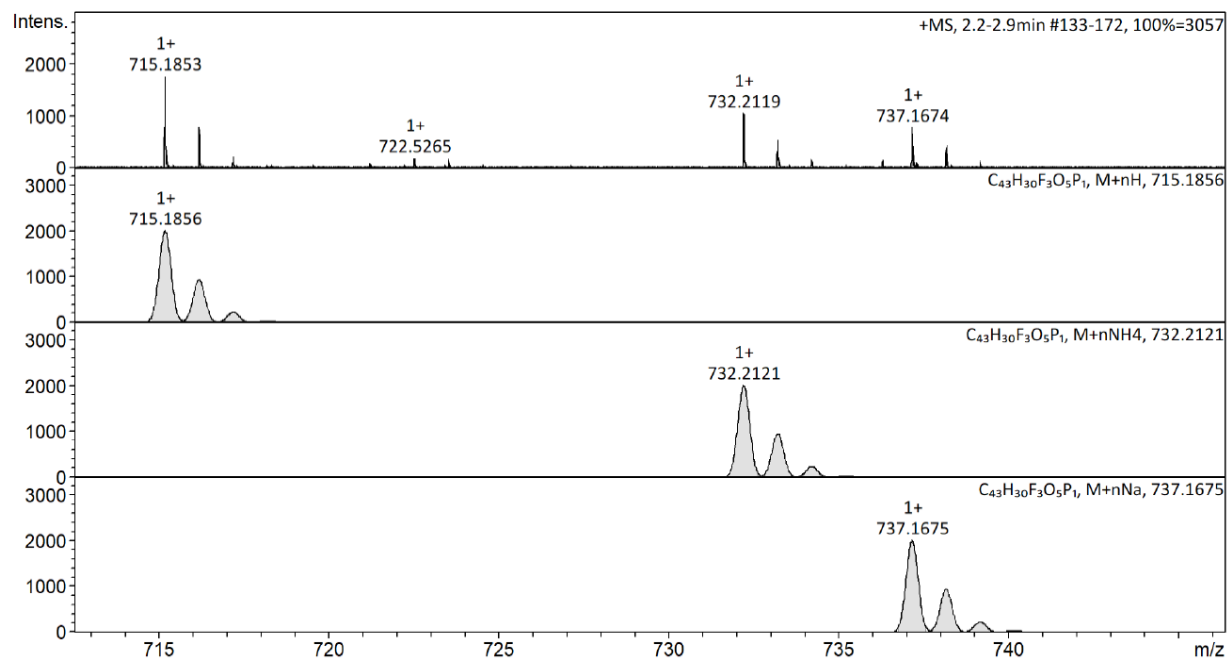
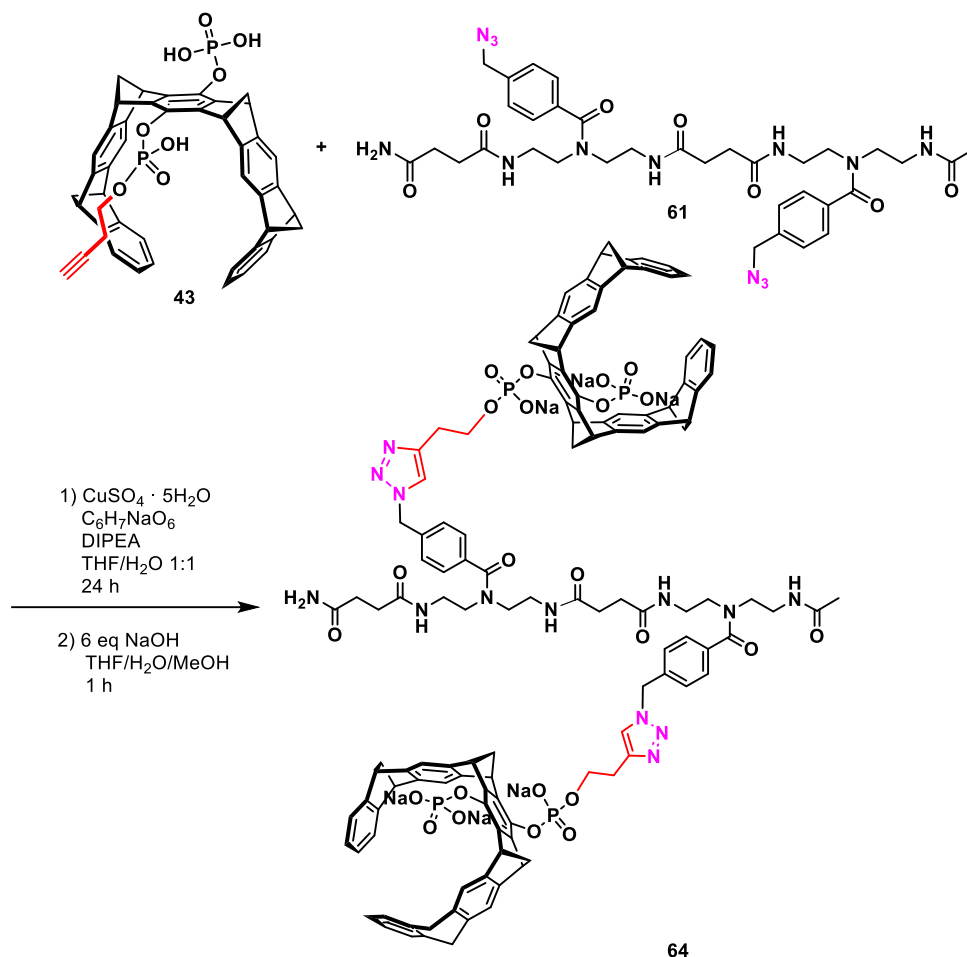


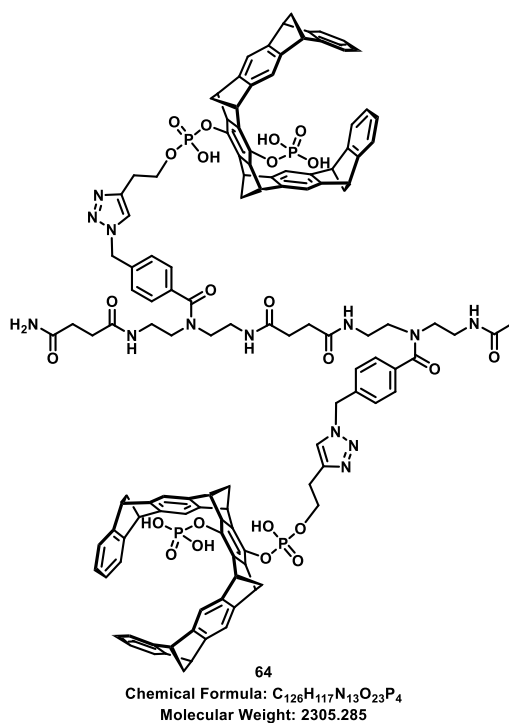
Figure 101. HRMS of 60.

7.2.5 Synthesis of **64**

**Figure 102.** Synthesis of double tweezer-precision oligomer conjugate **64**.

Monobutynyl tweezer **43** (10.0 mg, 12.8  $\mu\text{mol}$ ) was dissolved in 3 mL THF- $\text{H}_2\text{O}$  mixture (1:1) in a 10 mL round-bottom flask together with the precision oligomer **61** (10 mg, 13  $\mu\text{mol}$ ). Stabilizer-free THF was used exclusively. Freshly distilled DIPEA (22.6  $\mu\text{L}$ ) was added to previously degassed starting solution under argon atmosphere. Subsequently, the newly prepared copper sulfate solution (8.3 mg  $\text{CuSO}_4 \cdot 5\text{H}_2\text{O}$ , 33  $\mu\text{mol}$  in 1 mL water) was mixed with sodium ascorbate solution (13 mg  $\text{C}_6\text{H}_7\text{NaO}_6$ , 66  $\mu\text{mol}$  in 1 mL water), and the catalytic brew was immediately added to the reaction solution. The reaction mixture was stirred overnight at room temperature with restricted air contact. After the appearance of the blue color after 16 hours, which is indicating the presence of Cu (II), instead of reducing Cu (II) to Cu (I) *in situ*, a new amount of freshly prepared catalytic brew was added again, and the reaction mixture was left on stirring for additional

8 hours, at room temperature. Quenching proceeded with diluted HCl (2.5 %, 5 mL). The formation of a white sticky precipitate was observed immediately after the addition of diluted acid. THF was then carefully removed on a rotary evaporator, and the remaining solution was cooled before filtering through the D4-fritted funnel. The collected solid was subsequently washed with HCl (2.5 %, 2 x 2 mL) and water (2 x 1 mL), including washing the flask walls as well, since the product sticks on the glass walls and cannot be poured out at once. The crude product was then rinsed with THF from the funnel and dried on a rotary evaporator. The desired conjugate was obtained as a beige solid (8.1 mg, 4  $\mu$ mol, the crude yield 52 %). The crude product failed purification via preparative HPLC (H<sub>2</sub>O/MeCN gradient). Instead, the manual purification via column chromatography, using the short RP-18 silica column (H<sub>2</sub>O/THF gradient; 5:1  $\rightarrow$  1:1), was done. Due to its low solubility in MeCN/H<sub>2</sub>O as well as in PBS buffer, the conjugate was subsequently deprotonated in the presence of 6 equivalents of NaOH in the solvent mixture THF/H<sub>2</sub>O/MeOH = 1:1:1, which significantly improved its solubility (up to 5 mM in PBS buffer and 3 mM in H<sub>2</sub>O). After one hour of stirring at the room temperature, organic solvents were removed on the rotary evaporator, and the rest was lyophilized.



**$^1\text{H}$  NMR** (600 MHz,  $\text{DMSO-}d_6$ )  $\delta$  [ppm] = 2.11 – 2.36 (m, 21H), 2.87 – 3.00 (m, 4H), 3.02 – 3.17 (m, 4H), 3.17 – 3.37 (m, 8H), 3.39 – 3.52 (m, 4H), 3.55 – 3.66 (m, 2H), 4.01 – 4.19 (m, 11H), 4.24 – 4.38 (m, 8H), 5.66 (s, 4H,  $\text{CH}_2\text{-N}_3$  H), 6.68 – 6.86 (m, 9H), 6.93 – 7.19 (m, 16H), 7.36 (s, 8H, aryl-H), 7.82 – 7.95 (m, 2H), 7.95 – 8.07 (m, 2H), 8.10 (s, 2H, triazole H).

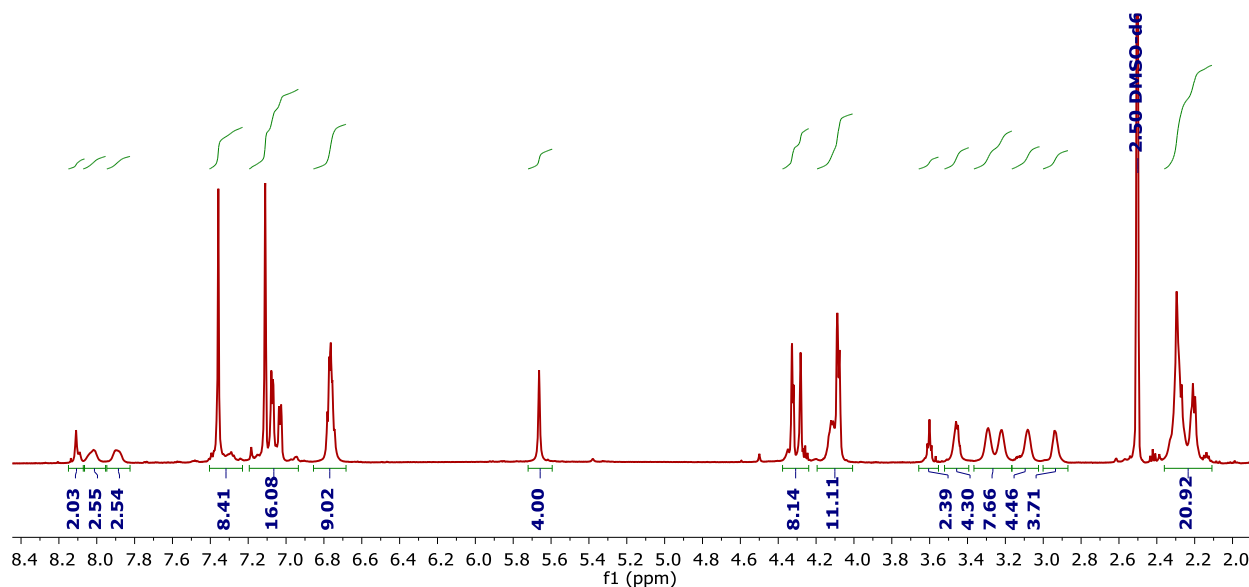


**Figure 103.**  $^1\text{H}$  NMR spectra of **64**.

**$^{13}\text{C}$ -NMR** (151 MHz,  $\text{DMSO-}d_6$ )  $\delta$  [ppm] = 25.07, 38.49, 40.05, 47.88, 47.95, 50.20, 50.24, 66.96, 67.73, 68.95, 69.05, 69.46, 116.66, 116.78, 121.38, 124.38, 126.92, 127.67, 136.64, 140.96, 141.51, 146.63, 146.87, 150.19, 170.44.

**$^{31}\text{P}$  NMR** (243 MHz,  $\text{DMSO-}d_6$ )  $\delta$  [ppm] = -5.41, -5.83

**ESI-MS** (m/z):  $[\text{M-H}]^{2+}$ : calcd. for  $\text{C}_{126}\text{H}_{117}\text{N}_{13}\text{O}_{23}\text{P}_4$  1151.4; found 1151.4.

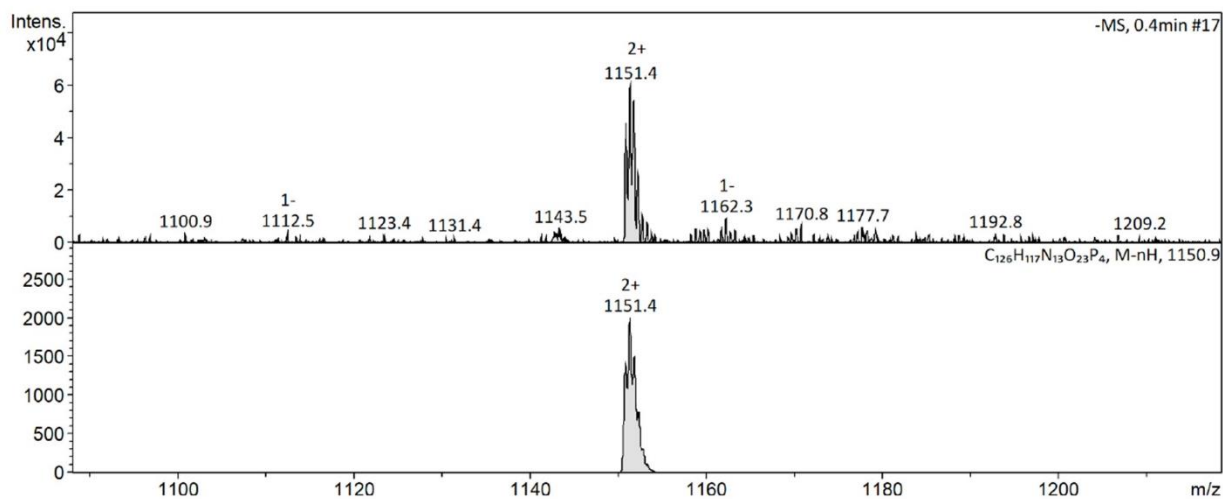


Figure 104. ESI-MS spectra of **64**.

## 7.2.6 Synthesis of **65**

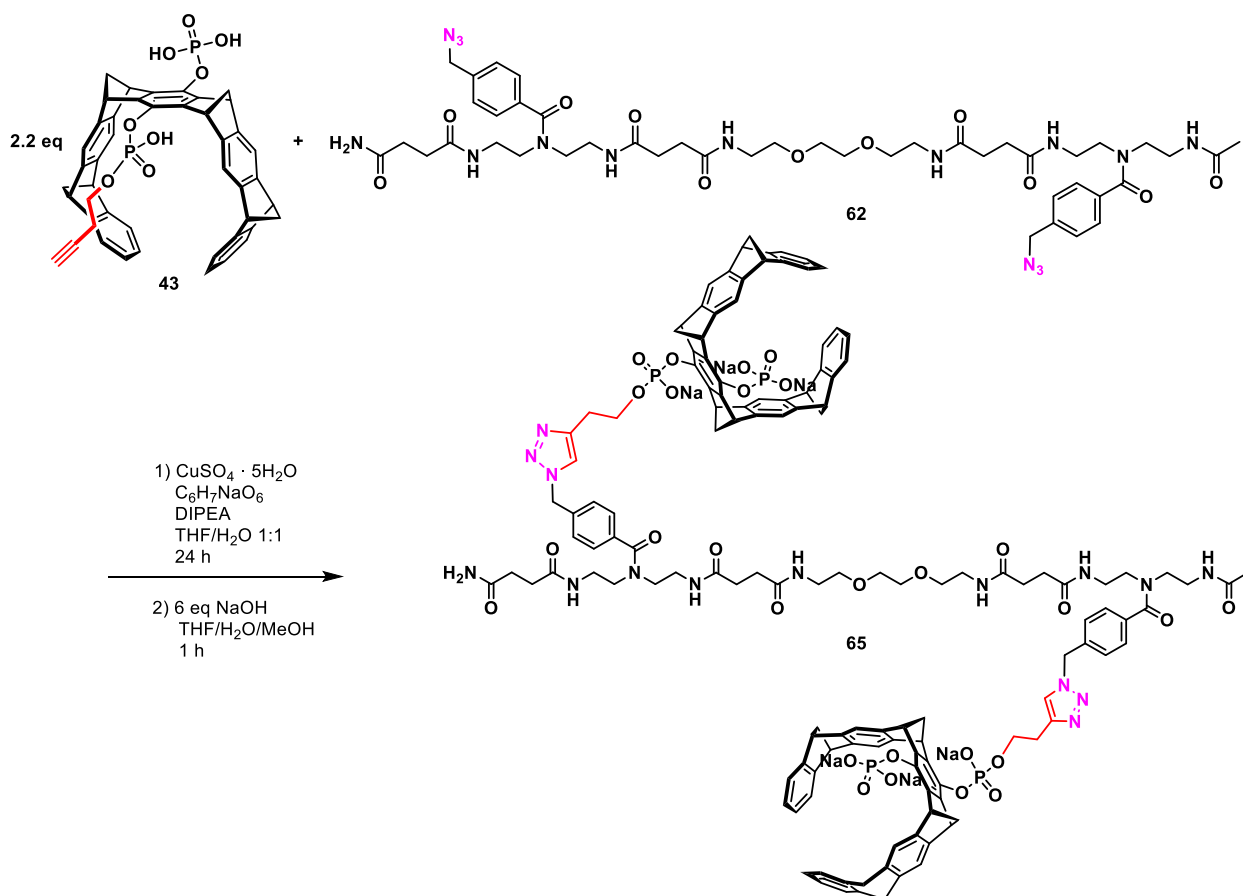
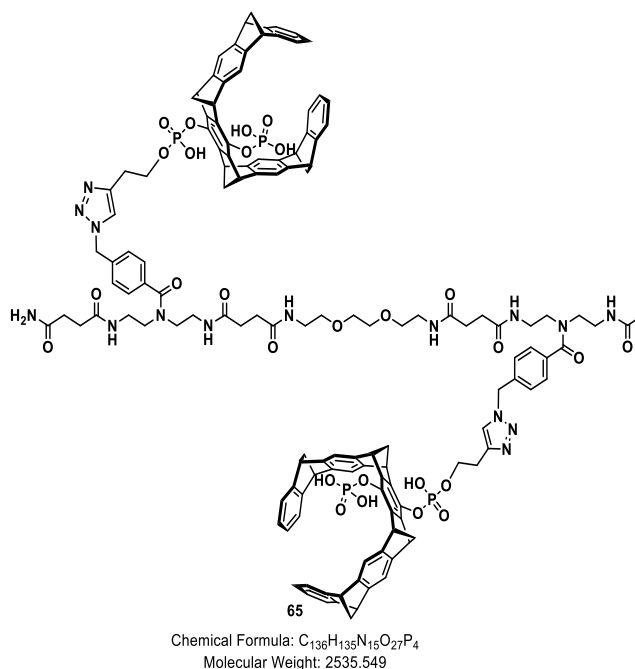


Figure 105. Synthesis of double tweezer-precision oligomer conjugate **65**.

The reaction procedure is the same as the previously described reaction of **64** (Chapter 7.2.5), with the only difference in the amounts of educts used at the beginning of the reaction. Here, and in the case of **66**, the molar ratio of educts is 2.2 : 1 = monobutynyl tweezer : precision oligomer (Figure 105). Monobutynyl tweezer **43** (26.2 mg, 33.6  $\mu\text{mol}$ ) was dissolved in 3 mL THF-H<sub>2</sub>O mixture (1:1) in a 10 mL round-bottom flask together with the precision oligomer **62** (15 mg, 15.3  $\mu\text{mol}$ ). The desired conjugate was obtained as a beige solid (26.7 mg, 10  $\mu\text{mol}$ , the crude yield 66 %). The purification proceeded in the same way as explained in 7.2.5 to obtain the pure product.



**<sup>1</sup>H NMR** (600 MHz, DMSO-*d*<sub>6</sub>)  $\delta$  [ppm] = 2.11 – 2.35 (m, 24H), 2.88 – 3.13 (m, 9H), 3.13 – 3.24 (m, 10H), 3.25 – 3.32 (m, 5H), 3.38 (t, *J* = 5.9 Hz, 6H), 3.42 – 3.52 (m, 9H), 3.56 – 3.64 (m, 9H), 4.01 – 4.16 (m, 12H), 4.24 – 4.39 (m, 8H), 5.67 (s, 4H, CH<sub>2</sub>-N<sub>3</sub> H), 6.71 – 6.81 (m, 9H), 6.99 – 7.18 (m, 16H), 7.30 – 7.35 (s, 8H, aryl-H), 7.90 (s, 4H), 8.00 (s, 2H, triazole H).\*

\*Due to the existence of rotational isomers and numerous signal overlapping events, the full characterization of 2D NMR spectra was not feasible.

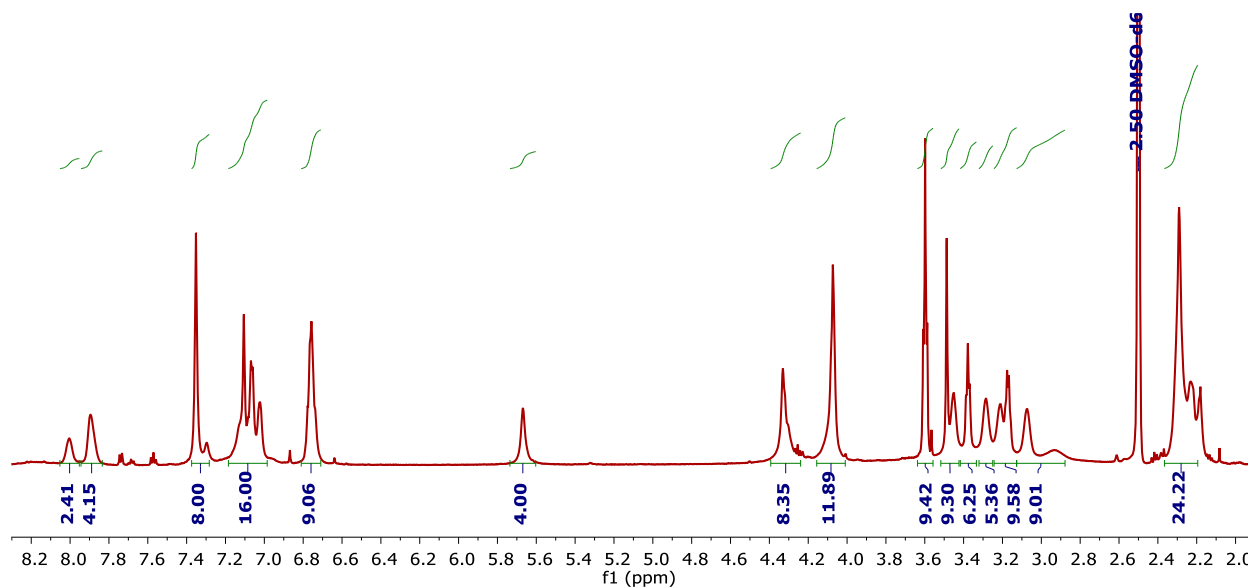


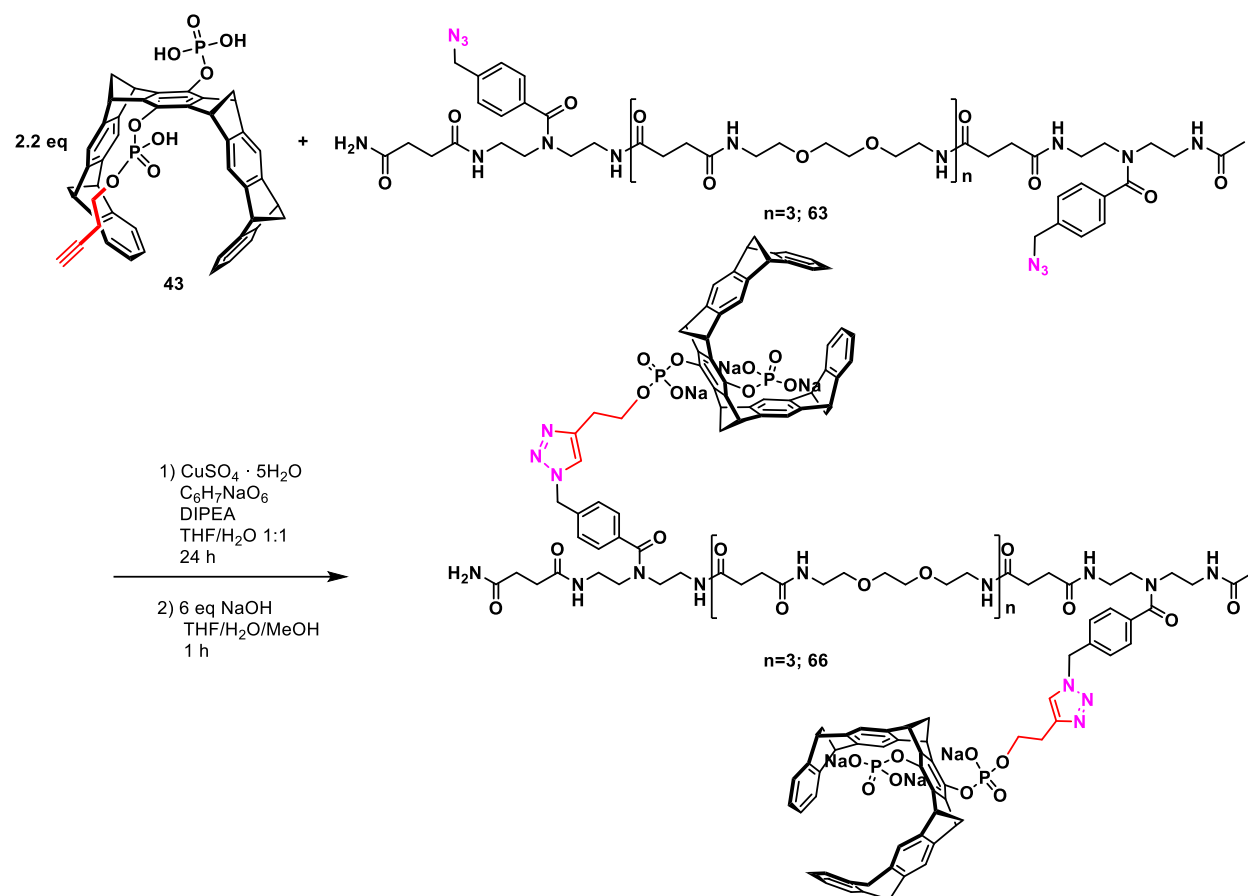
**Figure 106.**  $^1\text{H}$  NMR spectra of **65**.

$^{13}\text{C}$ -NMR (151 MHz,  $\text{DMSO-}d_6$ )  $\delta$  [ppm] = 22.42, 22.58, 25.08, 26.69, 26.74, 28.97, 30.19, 30.36, 30.58, 36.29, 36.87, 40.05, 44.32, 47.90, 47.96, 48.41, 50.21, 50.25, 52.38, 65.68, 65.72, 66.97, 67.76, 68.99, 116.71, 116.82, 121.38, 121.40, 121.44, 123.29, 124.40, 126.94, 127.67, 135.73, 136.64, 136.74, 140.92, 141.22, 141.60, 146.49, 146.57, 146.69, 146.81, 146.93, 150.20, 150.24, 169.22, 170.46.

$^{31}\text{P}$  NMR (243 MHz,  $\text{DMSO-}d_6$ )  $\delta$  [ppm] = -5.42, -5.86.

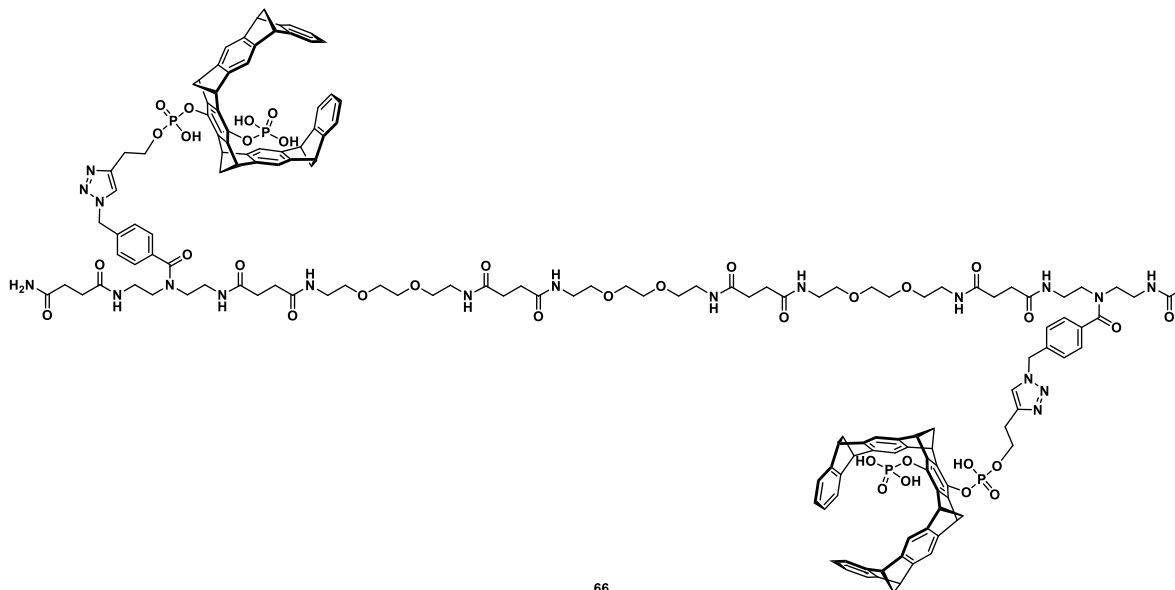
**HPLC-MS (ESI<sup>+</sup>):** [ $\text{H}_2\text{O}/\text{MeCN}$ , 15 $\rightarrow$ 95 %], Retention time: 6.59 – 10.58 min [ $\text{M}+\text{H}$ ]<sup>2+</sup>:  
calcd. for  $\text{C}_{136}\text{H}_{135}\text{N}_{15}\text{O}_{27}\text{P}_4$ , 1267.774; found 1267.990.



7.2.7 Synthesis of **66**

**Figure 107.** Synthesis of double tweezer-precision oligomer conjugate **66**.

The reaction procedure of **66** is the same as the previously described reaction of **65** (Chapter 7.2.6). The crude yield was 51 % (23.0 mg, 7.7  $\mu\text{mol}$ ). Purification, as well as deprotonation of the final product was done as previously described. Due to the broadness of signals obtained in  $^1\text{H}$  NMR at room temperature, the measurement was repeated at elevated temperature (60  $^\circ\text{C}$ ) in presence of 10 %  $\text{D}_2\text{O}$ , to increase bond rotations speed and gain on sharpness of the signals. Nevertheless, only minimal improvement in signal sharpening has been achieved. Besides, the existence of rotational isomers and numerous signal overlapping events in 2D NMR spectra, hindered the full assignment of all protons.



66

Chemical Formula:  $C_{156}H_{171}N_{19}O_{35}P_4$   
Molecular Weight: 2996.077

$^1\text{H NMR}$  (500 MHz,  $\text{DMSO-}d_6$  + 10 %  $\text{D}_2\text{O}$ ,  $T = 333\text{ K}$ )  $\delta$  [ppm] = 2.19 – 2.41 (m, 40H), 3.15 – 3.23 (m, 23H), 3.41 (t,  $J = 6.0\text{ Hz}$ , 25H), 3.50 (t,  $J = 2.6\text{ Hz}$ , 23H), 3.95 – 4.11 (m, 13H), 4.31 – 4.57 (m, 8H), 5.61 (s, 4H,  $\text{CH}_2\text{-N}_3\text{ H}$ ), 6.65 – 6.86 (m, 10H), 6.94 – 7.16 (m, 17H), 7.26 – 7.46 (m, 11H), 7.69 – 8.18 (m, 4H).

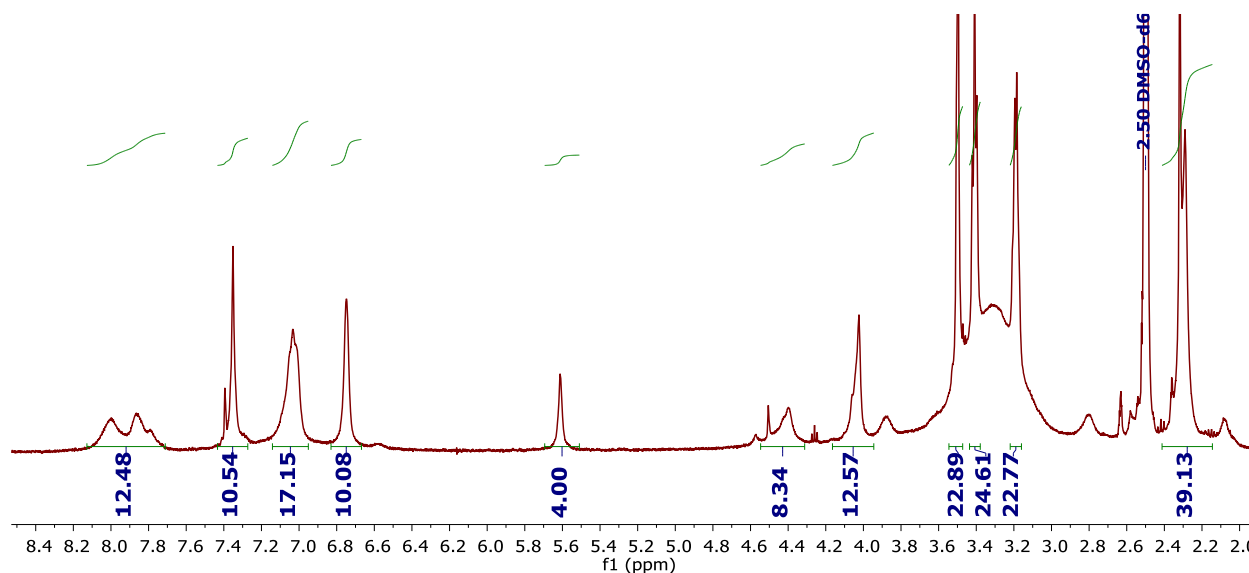


Figure 108.  $^1\text{H NMR}$  spectra of **66**.

$^{13}\text{C-NMR}$  (151 MHz,  $\text{DMSO-}d_6$ )  $\delta$  [ppm] = 22.42, 22.54, 25.01, 26.79, 26.80, 29.02, 30.19, 30.38, 30.61, 36.06, 36.39, 36.65, 40.02, 40.05, 41.12, 44.92, 46.98, 47.54, 47.86, 48.91, 50.11, 50.21, 50.25, 56.38, 65.41, 65.51, 65.62, 69.36, 69.46, 69.56, 69.67, 69.76, 73.61,

99.30, 99.50, 99.60, 99.71, 99.92, 116.51, 116.74, 116.82, 120.79, 121.35, 121.40, 121.44, 123.79, 125.20, 126.65, 127.02, 111.30, 125.60, 129.45, 129.55, 129.65, 129.76, 129.85, 133.59, 133.70, 133.80, 189.84, 193.68, 193.79, 193.89, 193.99.

$^{31}\text{P}$  NMR (243 MHz, DMSO- $d_6$ )  $\delta$  [ppm] = -5.42, -5.85

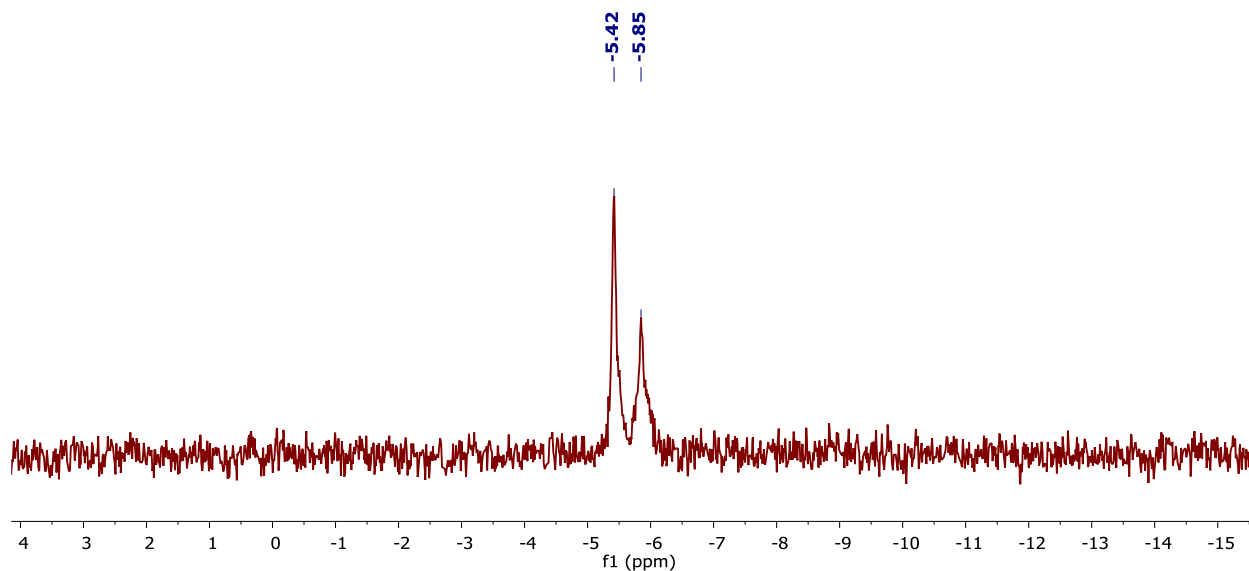


Figure 109.  $^{31}\text{P}$  NMR spectra of **66**.

**HPLC-MS (ESI<sup>+</sup>):** [H<sub>2</sub>O/MeCN, 15→95 %], Retention time: 7.37 – 11.89 min [M+H]<sup>2+</sup>:  
calcd. for C<sub>158</sub>H<sub>171</sub>N<sub>15</sub>O<sub>35</sub>P<sub>4</sub>, 1498.0397; found 1498.0408.

## 8 REFERENCES

- [1] K. L. Wolf, H. Frahm, H. Harms, *Z. Phys. Chem. (B)* 1937, 36, 237.
- [2] "Press release: The 1987 Nobel Prize in Chemistry.", can be found under <<https://www.nobelprize.org/prizes/chemistry/1987/press-release/>>.
- [3] J.-M. Lehn, *Angew. Chem. Int. Ed. Engl.* 1990, 29, 1304.
- [4] P. Samorì, F. Cacialli, *Functional supramolecular architectures. For organic electronics and nanotechnology*, Wiley-VCH, Weinheim Germany, 2011.
- [5] A. J. Savyasachi, O. Kotova, S. Shanmugaraju, S. J. Bradberry, G. M. Ó'Máille, T. Gunnlaugsson, *Chem* 2017, 3, 764.
- [6] a) D. E. Barry, D. F. Caffrey, T. Gunnlaugsson, *Chemical Society reviews* 2016, 45, 3244; b) S. Erbas-Cakmak, D. A. Leigh, C. T. McTernan, A. L. Nussbaumer, *Chemical reviews* 2015, 115, 10081; c) D. J. Tranchemontagne, J. L. Mendoza-Cortés, M. O'Keeffe, O. M. Yaghi, *Chemical Society reviews* 2009, 38, 1257.
- [7] "Press release: The Nobel Prize in Chemistry 2016.", can be found under <<https://www.nobelprize.org/prizes/chemistry/2016/press-release/>>.
- [8] K. Ariga in *Biomaterials Nanoarchitectonics*, Elsevier, 2016, pp. 25–40.
- [9] J.-M. Lehn, *Proceedings of the National Academy of Sciences of the United States of America* 2002, 99, 4763.
- [10] J.-M. Lehn, *Nobel Lecture 1987*, 444.
- [11] a) J. L. Atwood, J.-M. Lehn, *Comprehensive supramolecular chemistry*, Pergamon, New York, 1996; b) K. Müller-Dethlefs, P. Hobza, *Chemical reviews* 2000, 100, 143.
- [12] J. W. Steed, D. R. Turner, K. J. Wallace, *Core concepts in supramolecular chemistry and nanochemistry*, John Wiley, Chichester England, Hoboken NJ, 2007.
- [13] B. Legouin, M. Gayral, P. Uriac, J.-F. Cupif, N. Levoine, L. Toupet, P. van de Weghe, *Eur. J. Org. Chem.* 2010, 2010, 5503.
- [14] J.-M. Lehn, *Nobel Lecture 1987*, 444.
- [15] D. J. Cram, J. M. Cram, *Science (New York, N.Y.)* 1974, 183, 803.
- [16] J. W. Steed, J. L. Atwood, *Supramolecular chemistry*, Wiley, Oxford, 2009.
- [17] P. A. Gale, J. W. Steed (Eds.) *Supramolecular Chemistry*, John Wiley & Sons, Ltd, Chichester, UK, 2012.
- [18] M. Nič, J. Jiráť, B. Košata, A. Jenkins, A. McNaught (Eds.) *IUPAC Compendium of Chemical Terminology*, IUPAC, Research Triangle Park, NC, 2009.
- [19] C. J. Pedersen, *J. Am. Chem. Soc.* 1967, 89, 7017.
- [20] a) S. Amiri, S. Amiri (Eds.) *Cyclodextrins*, John Wiley & Sons, Ltd, Chichester, UK, 2017; b) J. Breitkreutz, *Pharmazie in unserer Zeit* 2005, 34, 216; c) C. D. Gutsche, *Calixarenes. An introduction* / C. David Gutsche, RSC Pub, Cambridge, 2008; d) D. J. Cram, M. E. Tanner, R. Thomas, *Angew. Chem.* 1991, 103, 1048; e) C. Li, J. Ma, L. Zhao, Y. Zhang, Y. Yu, X. Shu, J. Li, X. Jia, *Chemical communications (Cambridge, England)* 2013, 49,

- 1924; f) S. J. Barrow, S. Kaseira, M. J. Rowland, J. del Barrio, O. A. Scherman, *Chemical reviews* 2015, 115, 12320.
- [21] F.-G. Klärner, B. Kahlert, *Accounts of chemical research* 2003, 36, 919.
- [22] J. A. Bravo, F. M. Raymo, J. F. Stoddart, A. J. P. White, D. J. Williams, *Eur. J. Org. Chem.* 1998, 1998, 2565.
- [23] C. A. Stanier, M. J. O'Connell, H. L. Anderson, W. Clegg, *Chem. Commun.* 2001, 493.
- [24] A. M. Albrecht-Gary, M. Meyer, C. O. Dietrich-Buchecker, J. P. Sauvage, J. Guilhem, C. Pascard, *Recl. Trav. Chim. Pays-Bas* 1993, 112, 427.
- [25] P. R. Ashton, C. L. Brown, E. J. T. Chrystal, T. T. Goodnow, A. E. Kaifer, K. P. Parry, D. Philp, A. M. Z. Slawin, N. Spencer, J. F. Stoddart et al., *J. Chem. Soc., Chem. Commun.* 1991, 634.
- [26] K. S. Chichak, S. J. Cantrill, A. R. Pease, S.-H. Chiu, G. W. V. Cave, J. L. Atwood, J. F. Stoddart, *Science (New York, N.Y.)* 2004, 304, 1308.
- [27] A. Yerin, E. S. Wilks, G. P. Moss, A. Harada, *Pure and Applied Chemistry* 2008, 80, 2041.
- [28] S. Kassem, T. van Leeuwen, A. S. Lubbe, M. R. Wilson, B. L. Feringa, D. A. Leigh, *Chemical Society reviews* 2017, 46, 2592.
- [29] V. Bhalla, *Reson* 2018, 23, 277.
- [30] J. D. Badjic, V. Balzani, A. Credi, S. Silvi, J. F. Stoddart, *Science (New York, N.Y.)* 2004, 303, 1845.
- [31] The Royal Swedish Academy of Science, *Nature* 2010, 50005, 0.
- [32] M. Hardouin-Lerouge, P. Hudhomme, M. Sallé, *Chemical Society reviews* 2011, 40, 30.
- [33] S. C. Zimmerman in *Bioorganic Chemistry Frontiers* (Ed.: H. Dugas), Springer Berlin Heidelberg, Berlin, Heidelberg, 1991, pp. 33–71.
- [34] G. Kahl (Ed.) *The Dictionary of Genomics, Transcriptomics and Proteomics*, Wiley-VCH Verlag GmbH & Co. KGaA, Weinheim, Germany, 2015.
- [35] C. W. Chen, H. W. Whitlock, *J. Am. Chem. Soc.* 1978, 100, 4921.
- [36] S. C. Zimmerman in *Topics in Current Chemistry*, Springer Berlin Heidelberg, Berlin, Heidelberg, 1993, pp. 71–102.
- [37] M. Harmata, *Accounts of chemical research* 2004, 37, 862.
- [38] J. Leblond, A. Petitjean, *Chemphyschem : a European journal of chemical physics and physical chemistry* 2011, 12, 1043.
- [39] a) S. C. Zimmerman, C. M. VanZyl, *J. Am. Chem. Soc.* 1987, 109, 7894; b) S. C. Zimmerman, W. Wu, *J. Am. Chem. Soc.* 1989, 111, 8054.
- [40] H. Kurebayashi, T. Haino, S. Usui, Y. Fukazawa, *Tetrahedron* 2001, 57, 8667.
- [41] R. P. Sijbesma, R. J. M. Nolte in *Topics in Current Chemistry* (Eds.: J. D. Dunitz, K. Hafner, S. Ito, J.-M. Lehn, K. N. Raymond, C. W. Rees, J. Thiem, F. Vögtle, E. Weber), Springer Berlin Heidelberg, Berlin, Heidelberg, 1995, pp. 25–56.

- [42] A. E. Rowan, J. A. A. W. Elemans, R. J. M. Nolte, *Acc. Chem. Res.* 1999, 32, 995.
- [43] E. M. Pérez, N. Martín, *Pure and Applied Chemistry* 2010, 82, 523.
- [44] F.-G. Klärner, J. Benkhoff, R. Boese, U. Burkert, M. Kamieth, U. Naatz, *Angew. Chem. Int. Ed. Engl.* 1996, 35, 1130.
- [45] S. Dutt, C. Wilch, T. Gersthagen, P. Talbiersky, K. Bravo-Rodriguez, M. Hanni, E. Sánchez-García, C. Ochsenfeld, F.-G. Klärner, T. Schrader, *The Journal of organic chemistry* 2013, 78, 6721.
- [46] F.-G. Klärner, B. Kahlert, A. Nellesen, J. Zienau, C. Ochsenfeld, T. Schrader, *J. Am. Chem. Soc.* 2006, 128, 4831.
- [47] T. Schrader, G. Bitan, F.-G. Klärner, *Chem. Commun.* 2016, 52, 11318.
- [48] D. Bier, R. Rose, K. Bravo-Rodriguez, M. Bartel, J. M. Ramirez-Anguita, S. Dutt, C. Wilch, F.-G. Klärner, E. Sanchez-Garcia, T. Schrader et al., *Nature chemistry* 2013, 5, 234.
- [49] M. Fokkens, T. Schrader, F.-G. Klärner, *J. Am. Chem. Soc.* 2005, 127, 14415.
- [50] G. V. Oshovsky, D. N. Reinhoudt, W. Verboom, *Angewandte Chemie (International ed. in English)* 2007, 46, 2366.
- [51] J. Hatai, C. Schmuck in *Supramolecular chemistry in water* (Ed.: S. Kubik), Wiley-VCH, Weinheim, 2019, pp. 79–113.
- [52] A. Sygula, W. E. Collier in *Fragments of Fullerenes and Carbon Nanotubes* (Eds.: M. A. Petrukhina, L. T. Scott), John Wiley & Sons, Inc, Hoboken, NJ, USA, 2011, pp. 1–40.
- [53] F.-G. Klärner, J. Panitzky, D. Bläser, R. Boese, *Tetrahedron* 2001, 57, 3673.
- [54] F.-G. Klärner, B. Kahlert, A. Nellesen, J. Zienau, C. Ochsenfeld, T. Schrader, *J. Am. Chem. Soc.* 2010, 132, 4029.
- [55] F. Marchioni, A. Juris, M. Lobert, U. P. Seelbach, B. Kahlert, F.-G. Klärner, *New J. Chem.* 2005, 29, 780.
- [56] M. Kamieth, F.-G. Klärner, *Journal für praktische Chemie* 1999, 341, 245.
- [57] M. Kamieth, F.-G. Klärner, F. Diederich, *Angew. Chem.* 1998, 110, 3497.
- [58] Professor Bitan's research group, "Where did the Molecular Tweezers come from?", can be found under [https://images.indiegogo.com/medias/1326526/files/20140331102203-Where\\_did\\_the\\_Molecular\\_Tweezers\\_come\\_from\\_.pdf?1396286528](https://images.indiegogo.com/medias/1326526/files/20140331102203-Where_did_the_Molecular_Tweezers_come_from_.pdf?1396286528).
- [59] C. Jasper, T. Schrader, J. Panitzky, F.-G. Klärner, *Angewandte Chemie (International ed. in English)* 2002, 41, 1355.
- [60] M. Fokkens, C. Jasper, T. Schrader, F. Koziol, C. Ochsenfeld, J. Polkowska, M. Lobert, B. Kahlert, F.-G. Klärner, *Chemistry (Weinheim an der Bergstrasse, Germany)* 2005, 11, 477.
- [61] T. Schrader, M. Fokkens, F.-G. Klärner, J. Polkowska, F. Bastkowski, *The Journal of organic chemistry* 2005, 70, 10227.
- [62] M. Fokkens, F.-G. Klärner, T. Schrader, *Sensors (Basel)* 2006, 6, 860.

- [63] B. Branchi, P. Ceroni, V. Balzani, M. C. Cartagena, F.-G. Klärner, T. Schrader, F. Vögtle, *New J. Chem.* 2009, 33, 397.
- [64] a) F. Diederich, D. B. Smithrud, E. M. Sanford, T. B. Wyman, S. B. Ferguson, D. R. Carcanague, I. Chao, K. N. Houk, *Acta Chem. Scand.* 1992, 46, 205; b) D. B. Smithrud, T. B. Wyman, F. Diederich, *J. Am. Chem. Soc.* 1991, 113, 5420.
- [65] F. Biedermann, W. M. Nau, H.-J. Schneider, *Angew. Chem. Int. Ed. Engl.* 2014, 53, 11158.
- [66] C. Heid, A. Sowislok, T. Schaller, F. Niemeyer, F.-G. Klärner, T. Schrader, *Chemistry (Weinheim an der Bergstrasse, Germany)* 2018, 24, 11332.
- [67] I. Hadrovic, P. Rebmann, F.-G. Klärner, G. Bitan, T. Schrader, *Frontiers in chemistry* 2019, 7, 657.
- [68] C. Heid, DuEPublico: Duisburg-Essen Publications online, University of Duisburg-Essen, Germany, 2019.
- [69] L. O. Tjernberg, C. Lilliehöök, D. J. Callaway, J. Näslund, S. Hahne, J. Thyberg, L. Terenius, C. Nordstedt, *The Journal of biological chemistry* 1997, 272, 12601.
- [70] P. Talbiersky, F. Bastkowski, F.-G. Klärner, T. Schrader, *J. Am. Chem. Soc.* 2008, 130, 9824.
- [71] S. Sinha, D. H. J. Lopes, Z. Du, E. S. Pang, A. Shanmugam, A. Lomakin, P. Talbiersky, A. Tennstaedt, K. McDaniel, R. Bakshi et al., *J. Am. Chem. Soc.* 2011, 133, 16958.
- [72] S. Sinha, Z. Du, P. Maiti, F.-G. Klärner, T. Schrader, C. Wang, G. Bitan, *ACS chemical neuroscience* 2012, 3, 451.
- [73] S. Prabhudesai, S. Sinha, A. Attar, A. Kotagiri, A. G. Fitzmaurice, R. Lakshmanan, R. Lakshmanan, M. I. Ivanova, J. A. Loo, F.-G. Klärner et al., *Neurotherapeutics : the journal of the American Society for Experimental NeuroTherapeutics* 2012, 9, 464.
- [74] M. Herrera-Vaquero, D. Bouquio, M. Kallab, K. Biggs, G. Nair, J. Ochoa, A. Heras-Garvin, C. Heid, I. Hadrovic, W. Poewe et al., *Biochimica et biophysica acta. Molecular basis of disease* 2019, 1865, 165513.
- [75] D. H. J. Lopes, A. Attar, G. Nair, E. Y. Hayden, Z. Du, K. McDaniel, S. Dutt, K. Bravo-Rodriguez, S. Mittal, F.-G. Klärner et al., *ACS chemical biology* 2015, 10, 1555.
- [76] A. Monaco, V. Maffia, N. C. Sorrentino, I. Sambri, Y. Ezhova, T. Giuliano, V. Cacace, E. Nusco, M. de Risi, E. de Leonibus et al., *Molecular therapy : the journal of the American Society of Gene Therapy* 2020, 28, 1167.
- [77] E. Lump, L. M. Castellano, C. Meier, J. Seeliger, N. Erwin, B. Sperlich, C. M. Stürzel, S. Usmani, R. M. Hammond, J. von Einem et al., *eLife* 2015, 4.
- [78] A. E. Röcker, J. A. Müller, E. Dietzel, M. Harms, F. Krüger, C. Heid, A. Sowislok, C. F. Riber, A. Kupke, S. Lippold et al., *Antiviral research* 2018, 152, 26.
- [79] "Press release: The 1987 Nobel Prize in Chemistry.", can be found under <<https://www.nobelprize.org/prizes/chemistry/1987/press-release/>>.
- [80] B. J. G. E. Pieters, M. B. van Eldijk, R. J. M. Nolte, J. Mecinović, *Chemical Society reviews* 2016, 45, 24.

- [81] Cyclodextrins (Eds.: S. Amiri, S. Amiri), John Wiley & Sons, Ltd, Chichester, UK, 2017, pp. 41–74.
- [82] O. Keskin, A. Gursoy, B. Ma, R. Nussinov, *Chemical reviews* 2008, 108, 1225.
- [83] S. van Dun, C. Ottmann, L.-G. Milroy, L. Brunsveld, *J. Am. Chem. Soc.* 2017, 139, 13960.
- [84] J. A. Marsh, S. A. Teichmann, *Annual Review of Biochemistry* 2015, 84, 551.
- [85] L. Iralde-Lorente, Y. Cau, L. Clementi, L. Franci, G. Tassone, D. Valensin, M. Mori, A. Angelucci, M. Chiariello, M. Botta, *Journal of enzyme inhibition and medicinal chemistry* 2019, 34, 657.
- [86] R. C. Melo, C. Ribeiro, C. S. Murray, C. J. M. Veloso, C. H. da Silveira, G. Neshich, W. Meira, R. L. Carceroni, M. M. Santoro, *Genetics and molecular research : GMR* 2007, 6, 946.
- [87] W. Guo, J. A. Wisniewski, H. Ji, *Bioorganic & medicinal chemistry letters* 2014, 24, 2546.
- [88] T. Clackson, J. A. Wells, *Science (New York, N.Y.)* 1995, 267, 383.
- [89] J. A. Wells, C. L. McClendon, *Nature* 2007, 450, 1001.
- [90] R. Kubota, I. Hamachi, *Chemical Society reviews* 2015, 44, 4454.
- [91] C.-C. Lee, M. Maestre-Reyna, K.-C. Hsu, H.-C. Wang, C.-I. Liu, W.-Y. Jeng, L.-L. Lin, R. Wood, C.-C. Chou, J.-M. Yang et al., *Angew. Chem. Int. Ed. Engl.* 2014, 53, 13054.
- [92] D.-D. Zheng, D.-Y. Fu, Y. Wu, Y.-L. Sun, L.-L. Tan, T. Zhou, S.-Q. Ma, X. Zha, Y.-W. Yang, *Chem. Commun.* 2014, 50, 3201.
- [93] P. B. Crowley, P. Ganji, H. Ibrahim, *Chembiochem : a European journal of chemical biology* 2008, 9, 1029.
- [94] a) A. R. Urbach, V. Ramalingam, *Isr. J. Chem.* 2011, 51, 664; b) C. Hou, Z. Huang, Y. Fang, J. Liu, *Organic & biomolecular chemistry* 2017, 15, 4272.
- [95] F. L. Aachmann, D. E. Otzen, K. L. Larsen, R. Wimmer, *Protein engineering* 2003, 16, 905.
- [96] R. Zadnani, N. S. Alavijeh, *RSC Adv* 2014, 4, 41529.
- [97] H. Hippus, G. Neundörfer, *Dialogues in Clinical Neuroscience* 2003, 5, 101.
- [98] J. D. Sipe, A. S. Cohen, *Journal of structural biology* 2000, 130, 88.
- [99] M. Sunde, L. C. Serpell, M. Bartlam, P. E. Fraser, M. B. Pepys, C. C. Blake, *Journal of molecular biology* 1997, 273, 729.
- [100] I. Cherny, E. Gazit, *Angew. Chem. Int. Ed. Engl.* 2008, 47, 4062.
- [101] J. F. Smith, T. P. J. Knowles, C. M. Dobson, C. E. Macphee, M. E. Welland, *Proceedings of the National Academy of Sciences of the United States of America* 2006, 103, 15806.
- [102] a) T. Lührs, C. Ritter, M. Adrian, D. Riek-Loher, B. Bohrmann, H. Döbeli, D. Schubert, R. Riek, *Proceedings of the National Academy of Sciences of the United States of America* 2005, 102, 17342; b) E. A. Fradinger, B. H. Monien, B. Urbanc, A. Lomakin, M. Tan, H. Li,



- S. M. Spring, M. M. Condrón, L. Cruz, C.-W. Xie et al., *Proceedings of the National Academy of Sciences of the United States of America* 2008, 105, 14175.
- [103] T. P. J. Knowles, M. Vendruscolo, C. M. Dobson, *Nature reviews. Molecular cell biology* 2014, 15, 384.
- [104] D. Eisenberg, M. Jucker, *Cell* 2012, 148, 1188.
- [105] E. Stroob, M. Koopman, E. A. A. Nollen, A. Mata-Cabana, *Frontiers in neuroscience* 2017, 11, 64.
- [106] C. Soto, *Nature reviews. Neuroscience* 2003, 4, 49.
- [107] F.-G. Klärner, T. Schrader, *Acc. Chem. Res.* 2013, 46, 967.
- [108] J. A. Hardy, G. A. Higgins, *Science (New York, N.Y.)* 1992, 256, 184.
- [109] a) B. Mroczko, M. Groblewska, A. Litman-Zawadzka, J. Kornhuber, P. Lewczuk, *Journal of neural transmission (Vienna, Austria : 1996)* 2018, 125, 177; b) G. Forloni, C. Balducci, *Journal of Alzheimer's disease : JAD* 2018, 62, 1261.
- [110] A. Attar, W.-T. C. Chan, F.-G. Klärner, T. Schrader, G. Bitan, *BMC pharmacology & toxicology* 2014, 15, 23.
- [111] V. J. Stella, W. N. Charman, V. H. Naringrekar, *Drugs* 1985, 29, 455.
- [112] W. M. Pardridge, *NeuroRx* 2005, 2, 3.
- [113] F. Cramer, G. Weimann, *Chem. Ber.* 1961, 94, 996.
- [114] D. Bridges, G. B. G. Moorhead, *Science's STKE : signal transduction knowledge environment* 2005, 2005, re10.
- [115] B. E. Moore, V. J. Perez, *Physiological and Biochemical Aspects of Nervous Integration* 1967, 343.
- [116] X. Yang, W. H. Lee, F. Sobott, E. Papagrigoriou, C. V. Robinson, J. G. Grossmann, M. Sundström, D. A. Doyle, J. M. Elkins, *Proceedings of the National Academy of Sciences of the United States of America* 2006, 103, 17237.
- [117] a) A. K. Freeman, D. K. Morrison, *Seminars in cell & developmental biology* 2011, 22, 681; b) C. L. Meyerkord, H. Fu, *Protein-Protein Interactions*, Springer New York, New York, NY, 2015.
- [118] C. Ottmann, L. Yasmin, M. Weyand, J. L. Veessenmeyer, M. H. Diaz, R. H. Palmer, M. S. Francis, A. R. Hauser, A. Wittinghofer, B. Hallberg, *The EMBO journal* 2007, 26, 902.
- [119] R. Kleppe, A. Martinez, S. O. Døskeland, J. Haavik, *Seminars in cell & developmental biology* 2011, 22, 713.
- [120] H. Hermeking, A. Benzinger, *Seminars in cancer biology* 2006, 16, 183.
- [121] H. Fu, R. R. Subramanian, S. C. Masters, *Annual review of pharmacology and toxicology* 2000, 40, 617.
- [122] H. Hermeking, *Nature reviews. Cancer* 2003, 3, 931.
- [123] P. Thiel, M. Kaiser, C. Ottmann, *Angew. Chem. Int. Ed. Engl.* 2012, 51, 2012.

- 
- [124] I. M. A. Nooren, J. M. Thornton, *The EMBO journal* 2003, 22, 3486.
- [125] C. Oecking, C. Eckerskorn, E. W. Weiler, *FEBS Letters* 1994, 352, 163.
- [126] C. Ottmann, S. Marco, N. Jaspert, C. Marcon, N. Schauer, M. Weyand, C. Vandermeeren, G. Duby, M. Boutry, A. Wittinghofer et al., *Molecular cell* 2007, 25, 427.
- [127] M. Molzan, C. Ottmann, *Journal of molecular biology* 2012, 423, 486.
- [128] C. Anders, Y. Higuchi, K. Koschinsky, M. Bartel, B. Schumacher, P. Thiel, H. Nitta, R. Preisig-Müller, G. Schlichthörl, V. Renigunta et al., *Chemistry & biology* 2013, 20, 583.
- [129] P. J. de Vink, J. M. Briels, T. Schrader, L.-G. Milroy, L. Brunsveld, C. Ottmann, *Angew. Chem. Int. Ed. Engl.* 2017, 56, 8998.
- [130] A. Gigante, J.-N. Grad, J. Briels, M. Bartel, D. Hoffmann, C. Ottmann, C. Schmuck, *Chem. Commun.* 2018, 55, 111.
- [131] N. N. Sluchanko, A. S. Seit-Nebi, N. B. Gusev, *FEBS Letters* 2009, 583, 2739.
- [132] A. Arrendale, K. Kim, J. Y. Choi, W. Li, R. L. Geahlen, R. F. Borch, *Chemistry & biology* 2012, 19, 764.
- [133] B. Wang, H. Yang, Y. C. Liu, T. Jelinek, L. Zhang, E. Ruoslahti, H. Fu, *Biochemistry* 1999, 38, 12499.
- [134] L. M. Stevers, E. Sijbesma, M. Botta, C. MacKintosh, T. Obsil, I. Landrieu, Y. Cau, A. J. Wilson, A. Karawajczyk, J. Eickhoff et al., *Journal of medicinal chemistry* 2018, 61, 3755.
- [135] C. Petosa, S. C. Masters, L. A. Bankston, J. Pohl, B. Wang, H. Fu, R. C. Liddington, *The Journal of biological chemistry* 1998, 273, 16305.
- [136] T. Karlberg, P. Hornyak, A. F. Pinto, S. Milanova, M. Ebrahimi, M. Lindberg, N. Püllen, A. Nordström, E. Löverli, R. Caraballo et al., *Nature communications* 2018, 9, 3785.
- [137] A. Glas, D. Bier, G. Hahne, C. Rademacher, C. Ottmann, T. N. Grossmann, *Angew. Chem. Int. Ed. Engl.* 2014, 53, 2489.
- [138] S. P. Wheatley, D. C. Altieri, *Journal of cell science* 2019, 132.
- [139] M. A. Verdecia, H. Huang, E. Dutil, D. A. Kaiser, T. Hunter, J. P. Noel, *Nature structural biology* 2000, 7, 602.
- [140] L. Chantalat, D. A. Skoufias, J. P. Kleman, B. Jung, O. Dideberg, R. L. Margolis, *Molecular cell* 2000, 6, 183.
- [141] N. K. Sah, Z. Khan, G. J. Khan, P. S. Bisen, *Cancer letters* 2006, 244, 164.
- [142] H. Garg, P. Suri, J. C. Gupta, G. P. Talwar, S. Dubey, *Cancer cell international* 2016, 16, 49.
- [143] S. K. Knauer, C. Bier, P. Schlag, J. Fritzmann, W. Dietmaier, F. Rödel, L. Klein-Hitpass, A. F. Kovács, C. Döring, M.-L. Hansmann et al., *Cell Cycle* 2007, 6, 1501.
- [144] T. Jaskoll, H. Chen, Y. Min Zhou, D. Wu, M. Melnick, *BMC developmental biology* 2001, 1, 5.
- [145] A. Dickmanns, T. Monecke, R. Ficner, *Cells* 2015, 4, 538.

- [146] D. Li, C. Hu, H. Li, *Biomedical reports* 2018, 8, 399.
- [147] D. C. Altieri, *Oncogene* 2003, 22, 8581.
- [148] A. A. Jeyaprakash, U. R. Klein, D. Lindner, J. Ebert, E. A. Nigg, E. Conti, Crystal structure of a Survivin-Borealin-INCENP core complex, 2007.
- [149] A. A. Jeyaprakash, U. R. Klein, D. Lindner, J. Ebert, E. A. Nigg, E. Conti, *Cell* 2007, 131, 271.
- [150] M. S. Pavlyukov, N. V. Antipova, M. V. Balashova, T. V. Vinogradova, E. P. Kopantzev, M. I. Shakhparonov, *The Journal of biological chemistry* 2011, 286, 23296.
- [151] a) M. E. Johnson, E. W. Howerth, *Veterinary pathology* 2004, 41, 599; b) H. Marusawa, S.-I. Matsuzawa, K. Welsh, H. Zou, R. Armstrong, I. Tamm, J. C. Reed, *The EMBO journal* 2003, 22, 2729.
- [152] A. Mirza, M. McGuirk, T. N. Hockenberry, Q. Wu, H. Ashar, S. Black, S. F. Wen, L. Wang, P. Kirschmeier, W. R. Bishop et al., *Oncogene* 2002, 21, 2613.
- [153] a) J. Rosa, P. Canovas, A. Islam, D. C. Altieri, S. J. Doxsey, *Molecular biology of the cell* 2006, 17, 1483; b) D. C. Altieri, *Current opinion in cell biology* 2006, 18, 609.
- [154] H. Y. J. Fung, S.-C. Fu, C. A. Brautigam, Y. M. Chook, *eLife* 2015, 4.
- [155] K. Stade, C. S. Ford, C. Guthrie, K. Weis, *Cell* 1997, 90, 1041.
- [156] X. Dong, A. Biswas, K. E. Süel, L. K. Jackson, R. Martinez, H. Gu, Y. M. Chook, *Nature* 2009, 458, 1136.
- [157] T. Monecke, A. Dickmanns, R. Ficner, *The FEBS journal* 2014, 281, 4179.
- [158] T. Monecke, D. Haselbach, B. Voß, A. Russek, P. Neumann, E. Thomson, E. Hurt, U. Zachariae, H. Stark, H. Grubmüller et al., *Proceedings of the National Academy of Sciences of the United States of America* 2013, 110, 960.
- [159] S. Bäcker, Universität Duisburg-Essen, 2018.
- [160] R. Hill, B. Cautain, N. de Pedro, W. Link, *Oncotarget* 2014, 5, 11.
- [161] E. S. Newlands, G. J. Rustin, M. H. Brampton, *British journal of cancer* 1996, 74, 648.
- [162] Q. Sun, Y. P. Carrasco, Y. Hu, X. Guo, H. Mirzaei, J. Macmillan, Y. M. Chook, *Proceedings of the National Academy of Sciences of the United States of America* 2013, 110, 1303.
- [163] H. Y. J. Fung, Y. M. Chook, *Seminars in cancer biology* 2014, 27, 52.
- [164] D. Daelemans, E. Afonina, J. Nilsson, G. Werner, J. Kjems, E. de Clercq, G. N. Pavlakis, A.-M. Vandamme, *Proceedings of the National Academy of Sciences of the United States of America* 2002, 99, 14440.
- [165] S. Richard, J. Richter, S. Jagannath, *Future oncology (London, England)* 2020, 16, 1331.
- [166] T. Kashyap, C. Argueta, T. Unger, B. Klebanov, S. Debler, W. Senapedis, M. L. Crochiere, M. S. Lee, M. Kauffman, S. Shacham et al., *Oncotarget* 2018, 9, 30773.
- [167] J. E. Neggers, T. Vercruyse, M. Jacquemyn, E. Vanstreels, E. Baloglu, S. Shacham, M. Crochiere, Y. Landesman, D. Daelemans, *Chemistry & biology* 2015, 22, 107.

- [168] a) M. J. Ausserlechner, J. Hagenbuchner, *Molecular & cellular oncology* 2016, 3, e1076589; b) X. Chen, N. Duan, C. Zhang, W. Zhang, *Journal of Cancer* 2016, 7, 314.
- [169] S. K. Knauer, C. Bier, N. Habtemichael, R. H. Stauber, *EMBO reports* 2006, 7, 1259.
- [170] S. K. Knauer, O. H. Krämer, T. Knösel, K. Engels, F. Rödel, A. F. Kovács, W. Dietmaier, L. Klein-Hitpass, N. Habtemichael, A. Schweitzer et al., *FASEB journal : official publication of the Federation of American Societies for Experimental Biology* 2007, 21, 207.
- [171] T. Nakahara, A. Kita, K. Yamanaka, M. Mori, N. Amino, M. Takeuchi, F. Tominaga, S. Hatakeyama, I. Kinoyama, A. Matsuhisa et al., *Cancer research* 2007, 67, 8014.
- [172] C.-C. Chang, J. D. Heller, J. Kuo, R. C. C. Huang, *Proceedings of the National Academy of Sciences of the United States of America* 2004, 101, 13239.
- [173] X. Ling, S. Cao, Q. Cheng, J. T. Keefe, Y. M. Rustum, F. Li, *PLoS one* 2012, 7, e45571.
- [174] X. Shi, D. Wang, K. Ding, Z. Lu, Y. Jin, J. Zhang, J. Pan, *Cancer biology & therapy* 2010, 9, 640.
- [175] J.-B. Liu, C. Chen, L. Chu, Z.-H. Chen, X.-H. Xu, F.-L. Qing, *Angew. Chem. Int. Ed. Engl.* 2015, 54, 11839.
- [176] "A witches' brew for trifluoromethylation", can be found under <https://www.chemistryworld.com/opinion/a-witches-brew-for-trifluoromethylation/8978.article>, 03-Aug-20.
- [177] M. Baier, M. Giesler, L. Hartmann, *Chemistry (Weinheim an der Bergstrasse, Germany)* 2018, 24, 1619.
- [178] H. C. Kolb, M. G. Finn, K. B. Sharpless, *Angew. Chem. Int. Ed. Engl.* 2001, 40, 2004.
- [179] B. T. Worrell, J. A. Malik, V. V. Fokin, *Science (New York, N.Y.)* 2013, 340, 457.
- [180] Á. Piñeiro, E. Muñoz, J. Sabín, M. Costas, M. Bastos, A. Velázquez-Campoy, P. F. Garrido, P. Dumas, E. Ennifar, L. García-Río et al., *Analytical biochemistry* 2019, 577, 117.
- [181] S. Kubik (Ed.) *Supramolecular chemistry in water*, Wiley-VCH, Weinheim, 2019.
- [182] Q. Wang, Y. Zhang, L. Wu, S. Niu, C. Song, Z. Zhang, G. Lu, C. Qiao, Y. Hu, K.-Y. Yuen et al., *Cell* 2020, 181, 894-904.e9.

Software used for reading PBD codes, visualization, and generation of figures:

1. The PyMOL Molecular Graphics System, Version 1.2r3pre, Schrödinger, LLC.

Software used for inspecting host-guest systems, protein surface preparation, ligand minimizations, 3D docking and MD simulations:

2. Schrödinger Release 2020-2: Maestro, Schrödinger, LLC, New York, NY, 2020.
3. Schrödinger Release 2020-2: Desmond Molecular Dynamics System, D. E. Shaw Research, New York, NY, 2020. Maestro-Desmond Interoperability Tools, Schrödinger, New York, NY, 2020.

## 9 APPENDIX

### 9.1 List of Abbreviations

<b>Abbreviation</b>	<b>Full Description</b>
AD	Alzheimer's disease
AlphaScreen assay	Amplified Luminescent Proximity Homogeneous Assay
APCI	Atmospheric pressure chemical ionization
Arg	Arginine
ATP	Adenosine triphosphate
AZT	3'-azido-2',3'-dideoxythymidine
BBB	Blood-brain barrier
BIR	Baculoviral Inhibitor of apoptosis Repeat
BIRC5	Baculoviral Inhibitor of apoptosis Repeat-Containing 5
BSA	Bovine serum albumin
CB	Cucurbiturils
CD	Circular dichroism
CDC25	Cell division cycle phosphatase
CLR01	Diphosphate molecular tweezer (CLR = clearance)
CLRF	Fluorinated CLR01 derivate
CN-A	Cotylenin A
COSY	$^1\text{H}$ - $^1\text{H}$ correlation spectroscopy
CPC	Chromosome passenger complex
CRC	Collaborative Research Center
CRM1	Chromosome region maintenance 1
CuAAC	Copper(I)-catalyzed azide alkyne cycloaddition
DCM	Dichloromethane
DEPT	Distortionless enhancement by polarization transfer

DHBA	2,6-dihydroxybenzoate
DHNA	1,3-dihydroxy-2-naphthoate
DIPEA	<i>N,N</i> -diisopropylethylamine
DLS	Dynamic Light Scattering
DMSO	Dimethyl sulfoxide
DTT	Dithiothreitol
ER $\alpha$	Estrogen receptor
ESI	Electrospray ionization
FAM	Carboxyfluorescein
FC	Fusicoccin
FDA	Food and Drug Administration
FP	Fluorescence polarization
GBA	Generalized Born approximations solvation
GC	Gas chromatography
GCP	Guanidiniocarbonyl pyrrole
GDP	Guanosine diphosphate
GPU	Graphics processing unit
GSH	Glutathione-Sepharose
GST	Glutathione-S-transferase
GTP	Guanosine Triphosphate
HD	Huntington disease
HIV	Human immunodeficiency virus
HMBC	$^{13}\text{C}$ - $^1\text{H}$ heteronuclear multiple bond correlation
HPLC	High-pressure liquid chromatography
HRMS	High-resolution mass spectrometry
HSQC	Heteronuclear Single Quantum Coherence
HTT	Huntingtin protein

IAP	Inhibitors of apoptosis proteins
IAPP	Islet amyloid polypeptide
INCENP	Inner centromere protein
IR	Infrared Spectroscopy
ITC	Isothermal Calorimetry
IUPAC	International Union of Pure and Applied Chemistry
KPT	Drug family Selinexor
LMB	Leptomycin B
Lys	Lysine
MD	Molecular dynamics
MS	Mass spectrometry
MSA	Multiple system atrophy
MST	Microscale thermophoresis
MT	Molecular tweezer
MTT	3-(4,5-Dimethylthiazol-2-yl)-2,5-diphenyltetrazoliumbromid
NAD	Enzyme cofactor adenine dinucleotide
NES	Nuclear export sequence
NFSI	N-fluoro-benzenesulfonimide
NLS	Classical import signal
NMNA	<i>N</i> -methyl nicotinamide iodide
NMR	Nuclear magnetic resonance
NOESY	Nuclear overhauser enhancement spectroscopy
NPC	Nuclear pore complex
NPT	Isothermal–isobaric ensemble of substance (N), pressure (P), and temperature (T)
OPLS	Optimized Potentials for Liquid Simulations
PDB	Protein Data Bank

PBS	Phosphate buffered saline
PDB	Parkinson's disease
PPI	Protein-protein interactions
RAN	RAs-related Nuclear antigen
RNA	Ribonucleic acid
ROESY	Rotating frame overhause effect spectroscopy
RP	Reversed phase
SARS	Severe acute respiratory syndrome
SFB	Sonderforschungsbereichs
SI	Supporting information
SMAC	Secondary mitochondria-derived activator of caspase
SPR	Surface plasmon resonance
TCNB	1,2,4,5-tetracyanobenzene
THF	Tetrahydrofuran
TLC	Thin-layer chromatography
TMS	Tetramethyl silane
TOCSY	Total correlation spectroscopy
TOF	Time-of-flight spectroscopy
TPP	Thiamine diphosphate
TTR	Transthyretin
UCLA	The University of California, Los Angeles
UV	Ultraviolet
ZIKV	Zika virus



## 9.2 ACKNOWLEDGMENTS – DANKSAGUNG – ZAHVALNICA

First and foremost, I would like to thank my *Doktorvater Prof. Dr. Thomas Schrader* for giving me the opportunity to pursue my Ph.D. in the field of applied research. During my doctoral studies, I have grown professionally and personally, through continuous learning and improvement. Thanks to the scientific freedom that he gave me, I have learned how to become an independent researcher, how to manage problems, face the unknown, and most importantly, how to persist. I was inspired by his extraordinarily broad knowledge and subtle guidance.

I would also like to express my gratitude to my co-examiner, *Prof. Dr. Shirley Knauer* for the interest she has shown for my work, useful discussions within cluster meetings, as well as for all the effort she invested into our *Masterpiece* – the Nature Communication manuscript.

I would like to thank *Prof. Dr. Bettina Siebers* for accepting to overtake the Chair of the examination board.

\* \* \*

It was my honor to be a member of the graduate school CRC 1093, being offered to learn about different scientific disciplines than chemistry, visit national and international conferences, broaden knowledge in computational and various instrumental methods, get to know – first collaboration partners and then friends for life. Special thanks to *Dr. Lydia Didt* for her great engagement and keeping *Alles im Griff*.

As members of the same crew, I cannot fail to mention *Prof. Dr. Christan Ottmann* and *Dr. Christine Beuck* as exceptional scientists and lecturers. Thanks for inspiring academic conversations and great collaborations. Further on, I am grateful to *Prof. Dr. Markus Kaiser* and his group for using their preparative HPLC and LCMS instrument, *Prof. Dr. Hemmo Meyer* for letting me use their MicroCal ITC instrument, *Prof. Dr. Luc Brunsveld* for using their SPR, MST, and FP instrument, *Prof. Dr. Daniel Hoffman* for his lectures on PyMol. I owe acknowledgment to *Prof. Dr. Mathias Eppele* for the fruitful collaboration and the time he invested in our manuscript. The cheerful characters of *Prof. Dr. Barbara Saccà*, *Prof. Dr. Laura Hartmann*; *Prof. Dr. Peter Bayer*,

and *Jun.-Prof. Dr. Jens Voskuhl* and their calming words full of understanding and support will always remain in my memory.

Special thanks to *Annika Meiners*, for her patience to explain biological assays to a chemist, for reading through the biological part of this work, and for her splendid engagement in our joint projects. Besides, *Selina van der Meer*, *Dr. Xavier Guillory*, *Pim de Vink*, *Dr. Sandra Bäcker*, *Dr. Cecilia Vallet*, *Matthias Hayduk*, *Dr. Mischa Baier*, *Theresa Seiler* and *Jonas Neblik*, are truly acknowledged for effective and joyful collaborations within CRC 1093.

\*\*\*

*Prof. Dr. Gebhard Habahauer's* enthusiasm for chemistry was contagious and I enjoyed our academic and non-academic conversations.

\*\*\*

Now, fearing that I will miss someone whose name deserved to be mentioned here, I will start chronologically to express my gratitude to all of those who have paved the way to this place where I stand now, starting with my former teachers.

Big thanks to *Prof. Dr. Peter Chen* for offering me an opportunity to join his group at ETH Zürich and gain knowledge at its very source. I will always be grateful for life coaching lessons, trust and all the support he offered me.

Draga *Sanja* znaš da ne postoje riječi kojima bih Ti mogla zahvaliti na svemu što si učinila za mene. Vidjela sam svijet zahvaljujući Tebi i Tvojim širokim pogledima u smislu nauke, života i ostalih dešavanja u Svemiru. Hvala beskrajno što znam da si uvijek tu za mene.

Hvala *Prof. Dr. Fehim Korać* sto si onako sportski i lagano, kako samo Ti to znaš, pokazao onima što su se pravili velikim igračima, da se može biti i čovjek i profesor u isto vrijeme. Hvala za sve naučne i private razgovore koje smo vodili. Iskreno hvala i što si istrpio moje dvije katastrofalne odbrane. Veliki govornik nikad nisam bila, ali ovaj put sam trenirala, obećavam.

Rektoru, *Prof. Dr. Rifatu Škrielju* se od srca zahvaljujem što je priznao najljepšom mogućom gestom sav uloženi trud mene i mojih kolega do postizanja uspjeha koji smo ostvarili nas deset zlatnih znački PMF-a, te 2013. godine.

Dekanu, *Prof. Dr. Mustafi Memiću* hvala na odličnim predavanjima i pronalaženju načina da objasni principe analitičkih metoda i instrumentalnih tehnika na način, tako da nikada ne izbljede iz sjećanja.

\* \* \*

Ohne administrative und technische Unterstützung wäre diese Arbeit nicht möglich gewesen. Danke an Frau Kunter, Frau Heinrich, Herrn Karow, Frau Kante, Frau Nowak, dem ganzen Team der Entsorgungszentrale und dem Team der Glasbläserei für Ihre Hilfe. Danke an die Auszubildenden *Melis, Kevin, Joana, Dominik und Alex* für die tolle Unterstützung und die Hilfe im Labor.

\* \* \*

Dank an meine deutschsprachigen Kollegen und Freunden. Danke *Klaus*, dass du immer ready-to-help warst. Deine Unterstützung, über einen Zeitraum von drei Jahren, möchte ich nicht missen. Es ist deine Schuld, dass mein Abzug im Labor immer in einem vorbildlichen Zustand war. Aus diesem Grund hat auch immer alles geklappt.

Danke *Heike*, für die zahlreiche Peptiden-Synthesen, Abspaltungen und die Trennungen, die du für mich gemacht hast. Dein Wissen, deine Hilfsbereitschaft und deine Kollegialität waren mir eine sehr große Unterstützung. Schön, dass es dich gibt.

Danke *Torsten* für die Zeit und Geduld, welche du für mich aufgebracht hast, um meine dringendsten Fragen der deutschen Sprache zu beantworten. Durch dich ist mir erstmal klar geworden, was der Unterschied zwischen „*das Gleiche* und *das Selbe*“ ist. Danke auch für die unzähligen Stunden, welche du mit mir verbracht hast, um 2D NMR Sudokus zu lösen.

Danke *Eva* für dein Vertrauen, welches du in mich investiert hast, als ich nur die Namen der Laborgeräte auf Deutsch nennen konnte. Die Betreuung des OC Grundpraktikums und die große Verantwortung, die damit verbunden war, haben mich dazu gedrängt, intensiver Deutsch zu lernen. Auch in der Zukunft werde ich mein Bestes tun, um das entgegengebrachte Vertrauen zu rechtfertigen.

Danke *Felix* für die Unterstützung mit Modeling und Schrödinger. Unsere gemeinsamen Mittagspausen waren immer sehr spannend und lehrreich. Der Blick in dein pinky Handy wirkte wie ein Blick in die weite Welt voller Wissen. Immer eine schöne und willkommene Ablenkung.

Danke an *Herrn Don M. Voß, Petra, Angie* und *Jolanta* für die Unterhaltungen und die gemeinsam verbrachte Zeit. Diese habe ich immer sehr genossen.

Big thanks to *Herr Dr. Heid* for your friendship, all the funny moments that we had together, all tricks and tips on the tweezer synthesis, modeling intro, for welcoming me in D41, and for correcting my thesis.

Warm thanks to my day-to-day lab colleagues and friends *Philipp, Abbna, Vanessa, Álvaro and My*. It was pleasure to work with you guys. I wish the best of luck and great results to Tweezer-Crew successors *Antonio* and *Estelle*. Thanks, *Nahid* for spoiling us with sugar in its various forms. Besides, I would like to thank the group's former members *Daniel & Frescilia, Burk, Max, Lok, Cat, and Kyra*. Without you the life in AK Schrader would not be as amusing and colorful.

The ORCHEM Crew (a.k.a. Gin-Truppe) deserves to be acknowledged as well. Thanks *Alex, Julian, Cat, Andrea, Abbna, and Philipp* for the great moments spent together while, let's say, we were presenting other people's research.

Thanks *Jonas, Nina, Hana, Sven* and *Janine* for being my first – best students at Uni DUE and great SHKs, bzw. Assis.

ETH Zürich provided me not only the world's class lectures but also was a place to make great and never-ending friendships. My heartfelt thanks to *Barbie, Makić, Krista, Luki, Ilia, Mihai* and *Armin*. Also, thanks to *Yanan, Vale, SJ, Augustan, Marek, Raphi, Joël-ić, Juan* and *Laurent* for keeping the entertainment constantly at the highest level.

Hvala i *Katedri za Organsku hemiju UNSA*, a posebno *Ameli, Senćiju* na tehničkoj podršci tokom studija, a i kasnije. *Aneli* hvala sto je od najbolje asistentica postala najbolja drugarica. Hvala i *Katedri za Fizikalnu hemiju* koja me iznjedrila. Hvala *Buci, Almi, Safi, Jeli* na nezaboravnim druženjima i svemu što ste me naučili. *Sanjinu i Rialdi* dugujem hvala na drugarstvu, hiking turama i dugim diskusijama o nedorečenim teorijama u nauci.

\* \* \*

Posebno mjesto u mom srcu kao i ovom radu zaslužuju moja *Zilka, Branka, Maja, Alma* i *Amna*. Zatim slijede oni prijatelji koji su tu i onda kada su miljama daleko, moja *Anida, Samra, Amina* i *Šehićeva*. Hvala vam za razumijevanje i riječi podrške onda kada najviše trebaju.

\* \* \*

Cijeloj porodici želim da se od srca zahvalim na razumijevanju koje imali za mene u toku izrade ovoga rada. Posebno hvala *svekru, Harfidu, Eldinu, Melisi i Papetu*. Potruditi ću se da se popravim gdje god sam proteklih godina zakazala zbog nedostatka vremena kao snaha, strina, sestra i tetka.

\* \* \*

Sada želim da istaknem prave heroje moje priče. One uzorne, čestite i pedantne ljude, žuljevitih ruku i čistog obraza. One zadovoljne i skromne, učevne i skrušene. One koji su me naučili disciplini, izdržljivosti, samostalnosti i poštenju. One koji su mi darovali sestru i brata, bez kojih ja ne bih bila ono što jesam. Hvala *Mama* što si od marke znala napraviti dvije – uvijek čvrsto vjerujući u nas troje i hvala *Babuka* što si mi dozvolio da sama biram svoj put i sreću.

\* \* \*

Zadnje, ali najveće hvala mom *Meldinu*, najboljem drugu i partneru na svijetu. Tvoj šarm, humor i nesebična ljubav su mi bili najveća podrška i oslonac. Beskrajno sam sretna i zahvalna što te imam. Volim te.

### **9.3 CURRICULUM VITAE**

The CV is not included in the online version for data protection reasons.

*This page intentionally left blank.*

*Mogu osvojiti svijet jednom rukom,*

*dok me ti držiš za drugu.*

*Meša Selimović*

---